2015

Design and construction of high temperature thermoelectric power generator module characterisation system

Tomas Katkus
University of Wollongong

UNIVERSITY OF WOLLONGONG

Institute for Superconducting and

Electronic Materials

Design and Construction of High Temperature Thermoelectric Power Generator Module Characterisation System

Tomas Katkus

This thesis is presented as part of the requirement for the

Award of the Degree of Doctor of Philosophy

of the

University of Wollongong

March 2015

ABSTRACT

Thermoelectric (TE) power generators (TEGs) are used to convert thermal energy directly into electrical energy. Therefore, thermoelectric power generation is believed to be among key technologies that will allow harnessing of large amounts of waste heat produced in steel and automotive industries. Currently used TEGs have limited conversion efficiency and don't have capacity to penetrate these highly important industry sectors. Nevertheless, thermoelectric power generators are already successfully used for waste heat energy recovery or for pure power generation in some of the niche fields, such as space applications, scientific equipment and facilities, and lasers. With increasing demand on clean energy sources and advancing thermoelectric technology/materials, the use of thermoelectric devices is becoming more prominent owing to their long lifetime, high reliability, and silent operation.

Currently, the efficiency of a typical low temperature TEG is approximately 5 %. Thus, in order to make thermoelectric power generation more attractive as an alternative energy harnessing technology, the overall efficiency of a TEG has to be significantly improved. The most of the research efforts concentrate on the development of novel TE materials, which would have higher Figure of Merit (zT), a value that indicates how good/bad thermoelectric material is. It is a widely accepted fact that for practical considerations the Figure of Merit for any given thermoelectric material, p- or n-type, has to exceed unity. Recent studies on nanostructuring and chemical modifications of well-known semiconducting thermoelectric materials have shown peak ZT values as high as 2.4 in the vicinity of 300 K for Bi_2Te_3 and 1.8 at 850 K for PbTe. The concentration of research efforts in the field of TE materials can be explained by the fact that thermoelectric properties of materials can be readily characterised using off-the-shelf measurement systems. However, knowing fundamental characteristics of a given thermoelectric material cannot be directly related to the conversion efficiency of a TEG.

The manufacturing of a thermoelectric power module includes selection of TE materials, electrodes, insulating plates, adhesives, and module architecture. The complexity of this task is easily illustrated by a very small number of research papers describing characterisation of thermoelectric modules. Furthermore, in contrast to the thermoelectric material characterisation systems, there are no commercial systems available that would allow accurate characterisation of fabricated TEGs. The lack of such systems tremendously hinders the capacity to effectively characterise "lab-built" thermoelectric generators. Although few TEG measurement systems have been reported in the literature, they all lack one or more key features of a comprehensive TEG measurement system: high temperature capability, adaptability to modules of various sizes, ability to operate in an inert atmosphere, sufficient module clamping force, and/or accurate and seamless electrical characterisation ability.

The main aim of this thesis was to design and construct a comprehensive computer controlled characterisation system, which would allow efficient characterisation of in-house built TEG modules. This system incorporates all of the above mentioned features in a bench-top engineering solution integrating high power heating, liquid cooling, hydraulic compression, force and temperature sensing – all in a controllable atmosphere.

The measurement system has been specifically designed to accommodate wide range of TEG modules suited for low to high temperature applications. The system accurately reproduces application conditions the module may be subjected to in a real world environment. Moreover, it measures electrical and thermal performance properties of TEG modules.

The main advantages of the built TEG module characterisation system are:

- ✓ Capability to measure TEG modules of various sizes;
- ✓ Simultaneous characterisation of multiple TEG modules;
- ✓ Maximum hot side temperature – 1000 °C;
- ✓ Variable atmosphere including air, argon, and/or vacuum;
- ✓ 20 kN module compression force can be applied during measurements;

- ✓ A sophisticated custom built computer based interface for accurate data collection;
- ✓ Custom designed electronic load for seamless TEG electrical characterisation;
- ✓ Direct heat flux measurements using reference materials.

Bismuth telluride based Thermonamic TEHP-12656-0.3 and Everredtronics TEG 127-50D TEG modules were characterised. Their performance data was analysed and compared to the available manufacturer data. The measured data correlated well with anticipated values, however, some discrepancies were observed due to the commonly overlooked inaccuracies in the conventional module resistance measurements. Further development of the system will ensure its suitability for accurate evaluation of TEG module performance.

ACKNOWLEDGEMENTS

I would like to thank my supervisors Dr. G. Peleckis, Prof. X. L. Wang, and Prof. S. X. Dou for giving me an opportunity to work at the Institute for Superconducting and Electronic Materials and sharing their knowledge and expertise with me. I am grateful to the University of Wollongong for providing me with the scholarships for the PhD studies. Without those this work would have been impossible.

Special thanks go to the AIIM workshop personnel, Mr. R. Morgan, Mr. P. Hammersley, Mr. J. Wilton, and Mr. M. Davies. Their knowledge, skills and expertise in the field help me to design this measurement system and achieve proficiency in mechanical and electrical engineering. Their major input in the selection of materials and design of certain components have reflected in the system being highly efficient.

I would also like to express my gratitude to all of the friends in and outside of Australia. Their support meant a lot to me and helped me to concentrate on the tasks ahead.

Lastly, I would like to thank my family and relatives for trusting me in accomplishing this major step in my life.

TABLE OF CONTENTS

LIST OF TABLES

LIST OF FIGURES

LIST OF TECHNICAL DRAWINGS

LIST OF ABREVIATIONS

2D – two dimensional;

3D – three dimensional;

A – Ampere; Area;

AC – Alternating Current;

ADC – Analog to Digital Converter;

Ah – Ampere hour;

AI – Analog input;

ANSI – American National Standards Institute;

AO – Analog Output;

ASCII – American Standard Code for Information Interchange;

Atm – Atmosphere;

AU – Australia;

BSP – British Standard Pipe;

CAD – Computer Aided Drawing;

CB – Circuit Board;

Ch – Channel;

CJR – Cold Junction Reference;

CLAD – Certified LabView Associate Developer;

CNC – Computerised Numerical Control;

CPE – Ceramic Plate Effect;

CSV – Comma Separated Values;

CTE – Coefficient of Thermal Expansion;

DAC – Digital to Analog Converter;

DC – Direct Current;

DI – Digital Input;

DIO – Digital Input or Output;

DMPPT – Distributed MPPT;

F – Force;

FET – Field Effect Transistor;

FGV – Functional Global Variable;

FIFO – First In – First Out;

GUI – Graphical User Interface;

HCD – Hybrid Centralised Distributed;

HW – Hot Water;

Hz – Hertz;

I – Current;

I/O – Input / Output;

IC – Integrated Circuit;

INC – Incremental Conductance;

K – Kelvin; thermal conductance;

KF – Klein Flange. Same as QF, NW, and DN;

l – length;

L – Liter;

LabVIEW – Laboratory Virtual Instrument Engineering Workbench;

LED – Light Emitting Diode;

LTD – Limited;

MAE – Mean Absolute Error;

min – minute;

mol – mole;

MOSFET – Metal Oxide Semiconductor FET;

MPP – Maximum Power Point;

MPPT – MPP Tracking;

MS – Microsoft;

N – Number of thermocouples; Newton;

NC – Normally Connected;

NI – National Instruments;

NO – Normally Open;

NPN – Doping type of a Bipolar Junction Transistor;

NW – see KF;

NZ – New Zealand;

^{o}C – degrees Celsius;

P – Power; Pressure;

P & O – Perturb and Observe;

Pa – Pascal;

PhD – Doctor of Philosophy;

PID – Proportional Integral Derivative;

PV – Photovoltaic;

Q – Heat flow;

QS MPPT – Quick Scan MPPT;

R – electrical Resistance; Universal gas constant, 0.082057 LAtm/Kmol;

Rev. – Revision;

RPM – revolutions Per Minute;

RTG – Radioisotope Thermoelectric Generator;

S – Sample;

s – second;

SSE – Sum of Squared Errors;

SSR – Solid State Relay;

T – Temperature;

t – time;

Tc – Cold side temperature;

TC – Thermocouple;

TDMS – Technical Data Management Streaming;

TE – Thermoelectric;

TEC – Thermoelectric Cooler;

TEG – Thermoelectric Power Generation (-or);

Th – Hot side temperature;

TIG – Tungsten Inert Gas;

TPV – Thermophotovoltaic;

TXT – TeXT file extention.

U – Voltage;

USR – Uninitialised Shift Register;

V – Voltage; Volt; Volume;

VAC – Voltage Alternating Current;

VDC – Voltage – Direct Current;

VI – Virtual Instrument;

VM – Molar Volume (24.789 L/mol)

W – Watt;

Z – Figure of Merit;

ZT – dimensionless Figure of Merit;

α – Seebeck coefficient;

η – Efficiency;

κ – Thermal conductivity;

πa-b – Peltier coefficient for the junction of materials a and b;

ρ – Electrical resistivity;

σ – Electrical conductivity;

τ – Thomson coefficient;

Ω – Ohm;

1 INTRODUCTION

Thermoelectric power generation is believed to be among key alternative energy harnessing solutions in the near future. This technology is based on a thermoelectric phenomenon, a physical process allowing conversion of thermal energy directly into electricity. In contrast to other alternative energy generation technologies, such as solar or wind power, thermoelectric power generation has several advantages. They include long life time, silent operation, no moving parts, low maintenance, and suitability to be used in extremely wide range of environments. This is illustrated by the application of thermoelectric power generators in space, automotive industry, computer components, domestic appliances, and geothermal power harnessing.

Despite its high potential, this technology still needs to achieve several important milestones, before it can truly penetrate our daily lives. Several reasons can be highlighted here, as to why thermoelectrics haven't been used as abundantly as they could. Firstly, most of the presently used thermoelectric modules are built from well-known semiconducting materials such as bismuth telluride or lead telluride. These compounds are hazardous, expensive, and are not stable at elevated temperatures. Secondly, the typical conversion efficiency currently achieved in thermoelectric modules is only in the vicinity of 5%, which is simply not acceptable for widespread practical applications.

Many researchers around the globe are concentrating on the development of highly efficient thermoelectric materials, which is the backbone of thermoelectric power generators. Recent advances in this field have shown some breakthrough achievements, with thermoelectric materials showing very promising performance. However, in many cases such improvements in the performance are achieved in highly specialised materials, e.g. multilayer or superlattice structures, which cannot be considered for industrial scale fabrication. On the other hand, nanostructuring, such as inclusion of Na ions in PbTe bulk materials, has shown promising results and can be considered for upscaling.

Yet, little emphasis is being placed on the fabrication and characterisation of actual thermoelectric power generator modules. This is mainly caused by the complex tasks involved in the manufacturing of these devices. A thermoelectric power generator module consists of many parts including thermoelectric legs, electrodes, adhesive, ceramic insulators plates, and wiring. Finally, the architecture and design of the thermoelectric power module has to take into account intended application, which might vary greatly. For instance, selection of special materials has to be considered if thermoelectric power generator is to be used at high or low temperatures, oxidizing or inert atmosphere, and/or environment with significant mechanical loads. In principle, each thermoelectric power generator module is unique and specifically built for certain purpose. Finally, there are no commercial products available on the market which would allow fast and efficient characterisation of such modules. This is the main reason, why there is very little data available depicting actual conversion efficiencies of laboratory built thermoelectric power modules. Consequently, there is a large discrepancy between knowing fundamental properties of "promising" thermoelectric materials and their actual performance in a fabricated device.

In this thesis, a ground up approach has been utilized to design, manufacture, and evaluate a home built thermoelectric power generation module characterisation system. Much effort has been put in the accurate investigation of specific parameters needed, for the system to be as comprehensive and versatile as possible. A comprehensive literature review and state-of-the-art analysis was performed, to understand the current status of such systems in laboratory and industry environments. An emphasis was placed to construct a system, that would allow efficient characterisation of a wide range of thermoelectric power generator modules, yet to be simplistic and easy to use. A comprehensive design and manufacturing work was performed an all aspects of the system including hardware, electronics, software, and safety designs. A range of computational algorithms used for data acquisition and analysis were carefully chosen to reflect the need for accuracy and reliability. All obtained data and analyses in this work were used to further develop the system, which ensured its structural and electronic integrity, safety and accuracy. The performance of the system and essentially its capacity to undertake high quality measurement work was evaluated by investigating commercially available

thermoelectric power generator modules with known performance values. The thesis consists of three main parts: the literature review, system development sections, and discussions for its measurement performance.

Because our system is closely related to thermoelectric materials and thermoelectric technology, an understanding of key fundamental properties of thermoelectric phenomenon is highly important. The first part of the thesis deals with the introduction of basic concepts of thermoelectricity, heat flow, electronics, application of thermoelectric materials, thermoelectric power generators, and their design and applications. A comprehensive literature review on the current research on thermoelectric materials and thermoelectric power generators is given. This information is consolidated in Chapter 2.

The major part of the thesis is dedicated to the description of the design and manufacturing processes of our thermoelectric power module characterisation system. The bulk of the work is distributed among three Chapters, i.e. Chapter 3 to Chapter 5.

Chapter 3 deals with the design and fabrication of the hardware components, such as system's main body, design of the cooling and heating systems, and gas control. The information in this Chapter is supported by a number of technical drawings presented in Appendix A. All hardware components are described to the best possible accuracy, so any faulty hardware components can be remanufactured if needed. The selection of materials and specific design solutions are explained and illustrated.

Chapter 4 provides comprehensive information on the development and design of the electronic load and associated electronics used in the measurement system. Many of the electronic circuit boards have gone through multiple revisions and developments. In depth information of the components used is provided in Appendix B.

Chapter 5 describes the development and design of the computer interface. The interface was based on the LabView suite, which is among most widely used

equipment interface software packages worldwide. The development of calculation algorithms and data estimation and verification is also presented.

Chapter 6 concentrates on the evaluation of the built system by measuring commercially available modules. Relevant performance curves, analysis of data and discussions are covered in the Chapter.

Chapter 7 provides conclusions and recommendations for the future development of the system. The recommendations provided in the Chapter target improving systems responsiveness, accuracy, and reliability. This Chapter is followed by a set of Appendixes designed to provide reader with thorough information such as technical drawings and wiring tables. A list of the references used in this work concludes the thesis.

2 THERMOELECTRIC DEVICE FUNDAMENTALS AND LITERATURE REVIEW

Thermoelectricity stands for direct conversion of thermal energy into electrical energy (and *vice versa*) [1]. This Chapter introduces thermoelectric effects and principles of thermoelectric module construction. Thermoelectric phenomena have been known for over a century, and are widely used for cooling, temperature measurements, and power generation. This thesis solely focuses on thermoelectric power generator modules. Having good understanding of underlying thermoelectric effects is of crucial importance for thermoelectric system designers. This Chapter describes the thermoelectric effects, TEG module structure, and module characterisation principles.

2.1 Seebeck Effect

A conductor is a material which has free charge carriers – electrons, holes, or ions. The charge carrier flow is electrical current. It can be induced by applying voltage to the conductor, or by placing the conductor in a temperature gradient. If a conductor has a temperature gradient heat will be conducted by lattice vibrations – the phonons, and also by the charge carriers migrating from hot side to the cold side. Charge carrier concentration gradient will create a potential difference across the conductor, stopping the charge carrier concentration gradient increase. The resulting equilibrium potential difference is the so–called Seebeck voltage. Seebeck voltage across 1 K temperature gradient is called Seebeck Coefficient. Seebeck Coefficient is a function of temperature.

Two conductors are needed to close a current loop in a temperature gradient. Two conductors of the same material would cancel their Seebeck voltages and result in zero net voltage. Two dissimilar conductors, on the other hand, would result in a voltage equal to the difference of their respective Seebeck voltages (Equation 2.1). This thermoelectromotive force was discovered by T. J. Seebeck in 1821.

$$V = \int_{T_c}^{T_h} (\alpha_a - \alpha_b) dT$$

Equation 2.1. Voltage of two dissimilar conductors in a temperature gradient.

For applications, it makes sense to use materials having opposite Seebeck Coefficient signs. In this case their Seebeck voltages add up, instead of partially cancelling for materials with Seebeck coefficient of the same sign. For temperature sensing purposes materials are typically paired to produce Seebeck voltage which is proportional to the temperature in degrees Celsius. For example K–type thermocouple is made of Chromel and Alumel and has approximately 41 µV/K sensitivity from -200 to 1350 ºC. In contrast, for the power generation applications the absolute Seebeck voltage generated is more important than its temperature linearity. Typical Seebeck coefficient values of good materials for thermoelectric power generation are in the order of few hundreds µV/K, both negative and positive.

2.2 Peltier Effect

Peltier Effect is opposite to the Seebeck Effect. If a direct current is passed in a circuit of two dissimilar materials, heat will be liberated in one junction, and absorbed in the other. If the current direction is reversed, the heat liberation and absorption locations will also reverse. The effect was discovered in 1844 by J. C. A. Peltier. The heat liberation or absorption can be explained by the change in the kinetic energy of the charge carriers passing the junction of the two materials. The Peltier Coefficient is the ratio of heat flow rate of either of the junctions and the direct current flowing in the circuit (Equation 2.2).

$$\pi_{a-b} = \frac{Q}{I}$$

Equation 2.2. Peltier Coefficient.

Peltier Coefficient is measured at isothermal conditions. Its unit of measure is 1 Volt. Typically the maximum temperature difference a bismuth telluride based Peltier

module can reach is around 70 K. It is limited by the Joule heating due to the increasing module current.

2.3 Thomson Effect

In 1854 W. Thomson (Lord Kelvin) observed that a unit length of material with temperature gradient along it will dissipate heat in excess of Joule heating when current flows. The Thomson coefficient is defined as:

$$\tau = \frac{dQ}{I\,dT}; \quad Q = I\int_{T_c}^{T_h} \tau dT$$

Equation 2.3. Thompson Coefficient and heat released due to Thomson Effect.

The unit of measure for Thomson Coefficient is [τ] = 1 V/K. Thomson Effect is often neglected in thermoelectric calculations because usually it is much smaller than the Joule heating [2]. However, Thomson heat can become significant at large temperature gradients [3, 4].

2.4 Kelvin Relationships

The Kelvin relationships describe the links between the Seebeck, Peltier, and Thomson Effects. Peltier Coefficient relates to Seebeck Coefficient as shown in Equation 2.4.

$$\pi = \alpha T$$

Equation 2.4. Relationship between Peltier and Seebeck Coefficients.

This relationship is experimentally confirmed and allows calculation of the heat flow due to the Peltier Effect as per Equation 2.5.

$$Q = \alpha IT$$

Equation 2.5. Peltier heat expressed through Seebeck Coefficient.

Thomson Coefficient relates to the Seebeck Coefficient as shown in Equation 2.6.

$$\tau = T_{avg} \frac{d\alpha}{dT}$$

Equation 2.6. Relationship between Thomson and Seebeck Coefficients.

2.5 Thermoelectric Power Generation Module Design

TEG module is a solid state device which converts heat flux into electrical current. Thermoelectric generators have the advantages of being simple, rigid, do not have moving parts or working fluids, and operate silently. The module produces DC voltage which depends on the module temperature gradient and the number of thermoelectric elements, or legs, used. A generator module usually consists of a multitude of pairs of alternating p- and n-type semiconductor legs, which are arranged thermally in parallel and connected electrically in series. Figure 2.1 shows the main parts of a flat plate type TEG module, which is the type of modules focused on in this thesis.

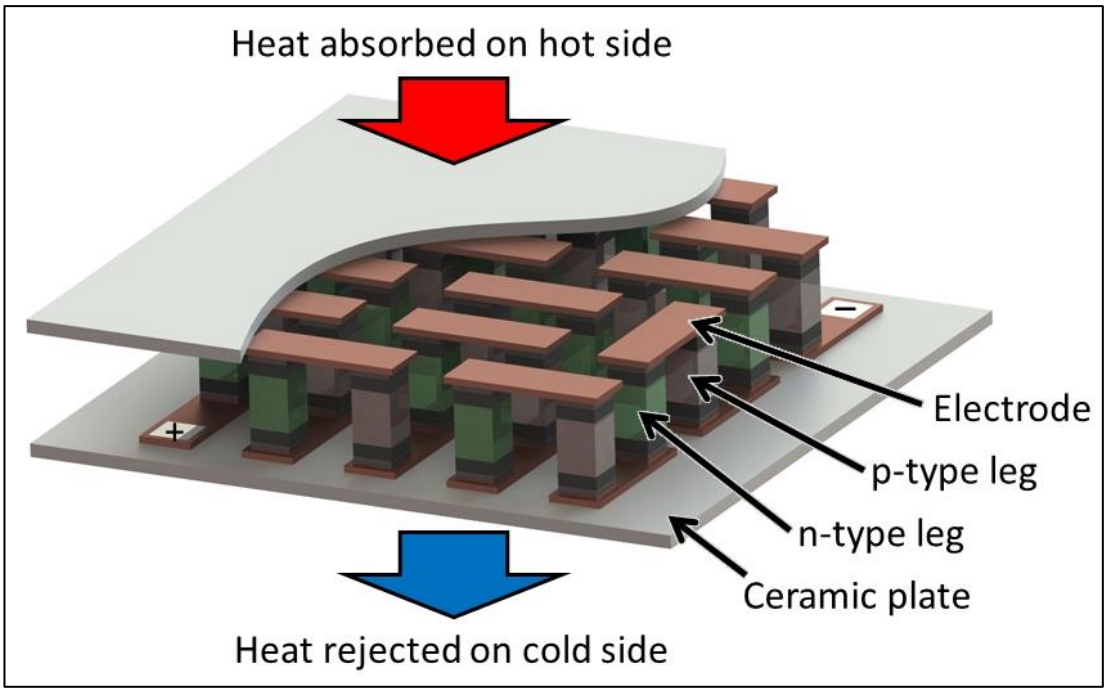

Figure 2.1. CAD model of TEG module showing main module parts [5].

Materials with the best thermoelectric properties usually are heavily doped semiconductors, which have their carrier concentrations tuned for the optimum combination of Seebeck Coefficient, electrical conductivity, and thermal conductivity. The module application temperature will depend on the thermoelectric materials used. The most commonly used material for TEG modules is bismuth telluride with a typical Seebeck Coefficient of approximately 350 µV/K. However, bismuth telluride module application temperature is limited to 350 ºC for the highest performance modules. Higher temperature applications, *e.g.* heavy industry and/or automobiles, require use of other materials such as silicides, oxides, skutterudites, sulphides [6].

Figure 2.1 shows a CAD model of 28 leg TEG module with the top ceramic plate cut away to illustrate the module internal construction. Typical 56 x 56 mm TEG modules can contain from 62 up to 900 legs. The open circuit voltage depends on the number of legs used, therefore it can be from 2.5 V to over 25 V. In Figure 2.1 model the heat is supplied to the top (hot) side, and removed from the bottom (cold) side. Thermoelectric material legs are soldered to copper electrodes andthese electrodes connect all the legs into a single chain. Charge carriers will move in the same

direction – from hot side to cold side. Since the Seebeck voltage is of opposite sign for electrons and holes, the voltages of each leg will be added up. Thin ceramic plates provide structural support and electrical insulation to the module assembly. Typically alumina ceramics is used, but when better substrate thermal conductivity is needed aluminium nitride ceramics may be used. Thermal stresses experienced bu the module, when it is in thermal gradient limit the physical size of a TEG module to 100 x 100 mm. The lateral expansion of the hot plate may cause sheer stress to the thermoelectric material legs. Mismatch of the coefficients of thermal expansion (CTE) may cause tension and compression forces on the legs.

The same thermoelectric module can be used as a power generator and as a heat pump. In either case all thermoelectric effects are taking place, but Seebeck Effect dominates in power generation mode while Peltier Effect dominates in the heat pumping or cooling mode.

2.6 TEG Module Physical Properties

Module thermal conductance (K) determines the heat flux through the module during open circuit operation. Ideally it should be as low as possible because it results in a heat flow which does not result in electric power generation. Thermal conductance of a real TEG module is reciprocal of series of thermal resistances of the module components as shown in Equation 2.7.

$$\frac{1}{K_{TEG}} = \frac{2}{K_{ceramics}} + \frac{2}{K_{electrodes}} + \frac{1}{K_{TE}}$$

Equation 2.7. TEG module thermal conductance during open circuit operation.

Thermal conductance of thermoelectric material legs depends on their thermal conductivities, leg length, and leg area. Since the legs are arranged thermally in parallel, their thermal conductances add up. For N thermocouples in the module the total leg thermal conductance is:

$$K_{TE} = N\left(\kappa_p \frac{A_p}{l} + \kappa_n \frac{A_n}{l}\right)$$

Equation 2.8. Thermal conductance of thermoelectric material legs.

As soon as electrical current is allowed to flow in the load, Peltier Effect and Joule heating increase the amount of heat conducted through the module. The increase in the effective module thermal conductance depends on the magnitude of the electric current. Module thermal conductance will be at its highest during short circuit operation. Based on this observation, a variable thermal resistor has been proposed [7].

Module electrical resistance (R) determines the maximum electrical current flow in the module. Preferably it should be low, as it causes Joule heating, which is a parasitic effect. Equation 2.9 shows an expression for TEG module internal resistance. Thermoelectric material legs are connected in series by metal electrodes, therefore the resistances of legs, electrodes, and leg to electrode contacts are added.

$$R_{TEG} = N\left(\rho_p \frac{l}{A_p} + \rho_n \frac{l}{A_n} + 2R_{Electrode} + 4R_{contact}\right)$$

Equation 2.9. TEG module electrical resistance.

The contribution of electrode resistance to the total module resistance is typically minor. However, the soldered contact resistance can be significant and be as high as the thermoelectric material leg resistance.

Module voltage (U) depends on the number of thermocouples in the module and the thermal gradient at the thermoelectric material legs (Equation 2.10).

$$V_{Open\ circuit} = N\int_{T_c}^{T_h}(\alpha_p - \alpha_n)dT$$

Equation 2.10. TEG module voltage.

All application conditions being equal, the module voltage is a trade–off with module current. High number of small legs will produce high voltage, but also high resistance resulting in lower current and higher module complexity. Alternatively, module with lower number of larger area legs will be more robust, will produce lower voltage, but will have much lower resistance and, thus, high current [8].

Leg length (contributing to the module height) determines module resistance (Equation 2.9) and consequently module current. Furthermore, it determines module thermal conductance (Equation 2.10), influencing module heat flux. Finally, very short legs may result in reduced module voltage, when the temperature drop over the ceramic plates becomes significant when compared to the temperature drop across the leg [9]. A typical leg length in a thermoelectric module ranges from less than a millimeter to few millimeters.

Module heat flux will vary with module current. The main contributor to the heat flux is thermal conduction. Peltier heat pumping and Joule heating contribute lesser, but significant amounts. Equations defining heat flux through TEG module hot and cold sides are shown in Equation 2.11 and Equation 2.12 respectively.

$$Q_h = V_{OC} T_h I + K\Delta T - \frac{I^2 R_{TEG}}{2}$$

Equation 2.11. Heat flux through TEG module hot side.

$$Q_c = V_{OC} T_c I + K\Delta T + \frac{I^2 R_{TEG}}{2}$$

Equation 2.12. Heat flux through TEG module cold side.

TEG module efficiency is defined as the ratio between the electrical power delivered to the load and thermal power absorbed on the hot side of the module (Equation 2.13). In practice, the hot side heat flow is difficult to measure accurately due to the radiation losses; therefore, cold side heat flow is often used for efficiency calculations. Assuming minimal radiation losses on the module, the hot side heat flow equals to the sum of cold side heat flow and electrical power extracted.

$$\eta = \frac{P_L}{Q_h} \cong \frac{P_L}{Q_c + P_L}$$

Equation 2.13. TEG module efficiency.

Similarly to thermoelectric material's dimensionless Figure of Merit ($zT = \frac{\alpha^2 T}{\rho\kappa}$) thermoelectric device's dimensionless Figure of Merit (Equation 2.14) can be used to compare the efficiencies of the devices.

$$ZT = \frac{\alpha^2 T_{avg}}{KR}$$

Equation 2.14. TEG module dimensionless Figure of Merit.

The module efficiency relates to the module Figure of Merit through Equation 2.15.

$$\eta = \frac{\Delta T}{T_h} \cdot \frac{\sqrt{ZT + 1} - 1}{\sqrt{ZT + 1} + \frac{T_c}{T_h}}$$

Equation 2.15. Efficiency dependence on the dimensionless Figure of Merit [10].

2.7 Thermoelectric Devices

Thermoelectric device is a device allowing conversion of heat directly into electricity and *vice versa*. Thermoelectric devices can be operated in two modes. (1) When electrical current is applied, thermoelectric device operates in a heat pumping mode. The direction of the heat pumping depends on the direction of the applied current. This mode can be used for cooling purposes by pumping heat out or for heating by pumping heat into the system. (2) When a thermoelectric device is placed in a temperature gradient, it will operate in a power generation mode. With the temperature gradient maintained through the thermoelectric device, the resulting heat flow will generate direct electrical current in the load connected to the device's terminals.

Thermoelectric devices operating in a heat pumping mode are used for a number of applications, such as laser and electronic device cooling [11], improving efficiency of refrigerators [12, 13], water heaters [14], and proposed improvements of large Rankine cycle power plants [15].

This thesis focuses on the development of a measurement system which allows precise characterisation of a thermoelectric generator module. Nevertheless, the measurement system can be easily modified to characterise thermoelectric heat pumps too.

Thermoelectric generators (TEGs) are very reliable, but have relatively low efficiency and high costs. These drawbacks have limited the use of TEGs to very specialised medical, space, and military applications [16, 17]. Thermoelectric generator reliability is very well demonstrated by the Radioisotope Thermoelectric Generators (RTGs) used by NASA space missions. RTGs have been used for U. S. space missions since 1961, e.g. Voyager 1 and 2 were launched in 1977. They still operate today, which is almost four decades of continuous operation [18]. Most RTGs use ^{238}Pu, which has a decay half-life of 87.7 years. It has been calculated that RTGs using this material will degrade in power output by a factor of 0.8% per year.

Various environmental concerns have driven much research effort towards alternative energy sources. Thermoelectric power generation is a viable option for waste heat energy recovery. Recent advances in thermoelectric materials and thermoelectric generators makes thermoelectric power generation an economically attractive choice, where large amounts of waste heat are rejected to the atmosphere and cannot be recovered using other technologies [19].

2.8 Applications of Thermoelectric Generators

Thermoelectric power generation from exhaust gas of internal combustion engines is very promising and receives a lot of interest. Power generation from automobile exhaust gas has the potential to reduce fuel consumption by removing mechanical load from the alternator. Typical exhaust gas temperatures are up to 600 ºC for diesel

engines, and up to 1000 ºC for petrol engines. The amount of heat available in such conditions ranges from 20 kW during highway cruising to hundreds of kilo Watts under heavy engine loads [20].

A practical viability of medium–temperature waste heat recovery has been demonstrated with four bismuth telluride modules on a stationary diesel generator [21]. 1350 W electric power was computer-modelled and experimentally verified in a five-section TEG system on a stationary diesel generator, however, very little design details were disclosed [22]. A cylindrical TEG generator has been designed, built, and tested. It has been installed in BMW X6 and Lincoln MKT vehicles with petrol engines. On-vehicle tests produced 600 W of electrical power on a matched resistor. The matched generator output voltage was found to be only about 1 V, and, consequently, very high current. It is very challenging to convert and return power generated in this form back to the vehicle's electrical system [23]. 358 W of electric power has been simulated from TEG generator mounted on the exhaust manifold of a petrol engine. It was calculated that it has the potential to reduce the fuel consumption by 2.5 % at 160 km/h [24].

Bismuth telluride is the most commonly used material for TEG applications. However, its application temperature should not exceed 300 ºC, and supply of tellurium is very limited. Furthermore, one has to account for tellurium's toxicity, which has been acknowledged by the European Union, which will prohibit the use of tellurides and selenides in thermoelectric applications in the near future. As a result other materials suited for high temperature applications with promising performance such as silicides and skutterudites[6], and oxides[25] were suggested for automotive applications. High temperature reaction prevention and reliable metallisation are some of the issues that need to be solved prior to their integration into commercial products.

TEG generators have been shown to work well with wood fired stoves. 4.2 W have been generated from a single module with convective cooling [26]. Over 10 W of power has been produced from TEGs with forced convection cooling [27, 28]. Authors report the significance of hot surface flatness and clamping force to the

generator's thermal contact and resulting performance reduction from the expected values [29]. TEG module fitted to a portable biomass cook stove can produce 3 Wh of electrical energy to charge a $LiFePO_4$ battery in one hour [30, 31].

Similarly to the aforementioned systems where TEGs heat air, power can be generated from stoves used to heat water [32]. Such systems generate electricity while heating water and are called combined heat and power (CHP) systems [33]. It has been shown that overall system efficiency is equal to the efficiency of conventional heating system, but the CHP system has the advantage of both – heat and electricity produced [34].

It has been calculated that additional 184 kW of electric power could be generated in a power generation station driven by a 10 MW internal combustion engine [35]. Similarly, it has been calculated that around 150 kW of electric power can be generated from waste heat in the vapour condenser of a 700 MW steam power plant using iron based alloys. With bismuth telluride based materials the generated power would reach 18 MW [36]. Thermoelectric generator made of sixteen 50x50 mm modules was installed on a 25 kW carburizing furnace in Komatsu LTD., Awazu plant. 225 W of electric power is being generated since 2009 [37]. 1 kW TEG system operating on geothermal energy has been theoretically modelled and optimised [38].

Efficiency increase of 8 to 23 % has been modelled using idealised model for TEG modules combined with Photovoltaic (PV) panels compared to PV panels alone. Nevertheless, the author agrees that realistically the overall conversion efficiency may be much lower than expected, practical implementation of such system is very difficult, and the costs could be tenfold higher than PV panels alone [39]. Similar results were obtained from PV–hot water (HW) and PV–TEG–HW system comparison. Theoretical calculations predict 30 % increase in overall system efficiency, but no improvement is gained practically [40]. Finite element modelling predicts 16.4 % conversion efficiency for three–stage thermoelectric module heated by 184 times concentrated solar radiation [41]. Thermophotovoltaic (TPV) cells have been cascaded with TEG modules. The cascaded system has slightly higher

efficiency than either components separately [42]. Innovative techniques for thermoelectric power generation using solar heat are reviewed [43].

It has been shown that a single 30 x 30 mm TEG module can produce enough power to operate a passive sensor with RF transmitter from only 30K temperature gradient [44]. TEG stacked with a solar cell, combined with 1.4 Ah lithium battery has been built as a sensor power source. TEG module improves solar cell efficiency by 5.2 % by cooling it down, but only generates 2 mW of power due to the very low temperature gradient (<4 K) over the TEG [45]. Power management systems for low voltage TEG power harvesting have been proposed [46, 47]. TEG systems using phase change materials have been modelled to harvest energy during aircraft taking-off and landing, to power wireless sensor networks [48, 49]. Likewise, TEG power generation was proposed for powering autonomous underwater vehicles. The system would use thermal mass and exploit depth dependant ocean water temperature [50].

Studies have been done showing potential energy cost savings in automotive, CHP, and heating applications. However, TEG contributions would be lower when compared to steam expanders in the same systems, but TEG generators are more advantageous in terms of size, simplicity, and reliability [51, 52]. Recent patents on TEG power generation are reviewed [53]. Recent research and findings for thermoelectric materials are reviewed [54-56].

2.9 Thermoelectric Generator Module Testing

The designers of thermoelectric power generation systems can only use TEG module specifications provided by the module manufacturer. It is crucially important for this information to be reliable. The TEG module characterisation can be challenging because temperature, electrical, heat flow, and compression force measurements have to be taken simultaneously at controlled conditions. Generally, heat flow measurement is the most challenging part due to the various heat losses in the measurement system.

Several TEG module testing systems have been built and reported. Rauscher et al. have developed a system to characterize bismuth telluride TEG modules [57]. It uses an absolute method employing guard heater and radiation screens for heat flow measurement. This system can characterise modules which are 23.5 x 23.5 mm^2 in size. Takazawa et al. have built a module testing system in which the heater temperature can reach 900 K [58]. It uses copper heat exchangers to measure heat flux on the cold side of the module. The system operates in vacuum and uses water–cooled radiation shielding. Sandoz-Rosado and Stevens have developed TEG testing apparatus capable of hot side temperature of 500 ºC for 14 x 15 cm^2 modules [59]. Power delivered to the module is calculated by subtracting calibrated heat losses from the power delivered to the heating block. The authors stress the importance of inclusion of the ceramic plates into the analytical models, as, in their case, the decrease in tested efficiency was 18 % lower than the modelled efficiency. Han et al. presented an analytical model to predict TEG module performance together with 40 x 40 mm^2 module experimental setup employing 40 W heater for a small temperature gradient [60]. Measurement equipment constructed by Anatychuk and Havrylyuk can measure modules up to 100 x 100 mm^2 in size, reach 600 ºC on the hot side, and apply compressive force of up to 1800 N [61]. It uses calibrated heat meter for heat flux measurements and is operated in air. Faraji and Akbarzadeh have designed a compact TEG module testing system [62]. This system measures 40 x 40 mm modules, with 200 W power available on the hot side and 460 W cooling power available for the cold side. The authors show the module output power dependence on clamping pressure. Populoh et al. describes a test stand built to characterise high temperature TEG modules based on telluride, heusler, and oxide materials [63]. The heat flux is calculated from a temperature distribution in the reference block. Modules of sizes up to 40 x 40 mm^2 can be characterised at temperatures of up to 1150 K. The system has controlled atmosphere available using a bell jar with rotary vacuum pump. Montecucco et al. present a test rig with hot side temperature of up to 800 ºC, clamping load of up to 5 kN [64]. The test rig can test four modules simultaneously, while heated by separate 2 kW heaters with testing performed in air. Hejtmanek et al. present a measuring device for TEG modules or bulk TE materials with maximum hot side temperature of 450 ºC, up to 10 kN mechanical loading in air [65]. The module heat flux is measured using copper heat exchanger on the hot side

of the TEG module. Nielsen et al. have developed a high–temperature TEG measurement system. It is designed for hot side temperatures of up to 1000 ºC, and operates in vacuum [66]. It uses Omega heat flux sensors on the cold side.

In most of the aforementioned systems the heater is placed on top of the thermoelectric module. This is done to minimise the convective heat transfer, if the measurements are done in air or other gas.

Even though the number of measurement systems constructed grows rapidly each year, the TEG module testing is not standardised. Consequently, measured module performance often differs from datasheet performance. For example a considerable difference in module resistance between measured and manufacturer's data was found by Kinsella et al. [31] using a testing setup based on Sandoz–Rosado design [59]. Any performance data inaccuracies would be amplified in larger scale applications.

A TEG module testing system was designed and built to characterise modules built at the Institute for Superconducting and Electronic Materials, University of Wollongong. Most of the measurements systems described above are somewhat limited in their operation, for example low temperature, fixed module size, and/or operation in single atmosphere. The design of out system addresses these limitations. The heater can operate continuously at 1000 ºC with plenty of power available to generate adequate heat flux. Modules of up to 100 x 100 mm in size can be measured. The TEG module can be clamped with up to 20 kN of force. Measurements can be done in air, vacuum, or inert gas atmosphere. Instrument is controlled with computer software and electrical module characterisation is done with the help of purposely built electronic load.

Typically, for electrical characterisation, a constant temperature gradient is maintained across the module. With the temperature applied, the module is essentially a constant voltage source with a series resistance [9, 67]. As a result the module current–voltage behaviour is linear. Maximum power is extracted from the module when its voltage and current equals to half of their respective maximum

values. This happens when the load resistance equals the module internal resistance. Such situation is called the Maximum Power Point (MPP). If the system adjusts itself for the changes in operating conditions to stay on MPP, it is called Maximum Power Point Tracking (MPPT) [68].

Analytical modelling of steady state behaviour is often done for comparison with experimental results [59, 60]. Some papers simulate thermoelectric systems with thermal and electrical transients [69]. Transient state operation would be dominant in automotive applications and in stove applications when heating up or cooling down [70, 71]. SPICE and ANSYS electronic circuit simulators are used to aid in the simulations. For this purpose, thermoelectric systems are modelled using equivalent electronic components such as resistors and capacitors [67, 72]. It has been shown that thermoelectric generator modules respond to electrical load transients almost instantaneously, in the order of nanoseconds. In contrast, the thermal response is much slower due to the thermal masses in the system, and is in the order of minutes [73].

2.10 Power Extraction from TEG Modules

Practical TEG module applications often have varying thermal conditions. For example automobile exhaust temperature change can be very rapid. In such cases TEG module power must be extracted in precisely controlled manner, matching the load resistance to the varying module resistance. Additionally, the resultant MPPT voltage often has to be stepped up or down. This typically requires the use of DC–DC converters with MPPT algorithm.

MPP tracker output compared to the maximum power available from the TEG module is referred to as MPPT efficiency. MPPT voltage is then converted to the desired level with the efficiency of the DC–DC converter. MPPT algorithms set the duty cycle of the DC–DC converter's inductor current so that the apparent inductor resistance matches TEG module's resistance.

Many MPPT algorithms are suitable for TEGs. Most of them are adapted from PV MPPT systems. Most common MPPT algorithms are Perturb and Observe (P & O) [74, 75], Incremental Conductance (INC) [76], and Fractional Open–Circuit (FOC) [77, 78]. P&O algorithm periodically measures TEG module voltage and current, calculates power, and compares it to a previously measured value. If the power increases, the algorithm will step module voltage in the same direction, if the power decreases, indicating the MPP being passed, the voltage stepping will change direction. Once the MPP has been reached, the P&O will oscillate around it. INC algorithm tracks by stepping the voltage just like P&O. Only the direction of stepping is determined by comparing incremental conductance of the source to the negative of instantaneous conductance. Step size for these two algorithms is a trade-off between fast dynamic response and small oscillation amplitude during steady state operation. FOC algorithm periodically measures module's open circuit voltage. Then it sets the MPP voltage to the open circuit voltage multiplied by a relation factor, which for thermoelectrics is 0.5. The algorithm disconnects the module from the power converter for open circuit voltage measurements and no power is produced during that time. This algorithm may also be used in short current mode, where instead of the open circuit voltage a short circuit current is measured, and MPP current is calculated [68].

In larger TEG systems, where multiple TEG modules are used, it is beneficial to use several MPPT converters for modules segregated into arrays. This results in autonomous dedicated MPPT subsystems (DMPPT) [79]. Hybrid Centralised Distributed (HCD) solution has been proposed. In this system the TEG modules are connected in series to a central converter, while at the same time being connected to distributed converters as well [80]. It has been shown for large PV systems that DMPPT power benefits outweigh the power electronics costs [81]. Similar results can be assumed for TEG systems, especially where temperature mismatch is expected. TEG - power grid interfacing solutions have been proposed [82].

Various converter topologies may be used depending available input voltage and required output voltage. High step–up gain converters have been proposed [83, 84], while the Buck–Boost converters are the most popular choice. SEPIC [31, 33] and

Cuk [85] converters are used for battery charging. Boost converters have been proposed for very low input voltages [46, 86-88].

2.11 TEG Module Electrical Characterisation

Each thermoelectric leg is effectively a voltage source with an internal resistance. Since all legs are connected in series, the voltages they generate add up to the overall generator voltage. Similarly, TEG module resistance is a sum of all the leg resistances, connecting electrodes, and contact resistances as explained earlier. As a result, TEG module can be modelled electrically as an ideal voltage source with a series resistor standing for the internal resistance (Figure 2.2 left), as per Thevevin's theorem [67]. The typical voltage as a function of current at constant ΔT is shown in right side of Figure 2.2.

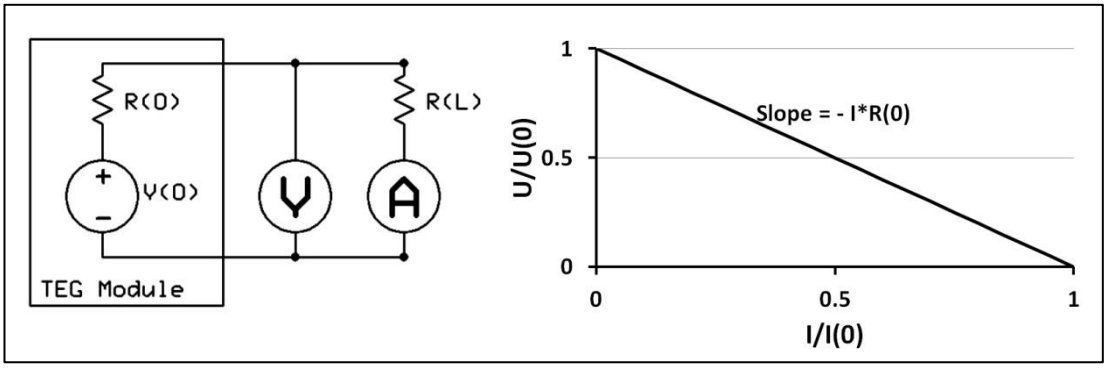

Figure 2.2. TEG module equivalent circuit with electrical load connected in series (left). Typical Voltage–Current curve of a TEG (right).

For a single TEG module the load voltage equals module voltage, also, the load current is equal to the module current. The voltage–current curves are recorded by changing the load resistance (R_{Load}). Infinite load resistance or open circuit results in no current and the open circuit voltage (V_{OC}), while no resistance or short circuit allows recording of the short circuit current (I_{SC}). As a result the range of load resistance values required for recording V–I graphs is from 0 Ω to +∞ Ω. Voltage drop across the load is shown in Equation 2.16.

$$V = V_{OC} - R_{TEG}I$$

Equation 2.16. Load voltage.

Electrical power extracted from a TEG module will depend on the load current, which is determined by the load resistance. Most TEG applications are inclined to extract the maximum electrical power available. This requires finding the Maximum Power Point (MPP) current. Equation 2.16 multiplied and differentiated by the load current gives Equation 2.17.

$$\frac{dP}{dI} = V_{OC} - 2R_{TEG}I$$

Equation 2.17. TEG module power differentiated by current.

Equating Equation 2.17 to zero and solving for the MPP current gives Equation 2.18.

$$I_{MPP} = \frac{V_{OC}}{2R_{TEG}} = \frac{I_{SC}}{2};\ V_{MPP} = \frac{V_{OC}}{2};\ P_{MPP} = I_{MPP}V_{MPP} = \frac{V_{OC}^2}{4R_{TEG}}$$

Equation 2.18. TEG module MPP current, voltage, and power.

The solution in Equation 2.18 is possible when the load resistance equals the module resistance. When it happens the load voltage is half the open circuit voltage and the load current is half the short circuit current. Whenever the load resistance is equal to the internal resistance of the TEG module, the two resistances are said to be matched.

Typically the TEG module electrical characterisation involves recording of the voltage–current and power–current curves during the steady state temperature conditions. The current is scanned from 0 A to the short circuit current, while the module voltage is recorded and the power is calculated. As seen from Equation 2.11, the heat flux through the module will increase with increasing current. As a result, the module hot and cold side temperatures might drift from their initial values. Consequently, a common practice is to adjust heating and cooling powers as necessary to maintain constant module surface temperatures as the current setting is changed.

Figure 2.3 shows steady temperature voltage–current and power–current curves recorded for Thermonamic TEHP-12656-0.3 TEG module electrical characterisation at ΔT of approximately 174 K. Open circuit voltage and module resistance are extracted from V–I dataset using Equation 2.16. Measured module open circuit voltage V_{OC} = 5.3 V, and the module resistance R_{TEG} = 0.84 Ω. Measured module maximum power is P_{MPP} = 8.4 W when module voltage is V = 2.65 V, and the module current is I = 3.15 A. These values agree nicely with the relations shown in Equation 2.18.

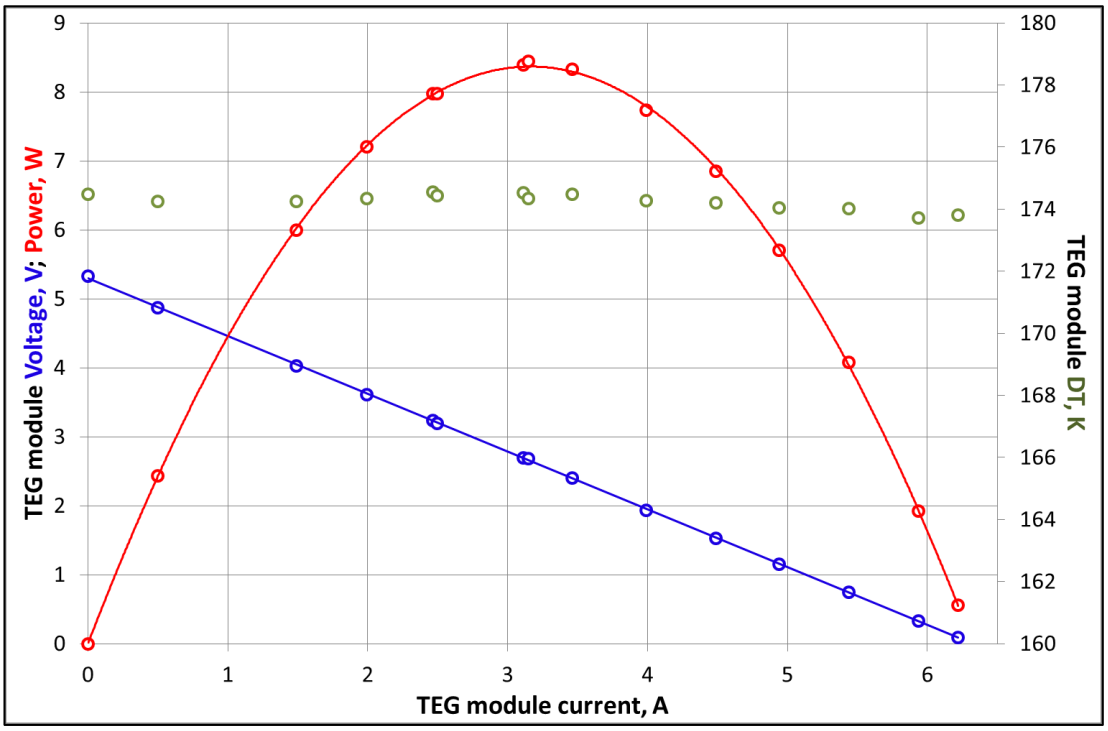

Figure 2.3. Typical steady state Voltage - Current and Power - Current curves recorded during TEG module electrical characterisation. Data points are shown in circles. Solid lines are mathematical fittings using the least square method.

Most TEG module manufacturers recommend operating TEG modules on the left side of the power curve. The reason for this is that the right side of the power curve is less thermally efficient due to the increasing heat flow through the module and decreasing module power. It is worth mentioning that the maximum power point is not the most efficient point of the module operation. The point of maximum efficiency lays just left of the MPP. While the ratio of the load resistance to the

module resistance is one for MPP, the ratio for maximum efficiency depends on the module ZT and is shown in Equation 2.19. For common TEG modules the MPP is very close to the maximum efficiency point.

$$\frac{R_{Load}}{R_{TEG}} = \sqrt{1 + ZT}$$

Equation 2.19. Load and module resistance ratio for maximum conversion efficiency.

3 MEASUREMENT SYSTEM: HARDWARE DESIGN

3.1 Objectives

Several ongoing research projects at the Institute for Superconducting and Electronic Materials deal with the development of thermoelectric materials and their subsequent integration into thermoelectric modules. Although thermoelectric materials can be readily characterised using off-the-shelf measurement systems, there are no commercial systems available that would allow accurate characterisation of fabricated thermoelectric modules. Therefore the main objective of this PhD thesis project is to design and build an in-house thermoelectric module performance characterisation system. The system has to be specifically designed to accommodate wide range of thermoelectrics suited for low- and high-temperature applications. This means that the system has to accurately reproduce real world application conditions the module has been designed for and accurately measure its electrical, thermal, and performance properties. These properties are temperature dependant and include open circuit voltage, current–voltage characteristics, maximum power output, module resistance, module thermal resistance, power conversion efficiency, and reliability during thermal cycling. Real world application conditions to be reproduced by the system are: module clamping force, gas atmosphere, hot side temperature, cold side temperature, and heat flow.

3.2 System Capabilities

Maximum hot plate temperature: 1000 °C
Maximum hot plate power: 2.4 kW
Module sizes up to 100 x 100 mm^2
Maximum cooler water flow rate: 600 cm^3/min
Maximum compression force: 20 kN
Measurement environments: Argon, Air, vacuum
Maximum measurable module current: 20 A
Maximum measurable module voltage: 60 V
Maximum power point tracking

3.3 SolidWorks

Dassault Systemes SolidWorks Premium Computer Aided Drawing (CAD) software 2011 and 2014 versions were used to create 3D computer model, which were then used to fabricate system components. SolidWorks is an excellent tool to visualise parts, put them into assemblies, and check if they fit together. Technical drawings, which are required for machine shop jobs, can be produced from a part model. Some machinery, such as CNC routers and 3D printers, can use the modelled part SolidWorks files directly to produce real parts, while other machinery, such as Plasma or laser cutters, may require the part models to be saved to a specific format.

SolidWorks 3D part creation typically starts by creating a 2D sketch with lines, arcs, splines, points, etc. The sketch items have their dimensions defined together with relations such as tangency, parallelism, perpendicularity, and concentricity [89]. The fully defined sketch is then used to extrude, revolve, sweep, or loft bosses or cuts [90]. The resulting feature is then used to create sketches for subsequent bosses or cuts. Finally, 3D parts can be put into an assembly by creating mates, which define the tangency, parallelism, perpendicularity, and concentricity relations between planes, lines, arcs, and points similarly to the sketch relations. When constricted to a single degree of freedom, the parts can be moved relatively to each other to visualise part movements in the real system. Drawings are created from a 3D part model by projecting its views onto a 2D sheet [91]. Dimensions are then added to the projected views.

Assemblies can be taken apart into an exploded view, as seen in few instances later in this Chapter, which allows visualising and planning the real assembly. PhotoView 360 feature can be used to produce renderings of parts or assemblies. Sample render is shown in Figure 3.1. All 3D models shown in this Chapter are only screen captures, because image rendering is very time consuming. Drawings for measurement system parts are moved to APPENDIX A – TECHNICAL DRAWINGS.

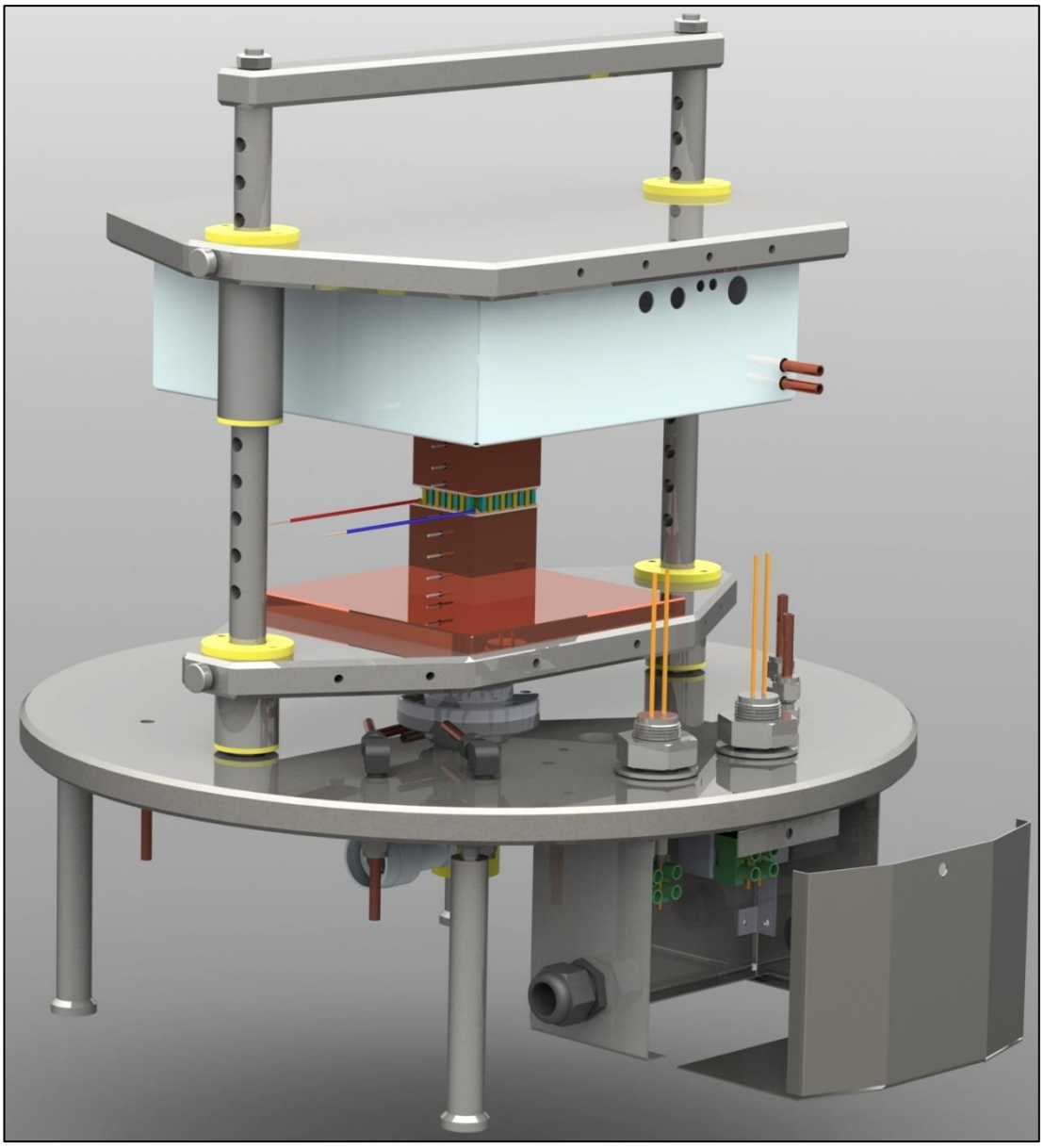

Figure 3.1. SolidWorks PhotoView 360 2014 render of the measurement system assembly model.

3.4 Baseplate

The baseplate is the most important structural component of the measurement system. It supports the weights of all the assembly components. It houses a hydraulic cylinder, which can create up to 20 kN of force. It also acts as a pad for a bell jar, which, with vacuum present, can effectively weigh 1.7 tonnes. It has also two vertical 20 mm diameter support shafts with pinning holes every 20 mm installed that are designed to hold the weights of the cooler and the heater (Technical Drawing 1).

These shafts allow only vertical movement of both the cooler and the heater. Such setup along with a 25 mm travel window for hydraulic cylinder piston allows measurements of up to 280 mm high measurement assembly stack consisting of cooler–Cu reference block–TEG module–heater under compression force. At the top the support shafts are connected with a horizontal stainless steel bar (Technical Drawing 2) for additional stability and minimised flex and twist.

The baseplate itself is a 500 mm diameter and 20 mm thick stainless steel disk with a 3 mm chamfer (Figure 3.2), (Technical Drawing 3). Colchester mascot 1600 lathe was used to machine the disk. It has four blind holes with a M10 thread for supporting legs (Technical Drawing 4), a 1.5 inch thread in the center for the hydraulic cylinder, two 1 inch through-holes for high current electric feed-throughs, 70 × 20 mm rectangular through-hole with eight M8 blind threads for 6 inch Con Flat 50 conductor electric feed-through, 1.5 inch thread for vacuum fittings, six 1/8 pushfit fitting threads for water and gas inlets and outlets, two 10 mm through-holes with 2 mm deep 20 mm cut-outs for the support shafts, one M6 blind hole for cold junction reference fixing, and M5 blind threads on both sides for earth wire fixing. Water inlets are situated closely to the outlets so the excessive heating generated by returning hot water at the outlets, and thus resulting thermal stresses, can be prevented. High current and small signal electric feed-throughs are placed as far away from each other as possible to minimise electrical noise.

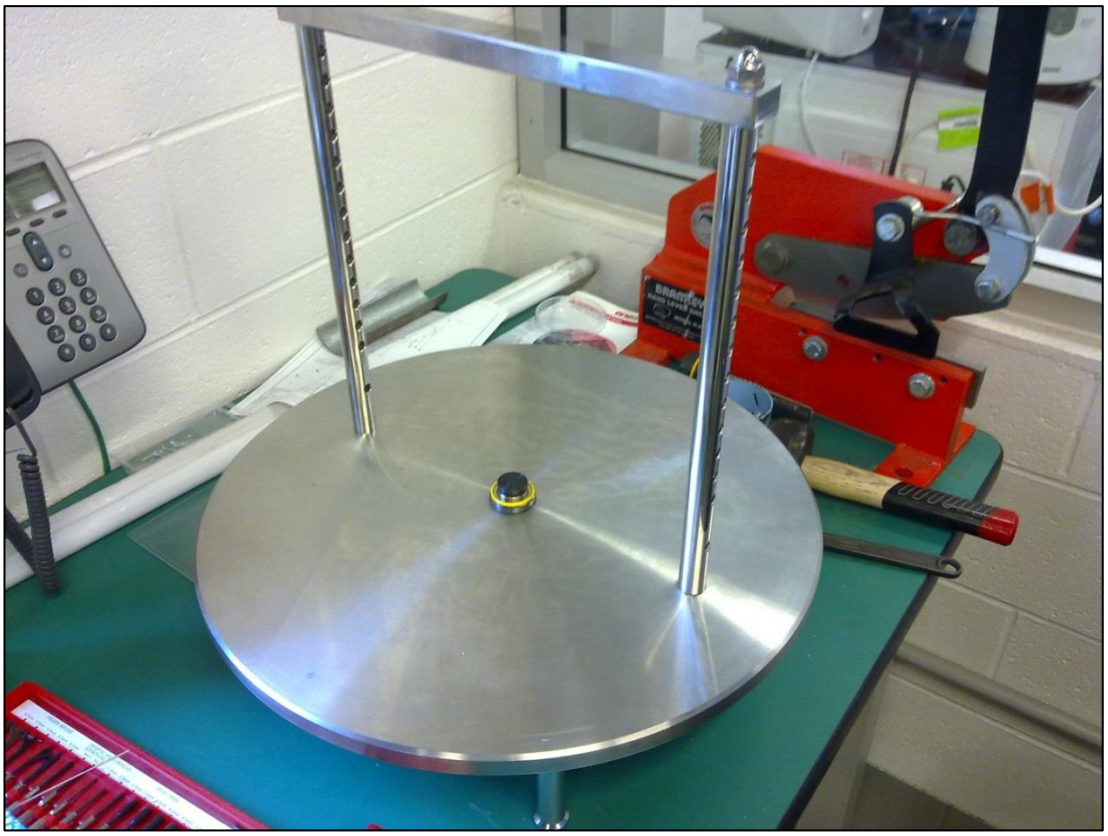

Figure 3.2. A view of assembled structural components: baseplate, legs, support shafts, top bar, hydraulic cylinder.

3.5 Heater

In our system, the heater (Figure 3.3) creates thermal gradient and sufficient heat flow through the TEG module. It must be robust enough as it must withstand the module clamping force (20 kN max) without breaking or significant movement during normal operation. Furthermore, it has to operate reliably in a wide temperature range, *i.e.* room temperature to 1000 °C, in air and not to release any gases, if it is operated in vacuum. Due to the different architecture of thermoelectric modules, the heater must also have adjustable position in relation to the baseplate.

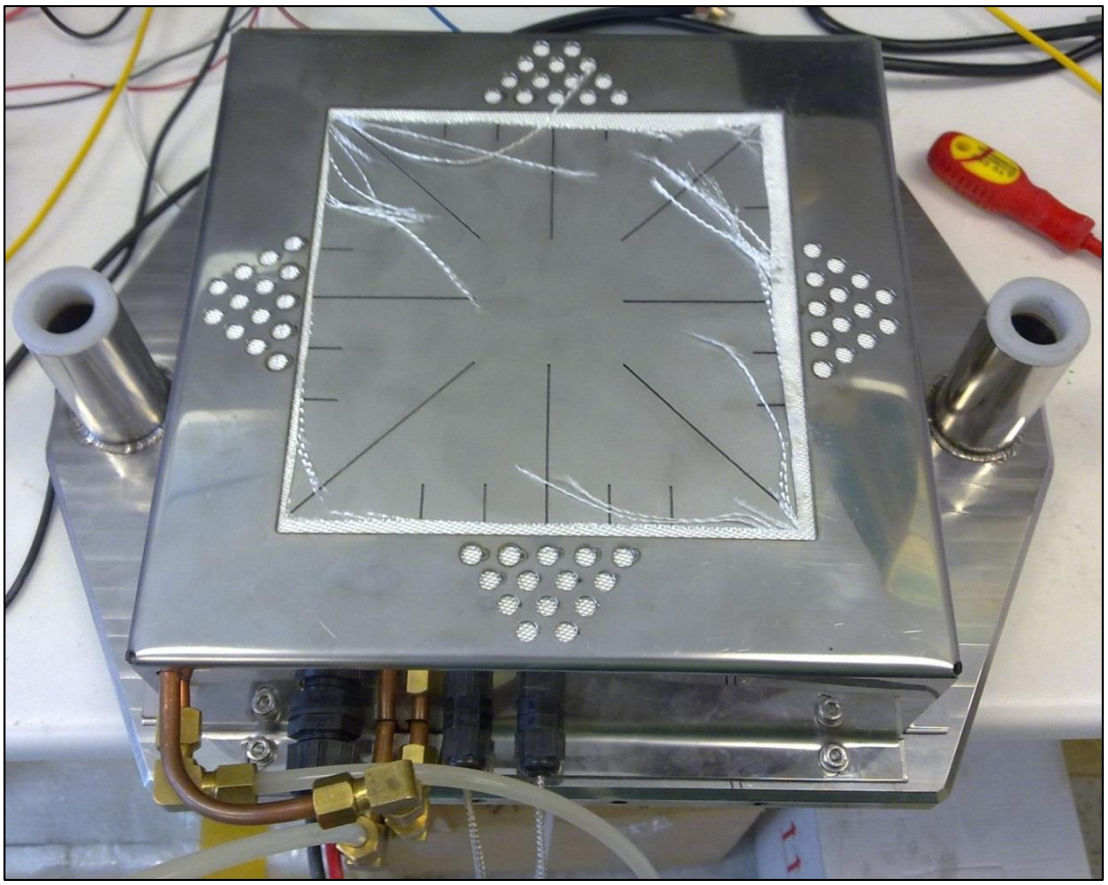

Figure 3.3. A view of the heater unit fully assembled for the first time.

3.5.1 Heater Support Plate

The heater support plate is made of 20 mm thick stainless steel plate with a 3 mm chamfer all round, (Technical Drawing 5) which has guide tubes (Technical Drawing 6) welded in. Each of the guide tubes has nylon bushings (Technical Drawing 7) pressed in. The nylon bushings are 100 mm apart and can slide on the support shafts. The tubes and bushings ensure that the heater support plate stays in parallel to the baseplate at all times with minimal swivel or rocking. To ensure smooth vertical sliding motion the sockets are lubricated using high vacuum silicone grease. Due to its weight, the heater can float over the cooler-TEG-heater stack, if no compression force is required, or it can be fixed in certain position using pinning holes in the support shafts and two 8 mm fixing pins (Technical Drawing 8).

The overall thickness of the heater assembly is ~100 mm. The thickness of actual hot surface is 3 mm and the diameter of heating wire coil is 8 mm. This leaves ~70 mm of heater height for thermal insulation, which can result in a significant amount of heat reaching the support plate. Consequently, this could cause a large temperature rise of the support plate (approx. few hundred degrees) and substantial thermal expansion. In order to eliminate such possibility, a water cooling track was cut in the heater support plate to remove excess heat and keep the top side of the heater cool. The track is 6 mm wide and 6 mm deep with a rounded bottom. A ¼ in annealed copper tube was pressed into the track. Thermally conductive paste was used to rectify any imperfections originated during manufacturing process, *e.g.* cutting, tube bending, and pressing.

3.5.2 Heater Thermal Insulation

Heater thermal insulation is a cast of a Shiralite MW160 castable refractory ceramic purchased from Shinagawa (Australia). This castable ceramic mixture consists of aluminium oxide (55 %), silicon oxide (39 %), calcium oxide (3.6 %), iron, titanium, magnesium, and alkali oxides. Its thermal conductivity at 250 °C and 1000 °C is approximately 0.45 $\frac{W}{mK}$ and 0.55 $\frac{W}{mK}$, respectively. Thermal insulation assembly consists of six ceramic pieces. Ceramics hold heater wire coil in place, provide structural strength to the heater, and thermally insulate the support plate.

A center bottom piece (180 × 160 × 36 mm^3) is a rectangle with a twelve line serpentine track in the bottom face for accommodating the heater coil. The track is 8 mm wide and 8 mm deep with a round bottom. There are 5 mm thick ceramic walls between every two track lines with a total heating area of 151 × 160 mm^2. The total hot surface area that the ceramic is exposed to for a 100 mm square is 3500 mm^2. The robustness and suitability of selected ceramic for insulation used in the assembly was evaluated using following estimations: assuming the lowest cold crushing strength (Shinagawa info sheet) of 10 MPa, a lowest cold crushing strength of the maximum intended area of 100 mm square is A × F = 35 kN, which is well above of the maximum intended compression force of 20 kN designed for our system. For characterisation of most common 50 × 50 mm^2 modules same assumptions result in a

maximum compression force of 10kN that the weakest parts of the refractories can withstand before crushing.

A center top piece (180 × 160 × 41 mm^3) is a simple rectangle with through-holes for thermocouples in the center and power leads in the two corners. On the top of the block, through-holes continue as channels going towards the back of the heater.

The rest of the pieces in this assembly tile around the stack of the two center pieces. The whole refractories cluster has a channel for a double ¼ in copper tube loop going round the bottom perimeter. This returning cooling water loop prevents the heater box from reaching excessively high temperatures. The two side pieces are 160 × 35 × 80 mm^3 and are interchangeable. The front and back parts are 247 × 44 × 80 mm^3 in size. On the bottom side, they have a 3 mm slot to position the hot surface of the heater. The back piece has space for a copper tube with a 180° turn. Additionally, it provides space for wire glands, fixed onto the rear wall of the heater box.

3.5.3 Heater Thermal Insulation Mould

The casting procedure suggests that the mould has to be constructed from strong materials which are water resistant. Generally, steel formers are favoured for this job because of their inherent strength and non-absorbent nature. The surface of the mould must be lightly but thoroughly oiled or greased to facilitate removal of the casting material from the face of the mould. The surface of the formwork should be uniform and smooth to give a good surface finish to the casting. It also aids in ceramic - mould release. Mould must be watertight, so all joints and holes must be sealed. During casting liquids and fines will 'bleed' through cracks in the mould. This liquid will be rich in cement and can thus leave a weakly bonded material adjacent to the leaking joint causing detrimental results [92].

A specially designed mould was used to cast the refractory ceramic parts (Figure 3.4). The design was made keeping a few things in mind: the mould has to form all parts in one cast; it has to account for 1 to 2% of linear shrinkage during high temperature cure of the refractories; it must be easily disassembled; it has to be reusable in case some of the refractory ceramic parts have to be replaced; and its parts have to absorb any human error during mould part manufacturing.

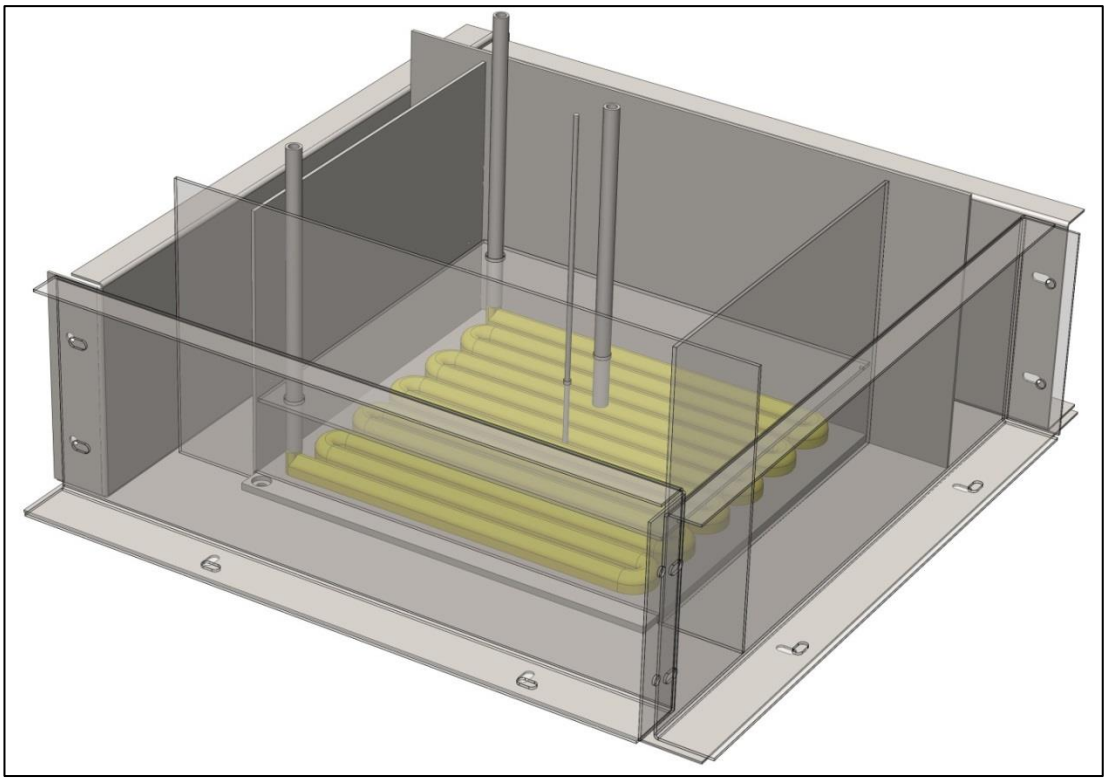

Figure 3.4. Heater ceramic thermal insulation mold as modelled in SolidWorks.

A 1 mm thick steel sheet was used to manufacture most of the mould parts. 300 × 300 × 1 mm^3 plate (Technical Drawing 9) was used as a base to assemble all the parts. A 181 × 181 × 3 mm^3 aluminium plate (Technical Drawing 10) was used to reproduce the shape of the heaters' hot surface. A serpentine shape was made to reproduce the shape of the heating wire element. It was printed in Objet Connex 350 3D printer using FullCure720 material directly from CAD drawing (Figure 3.5). Four identical side walls (Technical Drawing 11) were made from a 1 mm steel sheet. Two 160 × 116 × 1 mm^3 ("short"), two 254 × 120 × 1 mm^3 ("long"), and one 160 × 180 × 1 mm^3 ("middle") separator plates (Technical Drawing 12) were made from a steel sheet. Their function was to separate mould volume into sections for individual heater part casting. They were precisely scratched using a scratcher to indicate cast level during casting process. "Short" separator plates had 1 mm thick pins for levelling and supporting the "middle" separator plate. A 2 mm diameter welding wire was used to create hole for the center thermocouple, while 120 mm ¼ in steel tubes were used to create holes for the wiring of the heating element power supply and for the off-center backup thermocouple.

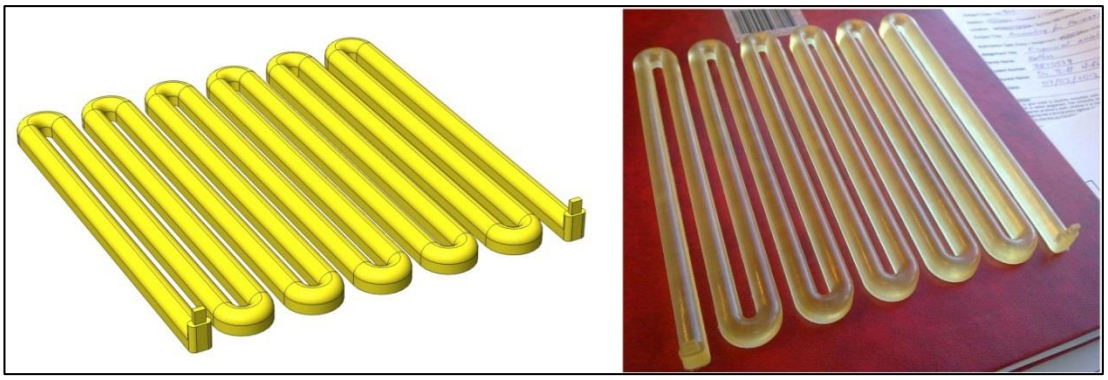

Figure 3.5. Serpentine part CAD model (left) and 3D printed part (right).

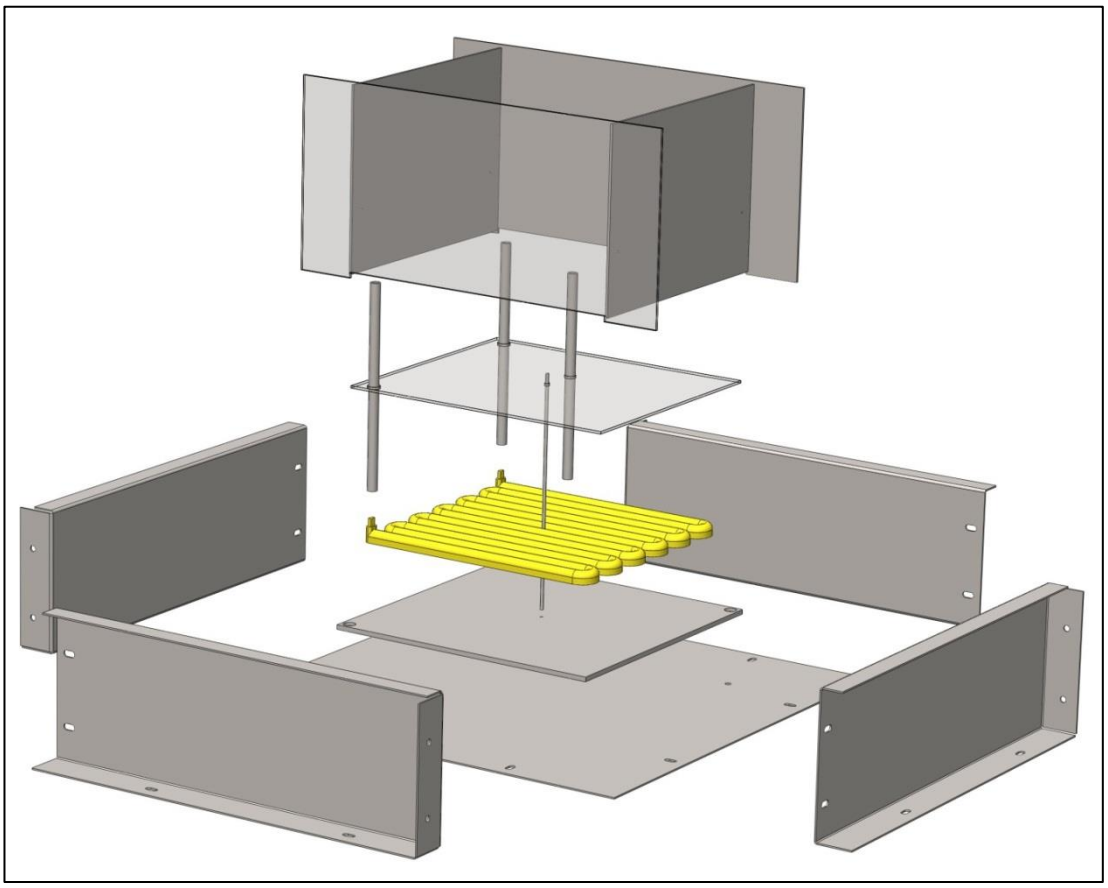

Figure 3.6. Exploded CAD model of the mould.

The mould was assembled (Figure 3.6) using M4 bolts, nuts, and washers. First, a 3 mm aluminium plate was attached to the bottom plate. Then, thin film of silicone sealant was applied to the flat surface of the serpentine shape. The serpentine shape was then positioned precisely at the center of the 3 mm plate. Care was taken to ensure that serpentine spacing is maintained at exactly 5 mm, also that the serpentine

shape does not slide off its position while the silicone sealant is still liquid. Four side plates were bolted to the bottom plate, ensuring they are at right angles and exact internal dimensions of 254 × 254 mm^2. Elongated holes in the bottom plate and side walls allowed for small manufacturing inaccuracies which are difficult to anticipate during design stage such as sheet metal bend radius or shifting of a small diameter drill. Some bottom plate flex was observed during assembly. Therefore, a 10 mm thick scrap aluminium plate was attached under the bottom plate to provide additional stiffness.

Most of the ceramic binder is dissolved in water during casting process. It is important to prevent any liquid phase soak through the gaps between mould parts. Otherwise, the ceramic parts may lack mechanical strength. To prevent liquid soaking and to aid in set ceramic part removal, corner radiuses of ~2mm were created by applying silicone sealant to every internal corner and then scraping excess sealant away using steel plate with a slightly rounded corner. The shape of the copper tubing in the heater box was created using silicone sealant. The silicone sealant is a free-standing gel, which makes it relatively easy to shape. It does shrink during curing, though; around 15% of linear shrinkage was observed. Approximately 13 mm high and 7 mm wide rectangular shape was formed along the internal perimeter of the mould. Excessive amount of silicone sealant was extruded in the internal corners to roughly represent rectangular shape. Then it was formed into a rectangular shape by scraping steel plate with 8 × 15 mm cut-out along the sidewalls. The formed silicone was left to set for 24 hours. Then the four internal mould corners were filled with silicone to create corners rounded to ~20 mm radius. The back refractory ceramic part had to accommodate a ¼ in copper tubing changing direction by 180°, the same copper tubing exiting the heater box, a copper tube from the heater support plate exiting the heater box, electrical power, and thermocouple glands in the heater box. Round shape of 24 mm radius and 7 mm thickness was formed at the back wall to create space for a ¼ in copper tube loop in the back ceramic part. More silicone sealant was added onto left side of the back ceramic part compartment, enough to provide space for a ¼ in copper tube departing from the sidewall and bottom plate and exiting the heater box at 10 mm from the side and at 20 mm from the bottom. Silicone sealant was left to cure for 24 hours.

Using a scalpel 1 mm cuts in the cured silicone were made at 46 mm from the sidewalls to fit and keep in place “long” separator plates. “Long” separator plates were placed in the cut slots. “Short” separator plates were placed between the “long” separator plates, following the alignment marks made on the “long” separator plates, and making sure the 1 mm pins are facing the center of the mould. The bottom parts of the “short” separator plates were touching the 3 mm bottom plate. The separator plates were temporarily fixed together using Blu-Tack (Bostik) at the top to prevent shifting and misalignment. A 2 mm wire was wrapped with a single layer of sticky tape and placed into the 3 mm plate canter hole. The ¼ in steel tubes were also covered with a single layer of sticky tape and placed onto the dedicated pins at the two ends of the plastic serpentine shape (Figure 3.7). The sticky tape was used to provide additional smoothness for the surfaces. Additionally, in case it was not possible to remove the tubes or the wire from the ceramic parts straight after casting, they could be left in there during the curing process. The sticky tape would then burn away at ~400 °C leaving ~50 μm of space per tape layer, allowing easy removal of the tube or wire. The rest of the ¼ in tubes were wrapped with a single layer of sticky tape. All internal mould surfaces were thoroughly lubricated by spaying them with WD40 lubricant to prevent cast sticking onto the mould surfaces and partially aid during removal. Two 90 × 35mm^2 rectangles were cut from 1 in thick ceramic insulation board and pressed together to form a 90 × 35 × 46 mm^3 rectangular stack.

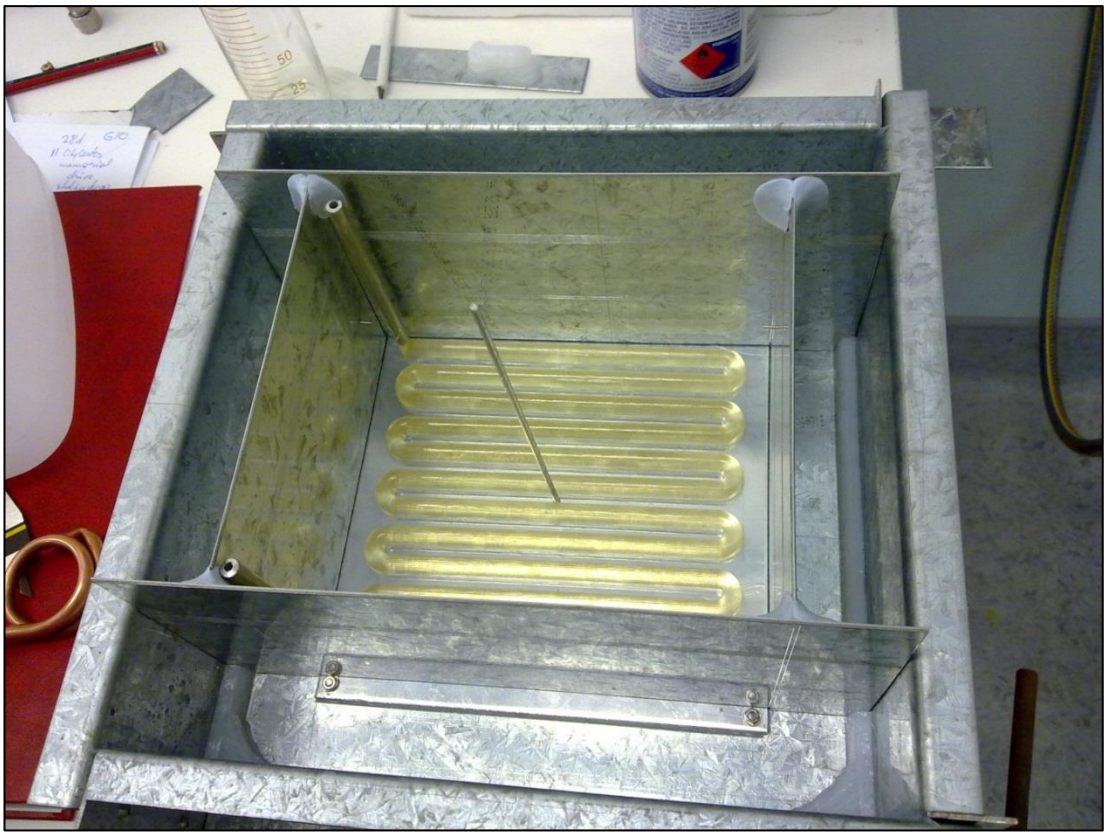

Figure 3.7. A view of assembled mould just before casting.

3.5.4 Casting of Heater Thermal Insulation

As mentioned above, Shiralite MW160 insulating material was selected to be used for heater thermal insulation. It is a low iron, high temperature insulating castable based on selected lightweight aggregates and high purity calcium aluminate cement. It combines good strength, volume stability, and thermal shock resistance with a good thermal insulation capacity [93].

Shiralite MW160 comes in powder form, which has to be mixed with water to a homogeneous mass at room temperature and then quickly placed in the mould. The water used for mixing has to be clean and of drinkable quality. Since the amount of water added to the castable does more to affect the properties than any other factor, its quantity must be accurately measured. As indicated on the cement bag, required water quantity is around 18% of the dry powder mass. A short curing time of the mould allows only 15 minutes between the preparation of the mixture and its casting in the mould. Therefore, six separate batches of cast were mixed and placed. Shiralite

MW160 powder was weighed and carefully placed into a mixing bucket. 80% of the required water was measured and added to the bucket. The bucket contents were carefully and thoroughly mixed using a steel plate until it became homogeneous. Small increments (5 – 10 ml) of water were added to the mixture as required to get a slowly flowing consistency, ensuring that mixture is homogeneous after every water addition. Resulting mixture was then carefully placed into the mould making sure that all voids, particularly around obstructions and in the corners are filled to eliminate any trapped air bubbles. After every cast mixture batch was placed in the mould, the assembly was vibrated for few minutes to help any air bubbles trapped in the mixture to rise to the top and escape, making the cast much stronger.

The mould architecture required for separated sections to be filled with cast in a particular sequence. First, the front part was filled with casting mixture to 80 mm mark on the "long" sideplate. Then, the back part was filled to a 50 mm mark. The ceramic insulation board rectangle was inserted to create space in the part for electric glands and copper tubing. Top of the rectangle was aligned with the 80 mm mark on the "long" separator plate. The end of the rectangle was aligned to the "short" separator plate plane. The back part was then filled to the 80 mm mark on the "long" separator plate. As the density of the insulation board rectangle is much lower than the casting mixture density, it had to be held down in place for ~10 minutes, the time required for the cast to set. Then, the two side parts were cast by filling the side compartments up to the 80 mm mark on either "long" and "short" separator plates. Care was taken to ensure sufficient strength of the Blu–Tack fixtures. Otherwise, the short separator plates could just flip into the mould due to the hydrostatic force exerted by the casting mixture.

Then, the casting mixture was placed into the center part of the mould. Extreme care was taken to avoid air pockets or bubbles around the serpentine part as the mechanical strength of the bottom center part is of critical importance to the heater. Enough mixture was placed to reach the 39 mm mark on the separator plates and the top of the 1 mm pins of the "short" separator plates. The middle separator plate was then sprayed with a WD40 lubricant and carefully placed onto the cast surface. Care was taken to prevent any air trapped under the plate. The plate was slowly lowered at

a slight angle to let any remaining air escape. Then, a ¼ in steel tube for the off-center thermocouple was slowly inserted through the dedicated hole in the "middle" separator plate until its rounded end touched the plastic serpentine, right in the middle above and between fourth and fifth tracks. Then, the center part was filled with casting mixture up to the 81 mm mark on the separator plates, taking into account the thickness of the "middle" separator plate. 20 mm and 50 mm long ¼ in steel tubes were inserted into the cast to provide passage for the thermocouples from the center of the heater towards its back. Similarly, 4 mm and 135 mm long pieces of HB pencil, which measures 6 mm between the faces, were inserted into the cast to provide passage for heating coil power leads going towards the back of the heater. It was expected that the pieces of pencil would not require extraction after the initial setting, because they will burn away during the cure process. The as assembled casting mixture (Figure 3.8) was left to set for 24 hours at room temperature.

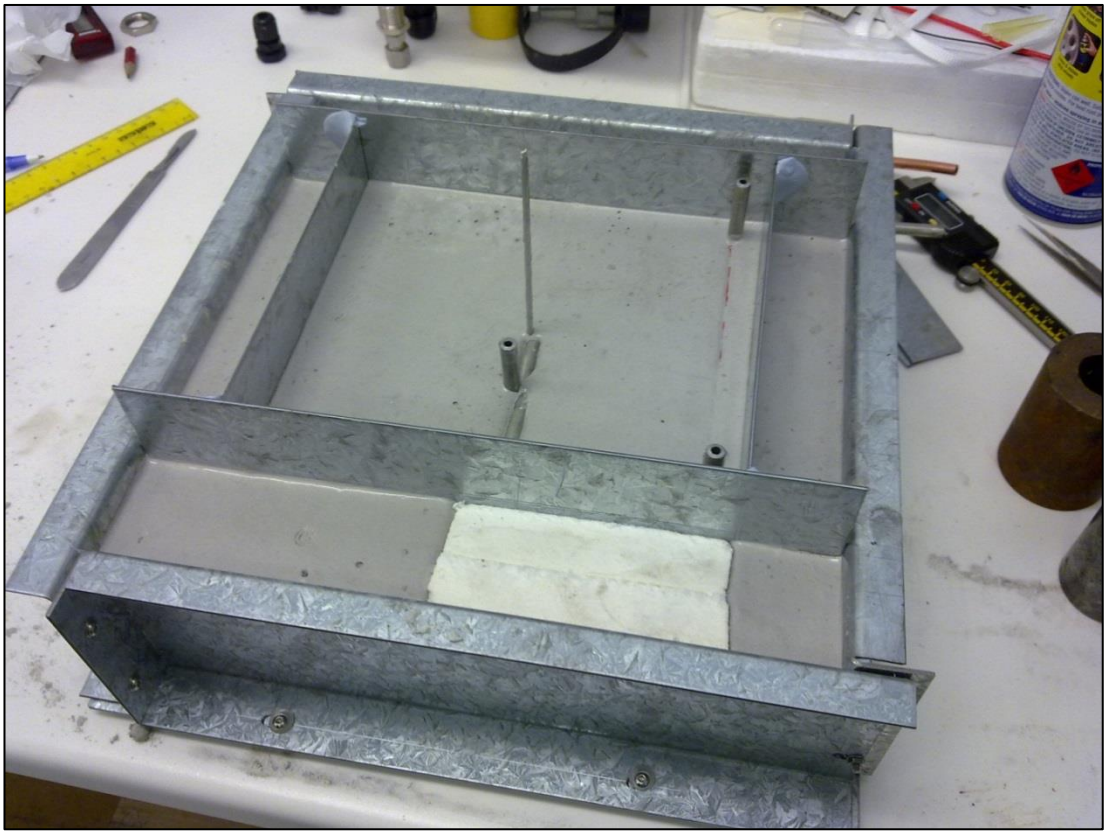

Figure 3.8. Cast after placement.

Mould removal

Initial solidification of the cast occurs within 15 minutes of preparing homogeneous mixture. However, the polymerisation reaction does not stop there. It takes much

longer to complete, normally, 1-2 days depending on the ambient temperature. Therefore, it is recommended to give allow at least 24 hours before taking cast parts out of the mold.

After 24 hours of setting the mould sidewalls were shelled away, outer parts removed, separator plates removed, and center parts taken out. Mould disassembly was much more difficult than it was initially anticipated. This was caused by an extremely good silicone adhesion to the sheet metal surfaces. Even when all the mould bolts were removed everything was still tightly held together by the silicone tracks. The sideplates were very carefully pried so to run a scalpel blade along the sidewalls to detach the silicone. Fortunately, there was no ceramic part adhesion to the metal surface. Therefore, once all sideplates were removed, the outer ceramic parts could be easily taken out. Subsequently, "long" and "short" separator plates were removed. The 2 mm wire and ¼ in steel tubes were gently pulled out of the cast. The sticky tape was soft and slightly swollen from the prolonged contact with the WD40 lubricant, which helped for the tubes to come out of the cast much easier. This was followed by removal of top center piece and "middle" separator plate. Bottom center part was stuck onto the 3 mm plate. The 3 mm plate was then flexed slightly in all directions away from the bottom center part. With each flex a small area of silicone was checked for detachment. Finally, the 3 mm plate was removed, but the serpentine shape was still embedded into the bottom center part. Any attempts to force the serpentine part out could result in a broken bottom center part.
The bottom center part was placed bottom up on a hotplate with a low heating setting. When the whole part reached ~40 °C temperature, the serpentine part softened and became more elastic. One end of the serpentine was then pushed out by applying light pressure on it with a rigid wire through one of the heater coil lead holes. The serpentine was completely removed by raising it in small increments along its length, taking care not to create departure angles of more than 15° off its plane, especially around the 11 sharp 180° bends. After this, the serpentine shape was again heated up to 40 °C, had its original shape restored, and was left to cool down retaining its shape for possible future use.

Curing

Cast parts need to be cured to finalise solid-state polymerisation reactions, remove excess moisture, and to reach their final dimensions and mechanical strength. Curing was done using HS/002 - Conventional Insulating Castables procedure as a guide [94]. The HS/002 procedure recommends a ramping at 25 °C/hr rate and initial dwelling at 200 °C for 1hr for every 25mm of part thickness, ramp at 50 °C/hr and dwell at 550 °C for 1hr for every 25mm of part thickness, and lastly ramp at 50 °C/hr to the maximum intended operating temperature of the part. It is important to note that temperatures in this heating program are referring to parts, not furnaces. It also recommends monitoring the surface temperature of the parts in two locations, where the temperatures would be highest and lowest. Such temperature monitoring method in the HS/002 procedure is very difficult to implement in practice, especially in a general laboratory environment. Therefore, the temperature program recommended there had to be modified to work with available facilities.

As the HS/002 procedure recommends, the parts were left to dry in air for 24 hours. After drying the parts were cured in a Ceramic Engineering model 1200c muffle furnace using following program (temperatures here refer to furnace temperatures): a 20 °C/hr heating up to 1100 °C, followed by a 5 hour dwell, and 100 °C/hr cooling to room temperature. It was expected to have a slight offset from the furnace temperature sensor reading to the actual part temperature. Nevertheless, such a slow heating rate gives plenty of time for heat diffusion and even temperature distribution throughout the parts. Furthermore, the two dwell steps in the HS/002 procedure can be omitted, because the parts are rather thin and do not require prolonged dwell steps.

After the curing, the parts were taken out of the furnace and inspected for imperfections such as cracking and warpage. Where required the parts were sanded using a Metalmaster BS-75A belt sander so they can fit snuggly together and into the heater box. The two center parts were slightly convex, as well as the bottom side of the bottom center part. All convex and curved surfaces were sanded till flat using 400 grit sand paper on a flat surface. The middle area of the part was coming out of the

surface plane. The surface was sanded until flat by moving the part along the track wall length on a 600 grit sandpaper sheet on a flat surface. (Figure 3.9)

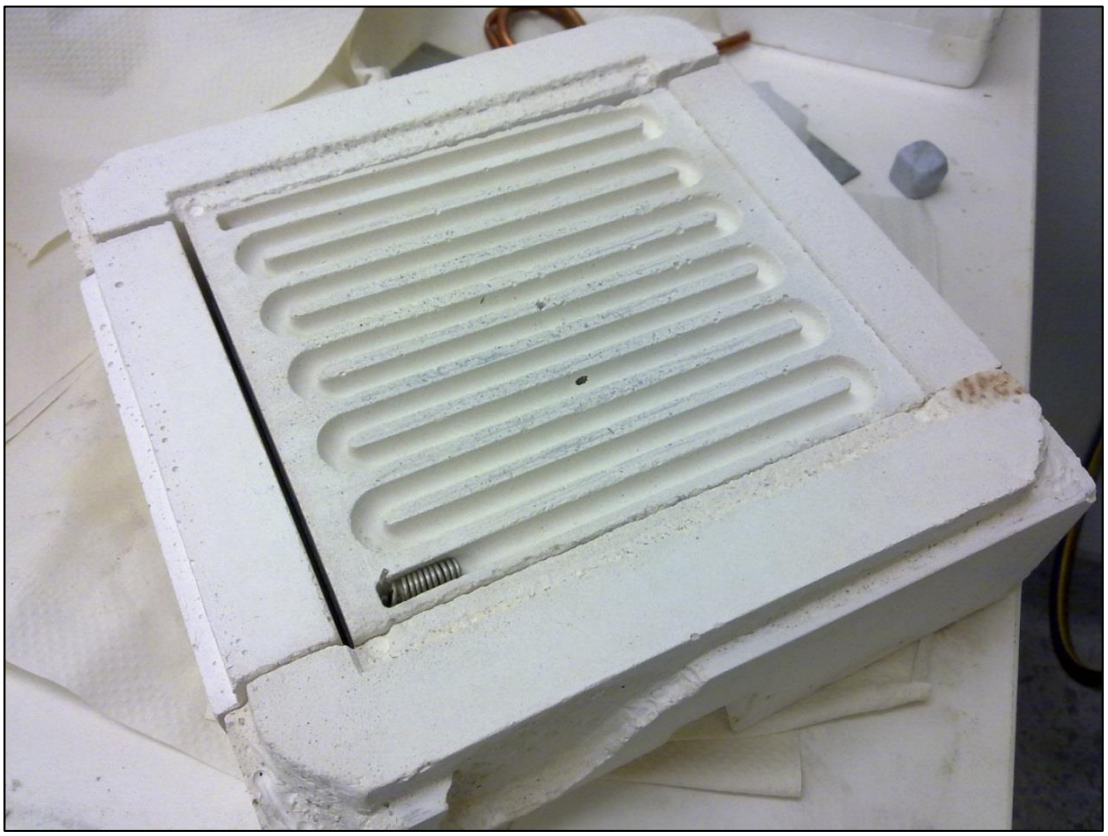

Figure 3.9. Cured ceramic thermal insulation parts.

3.5.5 Heating Wire Coil

Two resistive alloys were considered as heating elements for the heater: a nickel–chrome (NiCr) alloy and iron-chrome-aluminium (FeCrAl) alloy. NiCr (80% nickel, 20% chrome) is preferred over FeCrAl, because NiCr does not deform or become brittle upon heating. This wire composition has good oxidation resistance even under switching conditions or wide temperature fluctuations. During the very first heat up oxidation reactions take place (Equation 3.1 - 1) and an oxide film is formed. Upon further heating to higher temperatures, the oxide film changes into Cr_2O_3 protective film by reaction (Equation 3.1 - 2) [95].

$$4(Ni, Cr) + 5O_2 \rightarrow 4NiO + 2Cr_2O_3 \quad (1)$$
$$3NiO + 2Cr \rightarrow 2Cr_2O_3 + 3Ni \quad (2)$$

Equation 3.1. Oxidation reactions taking place on the heating wire surface.

A 1.42 mm thick RW80 nickel–chrome resistance wire (Alloy Wire, United Kingdom) was used to make a heating wire coil. Maximum operating temperature of RW80 alloy is 1200 °C, melting point 1400 °C, and resistivity – 108 μOhm × cm. The thickness of the wire to be used in the heating coil was carefully considered due to the following constraints: the available physical space, *i.e.* 1.8 m long channel with 8 mm in diameter, and maximum available current of 20 A. Also, recommended wire bend radius to wire radius ratio (usually between 5 and 15) as well as minimum recommended pitch between two wire turns (at least as large as the diameter of the wire) were thought about. In general, the thicker wire results in a longer heating coil life and a more reliable heater [96]. Another important factor to consider when designing a furnace was the wire surface thermal loading, *i.e.* the amount of power radiated per wire surface area. The optimum surface loading is mainly a function of desired furnace temperature and ranges from 4.6 $\frac{W}{cm^2}$ at 800 °C to 2.3 $\frac{W}{cm^2}$ at 1300 °C. [97]

Initially the core to wind the heating wire on was manufactured. It was experimentally determined that a 4.75 mm diameter steel rod will account for coil rebound after winding and result in a 7.95 mm average diameter wire coil. A 4.75 mm steel rod was manufactured from a 5 mm diameter steel rod stock. This rod was first hammered down at one end with a Yoshida Kinen SD-500 hammering machine to a 4.9 mm diameter and then cold drawn through a 4.9 mm die using Allen Bradley 1336 plus drawing machine. The resulting 4.9 mm diameter rod was hammered and drawn to a 4.8 mm diameter rod. In the final step, the rod was pre-hammered and drawn through a 4.75 mm die. The heater wire coil was wound up using a Dashin Champion 2500VS lathe. The lathe has a limit for the part size and can accommodate long ~1.2 m wire. This was less than 10 m length required, therefore, a close packed coil was wound to fit in the space available. The core rod, together with a 25 cm of heater wire, was clamped in the lathe jaw. With the spindle rotating at 100 RPM the wire was fed through a firm finger grip through a welding glove. The grip provided friction creating pulling force and resulting in a tightly packed wire coil. The pulling force had to be counteracted at the place where the wire meets the core to prevent excessive deflection of the coil from rotation axis. This was achieved by sliding a

lubricated plastic band just in front of the wire coil with a pulling force required to counteract the deflection. The wire was wound till a 65 cm mark on the rod. The wire was cut leaving a 25 cm of straight wire on the coil. The wire end was let to unwind for several turns to relieve the elastic stress resulting in a coil having 445 wire turns. The wound close packed coil was then removed from the core rod and hand stretched to roughly 1.8 m. Then, it was checked and adjusted so that every gap between two wire loops is exactly 2.65 mm wide. Gap irregularities, such as denser or closer packed loops, could cause hot spots on the coil or even melt it during operation. Using the bottom center ceramic insulation part as a template, eleven 180° bends were made (Figure 3.10). 36 loops were left for the first and the last straights, while 34 loops were counted for every other straight. On average, 2.2 loops were used for each of the 180° bends around 5 mm diameter wall ends. The bends were made in a way that the minimum distance between two heating wire loops is at least 2.6 mm. The straight wire at the ends of the coil were trimmed to 10 cm, folded in half, and twisted. Seven 25 cm long strands of 0.8 mm diameter copper wire were twisted on top of the heating wire twist. The twisted strands were welded using an acetylene burner and flux. The copper wire has low resistance compared to the heating wire and ensures that heating takes place only at the coil and not on the wires leading to it. Silica sleeves were put on the twisted leads.

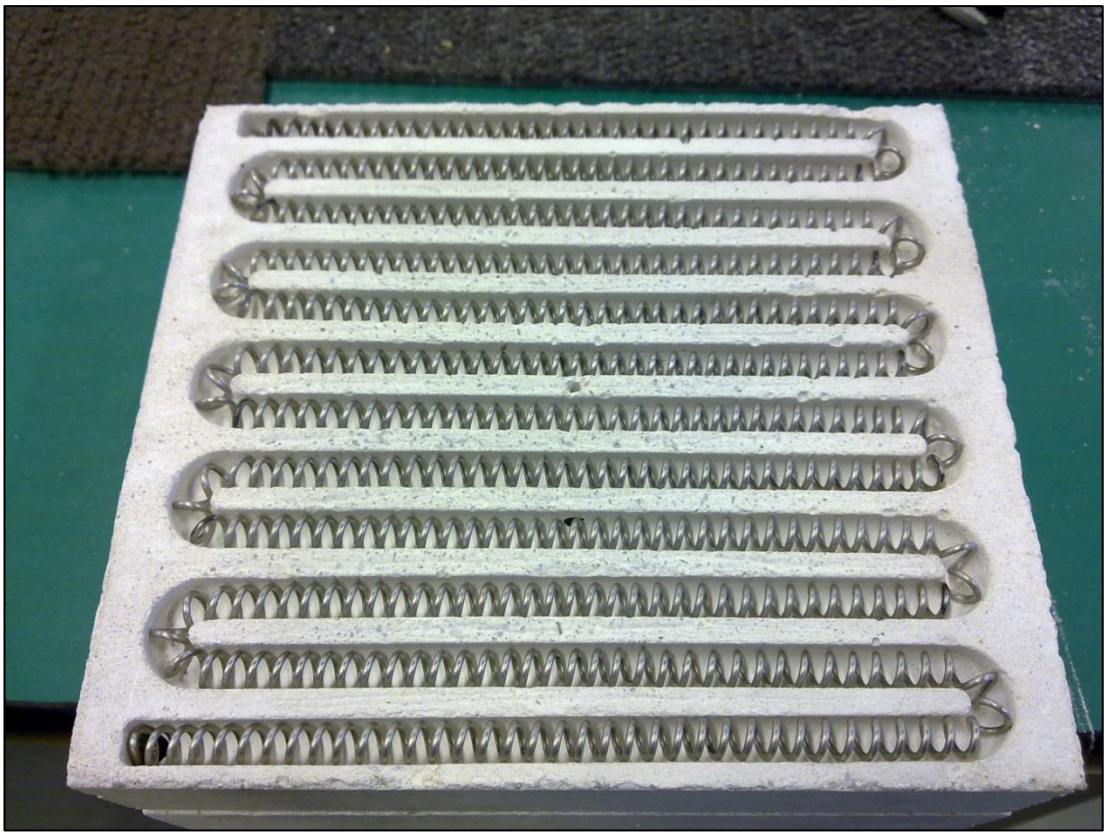

Figure 3.10. Heating wire coil shaped to fit in the bottom ceramic part channel.

3.5.6 Heater Box

Heater box encloses and supports all the internal heater parts (Figure 3.11). It is made from a 1 mm thick stainless steel sheet. It was designed to be manufactured from a single sheet, and does not require bolting, riveting or welding. The design only requires eight 90° bends to be made to form the box. At the design stage, the practically achievable sheet metal bend radiuses were not known. Therefore, 1 mm was used for the bend radiuses as a default value. (Technical Drawing 13) The stainless steel sheet was cut using PlasmaCam plasma cutter, made by the Metal Form Group. Then, the cut flat shape was folded using Metalmaster type KP.4 sheet metal folding machine. Actual bend radiuses were larger than 1mm, which resulted in the heater box wall height of less than 80 mm. The ceramic insulation parts would not fit in the box. Therefore, four 2 mm thick spacers were manufactured to be placed between the heater box and the heater support plate thus in effect increasing the heater box wall height. (Technical Drawing 14)

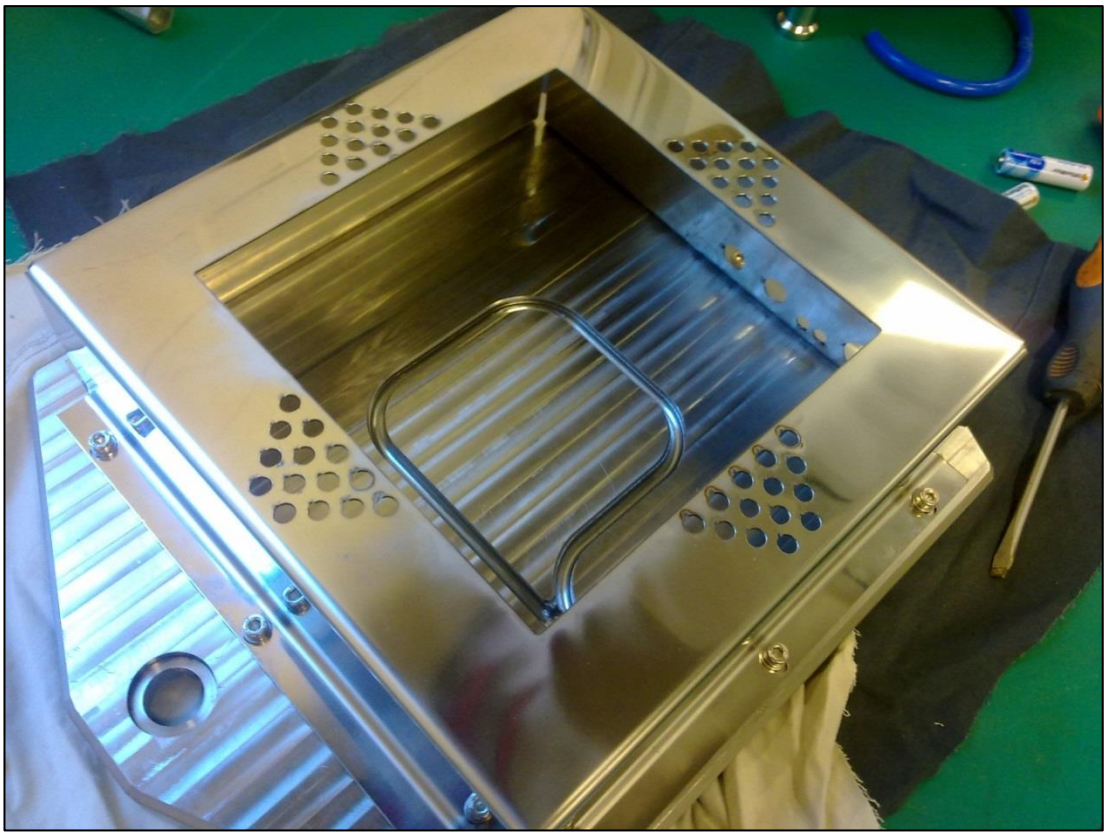

Figure 3.11. Heater box, laser cut from stainless steel sheet and folded.

3.5.7 Heater Hot Surface

The hot surface of the heater provides a flat heating surface and supports the weight of the center ceramic parts when the heater is suspended on the support shafts. It also must be thermally conductive to allow heat flow, but has to be electrically insulating to avoid shorting of the heating wire coil. Heater hot surface is made of two layers of 180 × 180 × 1 mm^3 stainless steel rectangles and a layer of a 1 mm thick alumina tiles. The two stainless steel sheets are cut in order to prevent warpage due to the large thermal gradients throughout the sheets (Technical Drawing 15). The alumina tile layer prevents heating wire coil from being short circuited with electrically conductive stainless steel sheets.

3.5.8 Heater Assembly

The heater assembly is a standalone unit, which can be operated even outside of the measurement system. It can be used either way - hot surface facing down or up. The heater has been designed to be easily disassembled in case one or more of its internal

parts have to be replaced. The exploded diagram of the heater is shown in Figure 3.12.

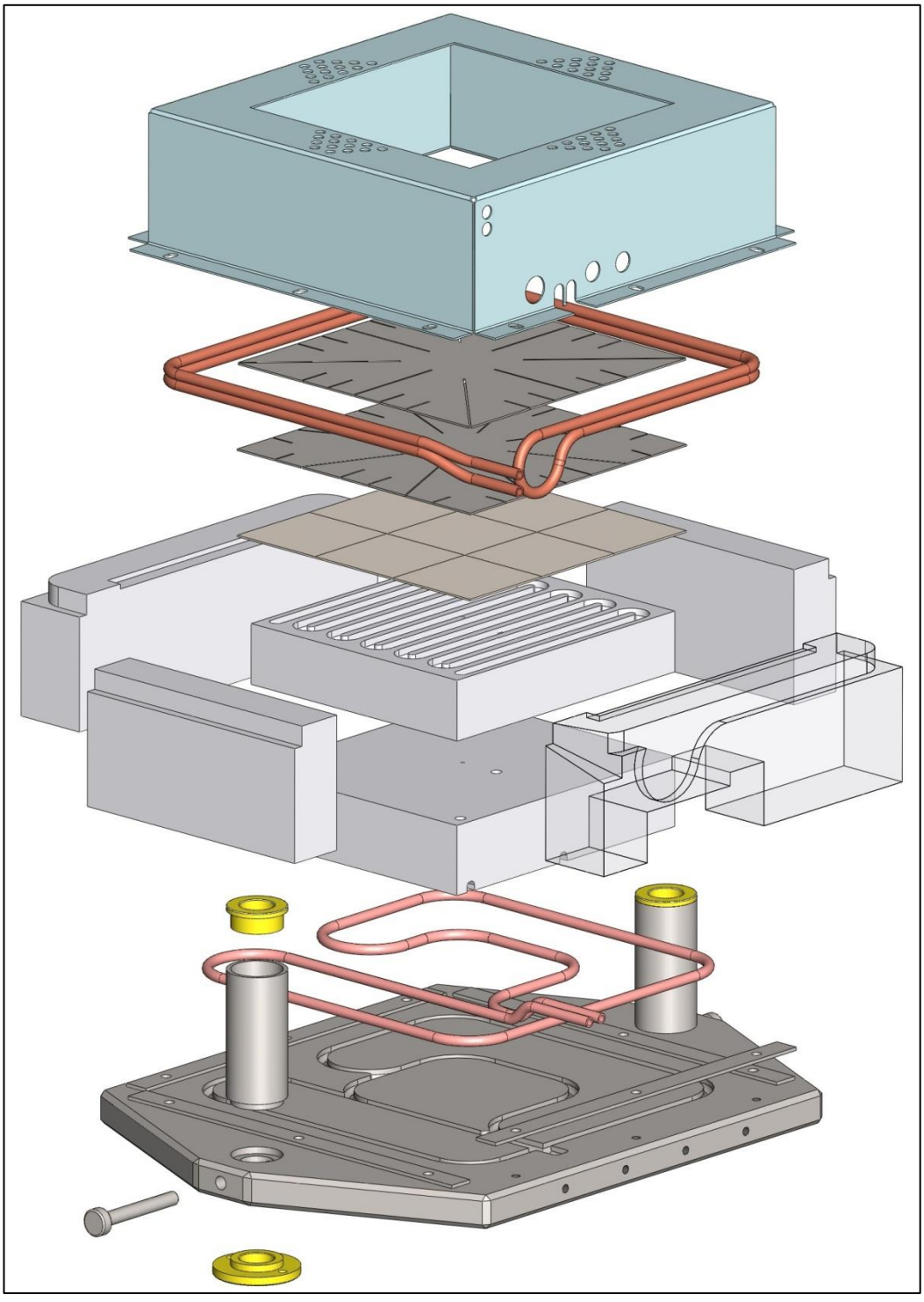

Figure 3.12. Exploded view of the heater assembly CAD model.

Firstly, heater support plate was prepared for the assembly. Two machined guide tubes were TIG welded onto the LG-500 Hartford CNC machined heater support

plate ensuring that the axis of the guide tubes is perfectly perpendicular to the heater support plate plane. Welding process is likely to shift the parts being welded due to the thermal expansion and following contraction. This phenomenon was avoided here by creating matching shapes of the two parts. One end of the guide tube was interference-fitted into the heater support plate to ensure there was no lateral movement. The shoulder on the guide tube rested on the heater support plate flat surface and was clamped down tightly during welding to retain right angles for the two parts.

Next, the two bottom nylon bushings were pressed into the open ends of the guide tubes. Then, the two top nylon bushings (Technical Drawing 16) were fitted into the slots on the top face of the heater support plate and bolted using four 10 mm long M5 socket head cap stainless steel bolts. A ¼ in annealed copper tube was inserted into the 6 mm round bottomed channel in the heater support plate. The tube was selected owing to its favourable properties, such as annealed copper tube is relatively soft and it can easily be bent once even by hand, but then it hardens. As a general rule, minimum tube centerline bend radius is 2 to 2.5 times the tube diameter. Trying to achieve smaller radiuses would be prone to kinks and wrinkles on the inside side of the bend. Hence, for a ¼ in tube the centreline bending radius should not be less than ½ in or 12.7 mm. This was kept in mind while designing the heater support plate channel and the heater thermal insulation back piece. A 1.8 m of annealed ¼ in copper tube was cut from the reel and straightened. The tube was then shaped to its final form by firmly pressing it into the heater support plate channel and, while doing so, was shaped to fit the channel. The tube ends were raised out of the heater support plate surface by approximately 10 mm, keeping them parallel to the surface. Then, they were spread apart by 5 mm to allow space for brass fittings. Excess of the tube was cut off using a tube cutter. Tube shaping imperfections were filled with silver containing thermally conductive paste to improve copper tube–support plate heat exchange.

Center piece assembly

The leads were then carefully passed through the holes in the bottom center ceramic insulation part and the coil was placed into the channel. One layer of silica fabric was put on top of the bottom center part. The copper leads inside silica sleeves were fed through top center insulation block, with the top block being placed on the bottom block. The two block stack was not separated again throughout the assembly process. The copper conductors were bend 90° and laid into the groove on top of the top center insulation part. Finally, two thermocouples were inserted into the structure. A backup thermocouple was made from a 1.5 mm diameter wires and a 6 mm diameter two bore alumina tube. The thermocouple does not have immediate contact with the hot surface and measures temperature just behind the heater coil. Therefore, it is likely to display temperature values that are much higher than the actual hot surface temperature. The thermocouple was inserted into its hole to mark the place where it has to be bent, while alumina tube was broken to the length of straight wires, just before the bend. Both thermocouples were insulated with another piece of two bore alumina tube. Center thermocouple is a mineral insulated thermocouple with a stainless steel sheath. It is 1.5 mm in diameter and was inserted in the center hole until it reached the surface on the other side. Then, it was bent to fit the groove on top of the top center insulation part together with the backup thermocouple (Figure 3.13).

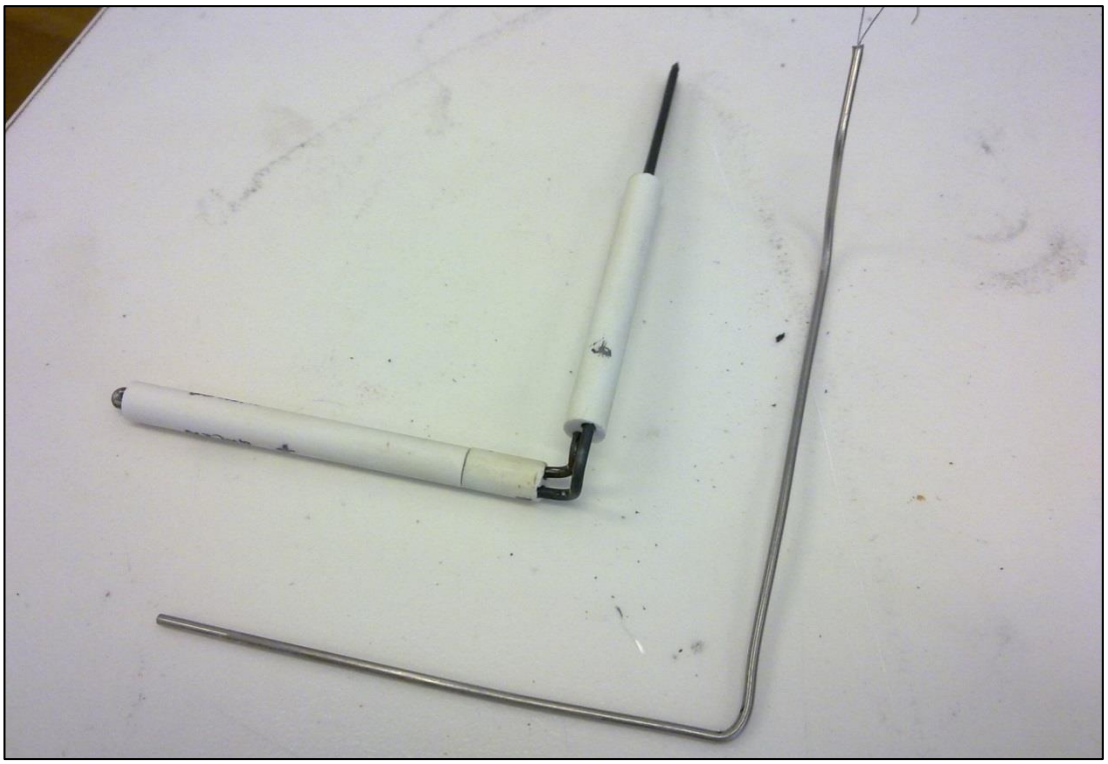

Figure 3.13. Heater thermocouples formed to fit heater thermal insulation.

The rest of the heater box was assembled in following manner. Firstly, a returning loop of ¼ in copper tube was formed by hand outside the box using a 20 mm aluminium rod to aid in bending. The tube was formed to tightly fit the inside bottom of the heater box. A 2.2 m copper tube was cut from the reel and straightened with a 13 mm outside bend radius 180° bend located at the middle of the tube length. Extreme care was taken to avoid kinks and blockage of the tube. The aforementioned bend was then continued to ~260°, with the following section of the tube being bent back to 180° direction to stack the two antiparallel tube loops. Three 90° bends were made minding the right chirality, dimensions, and angles to form a square double tube loop. S-shaped bends were formed from the spot where the two tube ends depart heater box corner to exit the heater box through the designated holes 10 mm away from the wall and 10 mm and 20 mm away from the bottom, keeping the tube ends parallel to the initial tube axis. 30 mm of the tube outside the heater box was left for brass fittings with excess tubing being cut away The whole tube assembly was placed into the heater box as shown in Figure 3.14.

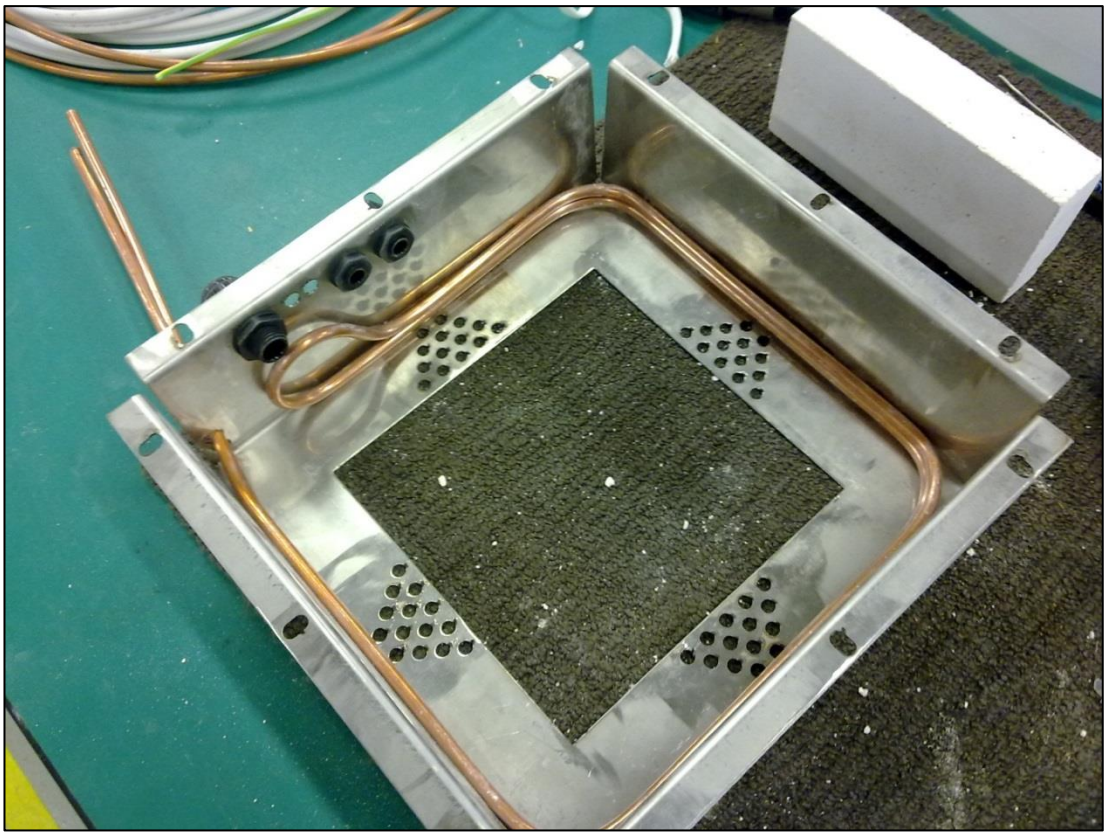

Figure 3.14. Bottom cooling loop just formed and placed in the heater box.

The bottom of the heater box was lined with a single layer of silica fabric. This fabric improves thermal insulation of the heater. Two hot surface 1 mm thick sheets were placed in the center of the heater box. A layer of silica fabric was placed on top of the two steel sheets to absorb any steel sheet, alumina plate, or ceramic center bottom part surface irregularities. A 1 mm thick alumina plates were tiled covering the surface of silica fabric. Heater thermal insulation back piece was placed. The back and the front pieces have slots on their bottom sides to position the heater hot surface plates. The heater hot surface plate stack was pushed as far as it goes into the slot in the rear piece. The center piece assembly was then placed in the middle of the heated box, the front piece was then inserted, making sure that the heater hot surface plate stack is sitting properly in its slot. Finally, two side pieces were inserted into the side pockets, completing the heater thermal insulation body.

One 16 mm gland for heater coil power leads and two 12 mm glands for thermocouple wiring were fixed into the designated holes in the heater box back wall. Two 50 cm long 32 A current rated insulated copper conductors were passed

through the 16 mm gland. The leads were trimmed ~15 mm outside the center top insulation piece for comfortable soldering. A heatshrink tube was put on the lead. The leads and the wires were held tightly end to end and soldered using Weller WD 1M soldering iron and lead-tin solder. Silica sleeves were then pushed back over the soldered joint and the insulated wire. The heatshrink tubes were moved over the soldered joints and shrunk using the soldering iron to ensure electrical insulation. A 50 cm long K-type shielded thermocouple extension wires were passed through each of the 12 mm glands. According to the ANSI coding thermocouple extension wire insulation colors are as follows: positive wire–chromel–yellow; negative wire–alumel–red. Thermocouple wires were twisted with extension leads, minding the correct wire polarity. The twists were then reinforced with solder. Electrical contact was created by the twists. The solder does not wet nickel alloys very well. Therefore, it is there to mainly provide structural support. The soldered twists were then electrically insulated with heatshrink tubes. The glands were tightened to lock and secure wire position. Unused space in the thermal insulation back piece was filled with insulating ceramic fiber wool.

During assembly, a slight variation in the height of the insulating ceramic part was observed. This variation could result in an undesired possibility of vertical part motion once the heater is fully assembled. Therefore, the gap between heater support plate and ceramic insulation parts was lined with several layers of ~0.5 mm thick silica fabric.

Heater support plate was placed on top of the heater box. Holding everything together, the assembly was flipped over so the heater hot surface was facing up. Heater box, heater box spacers, and heater support plate were aligned to the fixing holes. Twelve 15 mm long M6 socket head bolts were used to fix the parts and complete the assembly.

3.6 Cooler

The main function of the cooler (Figure 3.15) is to maintain relatively low temperatures at the thermoelectric module cold side. It has to effectively dissipate the heat flowing through the module. Moreover, it must be strong enough to transfer 20

kN of compression force from the hydraulic cylinder to the module and has to be able to move vertically, but always perfectly parallel to the baseplate surface.

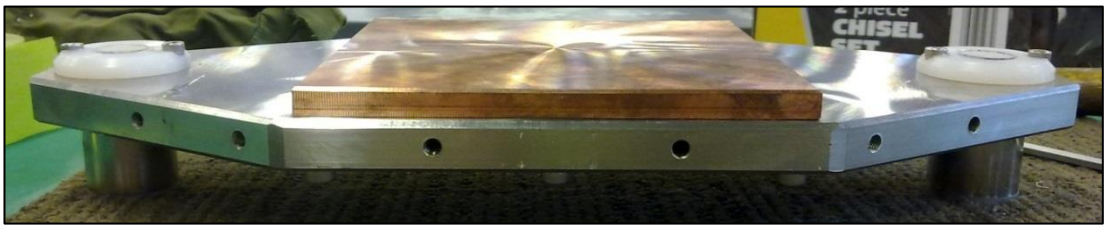

Figure 3.15. A view of a fully assembled cooler.

3.6.1 Cooler Support Plate and Guide Tubes

The cooler support plate is CNC machined from 20 mm thick stainless steel plate with a 3 mm chamfer all round, (Technical Drawing 17) which has guide tubes (Technical Drawing 18) welded in and have nylon bushings (Technical Drawing 7) pressed into them. The nylon bushings are 50 mm apart and can slide on the support shaft. The tubes and bushings ensure that the heater support plate stays in parallel to the baseplate at all times with minimal swivel or rocking.

3.6.2 Cooler Water Channel Plate

Cooler water channel is CNC machined in a 10 mm thick copper plate (Figure 3.16) (Technical Drawing 19). The channel itself is 7 mm deep and 6 mm wide, and is shaped as a double square spiral. It has a blind hole in the center going very close to the cooling surface deigned to accommodate a thermocouple. It is held on the support plate by eight M6 blind threads and silicone gasket.

The 1 mm thick channel walls serve several purposes. They direct the cooling water flow and work as heat exchangers between two antiparallel flows. Additionally, they provide stiffness for the copper plate dealing with up to 7 Bar hydrostatic pressure. Moreover, they provide sufficient crushing strength to transfer the compression force from hydraulic cylinder to the module. Compared to serpentine channel or parallel one direction channel, cooling water flow to the center of the plate and out in a spiral pattern eliminates the possibility of a thermal gradient throughout the copper plate. It might have some thermal gradient between two neighbouring flows, decreasing to minimum at the center of the plate. Nevertheless, this thermal gradient is practically

not noticeable because of very fast heat diffusion through a 3 mm thick cooler top surface.

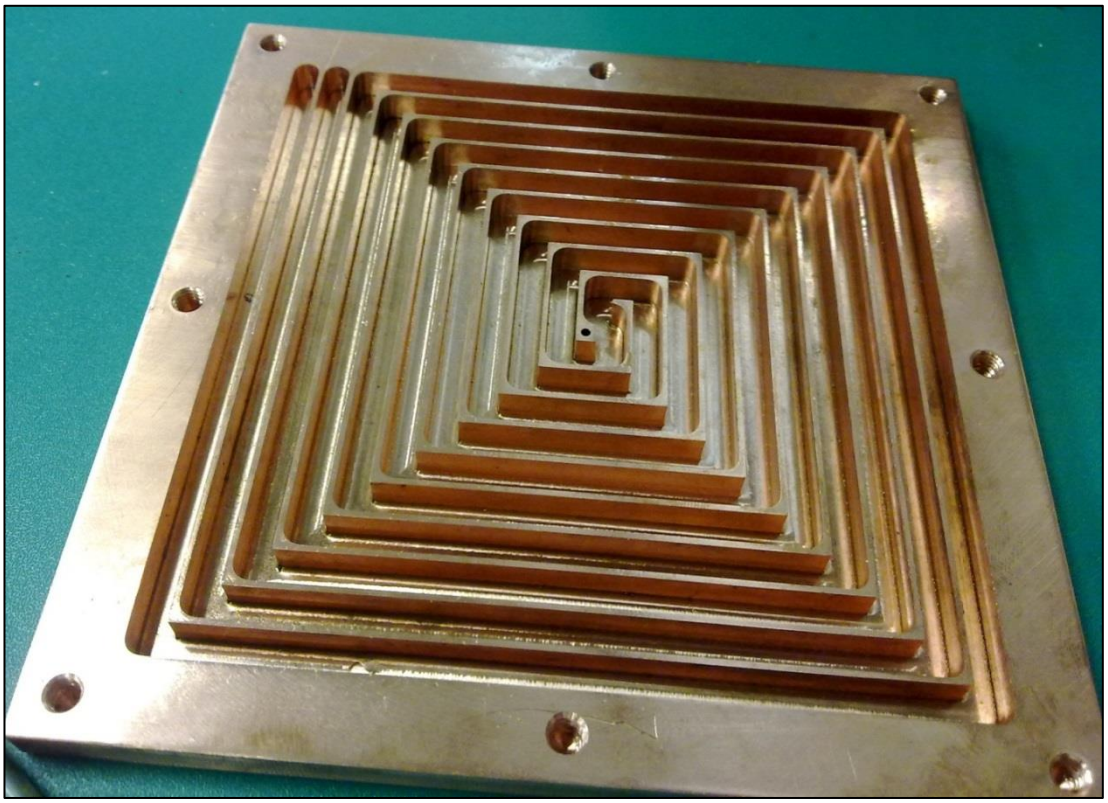

Figure 3.16. A view of a cooling water channel in the cooler plate.

3.6.3 Force Transducer

A miniature industrial compression load cell (LCGB-5K, Omega, United Kingdom) was used as a force transducer to accurately measure the compression force exerted on the thermoelectric module. The LCGB series comprises miniature low-profile compression load cells with excellent long-term stability. A stainless steel construction ensures reliability in harsh industrial environments. These cells are designed to be mounted on a flat surface using socket cap screws to secure them to the base. A load button is integral to their basic construction for even force distribution. The rated capacity of LCGB-5K load cell is 5000 pounds or 22 kN. It is mounted on the bottom side of the cooler support plate, in direct contact with the hydraulic cylinder. Its nominal output is 2 $\frac{mV}{V}$ at 10 V excitation.

3.6.4 Cooler Assembly

Similarly to the initial steps of the heater assembly process, first step in cooler assembly (Figure 3.17) was to guide tube TIG welding into the CNC machined and threaded cooler support plate. Then, bottom guide tube bushings were pressed into the guide tubes. Next, top bushings were fitted on top of the cooler support plate and bolted with four 15 mm long M5 socket cap bolts.

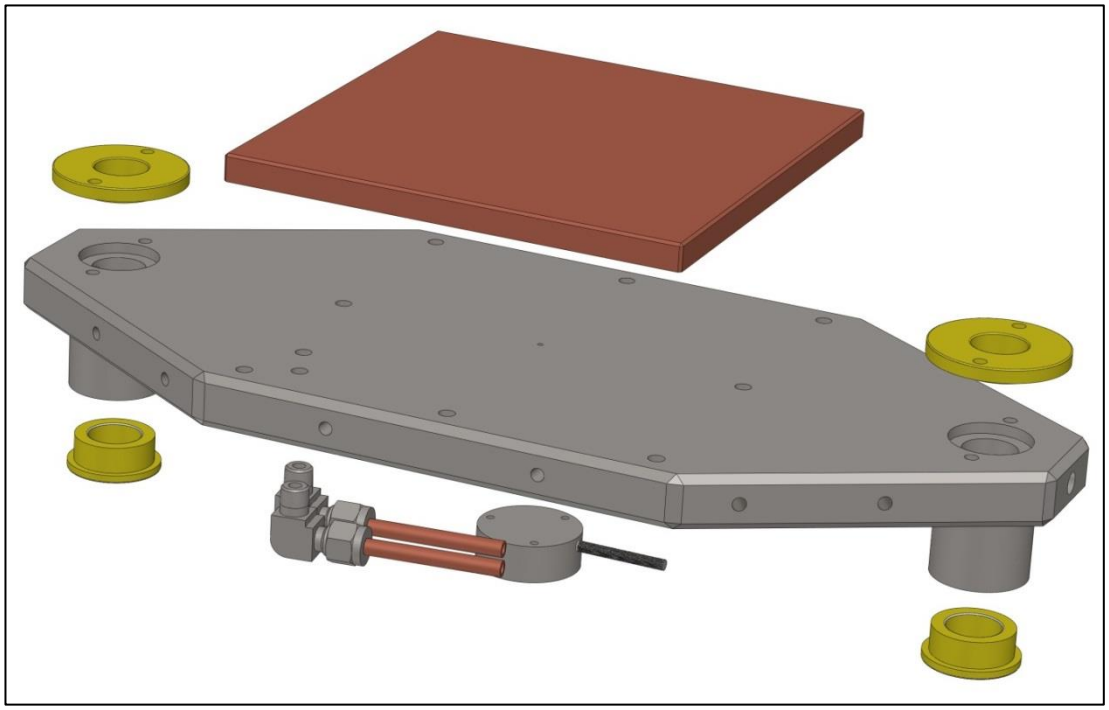

Figure 3.17. Exploded view of the cooler assembly CAD model.

Cooler support plate top surface was prepared for copper plate attachment. It was cleaned and degreased with acetone; its side was polished by moving it on a 1000 grit sandpaper sheet placed on a flat surface. It was then cleaned and degreased with acetone. Eight M6 socket cap bolts were cut to 28 mm in length and screwed into the copper plate to confirm that the thread depth and quality are good. Two strips of Scotch 233+ label tape were placed across the cooler support plate surface 17 cm apart, just on the boundaries of the intended copper plate position. Thick long bead of silicone sealant was extruded on one side of the support plate. Using a straight sharp plastic board, the silicone bead was evenly spread across the support plate. Running the board on top of the label tape creates ~100 μm thick layer of silicone sealant. After the silicone was evenly spread, excess of it was scraped away. The label tape strips were peeled off leaving just a layer of silicone sealant. Two M6 bolts

were placed into the corner holes to help with the copper plate alignment. The copper plate was placed on the two bolts and then carefully lowered onto the support plate surface. A 100 kg weight was placed on the copper plate to make sure it sits well in the sealant. M6 bolts were tightened to a 5 Nm torque and the assembly was left for 24 hr to cure the sealant.

The cooler assembly had to be leak–proof tested prior to any further development. The cooler was connected to buildings cooling water supply using ¼ in nylon tubing. The hydrostatic pressure in the building cooling water system can reach 6-7 Bar. At 7 Bar pressure, the force pushing the copper plate away from the support plate is 12 kN, enough to lift a small car. With the return tap still fully closed, the flow tap was carefully and very slowly opened. As the pressure in the system was building up the cooler was continuously observed. At one point, a crackling sound of silicone sealant being torn was heard and cooling water started escaping from under the copper plate and through the thermocouple hole. Water tap was quickly shut. Nylon tubes were pulled out of the fittings to relieve the pressure. The assembly was dried. The eight bolts were undone and the copper plate was pried off the support plate. The silicone sealant had a very good adhesion to the steel surface, but very poor adhesion to copper. The sealant had become slightly greenish blue color, color characteristic to copper ions, indicating a chemical reaction between copper and the sealant. Both parts had silicone sealant removed and cleaned. The sealant was removed mechanically using a razor blade. Then the steel surface was washed clean using kerosene. Both plates were degreased using acetone. A different type of silicone sealant was used for the second assembly. Selleys multipurpose non-acid curing silicone sealant was selected to avoid reactions with copper. The use of acid free sealant was successful, as the assembly was able to hold applied static water pressure. Furthermore, it was able to hold sudden tap opening and closing resulting in dynamic pressure spikes.

Cooler assembly was continued by inserting cooler thermocouple. First, the thermocouple hole and groove were filled with silicone sealant. Then, a 1.5 mm diameter mineral insulated K-type thermocouple with stainless steel sheath (TC direct, Australia) was bent to the shape inserted into the hole and groove, making

sure it sits as deep into the copper plate as possible. The sealant was levelled to the support plate surface and left to cure for 24 h. LCGB-5K force transducer was mounted onto the bottom side of the support plate using three 20 mm long M3 socket cap bolts.

3.7 Hydraulic Compression System

The force unit creates compressive force acting upon the thermoelectric module being measured. It employs structural components of the measurement system to transfer the force. Most of the force unit components are external to the vacuum system, except the hydraulic cylinder, which is mounted through the bell jar baseplate, which is a boundary of the vacuum system. The pressure in the hydraulic system is displayed on an analog gauge, whereas the actual force exerted on the measurement system components is measured by the force transducer mounted at the bottom side of the cooler support plate.

Compression plays a crucial role in thermoelectric generator installation. High clamping force will minimise thermal resistance between the module and the heat source/sink. Optimum clamping force and its influence on module performance can be found in research publications [98]. Additionally, compression force would keep the parts in good contact and keep module operational, even if cracks were to develop inside the module due to the thermal cycling. A typical clamping force for bismuth telluride thermoelectric module is around 150 $\frac{N}{cm^2}$ [99]. For a common 50 × 50 mm^2 module the required clamping force would be 3750 N, while for 100 × 100 mm^2 module this force would increase to 15 kN. These typical values are well within the design limits of the measurement system capabilities.

The clamping force in the designed system is achieved by employing RC51 hydraulic cylinder (Enerpac, Australia). It is one of the smallest cylinders available in Enerpac's range. It's rated for a 5 ton maximum load and 25 mm maximum ram extension. This extension, coupled with 20 mm steps for heater positioning provides enough flexibility to accommodate different size thermoelectric modules and objects, *i.e.* objects of up to 120 mm in height can be fitted between the heater and cooler.

P142 model hand operated pump was selected to pressurise the hydraulic cylinder. It is the smallest pump available, meaning that it has the best pressure control precision. It is rated to 700 Bar maximum pressure. At this pressure, the hydraulic ram force will be 35 kN and is beyond the maximum intended clamping force of 20 kN.. Thus, the measurement system was installed with sound and light alarms to indicate, if the pressure exceeds the maximum allowable limit.

Fully assembled hydraulic system was degassed, leak–proof tested and pressure-hold tested. Gas in a hydraulic system can make it unresponsive and unreliable. A typical example of such situation is vehicle brake system. The air present in the brake system compromises the effectiveness of the braking system. Therefore, it must be bled prior to using it. Unfortunately, bleeding of the hydraulic system in our measurement system is not possible. However, the system can be degased by pressurising it at a full cylinder extension and depressurising it several times. Any gases trapped in the hydraulic system will be compressed and dissolve in the hydraulic oil. Dissolved gas is then carried out to the hydraulic oil reservoir upon retraction of the piston and can escape to the atmosphere there.

Our initial pressure hold test (Figure 3.18) was not successful. At high pressure the transducer signal would slowly diminish due to elastic relaxation in the system. On the other hand, at low pressure settings the pressure would drop to zero very quickly. The conclusion was that the “one-way” valve installed in our hand pump is not perfectly “one-way” at low pressure. Therefore, an additional high pressure needle valve (Enerpac V-182) was installed between the pump and the gauge adapter. This valve prevented hydraulic oil to return to the pump when the system is pressurised. It solved the pressure drop issue. No oil leaks were observed at various pressure settings for extended periods of time.

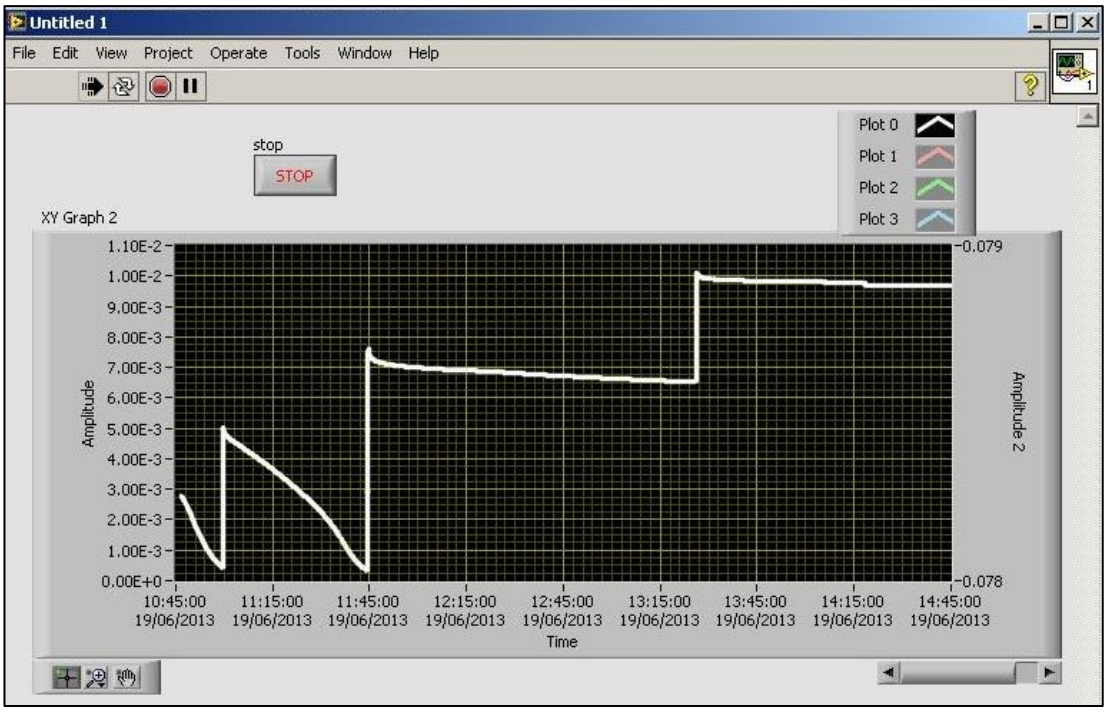

Figure 3.18. Evaluation of a low pressure hydraulic system pressure drop. Y-axis on the left displays force transducer signal. 1 mV represents 130.7 kg of clamping force.

3.8 Vacuum System

Vacuum system plays a very important role in the measurement system. Without it, only modules insensitive to air could be measured, such as bismuth telluride modules that can operate only at low temperatures or metal oxide based modules, which operate at high temperature. With the vacuum system present, it is possible to measure thermoelectric generator modules constructed from all kind of materials, even those sensitive to oxygen or moisture. The measurements can be carried out under vacuum or under Argon atmosphere.

Main components of the vacuum system are the baseplate, glass bell jar and a rotary vane vacuum pump. The baseplate provides structural support for the whole measurement system. It has to be able to handle the forces acting on it because of the vacuum in the bell jar and the stresses from the hydraulic system with no physical deformation. It accommodates feedthroughs for cooling water, gas, vacuum pump, heater power supply, sensor electronic signals, and module power output leads. All

of the feedthroughs and fittings must be vacuum tight. The schematic drawing of vacuum system is shown in Figure 3.19.

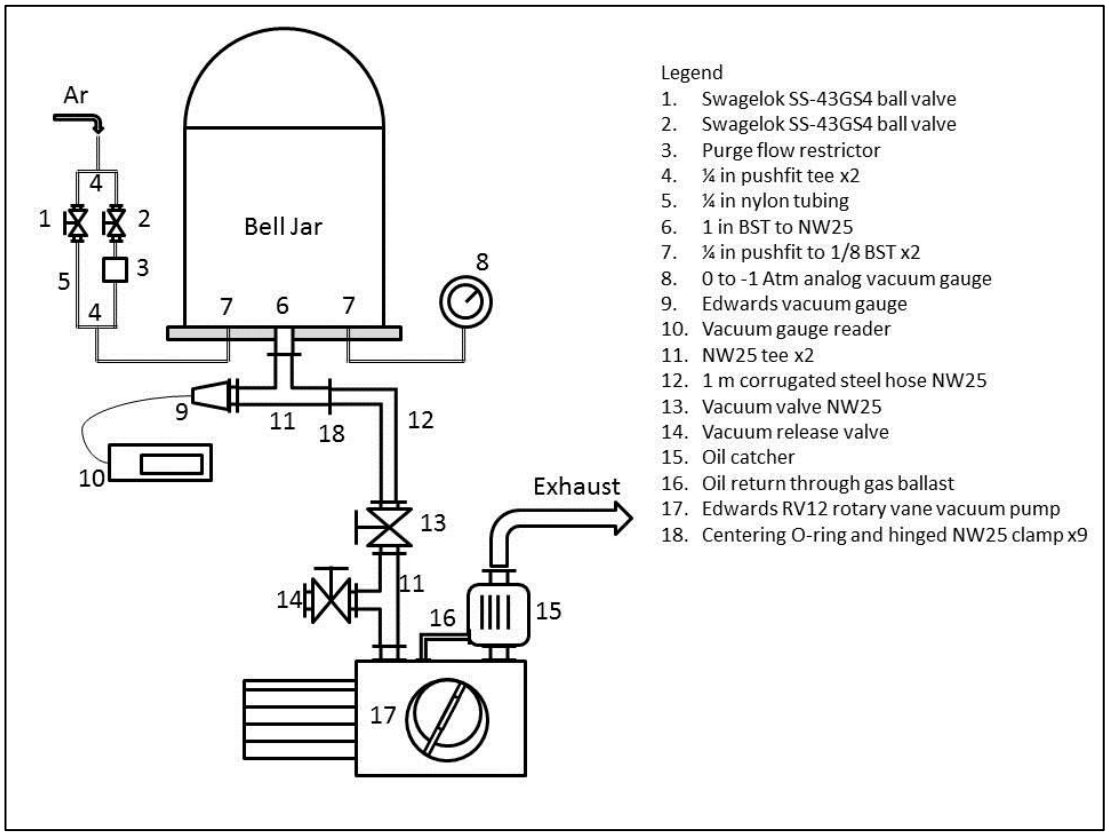

Figure 3.19. Schematic diagram of vacuum system.

The baseplate, as described previously, is 20 mm thick 500 mm diameter disk. Its size and its weight give stability to the whole measurement system. The guide shafts are fixed through the baseplate and joining points are sealed with silicone liquid gaskets.

The bell jar is made of see-through glass with a wall thickness around 7mm. Its cylindrical part is 15 inch tall with the dome part being 9 inch internal radius semi sphere. On the bottom of the jar, an 18 inch diameter L-shaped Viton gasket is used to seal the baseplate and the bell jar contact point. The gasket stays on the bell jar bottom. High vacuum silicone grease has to be used for baseplate–Viton gasket contact. If vacuum is needed, the bell jar has to be precisely aligned with the baseplate axis over the whole measurement system, and then carefully lowered

taking care not to touch guide rods or heater support plate. When the bell jar is no longer needed, it has to be lifted vertically until its bottom gets over the top steel bar. When compared, glass bell jars have advantages over steel vacuum chambers. They are lighter, cheaper, and transparent. Glass bell jars are widely used for high vacuum applications such as physical vapour deposition chambers. It is possible to break the jar by striking it with a hard object with a substantial momentum, causing an implosion. A plastic protection barrel should be fitted on the bell jar at all times.

The vacuum in the system is generated by rotary vane vacuum pump (Edwards RV12). KF-25 to 1 inch male BSP short stub adapter was screwed into the baseplate from the bottom side. Teflon tape and Loctite 243 thread locking compound were used to ensure vacuum tight seal. Three–way T fitting was mounted to the middle port to the adapter. Pfeiffer vacuum gauge (XLC model) was mounted on one side of the T fitting, and connected to Edwards active digital controller. A 1.5 m long corrugated pipe was mounted on the other side of the T fitting. The corrugated pipe was then connected to a vacuum valve. The valve was connected to the end of a T fitting a continued through another T fitting onto a vacuum pump. A breather valve was mounted to the middle port of the T fitting. Thin film of high vacuum silicone grease was applied to all mating fitting surfaces to ensure the system is leak free.

Rotary vane pumps tend to pulverize and spit vacuum oil out of the exhaust port. An oil mist adapter was mounted on the exhaust port and was connected to the fume cupboard to eliminate any unwanted oil coming from the pump. The oil mist filter was also connected to modified pump gas ballast selector, specially designed to accept gas and oil return from the exhaust port. The gas ballast was set to “I” position for minimal suction.

Analog vacuum gauge (-1 to 0 Bar) was connected to one of the two gas ports in the baseplate using a ¼ inch nylon tube and push-fit fittings with O-rings. Argon gas was connected to the other gas port in the baseplate through a Swagelok ball valve (model SS-43GC4). The best attained vacuum in this hardware configuration was $< 1 \times 10^{-2}$ mBar.

During a long (>72hr) operation, condensation on the internal wall of the bell jar was observed. During an extended operation of the vacuum pump at maximum vacuum, with no gas flow present, the vacuum oil vapour can diffuse into the vacuum chamber and condense on cold surfaces such as cooling water tubes or bell jar internal wall. Some of the oil vapour could also pyrolize on the hot surface of the heater. This vapour diffusion was rectified by inserting an activated alumina bead filter right on the inlet of the pump. The filter is an obstruction for the gas flow. As a result, it had slightly reduced maximum attainable vacuum. Unfortunately, in few days of pump operation, the filter saturated and the oil vapour diffusion and condensation resumed.

It was decided to introduce a small flow of Argon to the vacuum chamber. Ideally, to keep the measurement system as simple as possible, this small flow should come straight from the buildings Argon supply system without a pressure regulator. Argon pressure in the building supply system is around 5 Bar and is quite stable. This should result in constant gas flow rate through the flow resistor.

The alumina bead filter was removed. A second Argon valve was added in parallel to the first one. The second valve is the smallest needle valve (B-SS4) from Swagelok catalogue. These valves are preset in the factory for 4 to 10 mL/min gas flow at 1 Bar pressure with valve dial in closed position. This setting was altered so that the valve can be fully closed. It was soon realised that it is very difficult to set a very small flow rate. The vacuum chamber pressure would jump by two orders of magnitude if the dial was opened for more than 90°, while ten full turns are required to fully open the valve. Additionally, it is very easy to damage the needle or the needle seal while trying to fully close the valve by over tightening it. Due to the problematic setting and short predicted lifetime, it was decided to replace the needle valve with a ball valve to stop the flow and a small diameter tube to limit the flow rate.

High pressure difference and low flow rate makes it impossible to calculate the diameter of the tube needed for proper operation. The right tube diameter was found using engineering intuition and manual flow rate measurements. Small diameter channels were made inside spiggets - 14 mm long brass end inserts for ¼ in plastic

tubes, used to prevent tube crushing when using Swagelok fittings. A spigget was heated with soldering iron and filled with solder from one end ensuring there is no flux trapped inside the spigget. A wire with poor wettability (alumel or steel) was then inserted through the molten solder. The solder was let to solidify. The spigget was heated up, and the wire was pulled out when the solder reached its softening temperature. The spigget was inserted into a ¼ in nylon tube coming from the vacuum chamber and connected to the second Argon valve. The chamber was evacuated to 1×10^{-2} mBar. The second Argon valve was opened to check the resulting vacuum. Several analog pressure gauge readings and elapsed time were taken to estimate the flow rate through the spigget tube.

Three 0.12 mm diameter wires were twisted to form close packed structure and inserted through the molten solder in a spigget and left there permanently. Three close packed wires create a void between them. The void area is only 5% of the wire cross section area. When inserted through the solder the resulting void area can be 20 to 30% of the wire cross section area due to the creases outside the twist and the surface tension of the solder. However, that area is divided among four separate capillaries with very small effective radius. The flow restrictor was tested the same way as described above. Test results are shown in Table 3.1.

Table 3.1. Average flow rates through flow restrictors made using different wires converted to atmospheric pressure.

Wire diameter, mm	Equilibrium Chamber Pressure, mBar	Flow rate, mL/s
0.38	>1	45
0.18	>1	15
0.12	>1	8
0.12x3	0.13	0.2

Several assumptions were made for the flow rate calculations: the process is isothermal, atmospheric pressure is 1 Bar, ambient temperature is 25 °C, chamber volume is 50 L, and Argon is ideal gas. With these assumptions, ideal gas law was used to calculate flow rates:

$$PV = nRT$$

$$\Delta n = \frac{\Delta PV}{RT}$$

$$\frac{\Delta n V_M}{t} = \frac{\Delta PV}{RTt}$$

Equation 3.2. Flow rate calculation using ideal gas law.

All flow rate values were converted to milliliters per second for easy comparison. Only the flow restrictor with three twisted wires provided flow small enough to retain acceptable level of vacuum in the system. Upon introduction of 0.2 $\frac{mL}{s}$ gas flow the vacuum drops by one order of magnitude to 1.3×10^{-1} mBar with the pumping rate at this pressure of 4.8 $\frac{m^3}{hr}$. Average linear speed of gas through NW25 fittings is 3.5 m/s. This prevented oil vapour from diffusing into the vacuum chamber and, thus, no further condensation was observed in the chamber even after prolonged use of vacuum pump. It was concluded that gas flow restrictor can effectively regulate purge flow rate by very simple means. Complicated gas pressure reduction and regulation components are not required nor are flow rate adjustments. Purge flow is simply switched on or off by operating a single ball valve.

3.9 Thermocouple Cold Junction Reference

The temperature readouts in the TEG module measurement system are achieved through K–type thermocouples. K–type thermocouples consisting of chromel and alumel alloys were selected because they have broad measurement range (-200 to 1250 °C), high accuracy (2.2 °C or 0.75% whichever is higher), high linearity, and low cost. National Instruments NI 9213 16 - channel thermocouple input module was used to read all the signals coming from thermocouples. NI9213 module has a 24 bit analog to digital converter for up to 0.02 °C measurement sensitivity, up to 1200 aggregate samples per second reading, and built-in cold junction compensation.

Temperature measurement using thermocouples is a differential measurement method. It always needs a point of reference with known absolute temperature. In the past, ice baths were used to provide the reference point of 0 °C very accurately (Figure 3.20 Left). Nowadays, use of ice baths is impractical and obsolete. Integrated circuits are capable of accurately measuring the temperature of the thermocouple could junction. Commonly, they are integrated inside the measuring device (e. g. temperature controller). Alternatively, they can be placed away from the measuring devices in a cold reference junction, and thermocouples from there are connected to a measuring device with copper wires (Figure 3.20 Right).

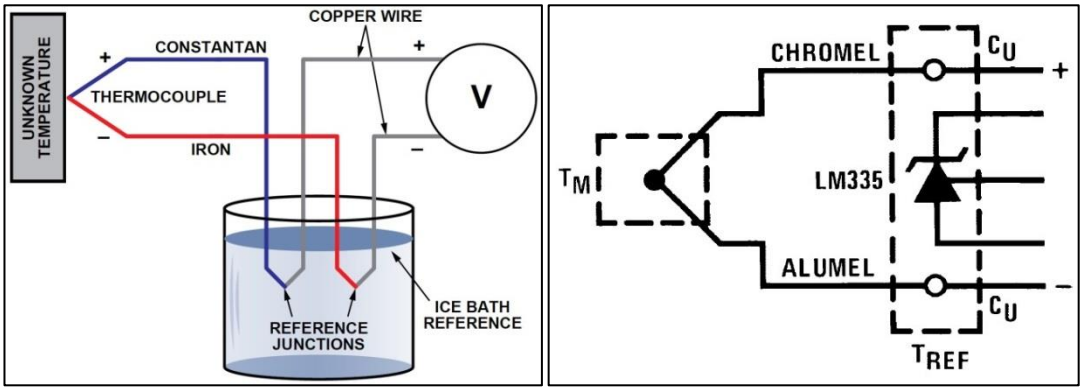

Figure 3.20. Thermocouple cold junction referencing: using ice bath (left) and using LM335 integrated circuit (right).

Temperature measurements inside of a vacuum chamber create additional problem of thermocouple wires transfer through the chamber wall. It is not impossible, but requires use of very expensive thermocouple feedthroughs. When multiple

thermocouples are used, the cost of their feedthroughs becomes very high compared to the overall system cost. Additionally, tens of meters of thermocouple wire would be needed to reach the measurement module and new feedthroughs would be required if thermocouple type had to be changed. Having a cold junction reference inside the vacuum chamber solves these problems. One multiple copper conductor feedthrough can be used, copper wires have to be used to connect it to the measurement module, and any type of thermocouple then can be used.

A Cold Junction Reference was designed built and installed inside the vacuum chamber. The CJR employs two LM335A temperature sensors due to its elongated form. The two temperature sensors are connected in series for average temperature measurement. The LM335A integrated circuit outputs absolute temperature with 10 mV/K sensitivity [100]. The sensors are excited by the auxiliary circuit board and measured by the NI 9219 module. Due to K–type thermocouple linearity, the NI 9213 thermocouple measurements are easily adjusted for CJR temperature in the control software.

The CJR has a "sandwich" structure: the bottom part (Technical Drawing 20) has grooves for solder contacts and wiring, three holes for ten conductor cables on one side, a 6 mm hole in the center, and two M6 threads through the part. The wire terminals and LM335A ICs are soldered into a 100 × 30 mm^2 prototyping board. The prototyping board has three 6 mm diameter holes for M6 bolts. The top part (Technical Drawing 21) is shaped to fit right between the two rows of wire terminals and around the LM335A sensors. It has two socket holes for two 15 mm long M6 socket head bolts and a 6 mm hole in the center. Sheet metal cover (Technical Drawing 22) is placed on top of the structure. Figure 3.21 shows the exploded view of the CJR assembly. Figure 3.22 shows the CJR just assembled (left) and installed onto the bell jar baseplate (right). CJR terminal assignments are shown in Figure 9.1, and listed in Table 9.2 together with its circuit board wiring and baseplate feedthrough connector wiring.

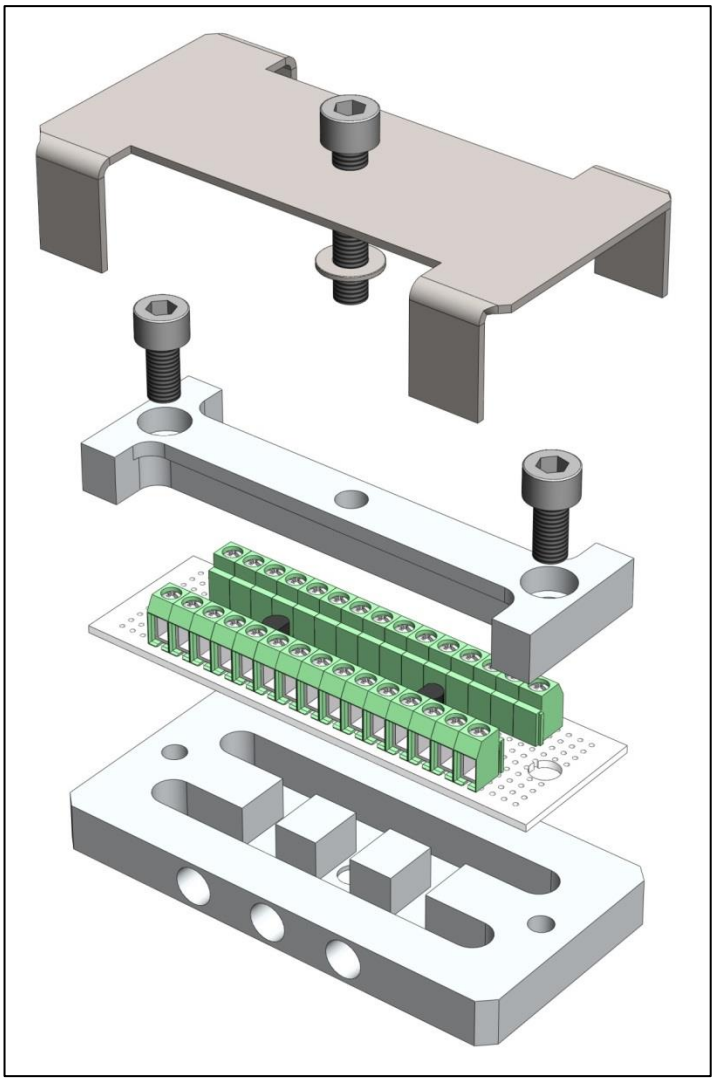

Figure 3.21. Exploded view of the cold junction reference assembly CAD model.

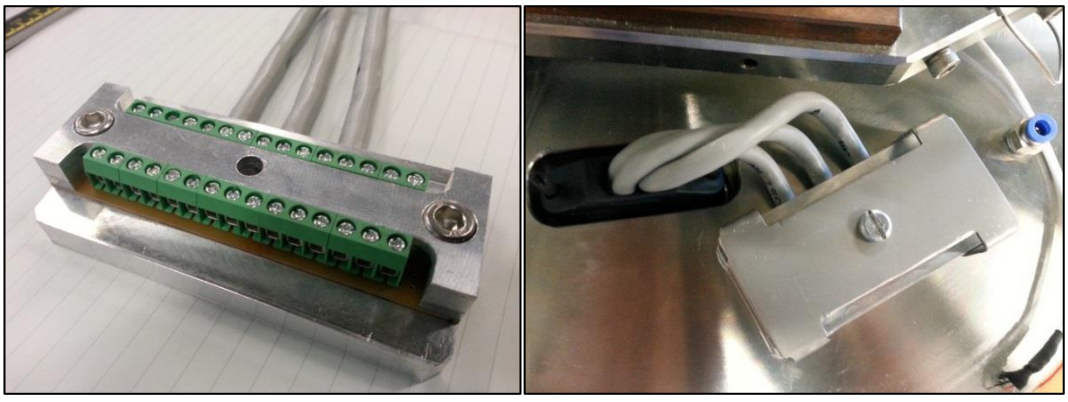

Figure 3.22. Cold junction reference just assembled (left) and installed (right).

3.10 System Assembly

The assembled measurement system is shown in Figure 3.23. The assembly was started by screwing in the four legs. Support shafts were inserted through the baseplate and rested onto liquid silicone gaskets. The support shaft holes were precisely aligned using an 8 mm diameter rod, ant the shafts were secured in place with M10 nuts. The hydraulic cylinder was screwed through the baseplate, vacuum sealed with a rubber O- ring, and locked in place with a retaining nut. The 6 inch Con Flat 50 conductor electric feed-through disk was bolted to the baseplate with an O-ring in between. 1/8 pushfit water and gas fittings, and BSP to NW25 adapter were fitted using Teflon tape and Loctite 243 thread locking compound. The high current electric feed-throughs were fitted using their O-rings and nuts. Additionally, steel plates with insulated electrical terminal blocks attached were fixed to the feedthroughs using nylon nuts. The feedthrough conductors were insulated with alumina beads and immobilised to the terminal blocks. Cold Junction Reference assembly was attached and connected to the sub D 50 feedthrough. Cooler assembly was lowered down the support shafts and rested atop the hydraulic ram. Heater assembly was lowered down the support shafts and fixed at its highest point using the 8 mm pins. Top support rod was fitted and tightened with closed nuts. Cooler and Heater water inlets and outlets were connected to their respective fittings on the baseplate using ¼ inch Nylon tube, making sure the tubes are well through the fitting O-rings. Building cooling water is supplied to Cooler and Heater baseplate inlets through 600 cm^3/min rotameters. Heater power leads were connected to its feedthrough terminal block. Cooler and Heater thermocouples were connected to their respective CJR terminals. Cooler and Heater assemblies were connected to the baseplate using color coded earth wires. Vacuum system was assembled as described in section 3.8. Hydraulic pump with needle valve, pressure gauge, and high pressure hydraulic hose attached was positioned next to the system, then the hose was plugged into the cylinder inlet and secured by hand tightening the hose retainer nut.

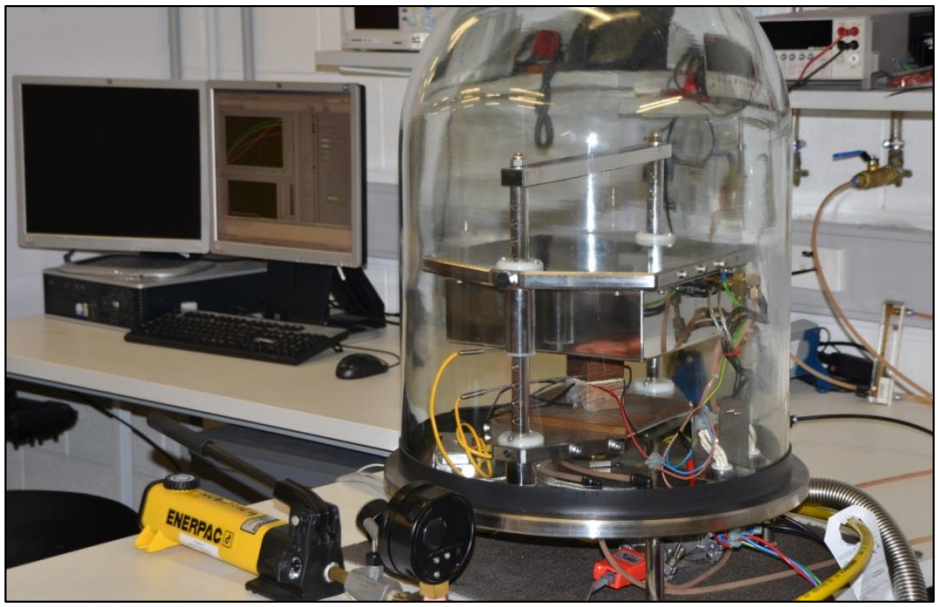

Figure 3.23. Photograph of a fully assembled measurement system.

As per electrical safety requirements, the high voltage electrical feedthroughs need to be enclosed, and the cabling needs to be immobilised with glands. High power electrical feedthrough enclosure was designed and built (Figure 3.24). It has four parts shown in Technical Drawing 23, Technical Drawing 24, and Technical Drawing 25. It is made of 1.2 mm thick stainless steel sheet. The sheet metal parts were cut using Metalmaster HG-440B guillotine and VB-450 band saw. They were folded using Metalmaster KP.4 metal bending machine. The enclosure box houses two 16 mm glands, one on each side. It is fixed under the baseplate using one M5 bolt. Additional stability is provided by the electrical feedthrough housings. The box back wall is riveted to left and right side corner pieces, which also provide support to the electrical terminal blocks. The box side walls are riveted to the corner pieces for additional rigidness. The feedthrough leads are immobilised in the terminal blocks. Heater power supply cable is connected to the right feedthrough, while the TEG module output cable is connected to the left feedthrough. Earth wires from both cables are connected to the baseplate. The enclosure is designed to be open at the front and the bottom for easy access. The enclosures front cover slides into the bottom part of the box and is secured by one M4 bolt at the top. Baseplate legs had to be modified to provide 5 cm of extra space under the baseplate (Technical Drawing 26).

Figure 3.24. High power electrical feedthrough enclosure added for improved safety.

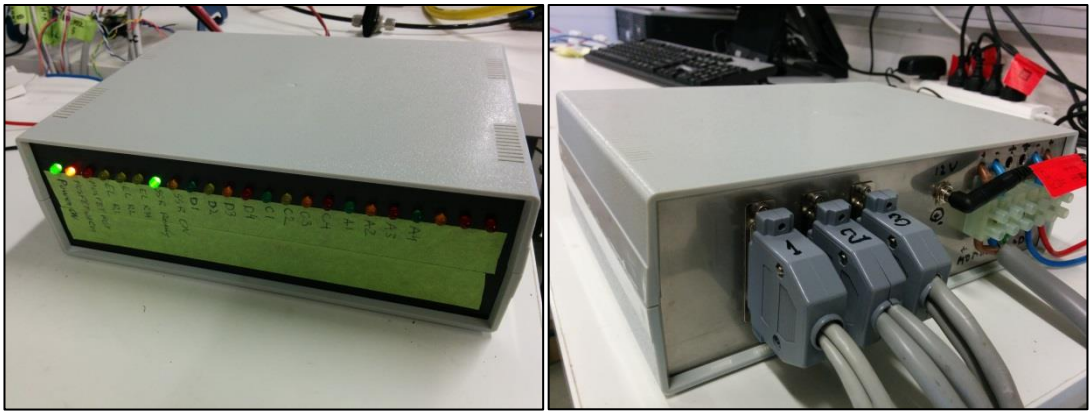

Figure 3.25. Auxiliary circuit board (CB01) and Electronic load (CB02) enclosure front view (left), rear view (right).

Auxiliary circuit board and electronic load circuit board were enclosed in a Pro Quality Vented Instrument Case (260 x 190 x 80 mm) from Jaycar (Figure 3.25). Front panel of the enclosure houses the instrument status indicating LEDs. The rear panel was remanufactured of steel plate to provide structural strength for three sub D 25 sockets, 12 VDC power socket, and six position terminal block.

4 MEASUREMENT SYSTEM: ELECTRONIC CIRCUITS

4.1 Introduction

Chapter 4 describes the instrument control, data acquisition hardware, electronic load, and auxiliary electronic circuitry. Design principles of electronic circuit components, their architecture, and the interconnected system are detailed. Wiring tables are moved to Appendix B.

The links between the instrument hardware and computer control software are shown in Figure 4.1.

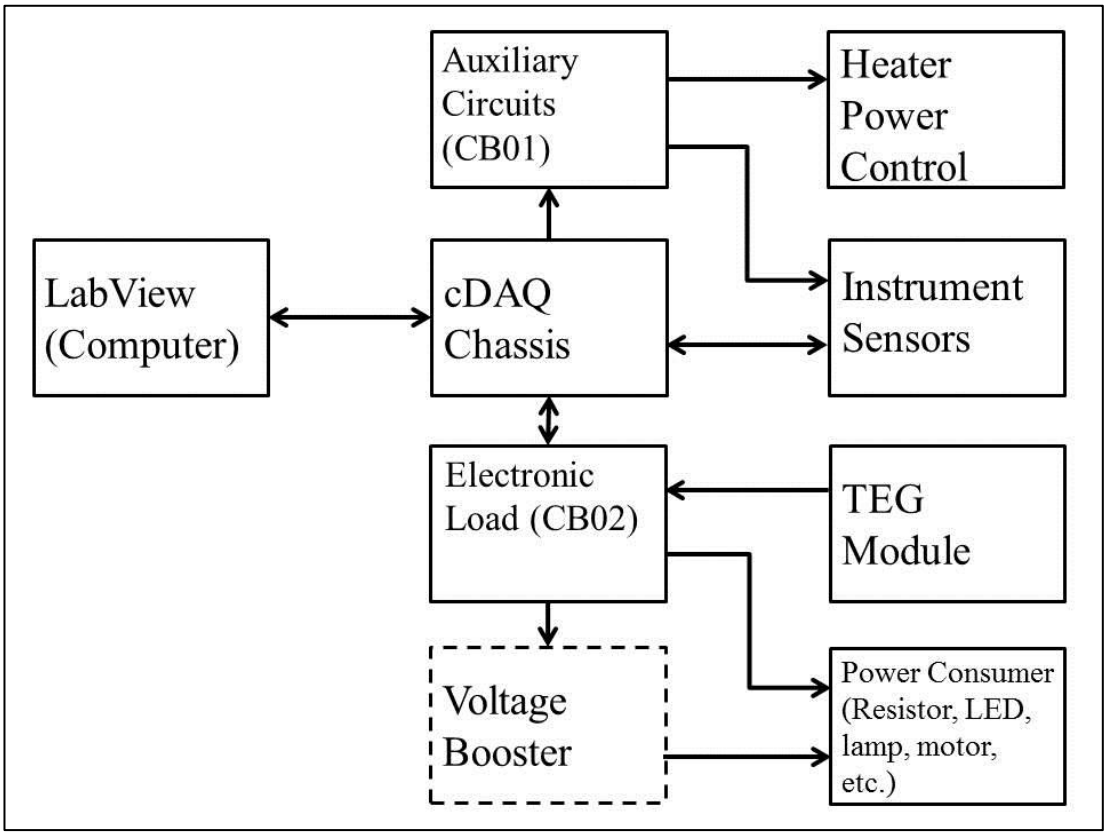

Figure 4.1. Diagram of the electrical connections in the measurement system. Arrows represent electrical signal or electrical current flow direction. Dashed boxes represent features, which are viable, but not implemented yet.

This Chapter detail the practical solutions applied to achieve set goals in this work:

- To provide excitation for force transducer, temperature sensors;
- To provide light indication of instrument status;
- To provide sound alarm;
- To provide means to programmatically switch auxiliary devices such as vacuum pump, water chiller, etc.
- To create variable load for the thermoelectric generator module;
- To accurately measure module current;
- To modulate heater power;
- To demonstrate electrical power generated by powering an electric light or a motor.

4.2 National Instruments CompactDAQ Data Acquisition System

4.2.1 Overview

This section describes the National Instruments data acquisition hardware. National Instruments supplies complete but simple to use acquisition systems and provides extensive technical support. Furthermore, NI's graphical programing language LabView is a simple and user-friendly tool to write the control software. This section is split into separate parts describing the chassis and each of the modules used.

4.2.2 NI CompactDAQ 9178 Chassis and Desktop PC

The NI cDAQ-9178 is an eight slot chassis designed for small, portable, mixed-measurement test systems. Its photograph is show in Figure 4.2. The chassis can be combined with up to eight NI C-series Input/Output modules for customised analog input, analog output, digital input and output measurement system. It has a hi-speed USB communication with the computer. It can run up to seven I/O tasks simultaneously. Moreover, it can acquire from analog input modules at different rates with multiple timing engines [101].

Currently four slots in the chassis are used for measurement modules, and the remaining four unoccupied slots can be used for future expansion and development.

Figure 4.2. Photograph of National Instruments CompactDAQ 9178 8-slot USB chassis.

Personal computer used for data acquisition and instrument control is HP Compaq desktop personal computer with two 19 inch monitors. It has Intel Core 2 Duo dual core processor and 2 GB of random access memory. It runs Windows XP Service Pack 3 operating system.

4.2.3 NI 9403 32-Channel TTL Digital Input/Output Module

The NI 9403 is a 32-channel, 7 µs bidirectional digital I/O module for any NI CompactDAQ or CompactRIO chassis. The direction of each digital line on the NI 9403 can be configured for input or output. Each channel is compatible with 5 V/TTL signals and features 1,000 Vrms transient isolation between the I/O channels and the backplane. The NI 9403 also features ±30 V overvoltage protection and can source up to 2 mA output current per channel [102].

NI 9923 front-mount 37-pin D-SUB to screw terminals connector is used with the NI 9403 module, as shown in Figure 4.3b. NI 9403 module terminal assignments and wiring is presented in Table 9.1.

In this project, the NI 9403 module is used to provide control signals to LED drivers, electromechanical relay drivers, sound alarm, field effect transistor, and solid state relay driving circuit.

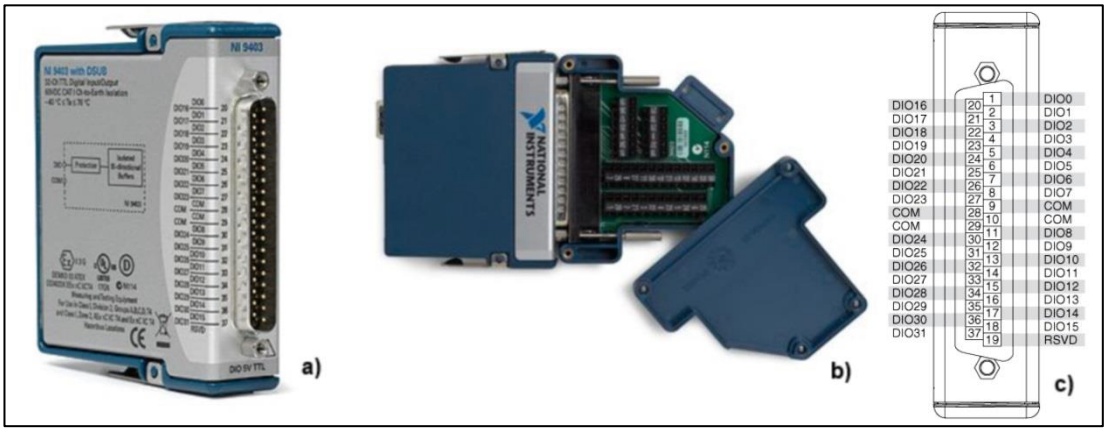

Figure 4.3. a) NI 9403 module. b) NI 9403 module with NI 9923 terminal block attached. c) NI 9403 module terminal assignments[102, 103].

4.2.4 NI 9263 4-Channel, 16-Bit Analog Voltage Output Module

The NI 9263 is a C-series high-performance analog output module for NI CompactDAQ chassis. It provides accurate signal generations. The module incorporates built-in signal conditioning and an integrated connector with screw-terminal. It has four channels with 100 kS/s/Ch simultaneous analog output. The nominal output range is ±10 V with 16-bit resolution [104]. The modules output resolution, adjusted for range, is 0.3 mV. Its photograph and terminal assignment diagram are shown in Figure 4.4. Output terminal wiring is listed in Table 9.1.

In this project, the NI 9263 module is used to provide a set point value to the electronic load board. Additionally, it can be used to directly switch the power MOSFET transistor in the electronic load circuit.

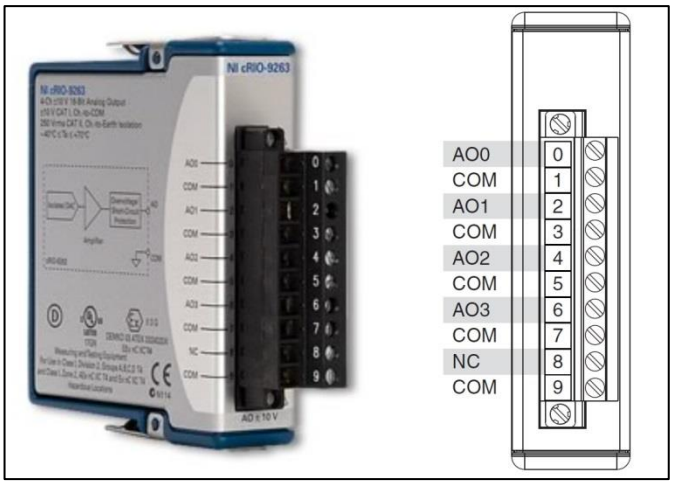

Figure 4.4. NI 9263 module and its terminal assignments[104, 105].

4.2.5 NI 9219 4-Channel, 24-Bit, Universal Analog Input Module

The NI 9219 is a four-channel universal C Series module designed for multipurpose testing in NI CompactDAQ chassis. The module and its channel pinout are shown in Figure 4.5. With the NI 9219 several signals from sensors such as strain gauges, RTDs, thermocouples, load cells, and other powered sensors can be measured. The channels are individually configurable, so different measurement type can be performed on each of the four channels. Measurement ranges will differ for each type of measurement. Maximum ranges are ±60 V for voltage and ±25 mA for current. Maximum sampling rate is 100 S/s/Ch simultaneous for all channels and full range resolution is 24-bit [106].

Five measurement ranges are programmatically selectable for voltage mode: ±60 V, ±15 V, ±4 V, ±1 V, ±125 mV [107]. 24-bit resolution in each mode effectively is 7.15 μV, 1.79 μV, 0.48 μV, 0.12 μV, 14.9 nV, respectively. In this measurement system, the NI 9219 module is used for voltage measurements only. Terminal assignments in voltage mode are: terminal 4 – positive wire, terminal 5 – negative wire. Channel assignments and wiring are listed in Table 9.1.

NI 9219 module is used to measure Cold Junction Reference (CJR) temperature sensor voltage, voltage of the thermoelectric generator module, and voltage drop over the external load, connected to the electronic load board.

For CJR temperature measurements on Channel 1, maximum voltage levels of 6 to 7 V can be expected, therefore, the voltage range on this Channel is set to ±15 V. for all other channels the voltage range is at its widest end of ±60 V by default, but it can be reduced in the control software for increased measurement resolution.

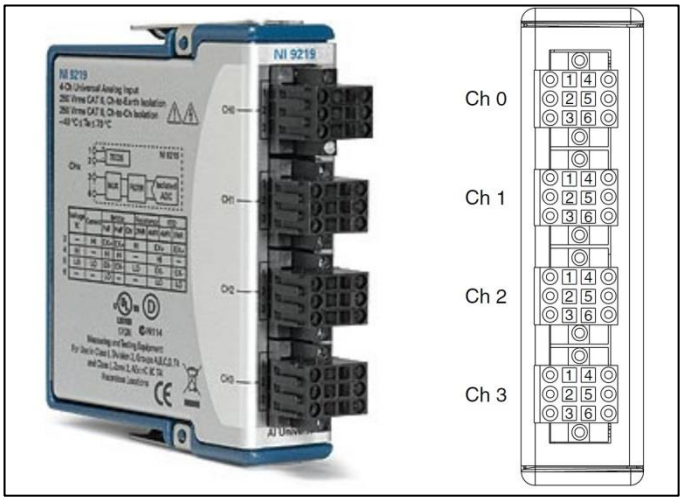

Figure 4.5. NI 9219 module and terminal assignments[106, 107].

4.2.6 NI 9213 16-Channel, 24-Bit Thermocouple Input Module

The NI 9213 is a high-density thermocouple module for NI C Series carriers designed for high channel count systems. With this module, 16 thermocouples can be added to a mixed-signal measurement systems taking only one slot in the chassis. When the NI 9213 is in high speed mode, each channel can sample at 75 S/s. When 12 or fewer channels are used, the maximum sample rate per channel can increase to 100 S/s [108]. NI 9213 module photograph, terminal assignments, and input circuitry diagram are shown in Figure 4.6. The module wiring is listed in Table 9.1.

In addition to the 16 thermocouple channels, the NI 9213 module features built-in cold-junction compensation and autozero channels. The cold junction compensation channel can be used to electronically adjust thermocouple output so as if the thermocouple cold junction was at 0°C, while it actually is at room temperature. This function is not used for this project, because it would duplicate the function of the Cold Junction Reference unit. Autozero function is used for every thermocouple measurement taken. This function compensates for the offset error of the analog to digital converter. The analog inputs are internally disconnected, the offset is measured, and then its value is subtracted from the thermocouple measurements [108].

The module employs a single analog to digital converter with a 24-bit resolution. This ADC resolution translates to 0.02°C measured temperature resolution for K-type thermocouple. The NI 9213 module works in scanning mode and it uses a multiplexer to connect or disconnect analog inputs. Two timing modes are available: (1) in high-speed mode ADC conversion time is 740 μs per channel, which allows 75 measurements of all channels per second. As mentioned earlier, sampling rate can be increased when fewer channels are used, but the maximum rate is 100 S/s. (2) in high-resolution mode the ADC conversion time is 55 ms, which gives maximum read rate of one sample from all channels per second [109]. In this work temperature measurements are made using the high-resolution mode.

In the high temperature TEG module testing instrument the NI 9213 module is used for, as its name suggests, temperature measurements using thermocouples. Additionally, it is used as a voltmeter to measure low voltages. Advantages of NI 9213 module compared to NI 9219 module for voltage measurements include better resolution and higher channel count. Disadvantages are in a small measurement range, and open thermocouple detection current, which cannot be disabled. The open thermocouple detection current is known to be 50 nA. It may offset the voltage readings for high impedance sources. Meanwhile, it will have little to no effect on sources with low impedance. In addition to thermocouple measurements, the NI 9213 module is used for the two current shunt voltage outputs and the force transducer output measurements.

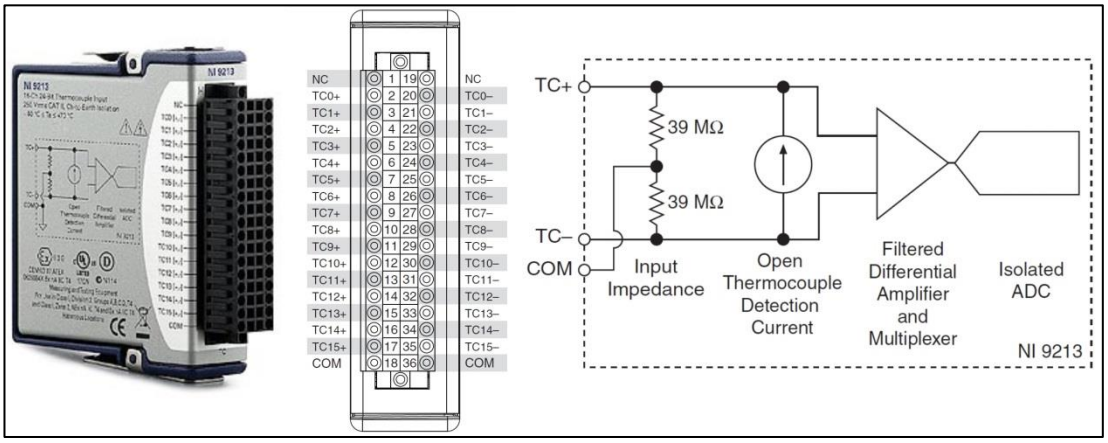

Figure 4.6. From left to right: NI 9213 module; NI 9213 module terminal assignments; input circuitry for one channel [108, 109].

4.3 Auxiliary circuit board (CB01 Rev.5)

4.3.1 Overview

Circuits in the CB01 convert digital signals into analog signals driving light indicators, sound alarm, mechanical relays, solid state relay, and a field effect transistor. Furthermore, it houses circuits for force transducer and cold junction reference temperature sensor excitation. CB01 component layout diagram is shown in Figure 4.7. Photographs of both sides of the circuit board are presented in Figure 4.8 and Figure 4.9.

The circuits are assembled on a universal 160x100 mm^2 prototyping board. The board has a 62 x 37 matrix of pre punched 1 mm diameter holes with copper pads on one side. The hole pitch is 2.50 mm. Gaps between copper pads are 0.5 mm wide. Such boards are ideal for experimenting, prototyping, and one-off projects.

The CB01 component layout diagram was retro-created from an assembled circuit board and is very useful to plan any modifications in existing circuits and addition of new circuits. The layout diagram was created using Microsoft Excel software for top and bottom sides separately. MS Excel worksheet was formatted so that each cell represents a single hole in the prototyping board. Electronic component symbols and

conductor tracks were placed to their respective positions. Images of the MS Excel diagrams were pasted to Paint.NET software. Top side image as a background, and bottom side image as a second layer. The second layer was then flipped horizontally and blended in “multiply” mode with opacity value of 100 out of 255. The resulting image was saved in Paint.NET .pdn format, then flattened and saved in jpeg format.

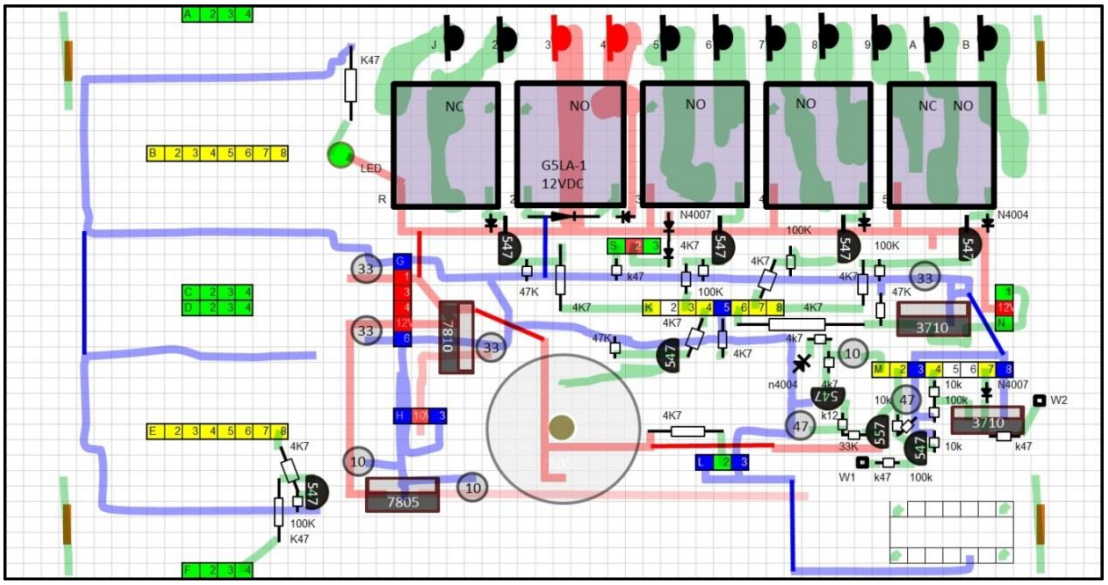

Figure 4.7. CB01 Rev.5 component and connector physical layout diagram. All electronic components are on the top side of the board and the conductor tracks are on the bottom side of the board, except of those in full solid colour. Only one LED driving circuit is shown, as the other 15 are identical to it. Blue tracks represent 0V; Red tracks, depending on colour intensity, represent 12V, 10V or 5V; Green tracks represent varying voltage levels. Yellow pins represent digital input; Green pins represent varying voltage levels.

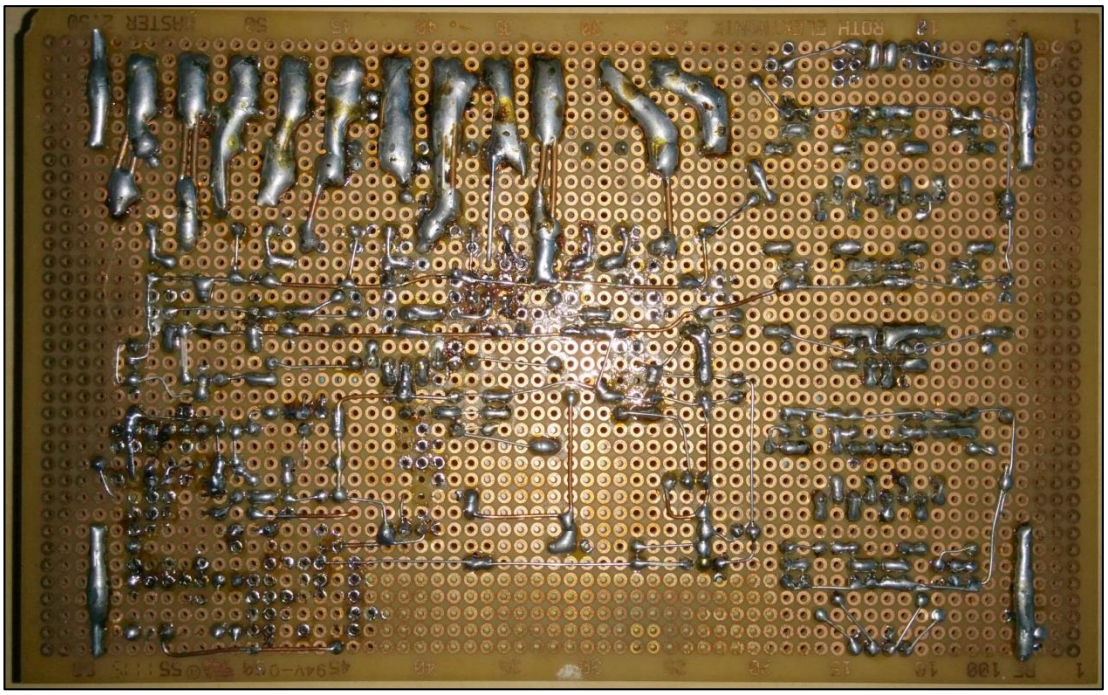

Figure 4.8. Photograph of CB01 Rev.5 bottom side.

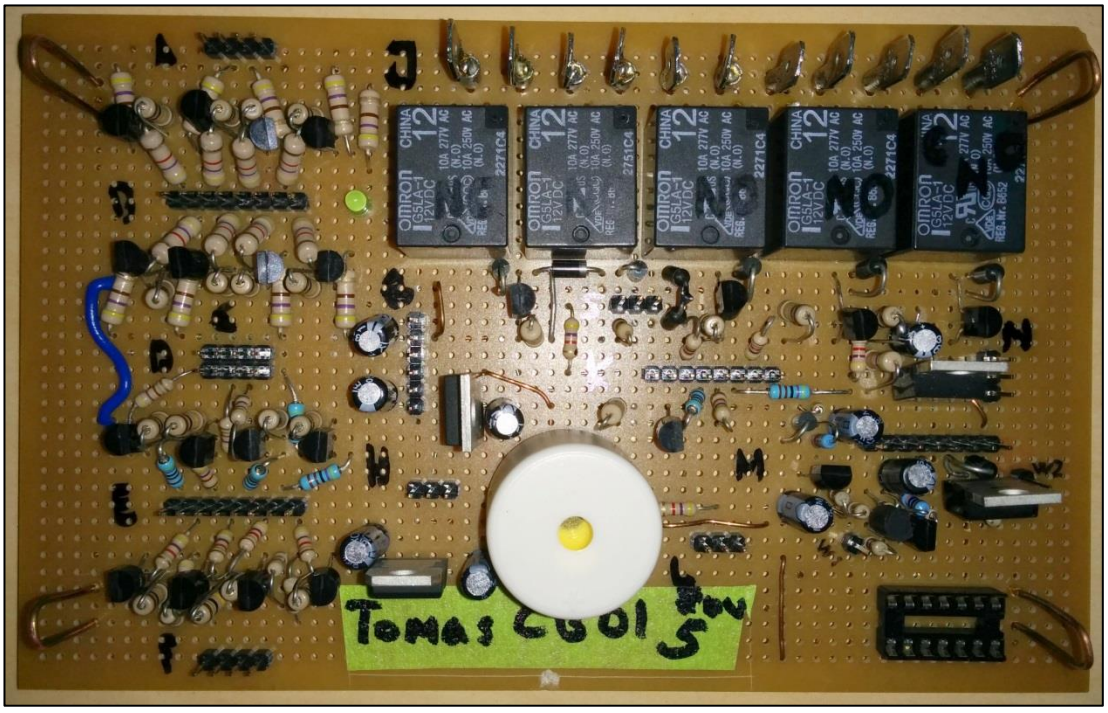

Figure 4.9. Photograph of CB01 Rev.5 top side.

4.3.2 Light Indication of Instrument Status

Light indicators provide instrument operator with important information about instrument's status. They work in parallel to the virtual indicators in the control software on the computer monitor. Nonetheless, they are more capable to attract operator's attention, in case of emergency, especially when blinking. In addition, they improve the visual appearance of the circuit board enclosure.

16 out of 32 bits on the NI9403 module are dedicated to light indication. Consequently, CB01 rev.5 houses 16 LED driving circuits. A typical light emitting diode requires up to 20 mA of current at 1.8 to 2.2 V to fully illuminate [110]. Less current will reduce emitted light intensity while more current will destroy the LED. Therefore, the LED drivers incorporate a current limiting resistor.

LED driver circuit diagram is shown in Figure 4.10. Each LED is switched on and off by a BC547B transistor. It is a general purpose NPN transistor capable to handle 100 mA collector current and 45 V collector–emitter voltage. Its DC current gain is $h_{FE} > 150$ [111]. The 4.7kΩ resistor limits transistor base current to 1 mA, which is well within the current the NI9403 module can source per each output. The 100 kΩ resistor ensures the transistor is off when the control bit value is 0, or when there is no connection to the NI9403 module. The 470 Ω resistor limits LED current to 20 mA with a 12 V power supply.

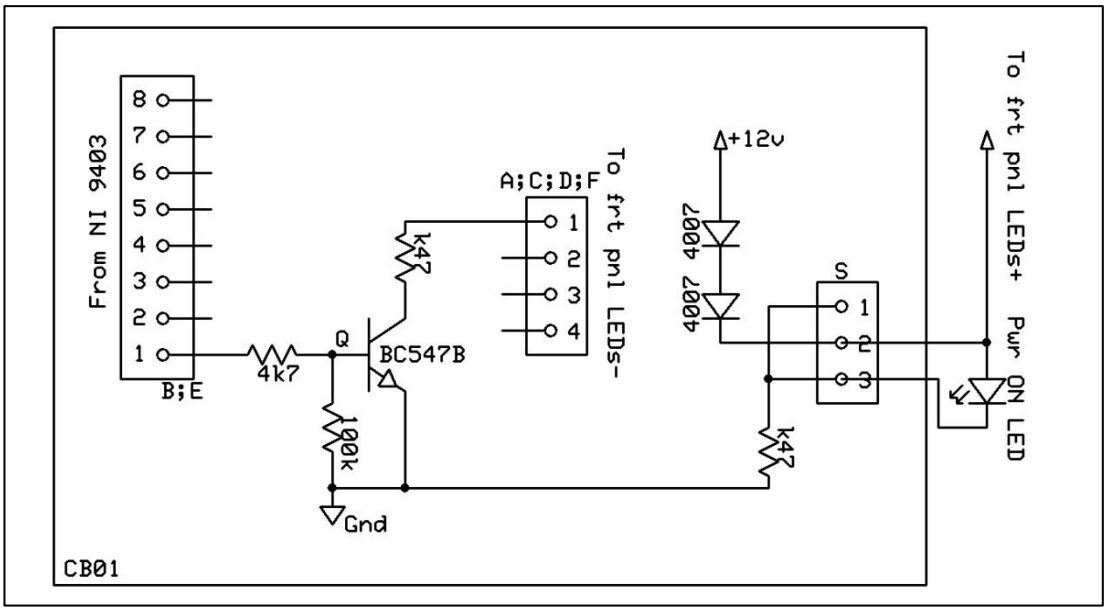

Figure 4.10. LED driver circuit diagram. See Appendix B table B1 for input and output pin pairs and wiring to the NI 9403 module.

All LEDs are placed on the front panel of the enclosure and have their anodes soldered to a 12 V rail. Meanwhile the LED driver circuits provide grounds to the cathodes and limit the LED currents. Two diodes were placed in series with the 12V LED power supply to drop the voltage by 1.4V in order to account for resistor tolerances and ensure that the LED current never exceeds 20mA even if field effect transistors are used instead of bipolar junction transistors.

In case there is a need for additional NI 9403 module outputs, the LED drivers can be replaced by a 16 channel LED driver integrated circuit such as MAX6969 or CAT4016. These ICs can be controlled using just three NI 9403 outputs for clock, serial input, and latch signals, ultimately freeing up to 13 NI 9403 outputs [112, 113]. The only downside to such a change would be additional LabView programming required to convert data into serial form and efficiently output it on the NI 9403 module.

4.3.3 Excitation Signal for the Force Transducer

Load cell model LCGB-5K (Omegadyne inc. USA) is used as a force transducer. It is a high accuracy, low profile, miniature size cell, which is rated to 5000 pounds of force. It can be safely overloaded to 150% and ultimately to 300% of the rated capacity. It is mounted under the chiller support plate and is in direct contact with the hydraulic ram.

Required excitation voltage for LCGB-5K is 10.0VDC. LM7810 voltage regulator is used to provide 10.0VDC regulated voltage [114]. Its circuit diagram in auxiliary circuit board is shown in Figure 4.11.

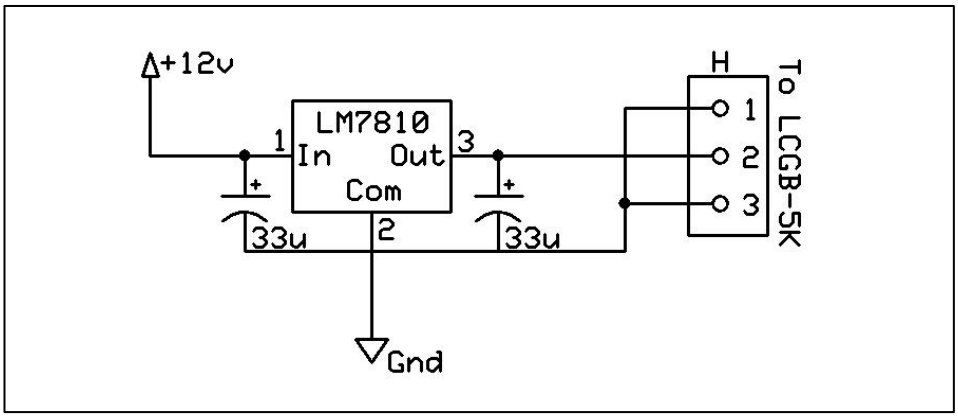

Figure 4.11. 10 VDC voltage regulator circuit diagram.

LCGB-5K force transducer is factory calibrated with 10.000VDC excitation. Its sensitivity is 1.736 mV/V for 5000 Lbs force and changes linearly with force applied, which ranslates to 1281 N/mV cell response at 10.0 VDC excitation.

LM7810 voltage regulator output voltage tolerance is ±2% at room temperature [114]. In practice, the measured output accuracy is within ±1% of the nominal voltage, meaning that 1% measurement error due to the variation of excitation voltage is possible. If there was a need for higher accuracy, few solutions are possible. LM7810 voltage can be measured directly by NI 9219 module and the variation in excitation voltage accounted for in the control software. Alternatively, an

accurate 10.000VDC excitation can be obtained directly from the NI 9263 analog output module. These two options would require some modifications in the control software code and are subject to channel availability on the NI 9219 and NI 9263 modules.

4.3.4 Cold Junction Reference (CJR) Temperature Sensor Excitation

LM335A integrated circuits are used as temperature sensors in the cold junction reference unit. LM335A is a high accuracy temperature sensor with typical error of less than 1°C. It operates as a 2 – terminal Zener diode and the breakdown voltage is directly proportional to the absolute temperature at 10mV/K slope. It can operate within a range of current values from 0.45 mA to 5 mA without changes in its characteristics [100].

For this application, two sensors embedded into the CJR body are used. The sensors are connected in series, thus, the sensor sensitivity is combined to 20 mV/K. Sensors connected in series allow average temperature measurements of two points in the CJR. Whereas sensors connected in parallel would show only the minimum temperature of the two sensors with 10 mV/K sensitivity.

The sensors are connected to the +12VDC rail through a current limiting resistor as shown in Figure 4.12. At around room temperature the voltage drop across the temperature sensors is approximately 6V. The resulting excitation current limited by the 4.7 kΩ resistor is ~1.27 mA and is well within the usable excitation current range. In case the CJR unit would reach 100 °C temperature, the excitation current would be ~0.96 mA, still well within limits of use.

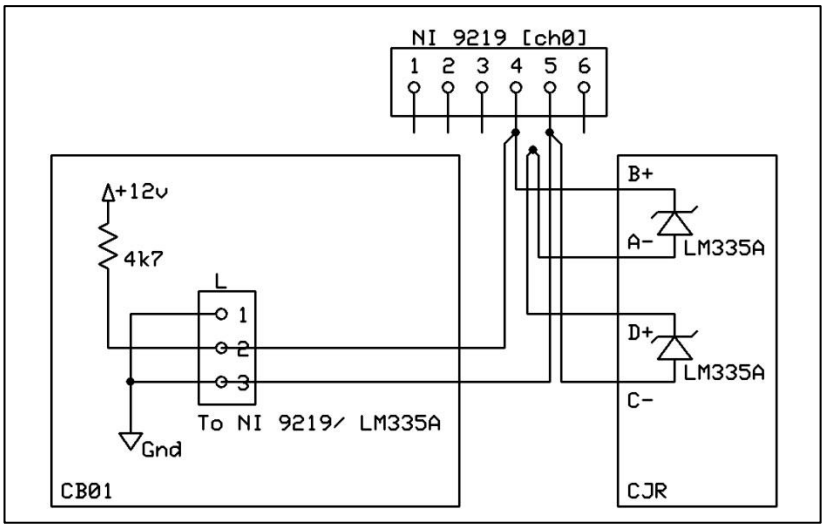

Figure 4.12. LM335A temperature sensor excitation and electrical connection circuit diagram.

NI 9219 module channel 0 is dedicated for CJR temperature measurement. It measures the voltage drop across the temperature sensors. The measured voltage value is then converted into centigrade temperature value in the control software. In a situation where one of the sensors would fail or for debugging purposes, one of the sensors can be shorted, leaving only one active sensor. The resulting excitation current in this case would increase to ~1.91 mA, which is still within the operating current range.

The two sensors can be measured separately for their individual, not averaged values. Excitation circuit does not need to be changed for that. NI 9219 should be rewired to take voltage drops across each sensor. Of course, this would require an additional unused channel on the NI 9219 module and additional LabView coding.

4.3.5 Sound Alarm

Sound alarm, in addition to the light indicators, is an excellent way to attract operator's attention in case there is an emergency. Moreover, the alarm can be used to communicate important information to the operator while the operator is not monitoring the computer screen.

High pitch piezoelectric buzzer, operating at 12 VDC, is used. A BC547B transistor switches the alarm on when the alarm bit is set to 1 on NI 9403 module channel 30. The sound alarm circuit diagram is shown in Figure 4.13. The alarm output is fully programmable in the control software to be continuous or pulsating. Additionally, the alarm can be used to beep out important information or events in short beep codes. For example, a successful system start up, similarly to personal computers, could be indicated by a single short beep. A loss of vacuum in the bell jar could be indicated by continuous beeping. At the time of this thesis writing, the alarm can be switched on and off manually in the control software in pulsating mode only for testing and debugging purposes. Automated operation is yet to be programmed.

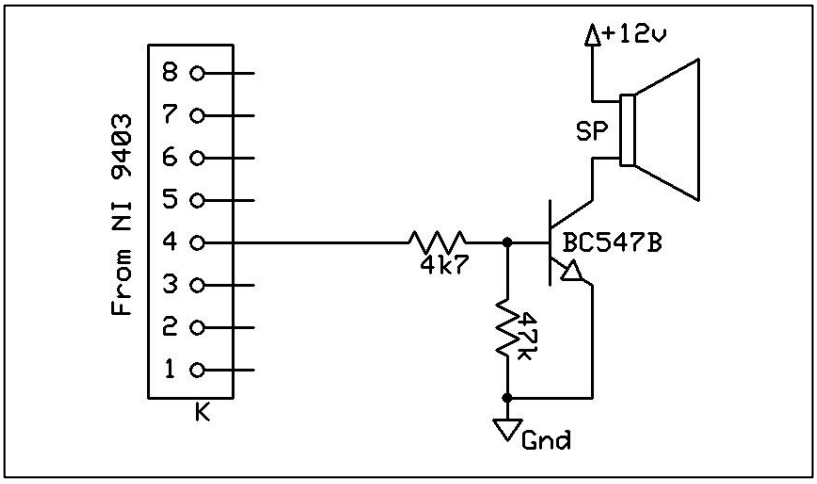

Figure 4.13. Sound alarm circuit diagram.

4.3.6 SSR Driver With Software or Computer Crash Detection

Solid state relays are commonly used when there is a need to modulate heater power. Usually, the solid state relay is coupled to a temperature controller. In this system, the solid state relay output is controlled by the control software through NI 9403 module and a SSR driving circuit in the auxiliary circuit board (Figure 4.14). PID algorithm is programmed into the control software. Gordos GA5-6D25 SSR rated at 25 A is used. It has a wide control voltage range of 3 to 32 V.

The SSR driving circuit uses two NI 9403 bits to power the relay. DIO00 bit must be switching to output a 1 Hz or higher frequency square wave. DIO01 has to be on.

The circuit has dual function. Firstly, it generates supply voltage to the solid state relay for a short period of time after the DIO00 bit has changed its value. Therefore, The DIO00 bit must be switching for the SSR to be powered. If the DIO00 output stays in either 0 or 1 bit state, the output capacitor will discharge in few seconds and the SSR will not be powered. The output capacitor discharge graph is shown in Figure 4.15. Secondly, it switches the generated supply voltage on or off to modulate heater power.

The main purpose for such an overcomplicated SSR switching way is to ensure that the SSR is off in case the computer or control software crash. Software crashing or entering an infinite cycle is a likely event, especially during the development stage. In case NI 9403 DIO00 and DIO01 bits would get stuck high, the solid state relay, would stay on for only about three to four seconds.

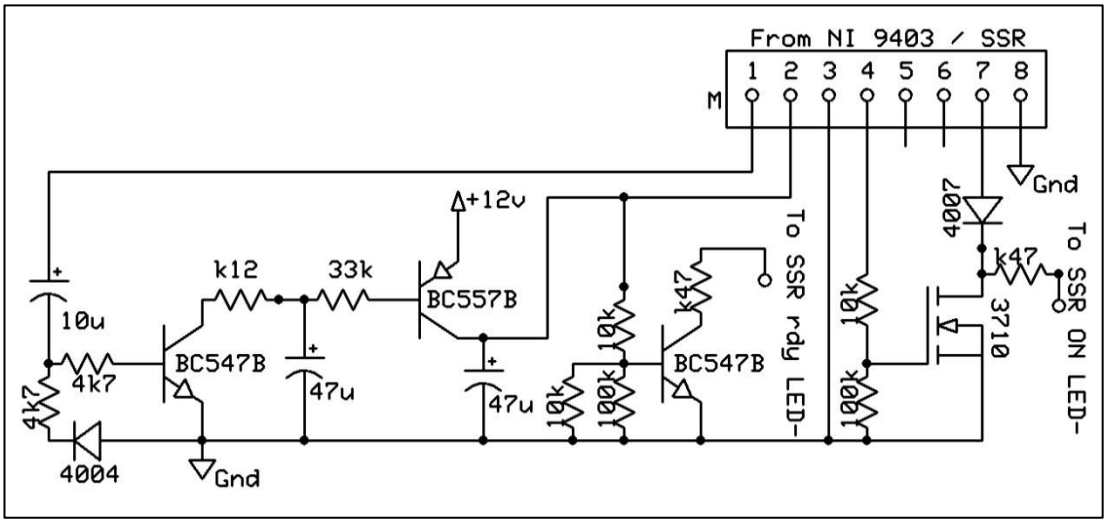

Figure 4.14. Circuit diagram for Solid State Relay control voltage generation and switching.

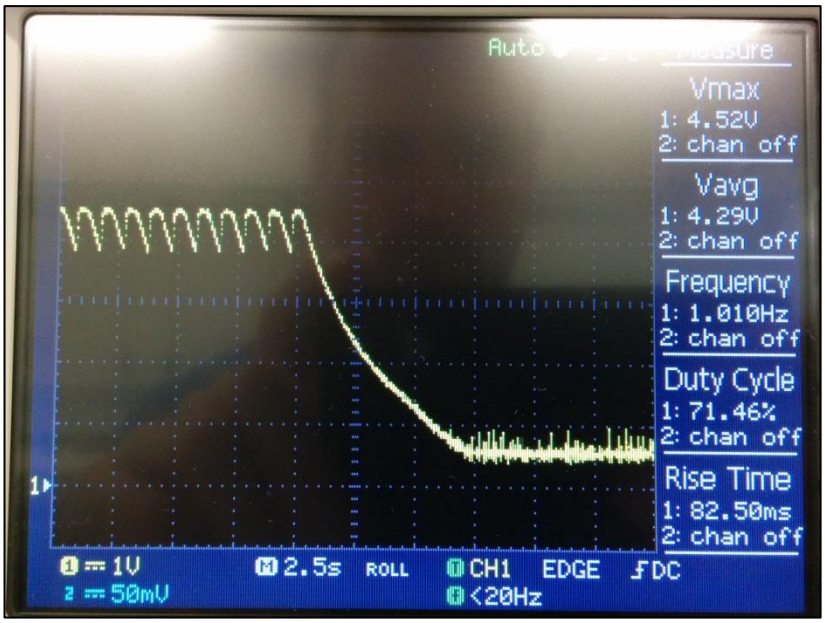

Figure 4.15. SSR voltage with DIO00 bit switching at 1Hz square wave (first half), and DIO00 bit at constant value (second half).

4.3.7 Electromechanical Relay Controls

The auxiliary circuit board houses five G5LA-1 single pole double throw relays. They are rated 10 A at 250 VAC, and operate with 12 VDC [115]. The purpose for these relays is making external device switching possible directly from the control software. Principle relay control circuit diagram is shown in Figure 4.16. Examples of the devices to be switched include vacuum pump, vacuum gauge, water chiller, neon indicators, etc. Spade connectors are soldered into the circuit board. Spade connectors are provided for R1 relay's "normally connected" (NC) terminals, for R2, R3 and R4 – "normally open" (NO) terminals, and for R5 – both NC and NO terminals. The relays are not in use currently, except for R2, which is used to ensure correct 12 VDC power supply polarity, as described in the subsequent section.

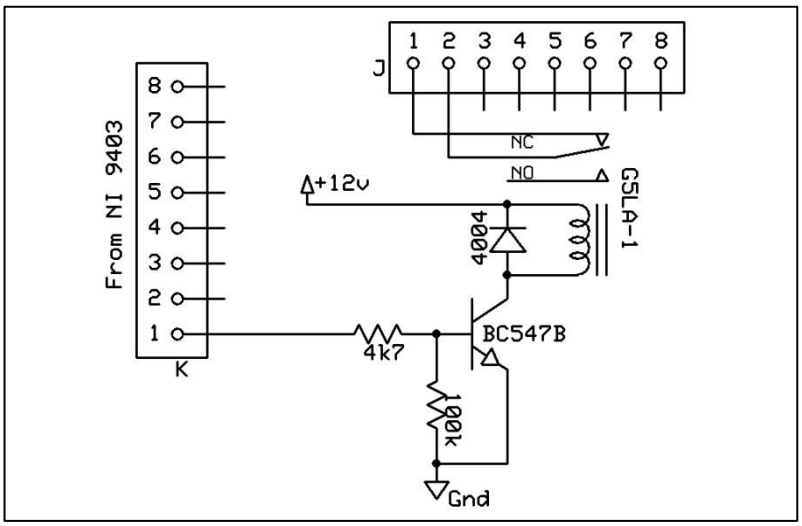

Figure 4.16. Relay control circuit diagram.

4.3.8 Protection from Inversed Power Supply Polarity

Powertech plus MP-3490 switching mode regulated AC adapter is used to power the auxiliary circuit board and the electronic load circuit board. The adapter is rated at 12 VDC and 2.5 A. It has interchangeable DC plugs, which can be used with inverted polarity. Incorrect supply voltage polarity would cause damage to the circuit board components. Therefore, a protection circuit from the inversed power supply polarity has been designed. The circuit diagram of a modified R2 relay control circuit is shown in Figure 4.17. The added diode ensures that the R2 relay is powered only

when the center pin of the power source plug has positive voltage relative to the outside shield voltage. Only when the R2 relay is powered, the power is supplied to the auxiliary circuit board, electronic load circuit board, and front panel LEDs.

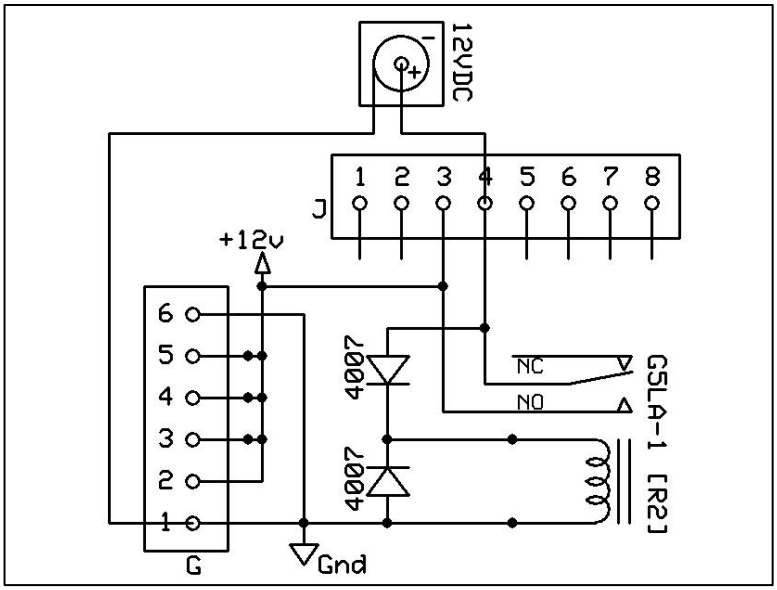

Figure 4.17. Modified R2 Relay control circuit diagram.

4.3.9 Field Effect Transistor Switch

A circuit for solid state relay switching consisting of a single field effect transistor that has been built and used in previous revisions of the auxiliary circuit board. The circuit schematic diagram is shown in Figure 4.18. It is not in use currently as the SSR switching function was transferred to the SSR driving circuit described earlier. Nevertheless, it is kept in the auxiliary circuit board as it likely to find use in the future.

N-type IRF3710 field effect transistor is the active component in this circuit. In current setting, with logic level gate voltage, the transistor current should be limited to 1 A. It will work with higher currents, but care must be taken to prevent significant heating [116].

The transistor is placed on the ground side of the circuit. The component to be switched will be at +12 VDC level at all times. The FET will be in conductive state when NI 9403 module DIO31 bit is set to 1.

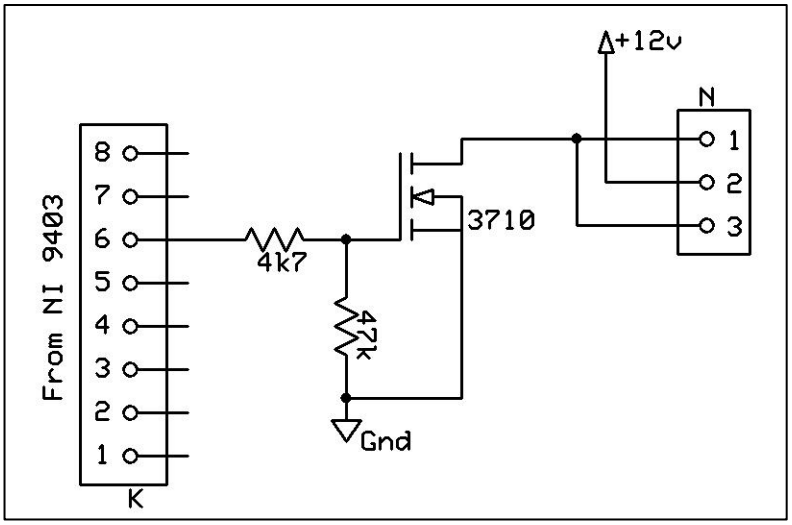

Figure 4.18. FET switch circuit.

4.4 Electronic Load Circuit Board (CB02 Rev.11)

4.4.1 Overview

This section describes hardware components, electronic circuits, functionality, operating principles, and the use of the Electronic Load. The Electronic Load circuit board gets its name primarily from the way it operates. It provides a resistive load to the TEG module. As well as, the resistive load is controlled electronically. The Electronic Load is an upgrade to, and substitutes the conventional resistor array shown in Figure 4.19 left. Electronic Load eliminates resistor array drawbacks such as limited number of resistors, need for resistor value range change for different TEGs, manual switching, switch current limitation, resistor heating and resistance drift with temperature.

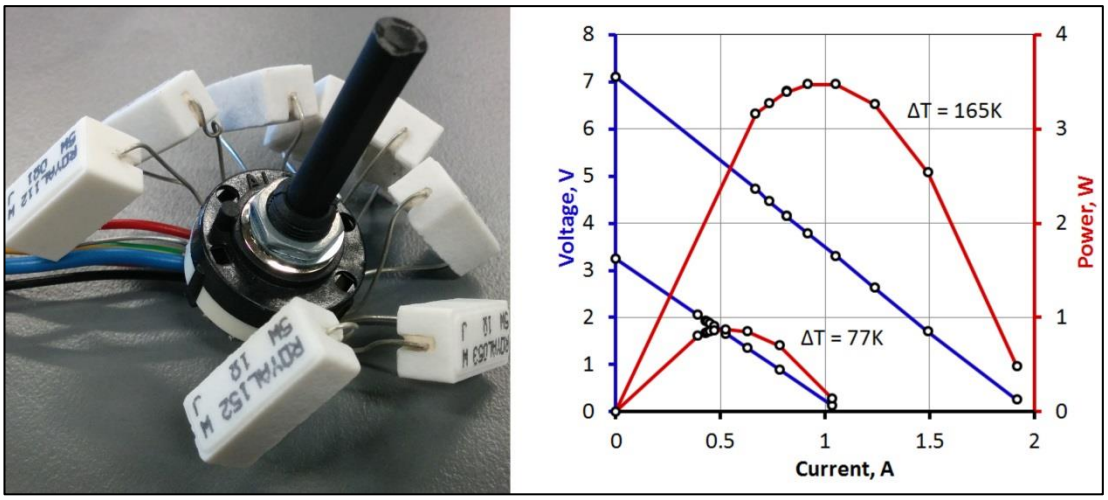

Figure 4.19. Resistor array on a multi position switch used for TEG module electrical loading (left). Sample Voltage vs Current and Power vs Current curves, measured using the resistor array. TEG module cold side temperature is 40°C (right).

The electronic load is assembled on a 160 x 100 mm^2 pre-punched prototyping board with copper pads on one side. The board has 62 x 37 hole matrix with a 2.5 mm pitch. CB02 component layout diagram is shown in Figure 4.20. The component layout diagram was created using MS Excel and Paint.NET software packages as described earlier for CB01. Top and bottom photographs of the latest revision of the electronic load board are shown in Figure 4.21 and Figure 4.22, respectively.

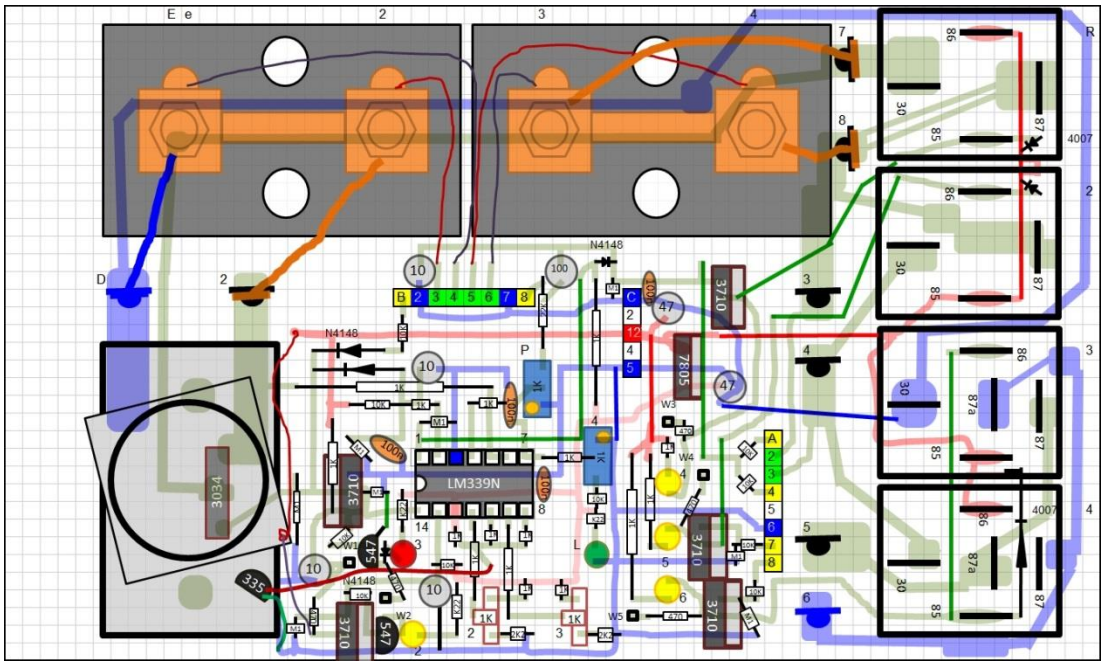

Figure 4.20. Electronic load circuit board (CB02) component layout diagram.

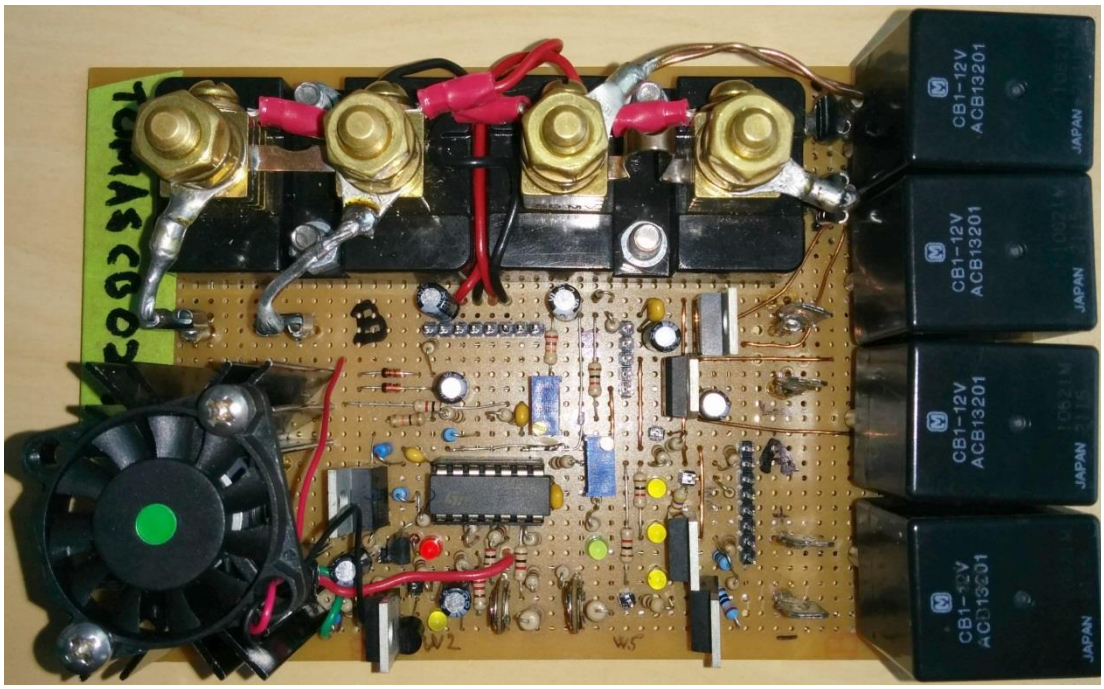

Figure 4.21. Electronic load circuit board (CB02 Rev.11) top view.

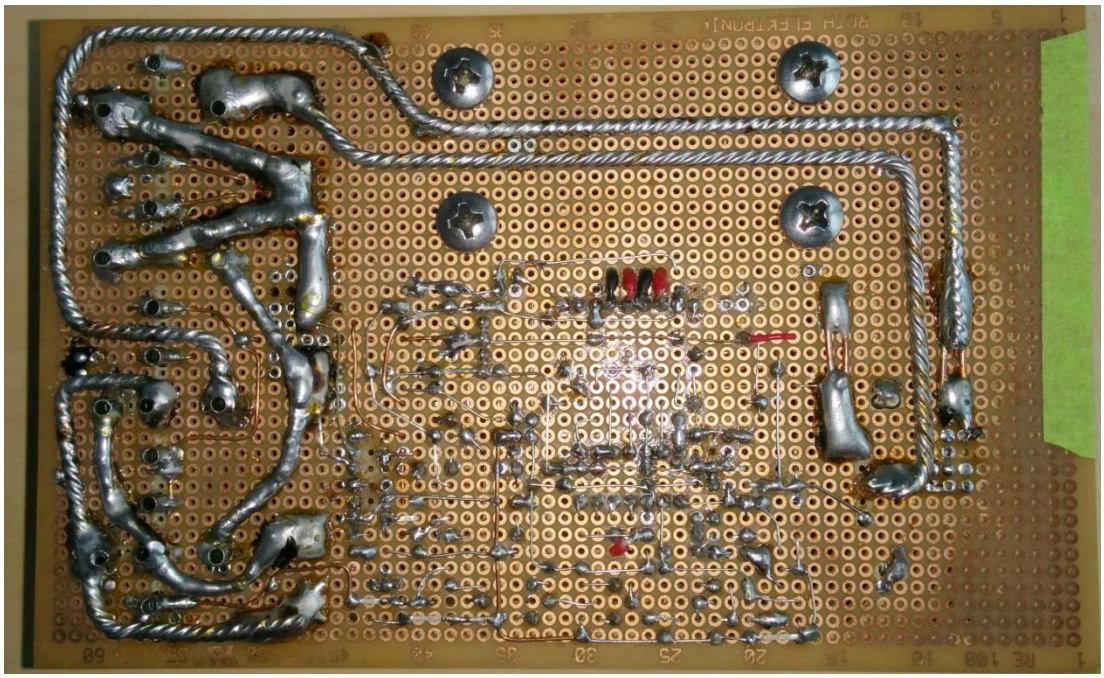

Figure 4.22. Electronic load circuit board (CB02 Rev.11) bottom view.

The key features of the Electronic Load board are:

- Works with all TEG modules regardless of their internal resistance;
- Is able to conduct and measure up to 20A of electric current;
- Maximum TEG voltage 40V;
- Able to internally dissipate ~15W of power;
- Inbuilt two stage overheat protection;
- Apply external load in series with the Electronic Load and TEG module;
- Ability to change module polarity;
- Fully controlled from LabView software;
- Direct power transistor control for high frequency switching applications;
- Allows for Maximum Power Point Tracking;
- Greatly improved data acquisition rate when compared to resistive load array;

4.4.2 Power MOSFET Control

4.4.2.1 Constant Current Load Concept

The active component in this circuit is a N-channel power MOSFET transistor. It is controlled by a closed feedback loop, which senses the transistor current, compares it to a value set by the NI 9263 module, and then adjusts the transistor gate voltage as necessary to match the setpoint. The feedback loop principle circuit for transistor control is shown in Figure 4.23. A voltage setpoint is set on the non-inverting (+) comparator terminal from the control software by the NI 9263 module. If the voltage on the non-inverting comparator input is higher than the voltage on the inverting (-) input, the comparator output value is logic 1. When the comparator output is high, there will be voltage present on the gate terminal of the power transistor, and the transistor will be in a conducting state. Current flowing through the low value resistor R will create a voltage drop across itself. Following Ohm's law, the voltage drop will be directly proportional to the current. Once the voltage drop at the resistor is over the set voltage level, the comparator output value level changes to logic 0. The gate voltage drops to 0 V and the transistor impedance becomes high, stopping the TEG module current. Any decrease in resistor current will result in a decrease of the comparator inverting terminal voltage. Finally, the loop will repeat itself endlessly, with the TEG module current oscillating about the preset constant value.

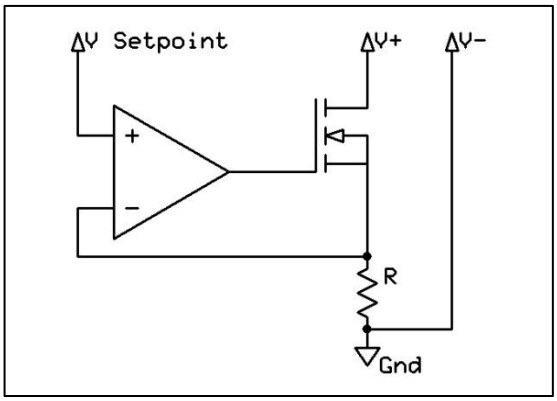

Figure 4.23. Circuit diagram demonstrating transistor control feedback principle.

4.4.2.2 Power MOSFET Control and Feedback Loop

The TEG module current flow path is shown in Figure 4.24. The current flows from the TEG module, through the external load, through a 5 A shunt resistor, IRLP3034PbF HEXFET Power MOSFET transistor, 20 A shunt resistor, and back to the module. If the external load use is not required, it can be bypassed by activating the R2 relay, which connects D3 and D4 terminals.

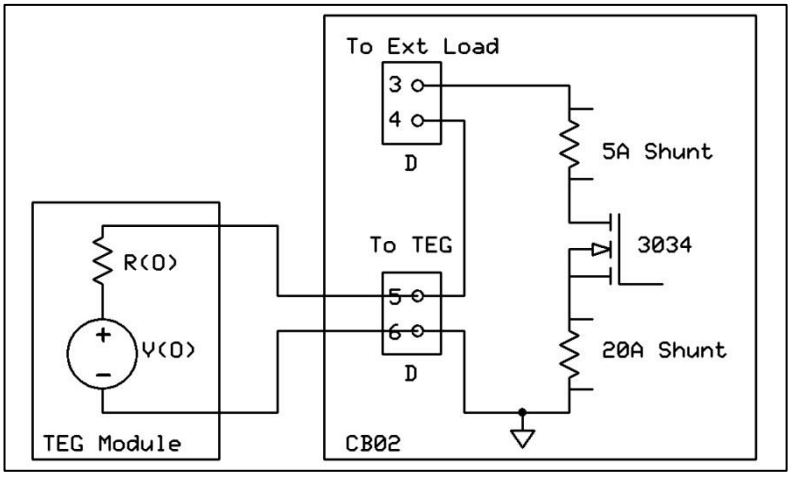

Figure 4.24. TEG module current flow path.

LM339 comparator is used in the power transistor feedback loop. The LM339 high precision comparator integrated circuit package contains four independent voltage comparators. It is designed to directly interface with TTL voltages. Typical input offset voltage is 2 mV, typical voltage gain is 200 V/mV, and typical output sink current is 16 mA. Finally, output switch time delay is less than one microsecond [117].

The LM339 comparator is powered by a 5 VDC regulated voltage. LM7805 voltage regulator is used to provide stable supply voltage to the comparator. Figure 4.25 shows the LM7805 voltage regulator circuit diagram in the CB02 circuit board. LM78XX are available with several fixed output voltages. They are rated at 1 A continuous current, and have thermal overload and short circuit protection inbuilt [114].

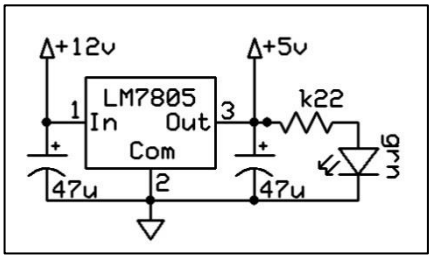

Figure 4.25. 5V regulator and power on indicator circuit.

The IRLP3034PbF power MOSFET N-channel transistor features very low drain to source resistance with typical $R_{DS(on)}$ of 1.4 mΩ. Additionally, very low resistance is reached at relatively low gate voltages (Figure 4.26) [118]. Effectively, being able to set gate voltage in a 1.4 V to 5 V range, allows setting any transistor resistance value from tens of Megaohms down to 1.4 milliohm. Subsequently, this translates to being able to set transistor current from 0 A to 195 A, which is limited by the transistor package. TEG module continuous current flowing through the CB02 board should not exceed 20 A. This limit is set by the 20 A shunt. Maximum drain to source voltage is 40 V; therefore, the TEG module voltage should not exceed 40 V [118].

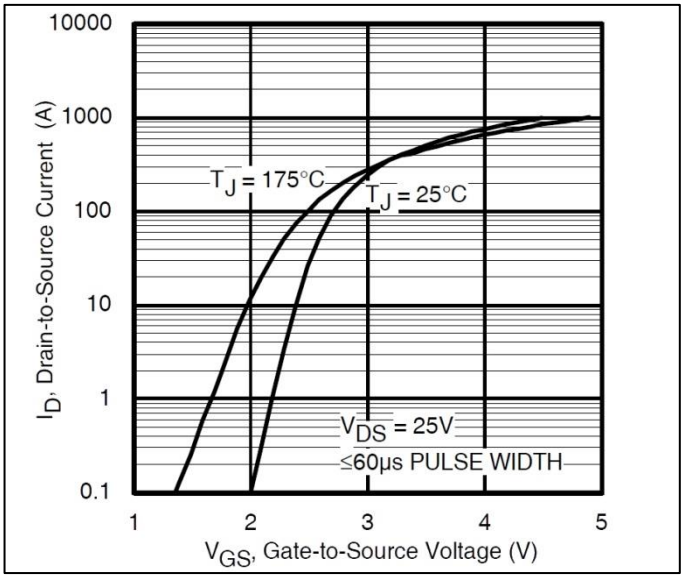

Figure 4.26. Typical transfer characteristics of IRLP3034PbF.[118]

Figure 4.27 shows the circuit diagram for the IRLP3034PbF power transistor control and feedback using LM339 comparator #4. LM339 comparator has high impedance in ON state and sinks up to 16 mA of current in OFF state. Such operation requires a pull-up resistor to be used at the comparator output. The actual output thus is the supplied voltage in ON state and 0 V in OFF state. In this circuit, a voltage divider is used to ensure the output gets to 0 V on power supply power-off. Additional pull-down resistor is placed at the gate terminal to prevent transistor capacitance from keeping the transistor on, when the comparator output is off. A 100 nF ceramic capacitor is used in parallel to the comparator output to smooth the high frequency switching output into a stable DC voltage. Comparator output voltage range on the transistor gate terminal is 0 V to 10 V. This range, is wider than the minimum required range, and, as mentioned earlier, allows full transistor control from fully off to fully on.

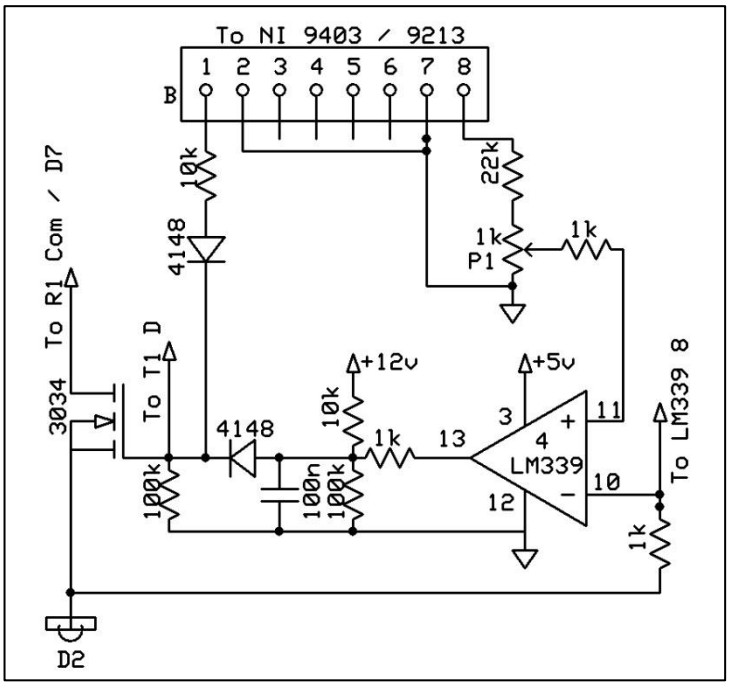

Figure 4.27. Power MOSFET control and feedback circuits.

Pin 10 on the LM339 chip (inverting input) senses the voltage drop across the source to ground resistor due to the transistor current. In this circuit, the sensing resistance consists of two distinct contributors: the 20 A shunt resistance, which is 2.5 mΩ and constant with temperature, and the copper conductor and spade connector

resistances, which are estimated to be around 2 mΩ. In contrast to the shunt, the copper conductor resistance is temperature dependant. Metal conductor resistance increases with temperature. It can be expected that the conductor temperature will increase during normal operation. Not so much from the Joule heating, but more from other heat dissipating components in the circuit board. Given a constant current, the voltage drop across the resistor will increase, as the resistance increases. Consequently, the desired constant current will have a drift, inversely proportional to the sensing resistor resistance change. The initially set current will drift to lower values. An algorithm in the control software is proposed to address this issue. The proposed algorithm is described in detail in the recommendations chapter.

Comparator non-inverting input voltage on pin 11 is set from the control software by the NI 9263 module. It can be anticipated that even with a safety margin, the setpoint voltage should be less than 200 mV. NI 9263 module's DAC resolution in this range would only be 9 bits. In order to make use of the NI 9263 module's full 16 bit DAC resolution at ±10 V range, its output is scaled down in the circuit board with a voltage divider by a factor of 50. The scaling factor is fine adjusted by connecting a DC power source to the TEG module terminals on the electronic load board, setting NI 9263 module output to 10 V, and tuning the P1 potentiometer till the power MOSFET current is 20 A.

4.4.2.3 5A Shunt Overload Protection

A 5 A shunt is used in series with the 20 A shunt as shown in Figure 4.24. It effectively duplicates the function of the 20 A shunt for current measurement, but, with the fourfold expense of range, it is four times as sensitive as the 20 A shunt.

Obviously, the 5 A shunt current should not exceed 5 A. Otherwise, an excessive heating might occur, and if the shunt temperature goes over 50°C, permanent changes to shunt resistance may occur. To limit the shunt current a protection circuit has been designed. It employs a 40 A relay, which, when activated, conducts in parallel to the 5 A shunt. Typical relay contact resistance is 2.5 mΩ, therefore the

shunt current is reduced five times. The relay can be activated anytime from the control software if required. Additionally, the relay will automatically be activated by the circuit shown in Figure 4.28, if the power transistor current reaches 5 Amperes.

Figure 4.28 shows automatic relay R1 control circuit using LM339 comparator #3. The comparator inverting input receives the same voltage input from the current sensing resistor as the comparator #4. The non-inverting input is set at fixed voltage, equal to the voltage drop across the current sensing resistor at 5 Ampere current. Similarly to the NI 9263 module voltage scaling, the comparator non-inverting input is set by connecting a DC voltage source to the TEG module terminals, setting the power transistor current to 5 A, and adjusting the P4 potentiometer till the R1 is activated. Ideally, the R1 relay should be activated when the transistor current is above 5 A, and not activated when it is less than 5 A with no intermediate states. If the transition from off to on states takes more than several milliamperes, the electronic load might be sensing the DC power supply output current switching. In such case, consider using a battery or TEG module instead of a power supply to set the 5 A triggering point.

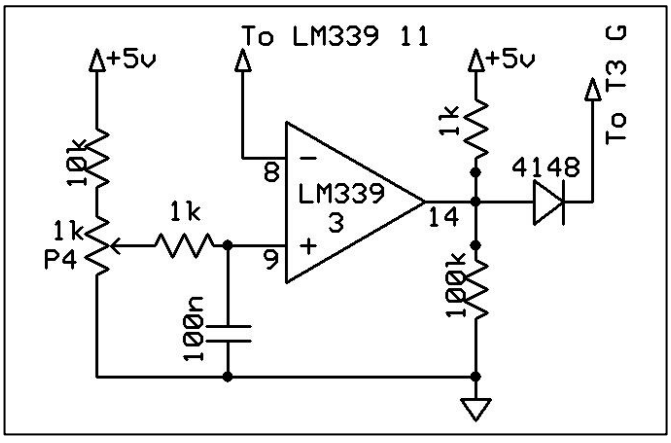

Figure 4.28. R1 relay automatic activation circuit diagram.

4.4.2.4 Power MOSFET Direct Control

The electronic load board has inbuilt functionality for the power MOSFET transistor direct control. That means the transistor gate voltage can be set directly from the control software by the NI 9263 module, and not by the feedback loop. The feedback loop setpoint should be set in the control software to 0 A to not interfere with the direct control. As shown in Figure 4.26, it would be extremely hard to predict the power transistor response to a gate voltage in the range form 1.4 V to 5 V because it depends on the transistor junction temperature and the drain to source voltage [118]. Henceforth, the direct control should be used with caution in that voltage range. In contrast, the transistor response to the extremities of the control voltage range is known with certainty to be fully off at 0 V and fully on at >5 V. Actual voltage range available on the gate terminal of the power transistor, calculated using the nominal component values shown in Figure 4.27 and NI 9263 module range, is 0 V to 8.4 V. Transistor gate voltage will be different from NI 9263 module output voltage. The gate voltage can be estimated by taking the NI 9263 output voltage, subtracting 0.7 V, which corresponds to a voltage drop across a diode, and multiplying by 0.91, which is the ratio of the voltage divider. If both, the direct control, and the feedback loop control are used simultaneously, the one with the highest output voltage will dominate for the transistor control.

Power MOSFET direct control functionality will find use for switching applications for example, a TEG voltage booster. Voltage booster concept is outlined in the recommendations for future development section.

4.4.3 Power MOSFET Thermal Protection Circuits

A field effect transistor will generate heat when operated in a so called “linear mode”, in a state, where the transistor is between the off and on states. The amount of heat generated in Watts is a product of current flowing through the transistor and voltage drop over the transistor. Maximum heat will be generated when the transistor resistance matches the resistance of the TEG module being tested. A small heatsink with a small fan mounted on top of it is used to dissipate the transistor heat (Figure

4.21). A LM335A temperature sensor is mounted on the heatsink. It provides temperature readings to two of the LM339 comparators. When the LM335A sensor voltage reaches voltage value set by potentiometer P2, the fan will be switched on, yellow LED on the circuit board will illuminate, and a LED, indicating the power transistor being warm on the front panel, will illuminate. Similarly, if the temperature sensor voltage reaches the voltage level set by potentiometer P3, the T1 transistor will switch to conducting state, and ground the gate terminal of the IRLP3034PbF transistor, setting it to an off state, having very high impedance. Additionally, a red LED on the circuit board, and a LED on front panel, indicating power transistor being hot, will illuminate. Current flow through the power transistor will cease, and it will be cooled down by the forced convection generated by the fan. As soon as LM335 sensor voltage drops below voltage level set by the P3 potentiometer, the power transistor will be allowed to resume normal operation. Potentiometers P2 and P3 are set to 3.10 V and 3.40 V, respectively, which translate to 37 °C and 67 °C. The two potentiometers may be adjusted if doing so is necessary and safe. Voltage setting equals desired temperature in degrees Celsius added to 273, then divided by 100. The maximum temperature LM335 sensor can be operated at is 150 °C. the maximum temperature setpoint on P3 is 110 °C, leaving a generous safety margin for thermal hysteresis, which is present because the temperature sensor is not mounted directly onto the power transistor, but further away on a fin of the heatsink. With current settings, the power MOSFET can handle approximately 40 W of electric power in continuous mode, with the fan running. Higher levels of continuous power may render the transistor to run intermittently due to the thermal protection circuit activating. Power MOSFET thermal protection circuit diagram is shown in Figure 4.29.

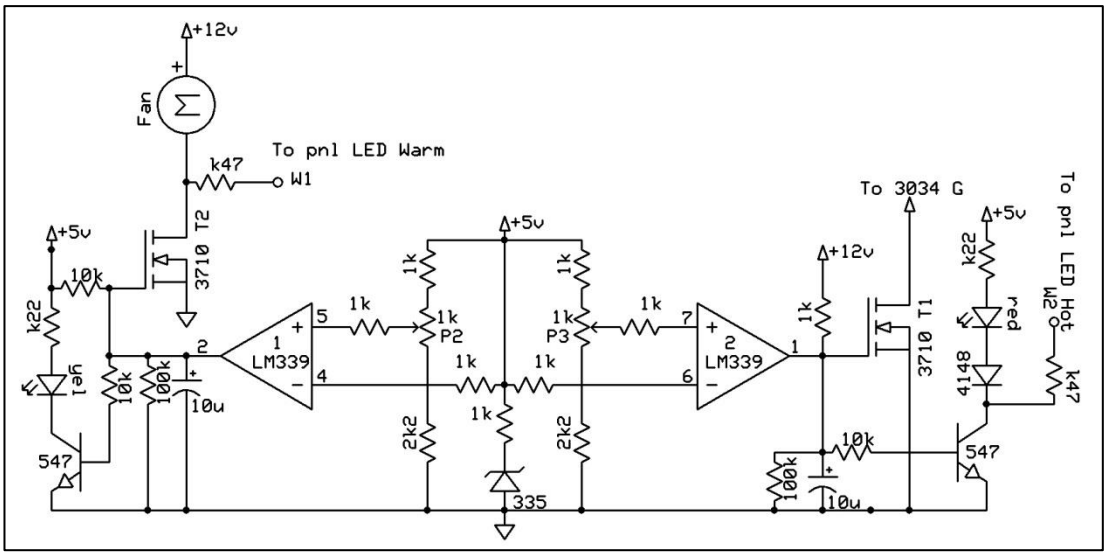

Figure 4.29. Power MOSFET thermal protection circuits

4.4.4 Electromechanical Relay Circuits

The electronic load board has four CB1a-12V single pole double throw relays rated at 40 A [119]. The relays are switched from the control software, by the NI 9403 module. The relay driving circuit diagram is presented in Figure 4.30. Each relay draws 120 mA of current at 12 V supply voltage. IRF3710 power MOSFET transistors are used to switch the relay power upon receiving a logic level signal from the NI 9403 module. Relay R3 and R4 coils are connected in series, and are driven by a single transistor. Relay R1 power transistor may also be automatically activated by the electronic load board internal circuitry. For this reason NI 9403 module can read the status of T3 transistor. In addition to the relay coils, each power transistor also drives two LEDs: one on the CB02 board and another in the front panel, indicating an activated relay.

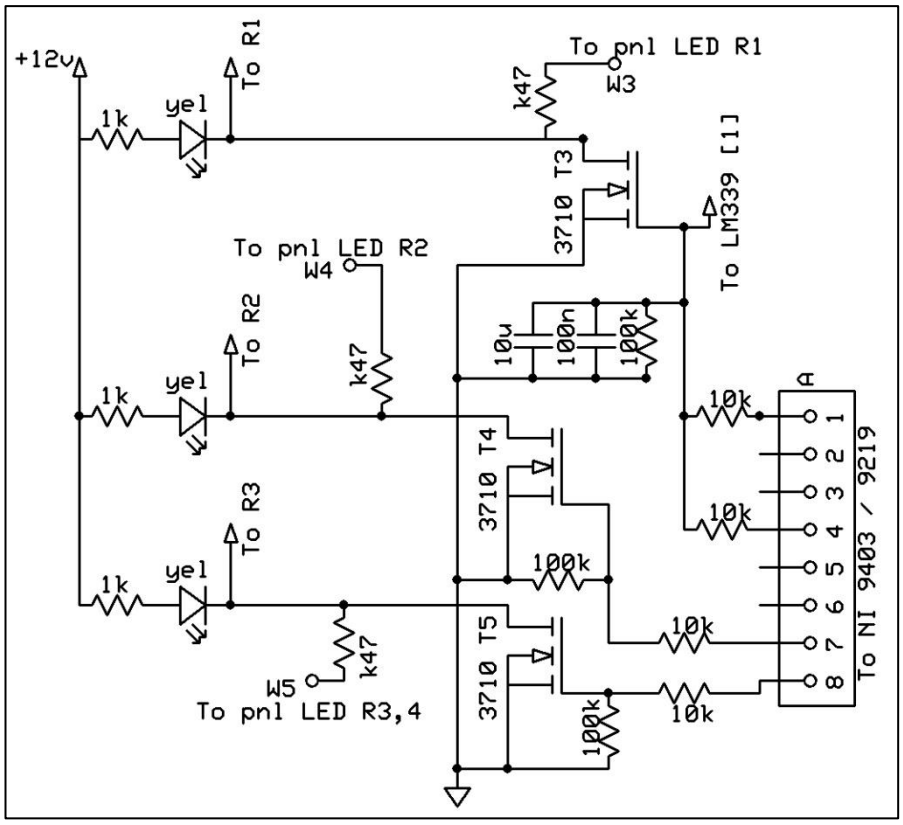

Figure 4.30. CB02 relay driving circuit schematic diagram.

The relay coils have flyback diodes connected as show in Figure 4.31. Flyback diodes allow current flow in the relay coils due to the energy stored in the inductive coils when the transistors are switched off. Without a flyback diode, an abruptly disconnected current would result in a voltage spike generated by the magnetic energy stored in the coil. It is possible that the high voltage spike will damage the switching transistor or disturb the power supply. A flyback diode prevents that by providing means for the coil current to flow in a closed loop and dissipate slowly.

Relay terminal wiring is shown in Figure 4.31 and have following functionalities. When activated, R1 relay shorts the 5 A shunt, creating a bypass, and prevents the shunt current to go over 5 Amperes. R2 relay connects D3 and D4 terminals for external load and must be activated, when there is nothing connected to the external load terminals to close the TEG module current loop. Relays R3 and R4 operate together and are wired to invert TEG module polarity when activated.

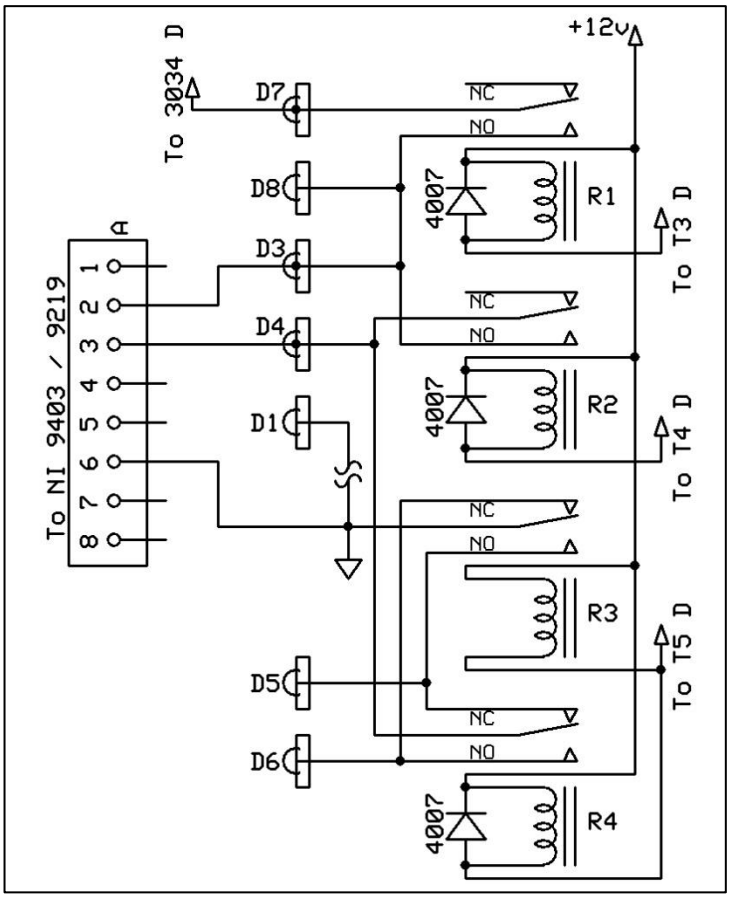

Figure 4.31. CB02 relay wiring schematic diagram.

4.5 Heater Power control

Heater power is controlled manually using a high power variable transformer (Green Dot Electric Limited, India model D-281-P), capable of delivering 28 A maximum load current. The transformer's primary winding is connected to 230 V mains power line through a 25 A class B double circuit breaker and Clipsal 32 A three-phase plug and socket (Figure 4.32). The power plug is wired following wire colour recommendations outlined in AU/NZ 3000:2007 standard [120]. The transformer primary winding is connected to the L1 phase, while all 10 A outlets in the lab, used for computer, vacuum pump, and/or cDAQ chassis are on L3 phase.

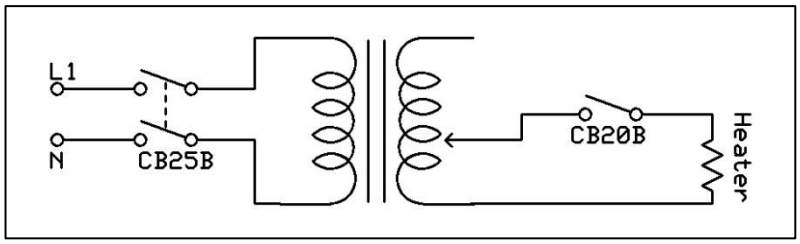

Figure 4.32. Heater power control using a variable step-down transformer.

The variable power transformer replaces an Omega CN9600 temperature controller coupled with Omega SCR19P phase angle controller used previously. It was observed that under high heater power, significant electrical noise is introduced into thermocouple signals because of the phase angle controller firing at high currents. Using a variable transformer solves this issue, because its output current is pure sinusoid as compared to a choppy phase angle controller output current which is a fraction of a sinusoid, switched on abruptly at a preset phase angle for every half wave.

The transformer's secondary winding is connected to the heater with a 20 A class B circuit breaker in series. The secondary winding output is selectable from 0 V to 270 V. Knowing that the heater coil resistance is around 7 Ω at high temperatures and the heater current is limited to 20 A, the transformer output range used for heater is 0 – 140 V.

5 MEASUREMENT SYSTEM: INSTRUMENT CONTROL SOFTWARE

5.1 Overview

This Chapter introduces the programming language, used to write the control software. Furthermore, it describes the functionality, principles, and usage of the control software; the programming code and functions governing the user interface are also explained.

The control software gradually evolved throughout the course of the instrument design and build. The software architecture grew from a single loop to producer–consumer architecture using queues and functional global variables as the programming language was learned. The programming style varies across the software as different parts of the code were written at different times with LabVIEW proficiency varying from none to Certified LabVIEW Associate Developer (CLAD) (CLAD is the highest certification level obtainable without charge for examination). Nevertheless, the code was kept readable, maintainable, scalable, and reusable to the best of author's ability at all times. The software provides a framework for future developers to easily modify existing functions or add new ones.

5.2 LabVIEW Programming Language

Laboratory Virtual Instrument Engineering Workbench (LabVIEW) is a graphical programming language from National Instruments [121]. Since its introduction in 1986, LabVIEW became a common choice for custom instrument control, data acquisition, and process automation software needs. The LabVIEW code is a graphical block diagram where the function nodes are connected by drawing wires between them. Information propagates from left to right along the wires connecting the nodes. The nodes will execute as soon as all the required inputs have data available. LabVIEW is inherently capable of parallel code execution by multithreading.

Independent LabVIEW programs are called Virtual Instruments (VIs). With LabVIEW being a graphical programing language, each VI has a front panel for user interface, a block diagram for program code, and a connector panel for input and output terminals. User interface uses controls for supplying information to the program, and indicators for information output to the operator. All controls and indicators have their respective nodes created in the block diagram. In addition, the block diagram also contains structures and functions, which are available from the function palette, to perform operations on inputs in order to generate outputs. LabVIEW programming involves connecting the control, structure, function, and indicator nodes with wires. The VI being a modular piece of code with inputs and outputs can either run on its own or be embedded as a building block in a larger VI as a subroutine.

LabVIEW is an attractive option to code simple programs, as it does not require an extensive programming knowledge. However, a large and complex high quality code will require the programmer to have a substantial knowledge of the special LabVIEW syntax and memory management. The control software for this measurement system is comprised of several hundreds of VIs.

The following sections introduce the important concepts of LabVIEW programming used for the control software code, as well as some of the most important functions.

5.3 Graphical User Interface

Graphical User Interface (GUI) allows operator to communicate with the control software. The GUI employs controls such as buttons, toggle switches, text boxes, check boxes, and combo boxes to acquire operator’s input and commands. It employs indicators such as text boxes, graphs, lists, tables, and Boolean indicators to output information to the operator on the computer screen. Additionally, the control software may use physical LED indicators or sound alarm on the circuit board enclosure.

The control software GUI was designed for 19” square monitor with 1080 vertical pixels, which came with the Dell Optiplex personal computer. The GUI is split into two sections: the main section with a tab control, which takes up around 85 % of the screen from the top, and a status messaging list box at the bottom. Three buttons are positioned above the tab control: Start button to begin data acquisition, Stop button to stop it, and Exit Program button to stop all running processes and stop the control software. The control software front panel is shown in Figure 5.1.

The tab control has three tabs. (1) Instrument Monitor tab contains controls and indicators required for normal measurement system control and information display; (2) Settings tab is subdivided into three tabs to contain controls and indicators for TEG module and reference block parameters, temperature settings, and measurement settings; (3) Manual Control tab contains graph indicators and controls to display and manipulate any acquired data, and to control the instrument features, irrelevant to regular operation.

The status message list box is a very useful software feature to inform the operator about the instrument status and processes running in the background. Any VI can broadcast status messages or process values and they will be immediately displayed in the list box with a date and time preceding the message. It is a great aid during software debugging or troubleshooting.

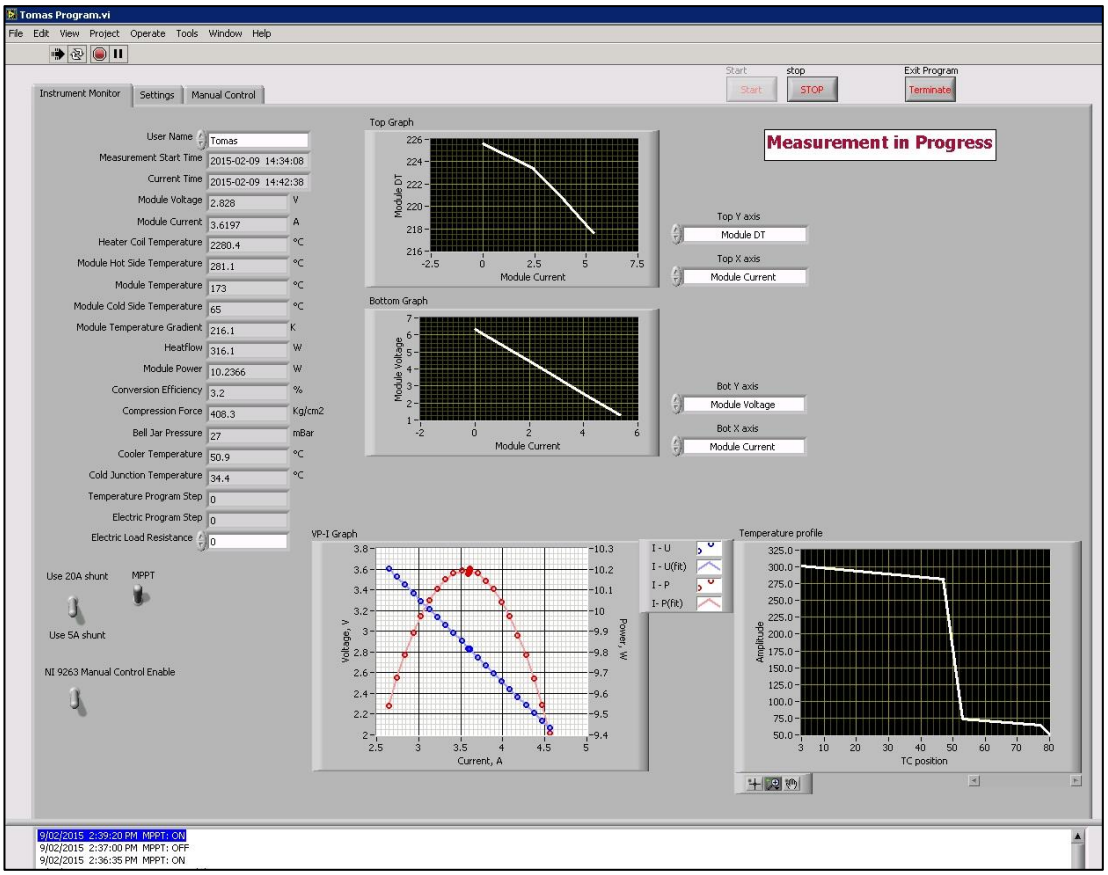

Figure 5.1. Control Software front panel.

5.4 Important LabVIEW Programming Concepts

Creating small simple single function programs in LabVIEW is quite an easy task. However, creating a comprehensive program with user interface, data acquisition, precise timing, instrument control, data manipulation and saving, information output to the operator, and/or custom settings requires an in depth knowledge of LabVIEW programming practices that are not intuitive to one who's used other object oriented programming languages. Few of such concepts and practices are introduced here.

5.4.1 Queues

In the producer–consumer design pattern commands and any required information generated in the producer loop are conveyed to the consumer loops using queues. A queue is a first in – first out (FIFO) buffer with the ability to enqueue (add) and

dequeue (take out) its elements one by one. The queue elements can be any type of data. For the producer–consumer design pattern the queue element type is at least a type–defined enumerator for case selection with additional data being optional.

A queue should have only one consumer, while the number of producers can be more than one. The producer and the consumer loop execution rates do not have to be identical. Usually the consumer loop executes much faster than the enqueueing rate, but if the production rate is higher than the consumption rate, the queue will fill up and the production rate will be reduced to be equal to the dequeueing rate.

5.4.2 Functional Global Variables

A Functional Global Variable (FGV) is a VI that allows storage and access to data or resources, typically also allowing for various actions to be performed on the stored data. For this reason an alternative name used by some for the FGVs is action engines. FGVs provide means to share data across the entire project, both vertically and horizontally. Using FGVs allows preventing "race" conditions. Figure 5.2 illustrates a FGV concept by showing a very simple FGV block diagram for storing a single Boolean value. The FGV functions are: read; set to TRUE; set to FALSE; and change.

Typically, the FGV is a While Loop with TRUE Boolean value wired to the stop condition. The loop stops after each execution and is there just to provide place for shift registers. Uninitialized shift registers (USR) are used with FGVs. A USR is a shift register, which does not have an input wired to its left side. The information is retained in the uninitialized shift register between successive runs of the FGV for as long as the parent VI stays in memory.

Inside the while loop a case structure is placed to handle the FGV's actions. The actions can be just for example Set and Get – in this case the FGV has the same functionality as a global variable. If more actions are added, the global variable becomes a functional global variable. Case selection is done using type–defined

enumerators. While other methods are possible, the enumerated list control provides a readable and expandable list of actions. Any changes in the type–defined control's list values automatically update in all instances throughout the project. The case structure contains the code to implement the actions for each defined enumerator value.

Race conditions occur when several processes are modifying the same variable at the same time, therefore competing, and data loss or data corruption occurs. Global variables are re-entrant, thus susceptible to the race conditions. Meanwhile, FGVs prevent race conditions by being by default non–re-entrant, meaning that once called the FGV is locked, and the subsequent callers have to wait until it completes its operations. Race conditions are eliminated, if all updates to the data are done inside the FGV and in a single call.

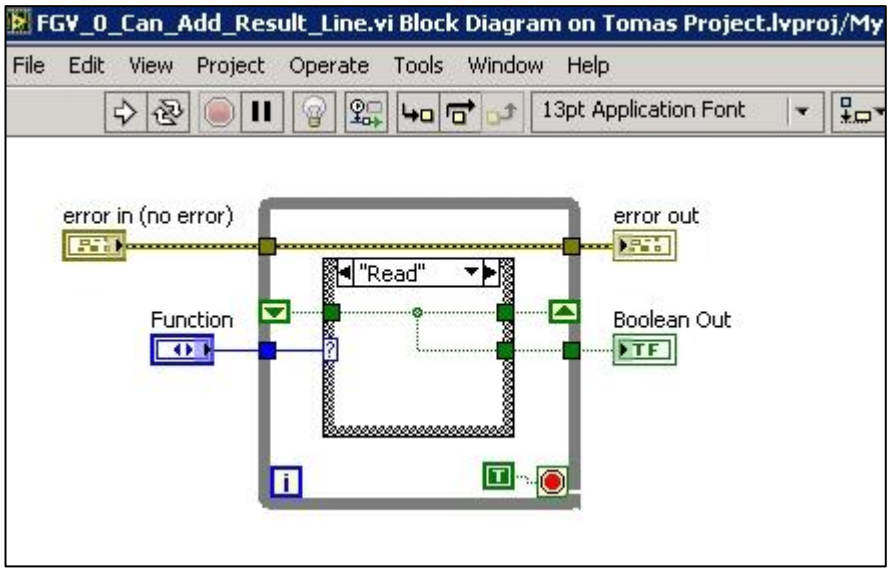

Figure 5.2. Block diagram of a Functional Global Variable used to store and manipulate a single Boolean value.

5.4.3 NI DAQ Tasks

A NI DAQmx task (task) is a VI where the configuration information of resolution, triggering, timing, and other properties for particular collection of hardware channels is saved. Tasks can contain multiple physical channels and global virtual channels with different gain, terminal configuration and custom scaling settings while using the same timing settings. A task represents a measurement or a generation to be performed. Tasks are necessary for data acquisition or signal generation that utilizes timing and/or data buffers.

Tasks only need to be created once – during the application initialisation. The create task VI can then be wired to a loop for multiple acquisitions or generations. When the acquisition or generation loop has finished its operations, the clear task VI outside the loop clears the task from the memory.

More than one task with same physical channels can be created at the same time. For example, if acquisition or generation of data at different sampling rates are required, then multiple tasks for the same channels are needed. Unfortunately, if one of the shared resource tasks is running, trying to acquire or generate with the other tasks will result in a resource unavailable error. A workaround this problem is possible using the NI-DAQmx task state machine (Figure 5.3). NI-DAQmx task state machine ensures that time consuming operations such as task verification, resource reservation, and hardware programming are performed only when needed. NI-DAQmx palette offers explicit commands that cause verify, reserve, or commit operations to be performed. After acquisition or generation have been finished, the un-reserve command is used to make the task channels available for use with other tasks.

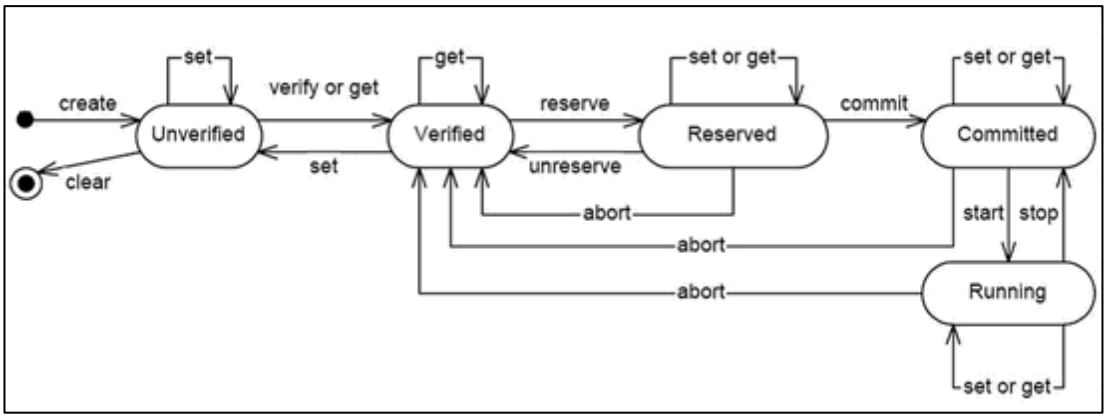

Figure 5.3. A state model for DAQ tasks. Configuration operations include checking the configuration (verify), reserving resources (reserve), and programming the hardware (commit).

5.5 Important Functions and Virtual Instruments

5.5.1 Perturb & Observe Maximum Power Point Tracking Algorithm

Perturb and Observe (P&O) algorithms are simple but effective ways to track the TEG module maximum power point and are widely used [68]. The P&O algorithm tracks by measuring TEG module output voltage and current, calculating the produced power, changing the module current, and then measuring and calculating the three parameters again to determine the direction of the next current step. This algorithm can be imagined as a hill climbing algorithm in a sense that it goes up the power curve till it passes the maximum power point and then it changes the direction until it passes the MPP again. It is worth mentioning that either the voltage or the current can be used as a base for the P&O MPPT. Voltage base is most commonly used for PV applications, but for this measurement system the tracking base is current, as the electronic load is operating in a constant current sink mode.

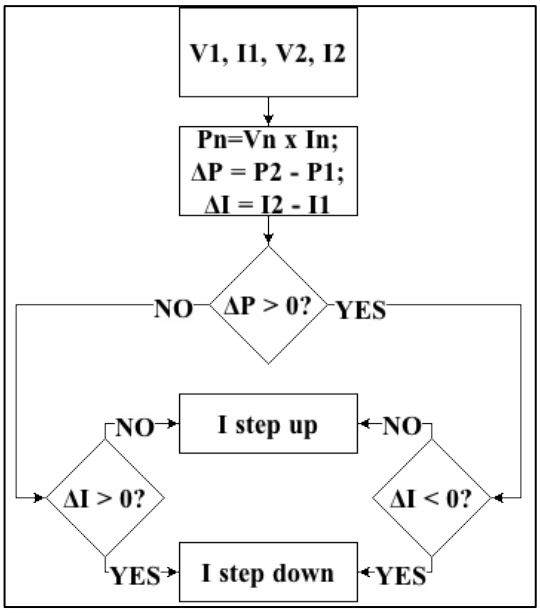

Figure 5.4. Flow diagram of the Perturb & Observe (P&O) algorithm.

The algorithm cannot tell if the MPP has been reached, therefore it always passes it by up to two steps. Once the MPP has been passed the algorithm changes the tracking direction and therefore oscillates around the maximum power point. The size of the oscillation depends on the current step size. The current step size is a compromise between the size of the oscillation at the MPP and the responsiveness of the P&O algorithm. A P&O tracking with a very small step size would take more steps and time to reach the MPP when changes in the thermal conditions occur. Then again, a variable step size can be introduced to overcome the dynamic response and the steady state error trade–off, with increasing system complexity, when the TEG module is a subject to drastic thermal condition fluctuations.

Figure 5.4 shows the flowchart for the current step direction determination function for the P&O algorithm implemented in this control software. The P&O algorithm uses a constant relative step size, which is 2% of the current value. During the initialisation stage the algorithm does a rough measurement for the TEG module short circuit current to determine the starting point for the tracking. This is an effective way to initialise the algorithm, as it provides a fairly accurate start point and then the steady thermal state is reached in under a minute. The P&O MPPT may be enabled from the manual control tab on the software front panel.

5.5.2 New MPPT Algorithm with True Module Resistance Measurement

A new Quick Scan (QS) MPPT algorithm was developed in the attempt to make TEG module characterisation process less time consuming. The simultaneous determination of the MPP and measurement of module's resistance is made possible by a very fast V–I curve recording under constant module temperature gradient and heat flow. This algorithm measures the true resistance of a TEG module, while the conventional V–I curve slope method usually overestimates resistance values due to the decrease of TE material temperature gradient with increasing module current.

Typically, the voltage–current curves are recorded at a constant module temperature gradient (steady thermal state) starting from an open circuit state. External resistors are connected to the module or electronic loads are used to measure module voltage at discrete current settings ranging from no current to the maximum the module can source with the minimum load resistor value available. When electrical current flows in the TEG module, heat pumping due to the Peltier Effect will occur. The Peltier Effect is considered parasitic in power generation, because in addition to the heat flow due to the thermal conductance, it pumps more heat from the hot to the cold side of the module (see Equation 2.11 and Equation 2.12). As a consequence, TEG module temperature gradient will be reduced. Henceforth, the heater power will need to be adjusted to compensate the increased heat flow and bring the module thermal gradient back to its initial state. Heater power adjustments will have to be made for every module current setpoint. Naturally, it will take some time to reach steady thermal state, which is in the order of tens of minutes, before an electrical measurement can take place.

QS MPPT algorithm is possible due to the fact that the TEG module electrical response to the changed operating conditions is immediate, while at the same time the thermal response is dampened by the large thermal capacity and thermal resistances of the system. Figure 5.5 illustrates this effect. After a step down in the module current, the current setting is held constant by the electronic load. Meanwhile, the module voltage keeps increasing due to the increasing module

temperature gradient, caused by a reduction of the module heat flow. This effect will get stronger with increasing current step size.

The QS MPPT algorithm overcomes the problem of the heat flow change after a change in electrical conditions by doing a quick electrical measurement as soon as the current set point has been achieved, before a significant thermal response can occur. The data acquisition system is set up for maximum acquisition rate, which is 100 S/s, resulting in a measurement duration of only 10 ms. The QS MPPT algorithm does a number of measurements in series, where the NI 9263 module sets the electronic load current setpoint value, the electronic load reaches the set point current and keeps it constant, NI 9219 and NI 9213 modules measure the resulting voltage and current values – and it all happens in 10 ms. The sampling rate of NI 9263 module is set to 10 kHz. A phase shift setting is introduced in the control software for analog output and analog input synchronisation. Illustrations for the NI 9263 module output waveform for the electronic load is show in Figure 5.6 left, and the resulting NI 9213 module read current is shown in Figure 5.6 right.

In addition to being fast, the QS MPPT algorithm operates at the MPP, where the heat flow value is in between the open circuit and short circuit heat flow values. Accordingly, in order to minimise thermal disturbance of the system, the QS MPPT algorithm alternates current settings, which increase module heat flow with those that decrease it. Ultimately, the algorithm begins with three measurements at the MPP, then changes the module current away from the MPP with increasing absolute value for a predetermined number of times, and finally, does another three measurements at the MPP. The MPP measurements prior to and after the scan match very well, indicating that there is no change in module temperature gradient and heat flow.

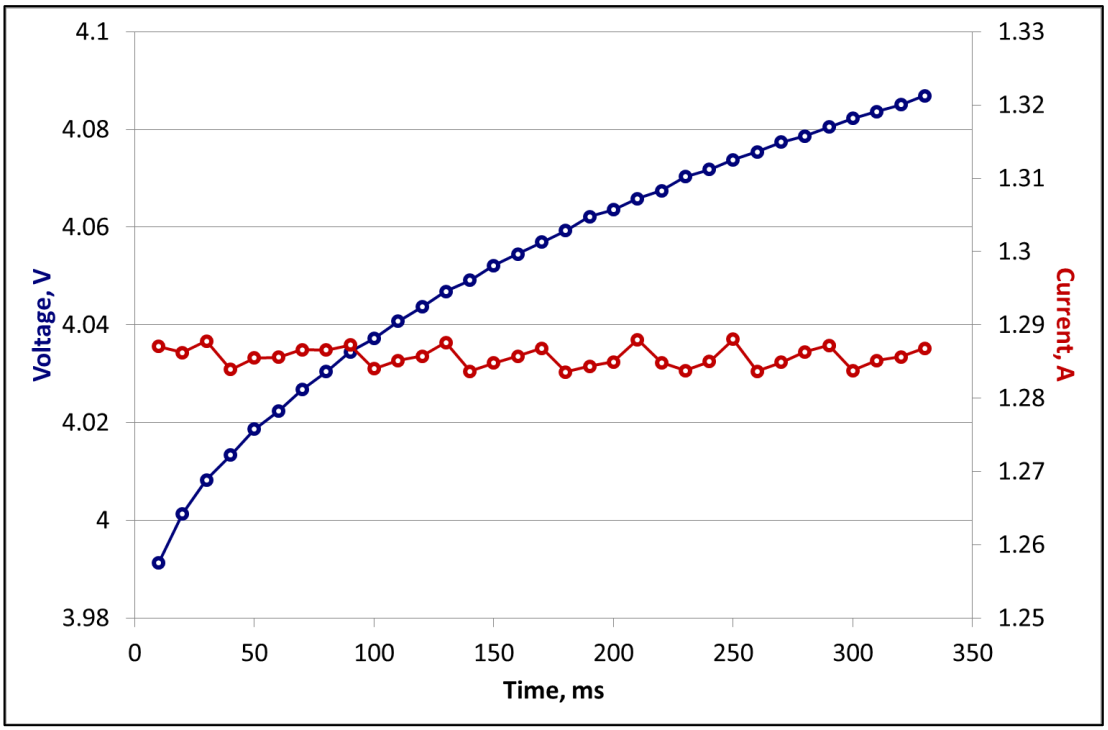

Figure 5.5. Module voltage variation in time while module current is held constant after a small step down in current setting.

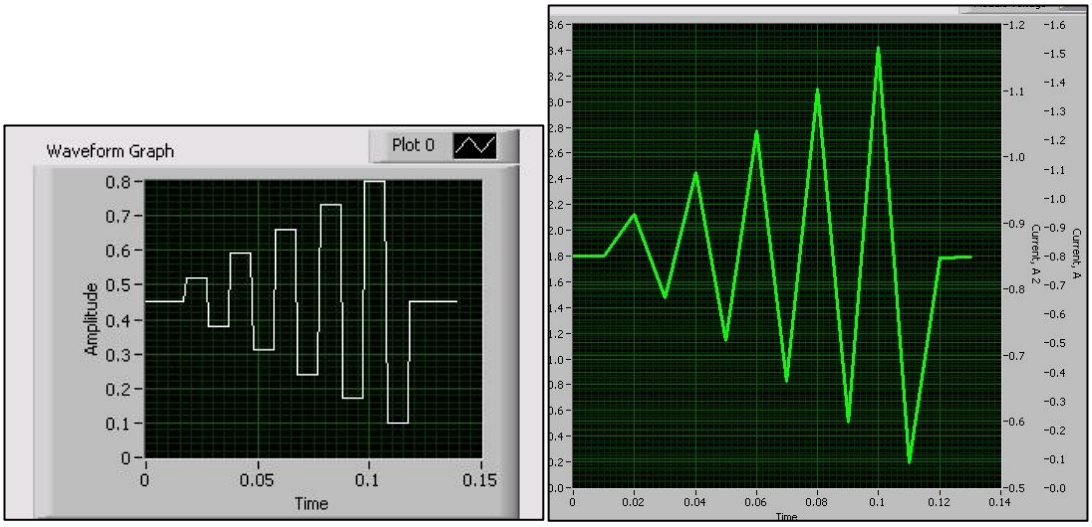

Figure 5.6. Screen snapshots of QS MPPT algorithm generated waveform shape for the electronic load set point (left) and TEG module current values measured during QS MPPT (right).

The algorithm works equally well, if the electronic load setpoint program is reversed in time, randomised, or the current change values are reversed in sign. Again, confirming that there is no noticeable change in the heat flow of the module. The number of swings – number of current steps up and down from the MPP is selectable by the instrument operator in the control software. Figure 5.7 illustrates ten point and one hundred point measurement data. Twenty measurement points are selected by default, because it results in measurement duration of just a fraction of a second and plenty of data points to extract linear regression parameters. Linear regression parameters do not depend on the range of the current scan. Maximum amplitude for the current set point program is set to 50% of the MPP current. It is possible that this percentage might need to be reduced, if the electronic load does not cope with the high steps in current set points. This is yet to be experimentally found. It is possible to measure more than one data point per current set point, but, as shown in Figure 5.5 for 33 measurements per one current setpoint, the change in module heat flow and resulting change in module temperature gradient will affect measured values. The goodness of the acquired data during measurement is determined by comparing the mean absolute error (MAE) value to the previous measurement's MAE values. As shown in Figure 5.8, MAE values, which fall over the threshold limit, indicate a bad measurement, which is then discarded.

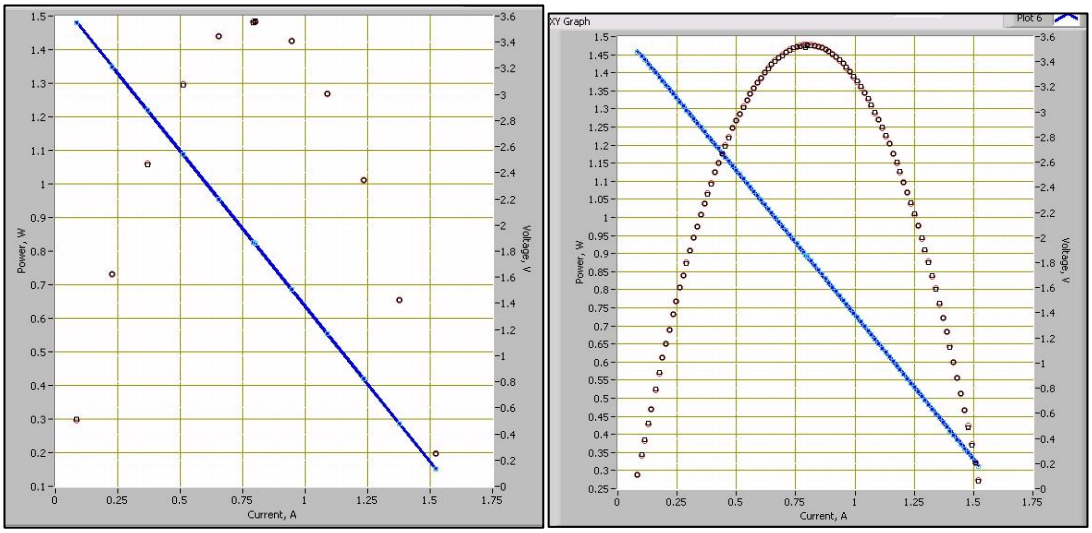

Figure 5.7. Screen snapshots of voltage - current and power - current curves. Four data points at peak power. Ten (left), one hundred (right) data points away from the MPP. Measured values are in light blue squares, linear fit of measured values is in blue, calculated power in black squares, second order polynomial fit of power values is in red circles.

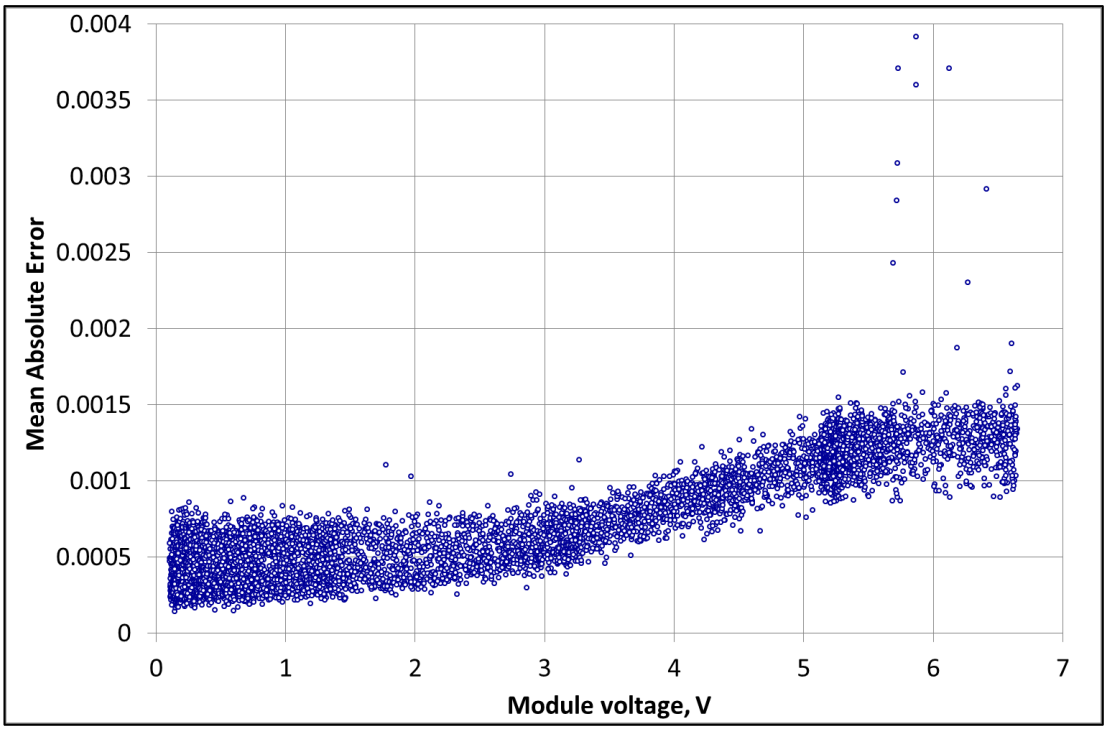

Figure 5.8. Mean absolute error values plotted versus module voltage for 26 data point voltage–current curves. One value for each curve.

Measured data is used to extract TEG module's resistance from the slope of the voltage–current curve, while the intercept is the module's open circuit voltage (Equation 2.16). Calculated module power values are fitted with a second order polynomial equation, which is then differentiated to find the MPP power and current. The so–obtained MPP current value is used to set the electronic load current for subsequent data acquisition loop runs. It is important to note that module's resistance and open circuit voltage measured using the QS MPPT algorithm are measured at the MPP with a constant module temperature gradient and heat flow regardless of the module current. However, the conventional V–I curve measurement method is subject to a constant temperature gradient, but module current dependent on the heat flow. Both the QS MPPT and conventional methods are subjects to the "ceramic plate effect" as explained in the next section.

5.5.2.1 Ceramic Plate Effect

Ceramic plate effect (CPE) refers to the influence of non–thermoelectric TEG module parts on the overall module performance. The correlation between the ratio of the TE material to the TEG module thickness with the TEG module performance has been modelled [122, 123]. However, analysis of the measurement data for TE modules available in literature shows that the ceramic plate effect is only considered (if at all), when it comes to the module compression and/or thermal interface material used [62, 65]. Consequently, module resistance measurements are often incorrect, as the ceramic plate effect influences the conventional electrical resistance measurements [10]. While there is no need to precisely quantify it, it is important to acknowledge CPE and understand its impact on the operation and measurements of TEG modules.

The influence of the ceramic plate effect can be easily illustrated by the difference between dimensionless Figure of Merit (zT) for TE material and ZT for TEG module, with the latter usually being significantly lower. These differences can be explained as follows: (1) in addition to the TE leg resistance, the module resistance includes electrode resistance and TE leg – electrode contact resistance. The later can be as high as and comparable to the TE leg resistance; (2) TEG module thermal resistance is a sum of the TE leg, electrode, electrode–ceramic contact, ceramic plate, and ceramic plate–heat source thermal resistances; (3) Temperature gradient over the TE material is lower than the temperature gradient measured over the TEG module resulting in a lowered Seebeck voltage.

A schematic diagram of a typical TEG module is shown in Figure 5.9. It also illustrates that the TE material temperature gradient is lower than the TEG module temperature gradient due to the ceramic plate and the electrode thermal resistances. Figure 5.10 shows TEG module as thermal resistance components with heat flow generating temperature drops across various parts of the TEG module. TEG module temperature gradient is actually the temperature difference between the heat source and the heat sink surfaces – the closest points to the module where the temperature can be measured. Therefore, the ceramic plate and electrode thermal resistor

(1/Kcpe) also includes the ceramic plate–electrode and the ceramic plate–heat exchanger contact thermal resistances. Ideally, 1/Kcpe should be as low as possible.

During a conventional steady state voltage–current curve measurement at constant temperature gradient as the module current flow is increased, the Peltier Effect will effectively reduce the 1/Kte component thermal resistance value, while the 1/Kcpe will remain unchanged. As a consequence, (1) the heat flow across the module will need to be increased to maintain the initial module temperature gradient due to reduced overall module thermal resistance, and (2) the temperature gradient of the TE material will be reduced because the ratio between the thermal gradients of TE material and TEG module is equal to the ratio between the thermal resistance of TE material and overall thermal resistance of the module. As a result, in the voltage–current curve the voltage values will go down with increasing current not only due to the module resistance as shown in Equation 2.16, but also due to the reduced Seebeck voltage caused by the drop of the TE material temperature gradient. Therefore, the use of Equation 2.16 for module resistance calculation is not correct in the conventional method as the resistance result will include the module voltage drop due to decreased TE material's temperature gradient. This may be referred to as the ceramic plate effect to the module resistance.

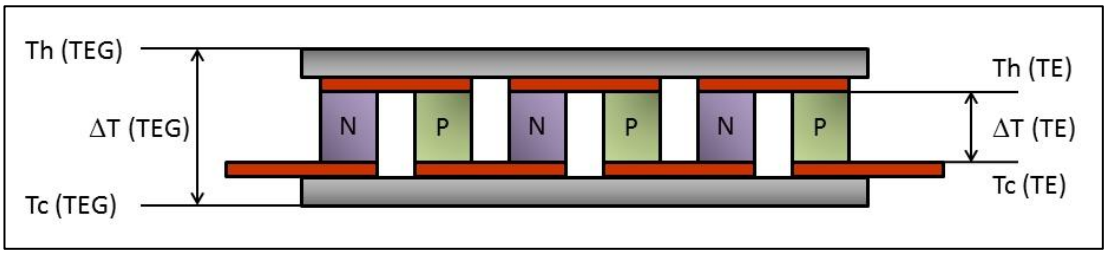

Figure 5.9. Schematic diagram of TEG module.

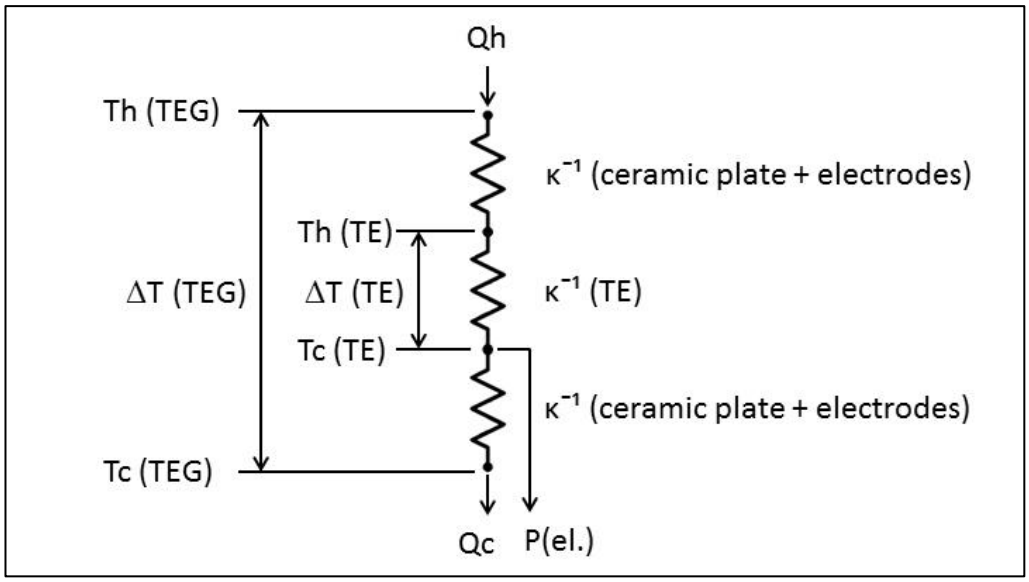

Figure 5.10. Thermal resistance model for TEG module.

Ceramic plate effect is not applicable to the resistance measurement using the QS MPPT method, because in this method there is no change in the module's or TE material's temperature gradients or heat flow. Henceforth, the QS MPPT measured resistance is true TEG module resistance without the Seebeck voltage reduction due to the drop in the temperature gradient of TE material component. The QS resistance measurements would not be different if the MPPT component was disabled and the measurements would be taken at a point on V–I curve other than MPP.

In contrast to the module resistance measurements, the open circuit voltage measurements by QS MPPT method are influenced by the ceramic plate effect. The QS MPPT algorithm measures module's open circuit voltage at the TE material temperature gradient during MPP thermal conditions. Obviously, at the actual open circuit state the TE material temperature gradient would be slightly higher. As a result the Voc values measured by the QS MPPT algorithm are lower than those measured by the conventional method. The relative Voc reduction is proportional to the relative decrease in the temperature gradient of the TE material, when module operating conditions change from open circuit to MPP. The comparison of the V–I curves measured by both the conventional and the QS MPPT methods is shown in Figure 5.11. A direct measurement should be used instead of the QS MPPT algorithm to obtain module's Voc values.

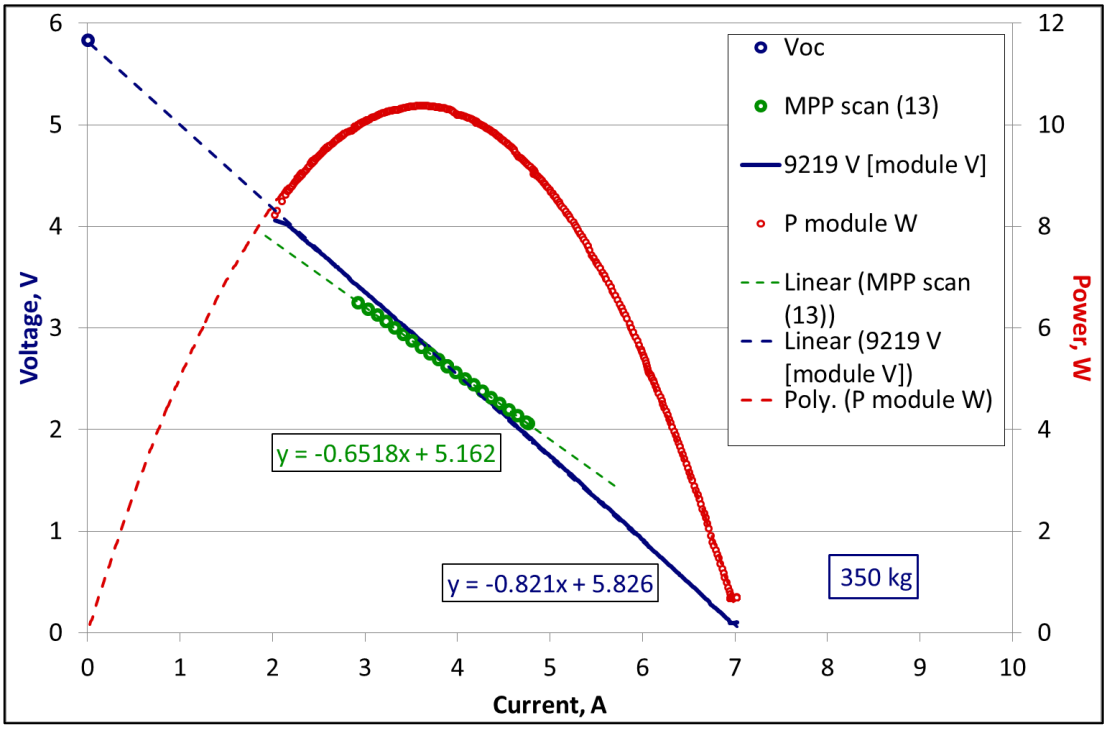

Figure 5.11. TEG127-50D module voltage and power dependences on module current. Module resistance measurement comparison between conventional V-I curve slope and the MPPT algorithm V-I curve slope.

5.5.3 MPPT Fit VI

The MPPT Fit VI mathematically fits the voltage and current data acquired during the cDAQ loop QS MPPT case run. It is coded using a flat sequence structure for easier readability. Firstly, the VI discards the least reliable data points, namely data points that are less than 50 mV or less than 50 mA. Next, the data set is fitted using the Linear Fit VI from the LabVIEW functions palette, points with more than 2% deviation are removed from the data set before it is fitted again using the Linear Fit VI using the Least Absolute Residual method. The obtained intercept value is the QS MPPT algorithm measured TEG module open circuit voltage, while the negative of the obtained slope value is the resistance of the module. Following step is the calculation of power as a function of the module current. The power curve is mathematically fitted using the General Polynomial Fit VI for the second order

polynomial using the least squares method. The first derivative of the obtained polynomial coefficients was obtained using the Nth Derivative of Polynomial VI. The Polynomial Root VI was used to find roots of the first derivative of the power curve. The current value of the resulting root is considered the current set point for the MPP. The following rules are used to judge whether the measurement is of a good quality and is worth keeping: (1) no data points are removed during the V–I curve fitting; (2) the mean absolute error value does not exceed the empirically determined threshold, which is shown in the QS MPPT algorithm section; (3) module's resistance is positive. Finally, measurement and fitting values are plotted in the V–I and the P–I graphs on the front panel.

5.5.4 MPPT Scan Data FGV

The MPPT Scan Data FGV VI stores the QS MPPT scan data in memory throughout the measurement and saves the data to the hard drive. Accordingly, the FGV has two main cases: (1) Add Data for appending the QS MPPT measurement data to the already accumulated data table; (2) Save to File, which periodically saves the data table to disk.

Upon receiving a data array with an Add Data command, which happens immediately after the data has been acquired and fitted, the case inserts a timestamp value to the beginning of the array and appends the resulting array to the end of the data table. The first column of the data table is therefore for timestamps, which indicate when the measurement has been taken, and can be used to interpolate the temperature, compression force and other relevant data from the cDAQ Data Array data table, containing results of the standard cDAQ loop measurements. The QS MPPT data table columns are: Timestamp, MPPT Voc, MPPT Resistance, MPPT scan MAE, MPP current, Scan data point count, followed by the actual data point current and voltage values.

The Save to File case writes the data table to the hard drive using a Write to Spreadsheet VI. First timestamp is read from the cDAQ Data Array and used in the

file name so that the QS MPPT data file and CDAQ data file are shown together in the */Data/ directory. The data file name is the timestamp in the YYYYMMDD HHMMSS format followed by "QS MPPT Data.txt" string. Two file writes take place. The first one reads the column names from the Data File Headers FGV and writes them to file in a string format. The second write appends the file created in the first write with the numerical data from the data table.

The Delete All Data case replaces the data table values in the shift register with an empty 2D array, thus destroying all the data. This case is used when measurement has to be stopped and restarted.

5.5.5 cDAQ Data Array FGV

Similarly to the MPPT Scan Data FGV VI, the cDAQ Data Array FGV VI stores the cDAQ loop measurement data in memory throughout the measurement and saves the data to the hard drive. Additionally, it has cases for calculating temperature stability, returning the last data row, returning the first timestamp, and returning the whole data table.

Right after the cDAQ loop data acquisition the acquired data array is sent to the cDAQ Data Array FGV Add New Row case. The Add New Row case modifies the data array before it gets appended to the data table. The modifications include: (1) inserting a timestamp to the beginning of the data array; (2) calculating the CJR temperature from the LM335A IC voltages and adjusting the thermocouple measurement data for the CJR temperature using the Adjust for CJR VI; (3) calculating the TEG module compression force with the factory calibration data of the force transducer using the Force kg VI; (4) having the force and TEG module geometrical parameters, calculate the module pressure in kg/cm^2 using the Pressure kgcm2 VI; (5) having the temperature measurements and reference block geometrical data, extrapolate TEG module hot side temperature, cold side temperature, calculate the module temperature gradient and average temperature; (6) having the reference block thermal conductivity lookup table, calculate the hot and

the cold side reference block heat flows; (7) calculate the current shunt currents, module power, and module efficiency. The measured and the calculated values are formed into a 1D array and appended to the data table.

The Save to File case writes the data table to the hard drive using a Write to Spreadsheet VI. First timestamp is indexed from the data table and used in the file name in the */Data/ directory. The data file name is the timestamp in the YYYYMMDD HHMMSS format followed by "cDAQ Data.txt" string. Two file writes take place. The first one reads the column names from the Data File Headers FGV and writes them to file in a string format. The second write appends the file created in the first write with the numerical data from the data table.

The Delete All case replaces all the shift register values with an empty 2D array, thus destroying all the data and freeing up the memory. This case is executed on the Stop or Terminate operator inputs.

The rate of temperature change can be monitored for any thermocouple in the measurement system. The operator defines the column number in the data table and a number of lines to use, then the Get Slope case uses this data table subset to apply a linear regression fitting, and outputs the obtained slope value together with the sum of squared errors (SSE) as a goodness of fit indicator.

The Read Last Line case, the Read, and the Get First Timestamp cases simply outputs the whole or portions of the data table for use outside the cDAQ Data Array, for example, for saving data to file, graphing, or displaying live data values purposes.

5.5.6 Set NI 9263 FGV

The Set NI 9263 FGV VI sets the NI 9263 module AO0 and AO1 with constant output values. The NI 9263 AO0 channel provides the current set points to the Electronic load, while the AO1 channel allows for a direct voltage control of the Electronic load power transistor gate terminal. This VI is used in the cDAQ loop data

acquisitions case along with the rest of the AO and AI VIs, but is kept as a standalone FGV. Nevertheless, it has to unreserve its resources for the QS MPPT case to execute, as the two cases share the same channels. The operator can enable the manual Electronic load control when the MPPT is not running and then use the front panel controls to manually set the desired TEG module current or the Electronic load power transistor gate voltage.

The Set NI 9263 FGV VI has cases for the task creation, resource reserving and unreserving, task clearing, and output setting (Figure 5.12). The Set case generates waveforms using the Gen Waveforms VI. The generated waveforms are just two samples long with 10 kS/s rate. After the Set case execution, the NI 9263 channel outputs remain at the last set point values even though the waveforms have expired. The NI 9263 outputs have to be set to 0 V values at the end of the measurements.

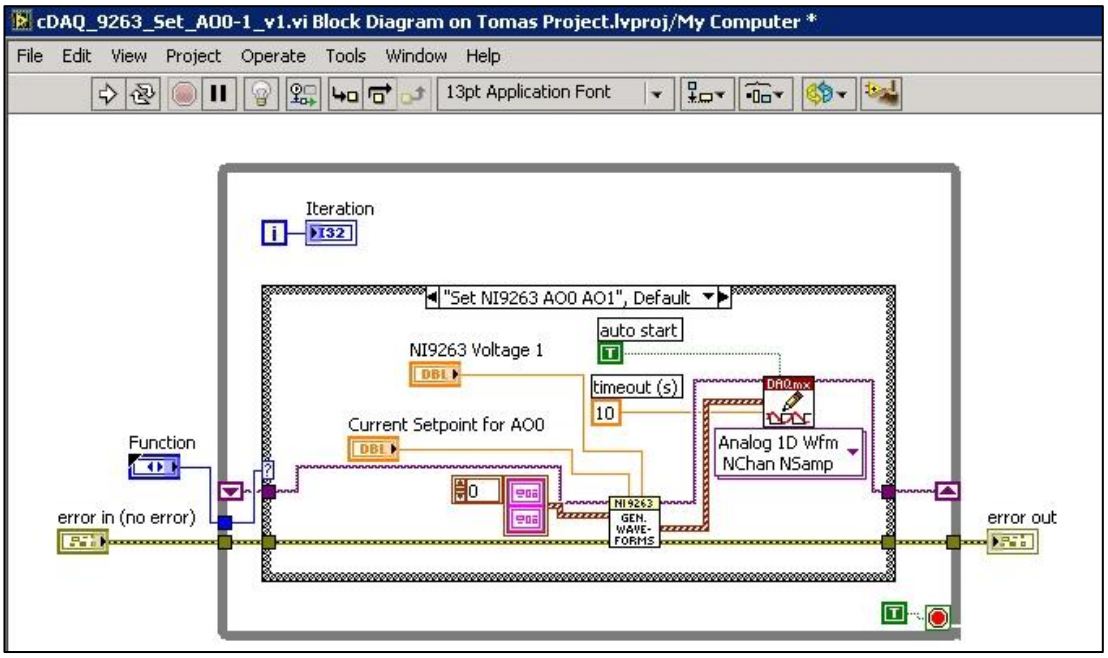

Figure 5.12. Block diagram of the Set NI 9263 FGV Set case.

5.5.7 cDAQ 9403 Set Bits; NI 9403 Set Bits Remote

The cDAQ 9403 Set Bits VI and the NI 9403 Set Bits Remote VI were created to facilitate the control of the NI 9403 module digital output. The cDAQ 9403 Set Bits

VI is a standalone VI which set the NI 9403 module output upon the operator interaction or updates the output waveforms at one second intervals when there is no operator interaction. The NI 9403 Set Bits Remote VI interfaces the cDAQ 9403 Set Bits VI to the rest of the program code.

The updating process continuously runs in parallel to the software crash protection electronics. It is specifically designed to do so to prevent any possible severe damage to the TEG module and the instrument, in case control software or PC stopped working. The NI 9403 module output remains at the last set point of the waveform, when there are no updates from the control software. In such situation, a possibility exists for the heater power control solid state relay control channel (Ch 1) to be left in an enabled state, which would continuously supply maximum power to the heater. NI 9403 channel 0 is the so–called "stay–alive" channel. Only when the "stay–alive" channel output is changing in time, the software crash protection electronic circuits on the Auxiliary circuit board will allow the SSR operation (see SSR Driver section in Chapter 4).

The design of these two VIs may look a bit awkward because they were created before any of the software design patterns were followed. Although the cDAQ 9403 Set Bits VI is neither a typical consumer loop nor a typical FGV, it has most of their features such as quick response or being able to be controlled remotely. The Remote control VI simulates the operator interactions to the Set Bits VI, and is integratable into other VIs for dynamic NI 9403 module control. The NI 9403 module controls may be accessed in the manual control tab on the front panel.

5.6 Control Software Architecture

The program uses a modified producer–consumer design pattern with multiple loops running in parallel, Functional Global Variables and Queues. The control software code is separated into several sections, which execute code for data acquisition, graphing, and saving, simply called "loops". All of them are running concurrently and independently of each other. Each code section is placed in a case structure inside a while loop. Case selection is achieved using queues. Each loop was saved as

a subVI to make the main program block diagram look neat and readable. The subVIs access controls and indicators on the main VI front panel by their refnums, wired to the subVI, and bundled in a cluster. Block diagram of the Status Messages loop VI is presented in Figure 5.13 as an illustration of the coding principle. Other loops have analogous structure, but differ from each other depending on the queue element types and case structure cases.

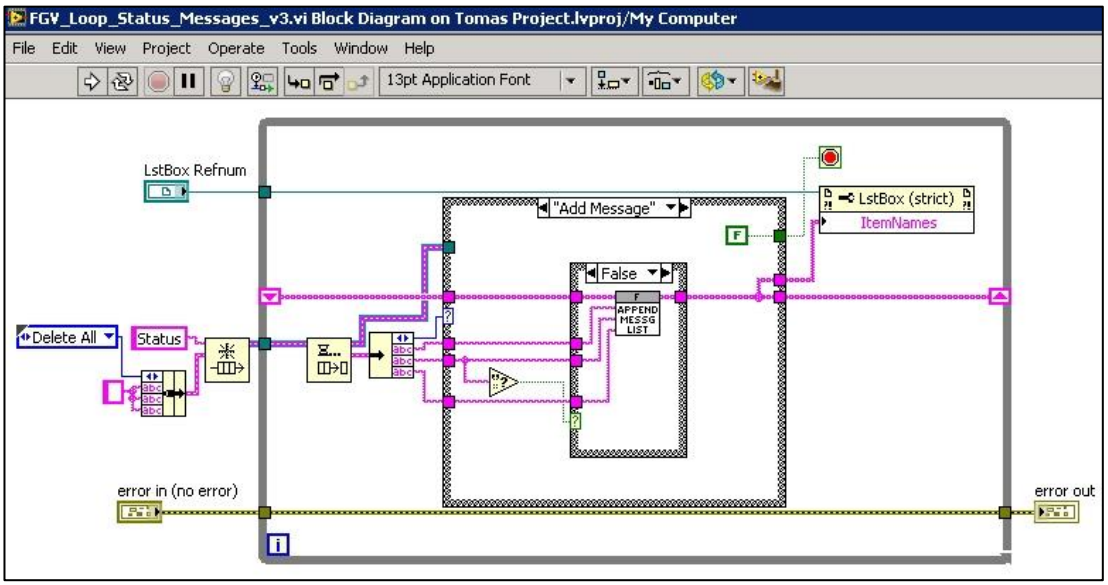

Figure 5.13. Block diagram of the Status Messages loop VI.

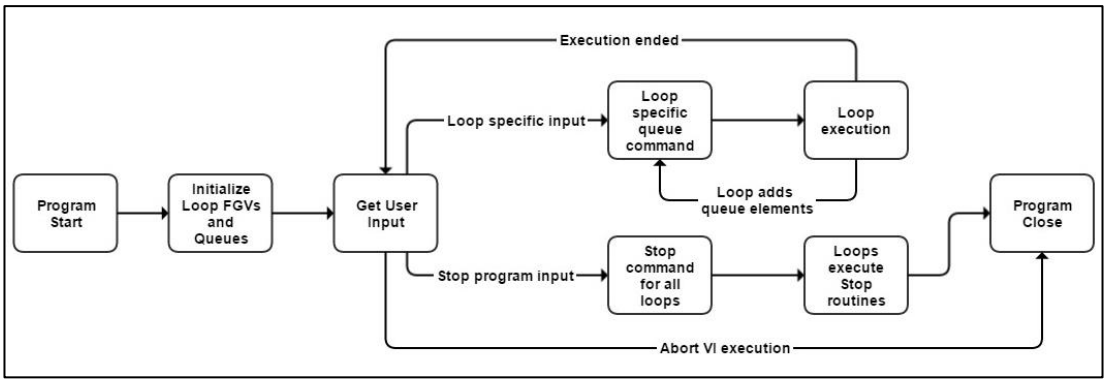

Figure 5.14. Generalized flow of the control software.

All program loops start immediately after the main program is initialised. They receive required control and indicator reference numbers. Queues are obtained with a loop specific names and element types. In most cases, the queue element type is simply a type-defined enumerator. Inside the while loop, the Dequeue Element

function waits for queue elements. Upon receiving an element, it unbundles the case selector enumerator and, optionally, any other data carried by the queue. The case structure executes code of the case determined by the enumerator value. The while loop goes to the next iteration, cycles once at every queue element received and is stopped from the "Stop" case, which also releases the queue. Finally, error out terminal receives data to indicate finished execution of the while loop. Table 5.1 lists the loops in the control software, their functions, and the dedicated queue names.

Table 5.1. Control software parallel loops.

Loop	Loop functions	Loop Queue Name
User Interface loop	Handle Operator input	(producer loop)
cDAQ loop	Acquire data from CompactDAQ system; Control analog output of the cDAQ system; Command and pace other loops	cDAQ
Status Messages loop	Store and display status update messages	Status
Save loop	Save acquired and processed data to disk; Save / Load control values on close / start	Save
Graph loop	Plot acquired and processed data in graphs	Graph

Cases in each while loop are selected by using queues with one dedicated queue required for each while loop to be controlled (consumer). Therefore, each loop VI has a dedicated queue VI. An example queue VI block diagram is show in Figure 5.15. This function obtains a queue with the same name and element data type as the respective loop did, and then it enqueues an element. All queue VIs, except Status Messages queue VI, have a case which, if the function value is "Stop", will enqueue the element at the opposite end, to be dequeued prior to any elements already present in the queue.

Usually queue element is just a type-defined enumerator. This makes it easy to use the queues in the LabVIEW code. The queue VI is placed on the block diagram, and a constant is created for the Function input. Loop execution sequencing may be controlled by wiring the error terminals. Status Messages queue is different in a sense that its elements consist of clusters of a type-defined enumerator and three strings. "Add message" function in the queue is made the default enumerator value. Consequently, it does not require function input to be wired for "Add message"

function. Status messages queue only needs one or more string inputs to execute, making it very easy to use.

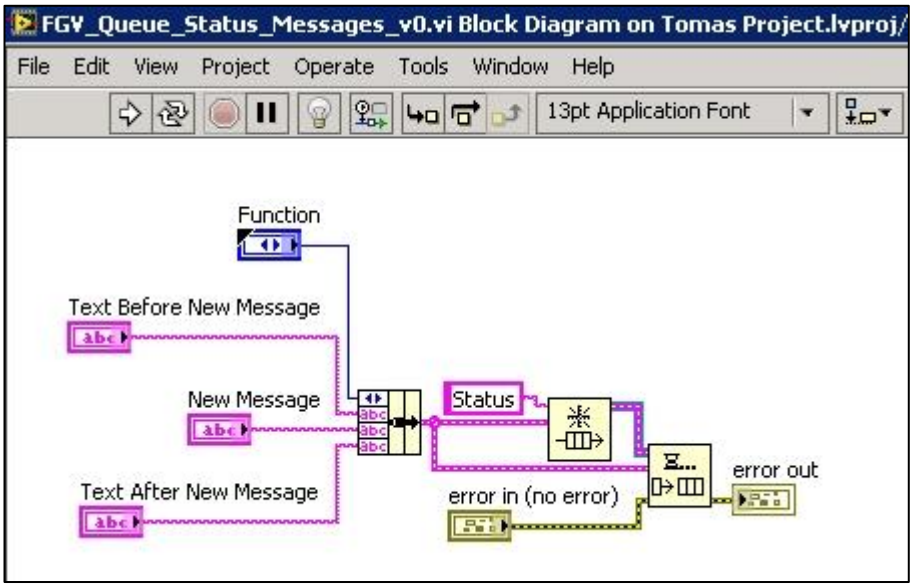

Figure 5.15. Block diagram of the Status Messages loop queue VI.

5.6.1 User Interface Loop

The User Interface loop handles user events such as button clicks, combo box selections made, switches toggled, etc. The user events are handled immediately as soon as they occur with no delay. This is a major improvement over a state machine design pattern, which periodically scans for changes in control values and then act upon them. However, while the code execution is taking place the user interactions is ignored. The user interface loop in this control software uses an Event structure inside a While loop. All possible user events to be handled are defined in the event structure and a case for each user event is created. The while loop waits for the event structure to receive a user event and execute, then resets it to wait for another user event. The code inside the event structure cases is kept to minimum, as shown in Figure 5.16, for fast execution. Typically the cases just enqueue elements to the consumer loop queues and enable or disable some front panel controls. The user interface loop is the first one to start when the program initialises. It only stops when the Exit Program button is clicked and its event case is executed. The user interface

loop is commonly referred to as the producer in the producer–consumer design pattern.

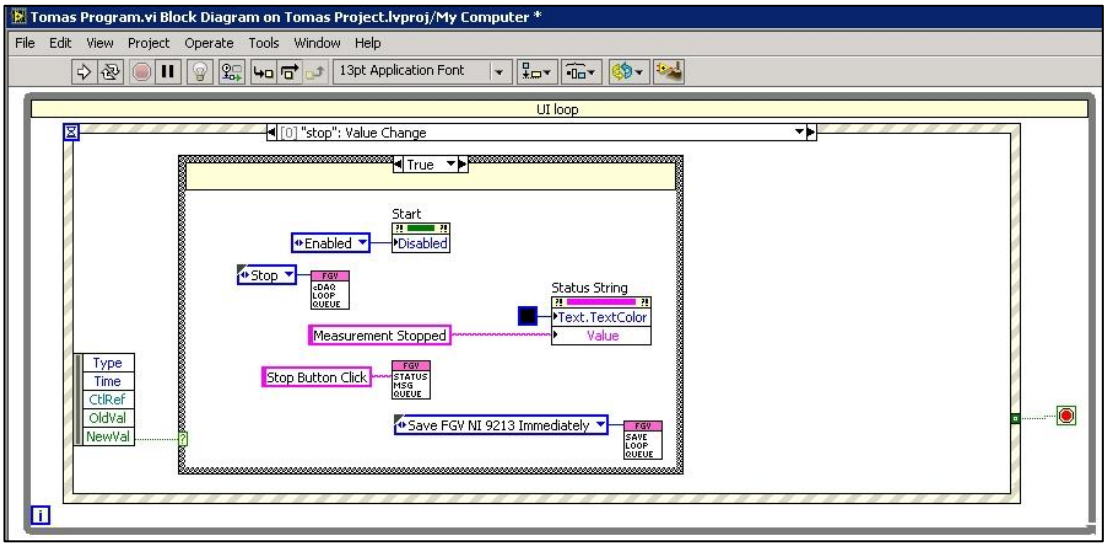

Figure 5.16. User Interface Loop block diagram showing the Stop button click case.

5.6.2 cDAQ Loop

cDAQ loop controls the data acquisition and electronic load control using the NI 9178 chassis with NI 9263, NI 9219, and NI 9213 modules. The core function for this loop is to continuously read the temperature and voltage signals from the measurement system. The loop also acts as a secondary producer, aiding the UI loop by adding queue elements to self, the Save, and the Graph loop queues. The cDAQ loop is hardware timed for a single read of all channels per second. At the end of the data acquisition case execution the loop will enqueue elements to the Save, the Graph, and cDAQ queues to respectively save and graph the acquired data, and reiterate the data acquisition case. The measured data is stored and processed in the cDAQ Data Array FGV. Once started, the cDAQ loop will keep repeating the data acquisition case until the operator stops it as illustrated in Figure 5.17.

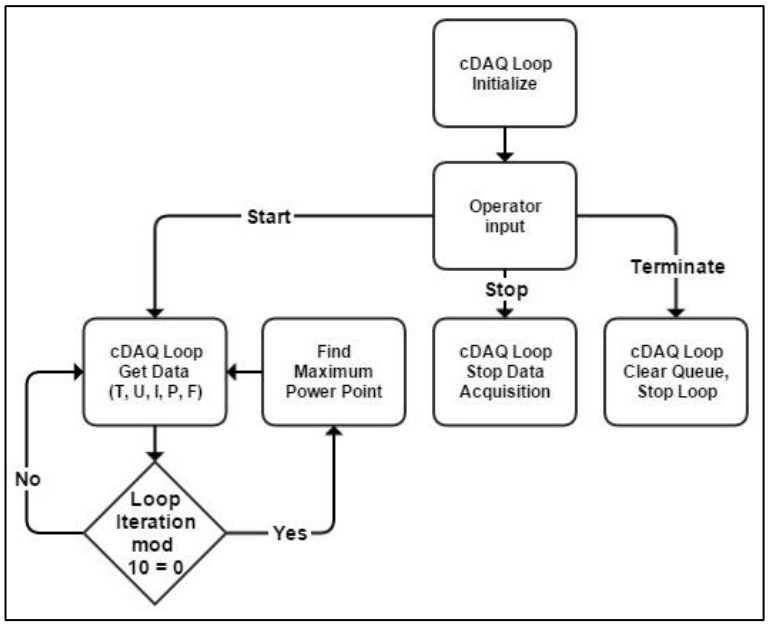

Figure 5.17. Generalised flow diagram of the cDAQ loop.

Once started, the cDAQ loop VI loads the front panel control and indicator refnums, initiates the cDAQ queue and three tasks, which are outside the While loop: (1) NI 9219–NI 9213 task for continuous data acquisition from all channels of NI 9219 and NI 9213 modules with high resolution timing modes, reading one sample per channel, and ±15 V range for NI 9219 module; (2) NI 9219–NI 9213 task for QS MPPT data acquisition for NI 9219 module voltage (1) and NI 9263 output (3) channels, and NI 9213 electronic load current shunt channels (13, 14) with high speed timing mode, multiple samples per channel, and 100 samples per second sampling rate; (3) NI 9263 task for Electronic Load control during the QS MPPT with 10 kS/s sampling rate, and 0 V to 10 V range. Once created, the tasks remain in memory until the While loop is stopped and the clear task VIs execute.

The sample count for the QS MPPT tasks is determined during the QS MPPT case run by the Power Scan Waveform Generator VI. The Power Scan Waveform Generator VI generates the NI 9263 module output waveform for a series of the Electronic load set points. The waveform is created using user inputs such as Start Current, Maximum Amplitude, and Number of Swings. The waveform starts with the Starting Current value, changes the current setting to increase and then decrease the current setting for a Number of Swings times, monotonically increasing in amplitude with the last swing being the Maximum Amplitude value. Finally, 30 ms of the Start

Current are added to each end of the waveform. The count of points read per scan is 6 plus the Number of Swings times two. Optional features of the Power Scan Waveform Generator VI are the ability to spread the current swings apart by inserting some waveform set points with the Start Current value, and the possibility to make the swing amplitude not monotonically increasing, but randomised.

The NI 9263 output, the electronic load set points, and the NI 9219 and NI 9213 data acquisition have to be in perfect synchronisation. Unfortunately, the Compact DAQ systems do not have the hardware synchronisation. The data acquisition is triggered by the NI 9263 module analog output. Even though the rates match, the AO and AI are not synchronous. Therefore, waveform offset parameter was introduced to shift the waveform by a number of NI 9263 samples. The amount of shift for a perfect write and read synchronisation was experimentally determined to be -20 samples, which is 2 ms.

The cDAQ loop iterates the Get Data case once per second. The acquired data is processed and stored in the cDAQ Data Array FGV. The electronic load set points are set using the Set NI9263 FGV. The big information label on the front panel will change its text color to random upon every cDAQ loop Get Data case iteration to indicate that the software is running. When the QS MPPT toggle is switched on, and the Get Data case reaches the number of iterations defined by the operator, e.g. 10, the cDAQ queue will be enqueued not with the Get Data, but with the QS MPPT element. As it has been explained in the NI DAQ Tasks section, if a task runs, it reserves the resources and keeps them reserved. Since the data acquisition physical channels are shared between the Get Data and QS MPPT cases, but have different rates and timing modes, the resources have to be unreserved before the switch between the two cases and tasks. Likewise, the NI 9263 resources have to be unreserved before running the task in a different case. This is done using the DAQmx Control Task VI from the DAQmx functions palette, which gives access to the task state machine state selection. Upon completion, the QS MPPT case unreserves the tasks, and enqueues the cDAQ queue with the Get Data element.

The QS MPPT scan data is mathematically fitted using the MPPT Fit VI. Then, if the fitting is successful, the data is stored in the MPPT Scan Data FGV. The mathematical fitting results are used to update the QS MPPT Start Current and Amplitude control values on the front panel.

5.6.3 Save Loop

The Save loop coordinates loading and saving of the front panel control values on the program start up and close respectively. Additionally, it controls saving the tables of the acquired data. Finally, it manages module and reference block parameter loading during program initialisation and their manipulation during the program run.

During the first run the loop sets the working directory to */Parameters/ for accessing the saved front panel control values, data file headers, module parameters, and reference block parameters. Likewise, it sets the directory for the acquired data to */Data/. Moreover, front panel control refnums are loaded and the Save queue is created.

The first queue elements the Save loop receives are to load the module parameters, the reference block parameters, and the data file headers to their respective FGVs, then to load the front panel control values straight into the controls. During the program run the Save loop will receive queue elements when the operator clicks on the Save, or Delete buttons for modules and reference blocks, and queue elements to save the data tables from the cDAQ loop. Data file header editor is not available yet. The Data file headers can only be edited by opening the Data File Headers.ini file in the */Parameters/ directory. Upon receiving a Stop queue element the Save loop saves the data tables and the front panel control values, then stops the While loop.

5.6.4 Graph Loop

The Graph loop handles the information output to the front panel matters. The graph loop streams the available live data to the indicators on the front panel, plots the temperature distribution along the hot side reference block–TEG module–cold side reference block stack, and finally plots all the acquired data versus time, while the operator can select what data is displayed on the graph.

The last row in the cDAQ Data Array FGV is read and written to the front panel indicators for Current time, Module voltage, Module Current, Module temperature gradient, Module hot and colt side temperatures, Module resistance, Module compression force, Module heat flow, Efficiency, etc. The temperature distribution graph is created using the Calc TC Positions VI, which uses the reference block and the TEG module geometrical parameters, selected or defined in the settings tab, to calculate the thermocouple positions along the heat flow path. The data plotting versus time is done using the 2DArray to XYGraph VI, which takes the first column from the cDAQ Data Array FGV data table, which contains timestamps of every measurement taken, as X–axis values, then bundles the first data column with every other data column from the 2D data table creating a 1D array of bundles of (1D arrays of timestamps and 1D arrays of data). In the current software version all the data is prepared for display in the graph, but this isn't the most efficient way to do this because it effectively triples the memory usage and increases processor load. This may become noticeable as a computer lag when the data set becomes large, if a measurement takes longer than 12 hours. The best solution to this issue would be instead of having all the available data ready for viewing, prepare only the portion of data that is requested by the operator because typically only 1 to 8 plots are viewed at a time. Additionally, the graph update time interval could be increased.

6 CHARACTERISATION OF TEG MODULES

6.1 TEHP1-12656-0.3 TEG Module Measurements

The following procedure was used for measurement and characterisation of Thermonamic TEHP1-12656-0.3 TEG module, consisting of 126 p- and n-type TE material leg pairs. The heater was moved to the top of the instrument and secured using the fixing pins. The cold side reference block was centered onto the cooler plate minding the correct thermocouple positions. The type of reference block used was defined in the control software settings tab. The module has graphite foil attached on both sides, therefore, no additional thermal interface material was needed. The TEG module was centered on top of the cold side reference block and pressed down with the top reference block. In this case the TEG module hot side was marked and its wires were color coded. Module wires were connected to the color coded feedthrough terminals. Heater was carefully lowered and fixed in to a position closest to the hot side reference block. Hydraulic pump was used to extend the hydraulic ram piston and move the cooler plate up towards the heater. Once the hot side reference block touched the heater, the hydraulic system was pressurised to achieve 10 kg/cm^2 pressure on the module. Hydraulic pump needle valve was closed to lock in the pressure value. Cooling water flow rate was set to 600 cm^3/min. A thin film of vacuum grease was applied to the bottom of the bell jar L–ring. The bell jar was lowered onto the baseplate. Vacuum pump was switched on and the Argon purge valve was opened until pressure settled at approximately $1x10^{-1}$ mBar. Data acquisition was then initiated.

The heater temperature was ramped at 1 K/min rate till the TEG module hot side reached 603 K, which is the maximum temperature the module can operate safely. Such a slow heating rate results in a less than 0.2 K/min temperature change rate in the cold side reference block, which is generally considered being the steady state. Two runs were made: one measuring the module open circuit characteristics, and second measurement with the MPP tracking enabled.

TEG module hot (Th) and cold (Tc) side temperatures are plotted versus their resultant temperature gradient (Figure 6.1). The rest of the data is plotted against the module temperature gradient and the corresponding Th and Tc can be found using Figure 6.1. When module manufacturer provided data is plotted, the required temperature gradient respective Th and Tc values are used to lookup the data points in the datasheet. When the data point count is more than 2000, the plots are shown as lines with no data point markers.

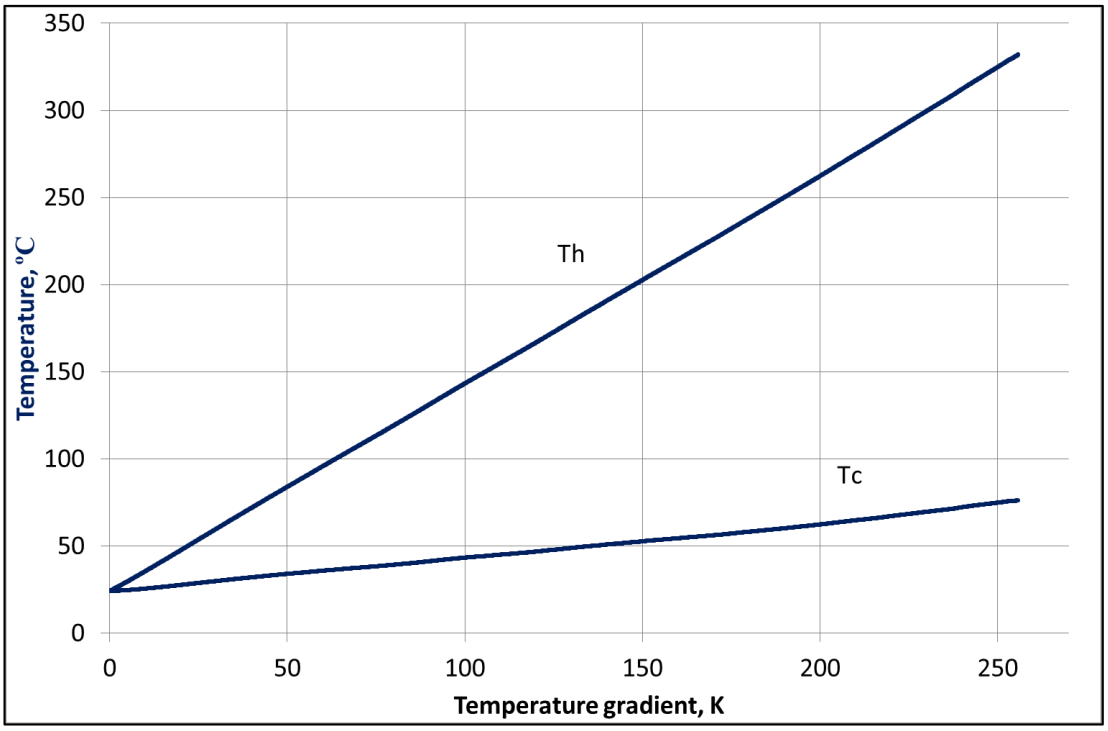

Figure 6.1. TEHP1-12656-0.3 module hot side temperature (Th) and cold side temperature (Tc) correlations with module thermal gradient (DT).

Data acquisition takes place at 1 s time intervals. When the MPPT is enabled, normal data acquisition will continue for a predetermined number of seconds, e.g. 5 s, then the acquisition hardware will reconfigure for high speed data collection, record the module voltage–current and power–current curves, find the MPP current, reconfigure the data acquisition hardware for high resolution mode, set the new MPP current and repeat this sequence until MPPT is switched off or the data acquisition is stopped.

The measured TEHP1-12656-0.3 module performance data is plotted starting with Figure 6.1 through to Figure 6.8. Where applicable, data values provided in the

manufacturer's datasheet are plotted together with the measured data [124]. The measured TEG module open circuit voltage (Voc), QS MPPT algorithm predicted Voc, and literature data is compared in Figure 6.2. Measured Voc agrees with the manufacturer's data very well up to 200 K temperature gradient. However, the QS MPPT algorithm predicted Voc values are lower than the measured values with a constant proportionality factor of 0.93. This measured and QS MPPT predicted data mismatch is referred to as the ceramic plate effect. As seen in Figure 6.3, the QS MPPT algorithm current matches the values of the MPP data provided by the module manufacturer. Furthermore, measured maximum power values are in a good agreement with the literature MPP values (Figure 6.4).

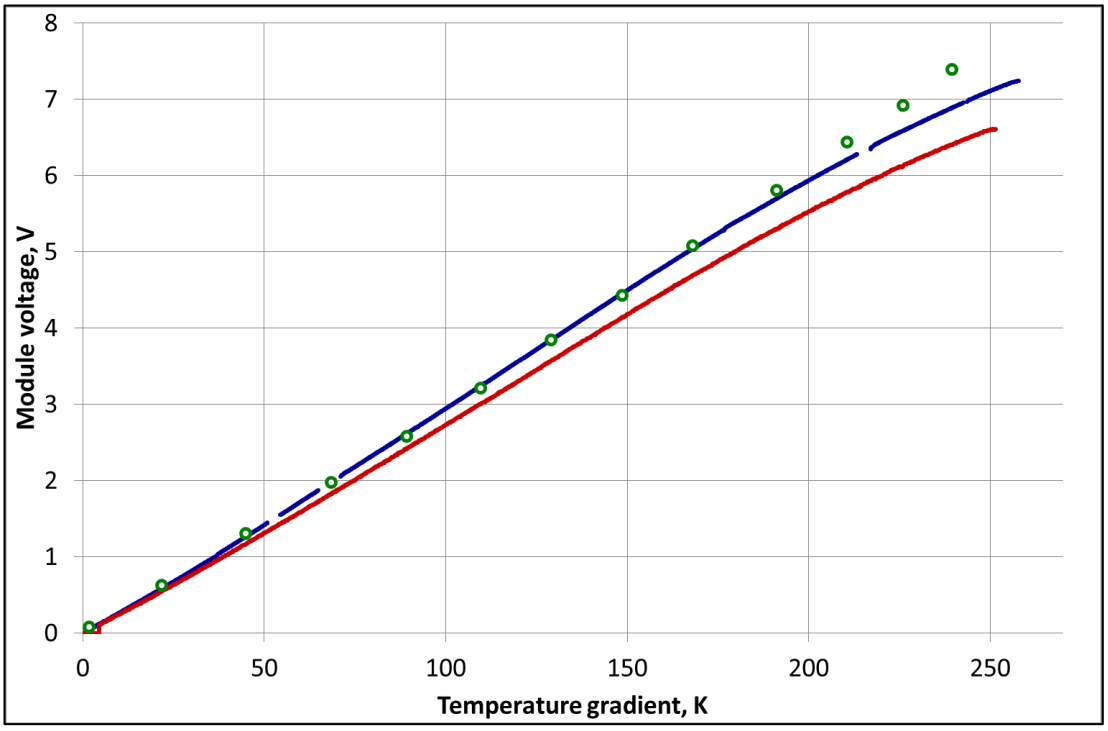

Figure 6.2. TEHP1-12656-0.3 module open circuit voltage (Voc) (blue line), MPPT algorithm predicted open circuit voltage (red line), and manufacturer's Voc data (green circles) dependences on module temperature gradient.

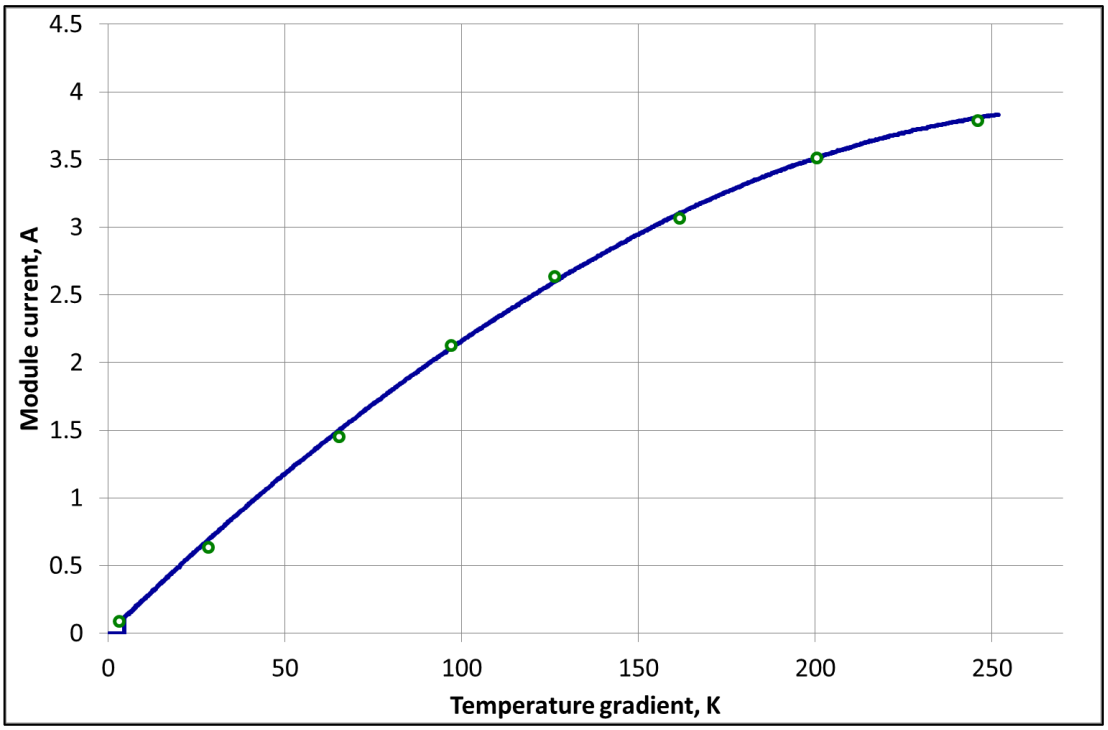

Figure 6.3. TEHP1-12656-0.3 module MPPT algorithm current (blue line) and module manufacturer's MPP current data (green circles).

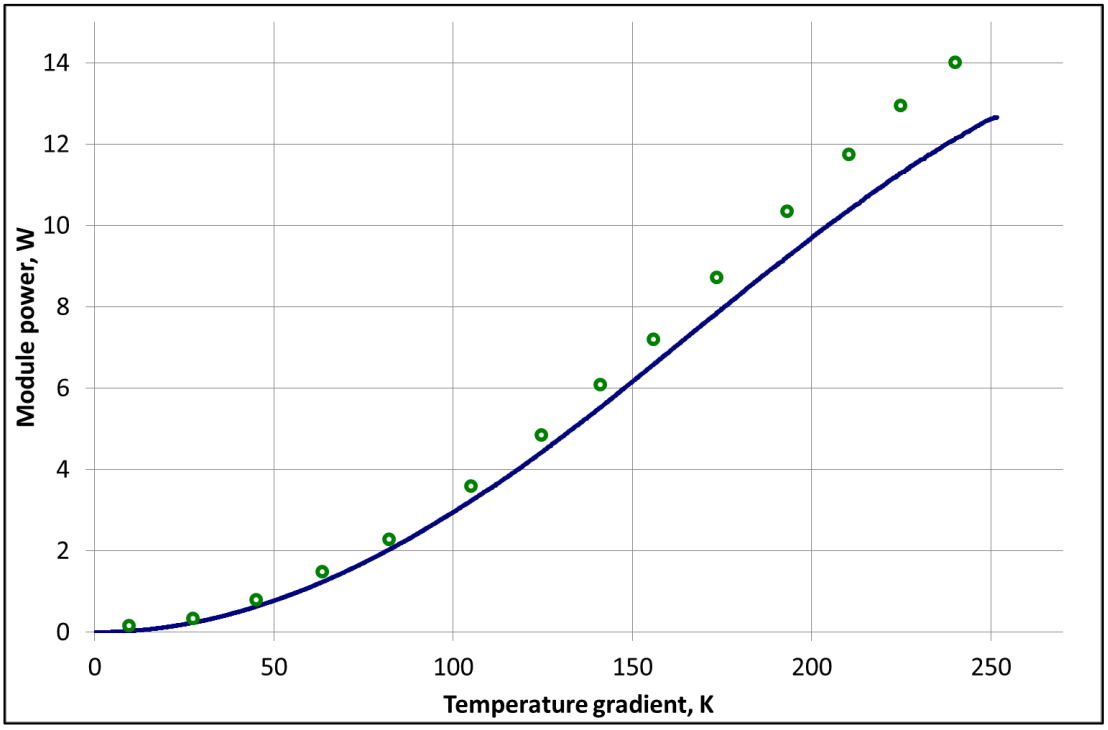

Figure 6.4. Electrical power generated by the TEHP1-12656-0.3 module dependence on module temperature gradient. Blue line is measured values, green circles are manufacturer's data.

TEHP1-12656-0.3 module's resistance measurements are summarised in Figure 6.5. QS MPPT algorithm measured module resistance values are compared to the ones calculated using the conventional voltage–current curve. Additionally, module resistance values from the module manufacturer's datasheet are shown. Lastly, for comparison reasons, module resistance values calculated from the voltage–current relations provided in the manufacturer's datasheet are plotted.

The TEG module resistance values calculated from the conventional V–I curves are overestimated due to the ceramic plate effect. Module's resistance values taken straight from the module's datasheet appeared suspicious having seen the voltage and current characteristics in the datasheet. Therefore, module's resistance was calculated using voltage and current characteristics provided in the datasheet and was compared with the published data. The two sets of the datasheet resistance values agree well above 100 K temperature gradient. Moreover, module's electrical resistance data measured using conventional V–I curve method agrees well with the values given in the module's datasheet. This indicates that the manufacturer's data was obtained using a conventional V–I curve method, which is incorrect, because it is influenced by the CPE. Meanwhile the QS MPPT algorithm resistance measurements are not affected by the CPE and provide the true module resistance values.

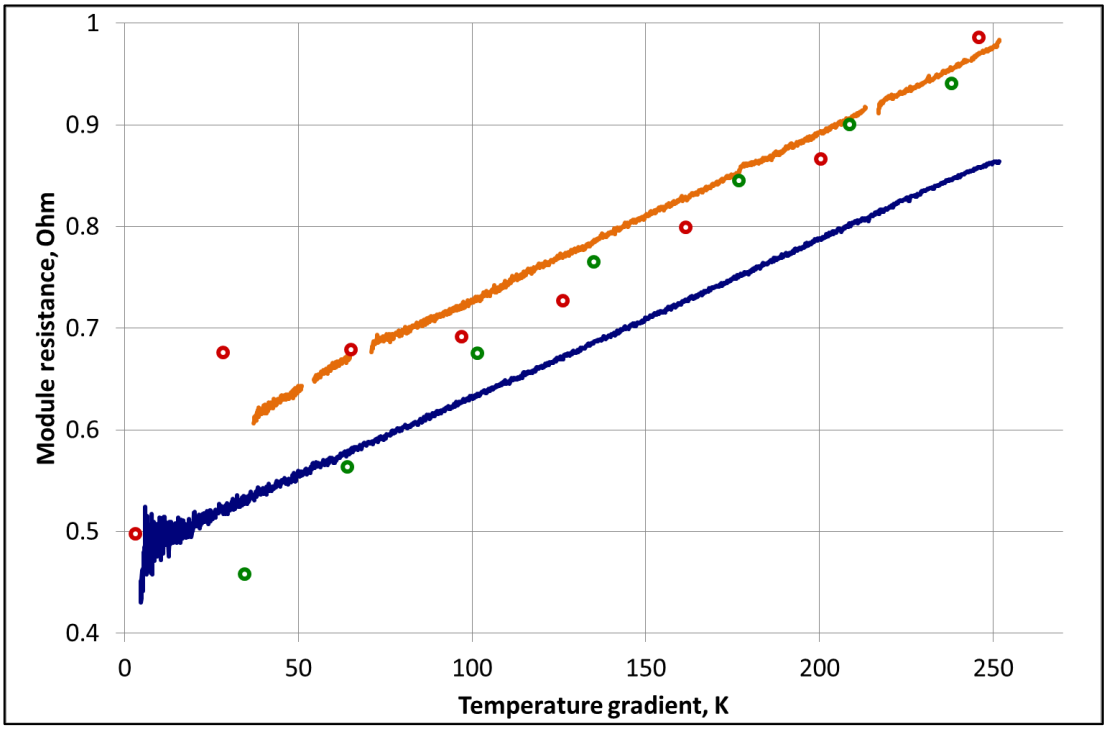

Figure 6.5. TEHP1-12656-0.3 module resistance measured by the MPPT algorithm (blue line), the manufacturer's data (green circles), module resistance values calculated using voltage and current data from the module datasheet (red circles), and the module resistance values calculated from conventional voltage–current curves (orange line).

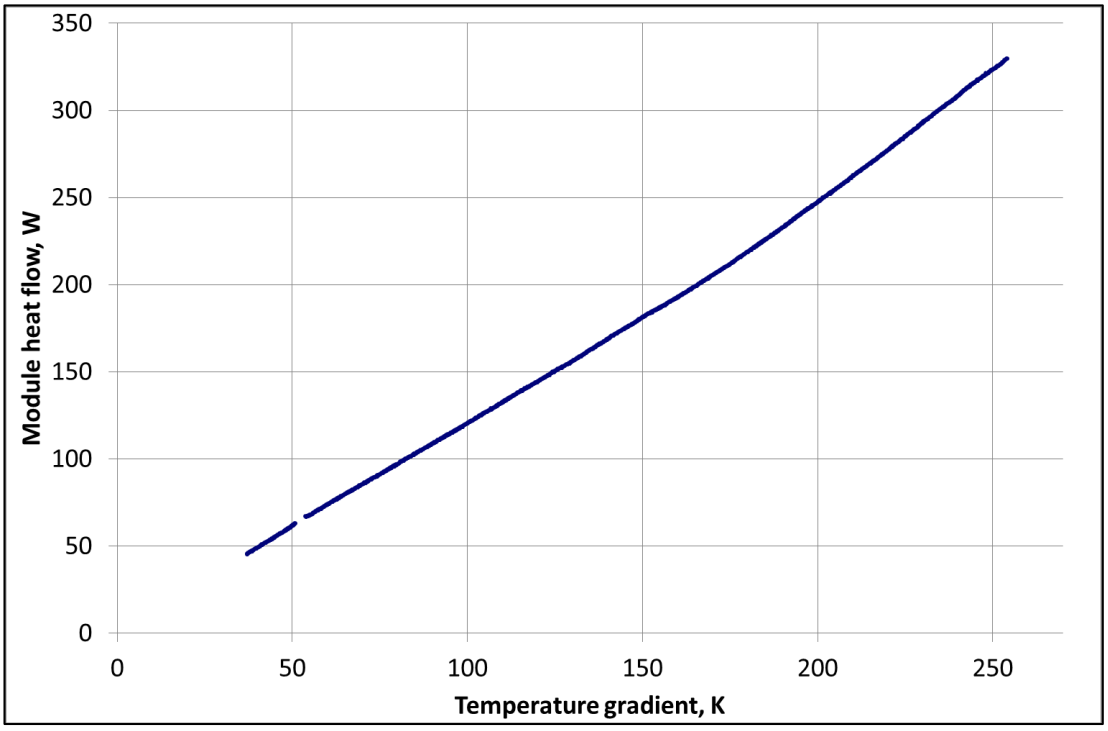

Figure 6.6. TEHP1-12656-0.3 module TEG module open circuit heat flow (Qoc), dependence on module temperature gradient.

The TEG module's open circuit heat flow measurement using the cold side reference block data is shown in Figure 6.6. This heat flow data is used to calculate the TEG module efficiency using Equation 2.13, and the dimensionless Figure of Merit using Equation 2.14. The measured TEHP1-12656-0.3 module efficiency is plotted in Figure 6.7 together with the module efficiency from the manufacturer's datasheet. TEG module's efficiency data values found in literature are higher than the measured ones. We argue that the main contributor to the discrepancy between measured and literature data is the overestimation of the module's heat flow, which might be attributed to the use of literature thermal conductivity data rather than measured data for the reference block heat flow calculations. Certainly, the use of copper reference block thermal conductivity values obtained by calibration would be a more appropriate practice, but the calibration of the Cu reference blocks is yet to be done.

The dependence of module's dimensionless Figure of Merit on temperature gradient is shown in Figure 6.8. It is possible that the ZT values are underestimated similarly to the efficiency data, because an overestimation of module heat flow would result in higher than actual module thermal conductance, which in turn would lower the resulting ZT.

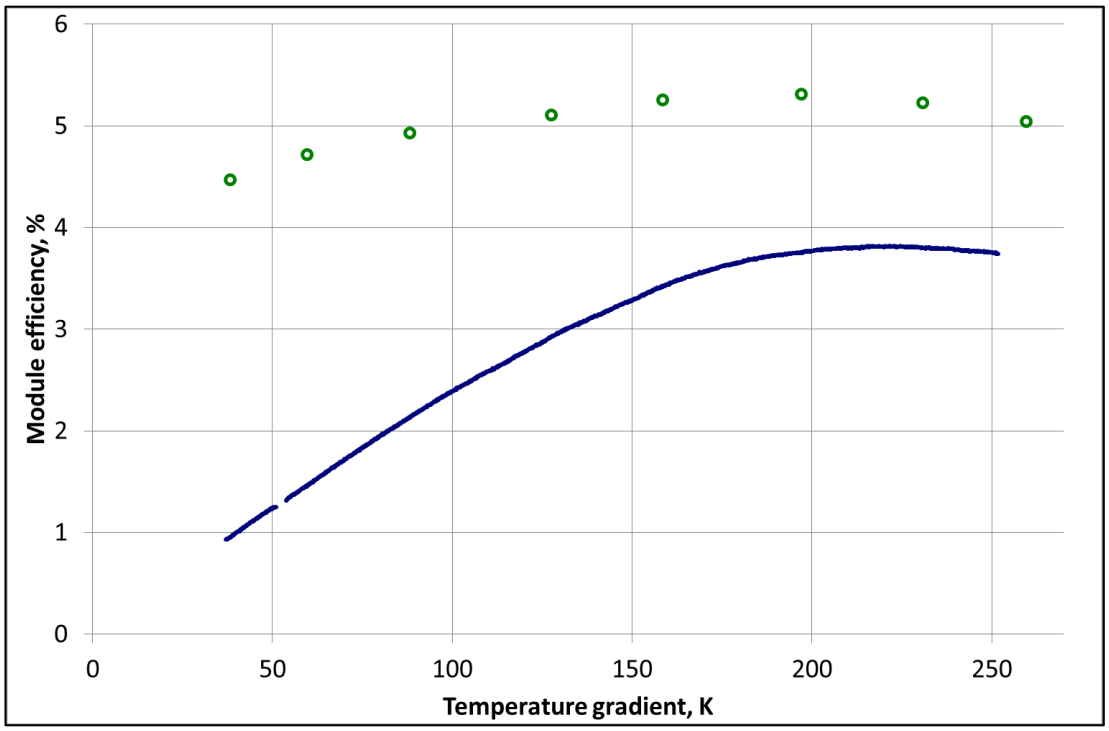

Figure 6.7. TEHP1-12656-0.3 module efficiency dependence on module temperature gradient. Blue line is measured values, green circles are manufacturer's data values.

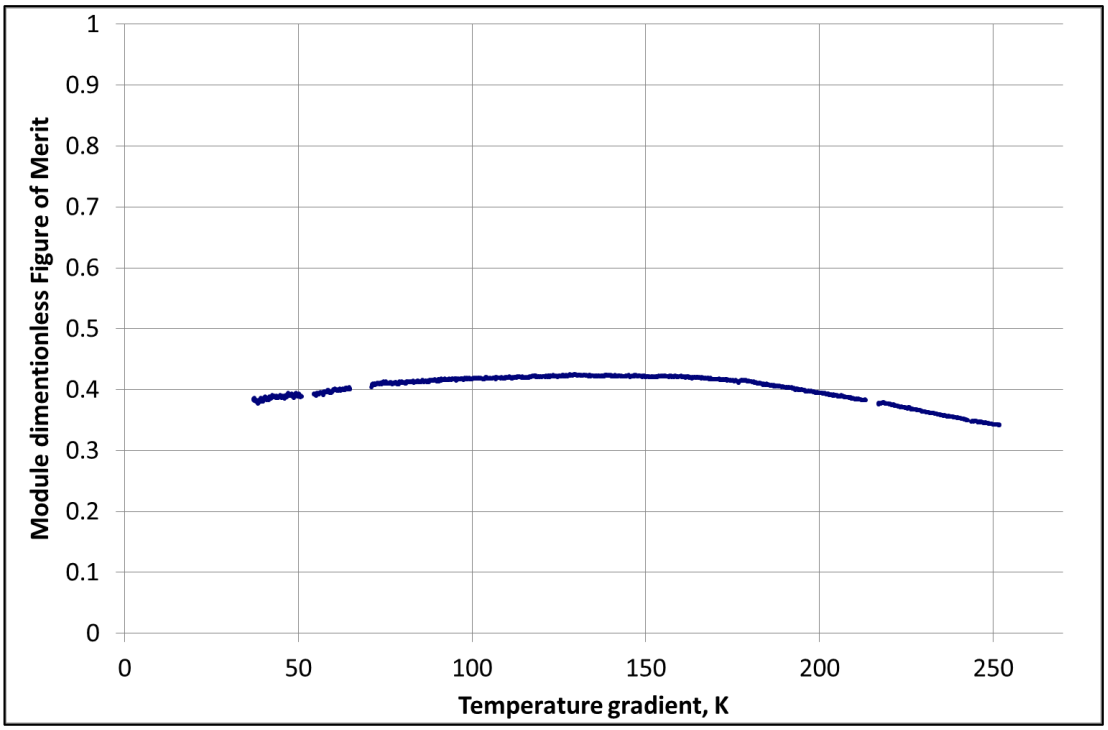

Figure 6.8. TEHP1-12656-0.3 module dimensionless Figure of Merit (ZT) dependence on the module temperature gradient.

After the measurements have finished, the TEHP1-12656-0.3 module has been taken out of the measurement system. Actually, the reference block and the module stack was taken out in one piece because of a strong graphite foil adhesion to the copper reference blocks under the compression. Unfortunately, the hot side ceramic plate has separated from the rest of the module while trying to detach the reference blocks (Figure 6.9). The ceramic plate seemed to be held in place by just a layer of thermal interface material paste and silicone sealant around the perimeter of the module. The graphite foil pieces stuck to the copper blocks could only be removed using a sharp blade and sandpaper. The internal module workings were not affected by the removal of the hot side ceramic plate and the module could still be used with the plate put back on.

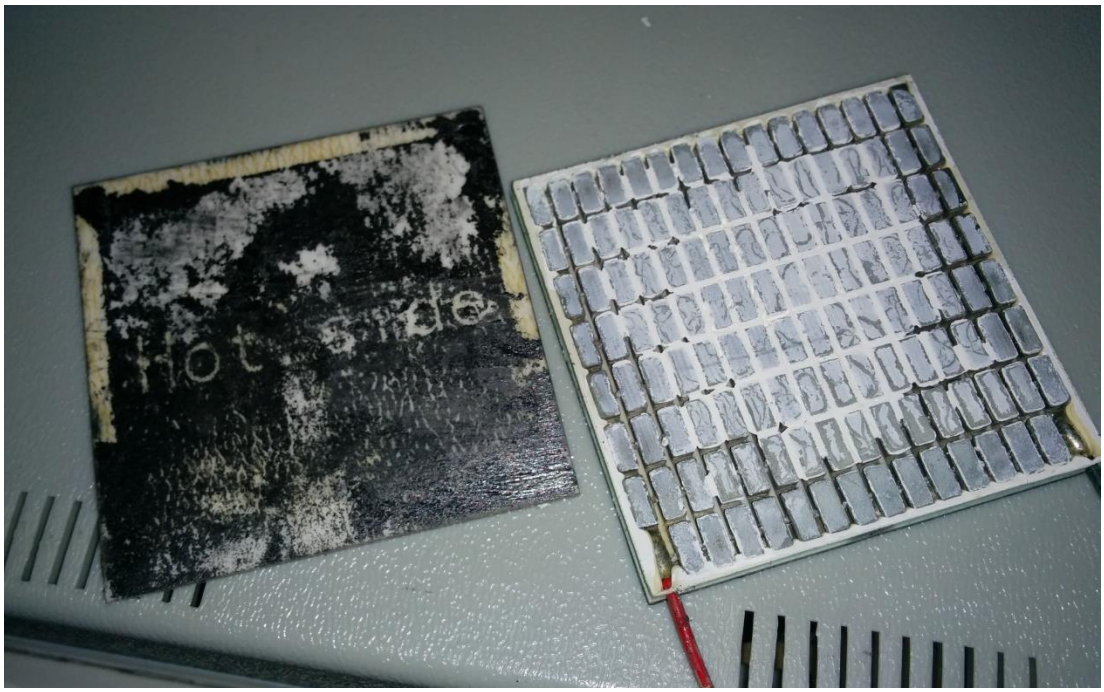

Figure 6.9. TEHP1-12656-0.3 module after it has been taken out of the measurement system.

6.2 TEG127-50D Module Measurements

The Ieverred TEG127-50D TEG module, consisting of 127 p- and n-type TE material leg pairs, was mounted into the measurement sytem using the same procedure as described for the TEHP1-12656-0.3 module, except for the module compression force and thermal interface material. While the TEHP1-12656-0.3 module comes lined with graphite foil, the TEG127-50D module comes naked, without any thermal interface material pre–applied. For this reason, two 0.127 mm thick graphite layers were placed between the module ceramic plate and the copper reference blocks to reduce thermal interface resistance. The module compression force was varied throughout the measurement from 250 kg to 1000 kg. The module maximum temperature was limited to 473 K due to the type of solder used in the manufacturing of the module. Three scanning measurement runs were done at different electrical conditions: open circuit, QS MPPT, and short circuit.

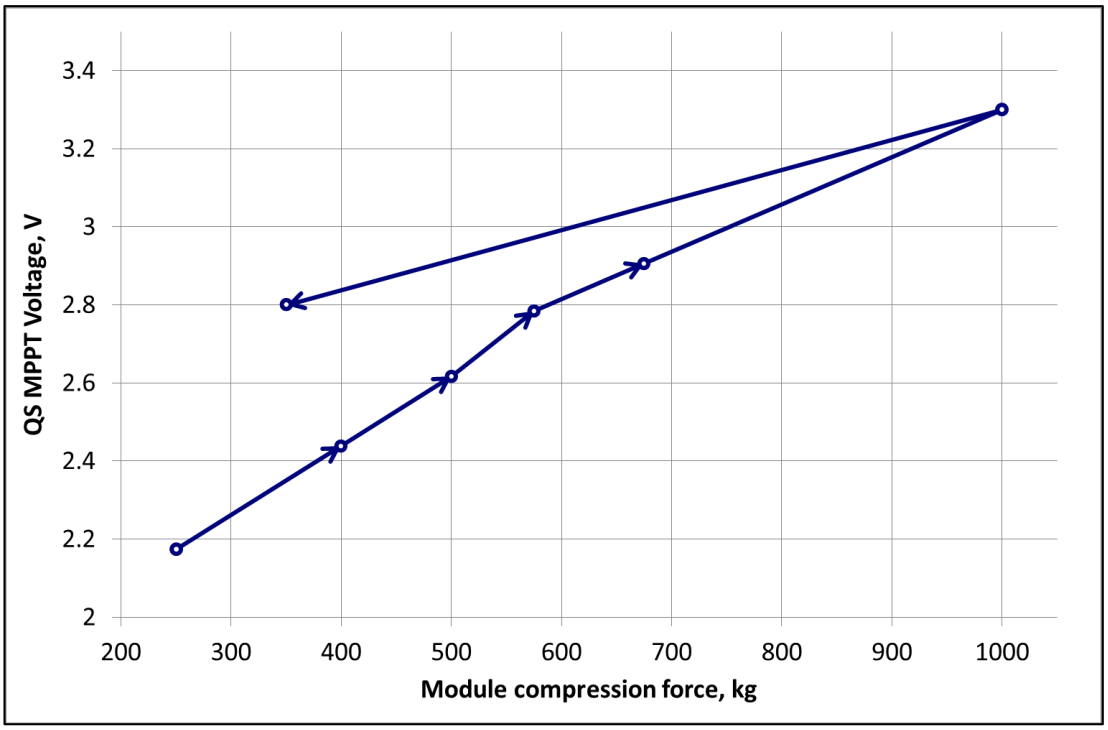

Figure 6.10. TEG127-50D TEG module QS MPPT voltage dependence on the module compression force.

Typically, the clamping pressure recommended by the manufacturers is approximately 10 – 15 kg/cm^2. In this test the clamping pressure was gradually increased from 10 kg/cm^2 to 40 kg/cm^2, and then decreased to the typical for applications – 14 kg/cm^2. This was done in order to find the best clamping pressure for the module's operation. The QS MPPT voltage for the module steadily increases with increasing compression force. Even with one tonne of weight placed on the module, it seems to be able to generate more power if more weight was added. On the other hand, a uniform compression force of such a magnitude would be difficult to achieve in practical applications.

The reason for the dependence of module's performance on compression force is the thermal resistance of the contact between two heat conducting bodies. Due to the surface roughness, which is always present, the two bodies are present only in a partial contact. The contact points conduct the heat well, but the voids filled with gas or vacuum obstruct the heat flow as illustrated in Figure 6.11. Interfacial

conductance is a quantity used to characterise the heat flow through a two solid body contact plane. Ceramic material surface contacts typically have much smaller interfacial conductance when compared to metal surfaces because of the characteristic porosity, surface roughness and rigidity. Typical value for ceramic–metal interfacial conductance is approximately 1500 W/m^2K [125], which, for the TEG127-50D module and typical compression force, corresponds to 0.27 K/W temperature drop on both sides of the module just over the ceramic plate and reference block contact plane.

Typically, the interfacial conductance is increased by using thermal interface materials. While any material filling the interfacial gaps would result in impoved interfacial conductance, graphite is is well known to be one of the best materials for this purpoce. Figure 6.10 shows the TEG module QS MPPT voltage dependence on the module with applied compression force. The module performance gets better with the increasing compression as the graphite foil deforms plastically and elastically and the interfacial conductance is improved. After the compression force is reduced, only the elastic deformations are reversed, whereas the plastic deformations remain to aid in thermal conductance.

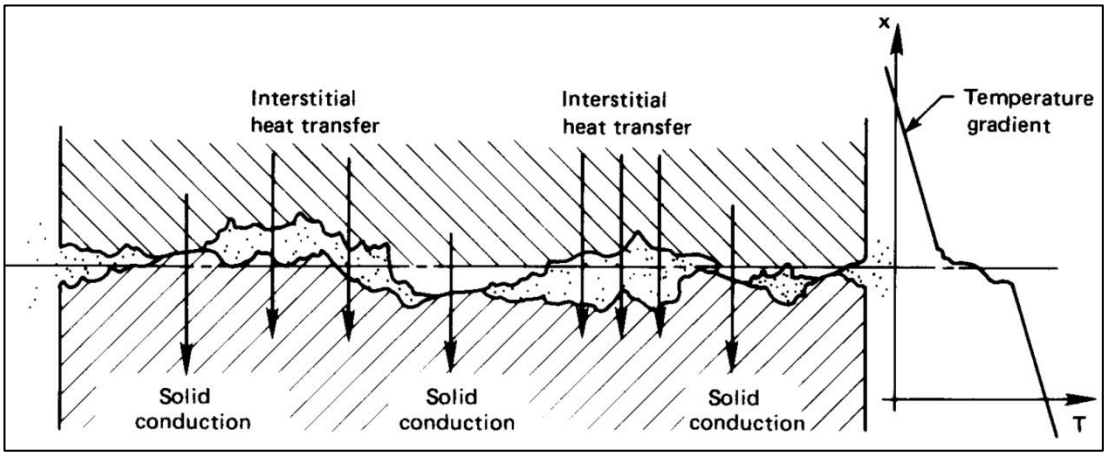

Figure 6.11. Heat transfer through a contact plane between two solid bodies [125].

Analogously to TEHP1-12656-0.3 module performance data, the TEG127-50D module performance data is plotted versus the module temperature gradient. All plots

compare data acquired with 350 kg and 1000 kg module compression force. Corresponding hot (Th) and cold (Tc) side temperatures can be found in Figure 6.13. Literature data available for the TEG127-50D module is very limited and it all is show in Figure 6.12. The original literature data is presented in a rather obscure format. Nevertheless, it was digitised and presented in an explicit format. Despite doing that, the data values still appear to be of questionable genuineness. The data seems to be mathematically generated using 0.52 Ohm value for module resistance and 50 mV/K Seebeck coefficient, which may be true values, but such a simple mathematical prediction disregards their dependence on the temperature and ceramic plate effects. Ultimately, only these two values at room temperature are compared to the measured data.

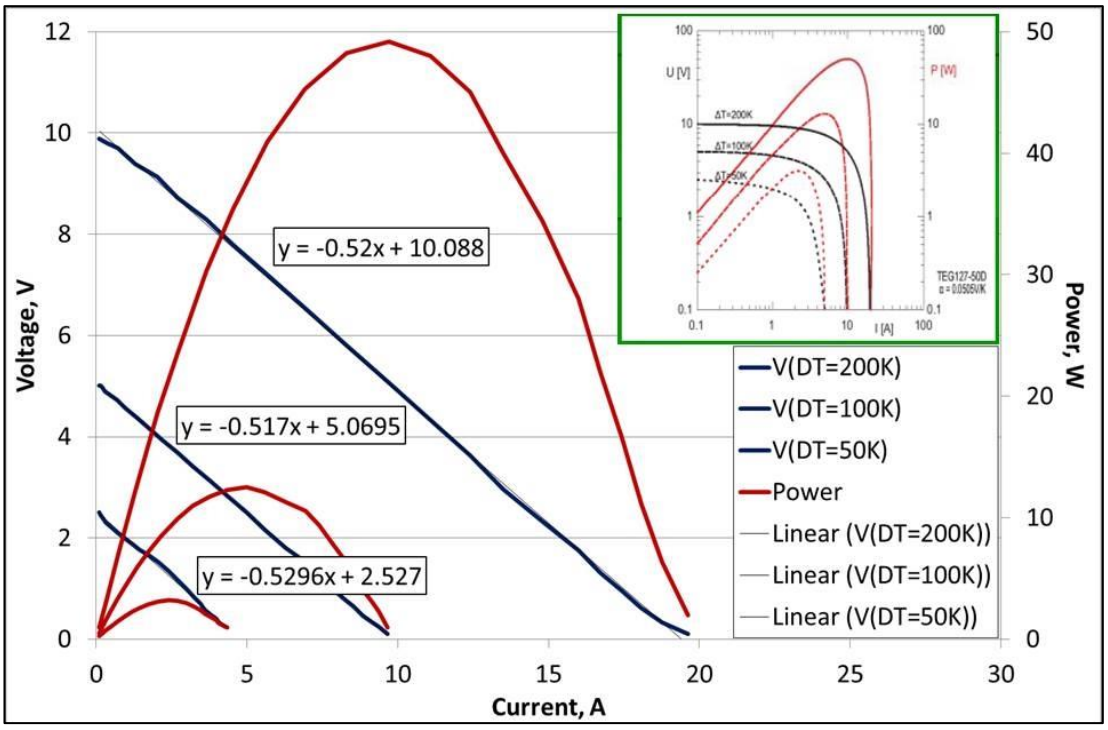

Figure 6.12. Digitised literature data for TEG127-50D module. Original data is show in the insert [126].

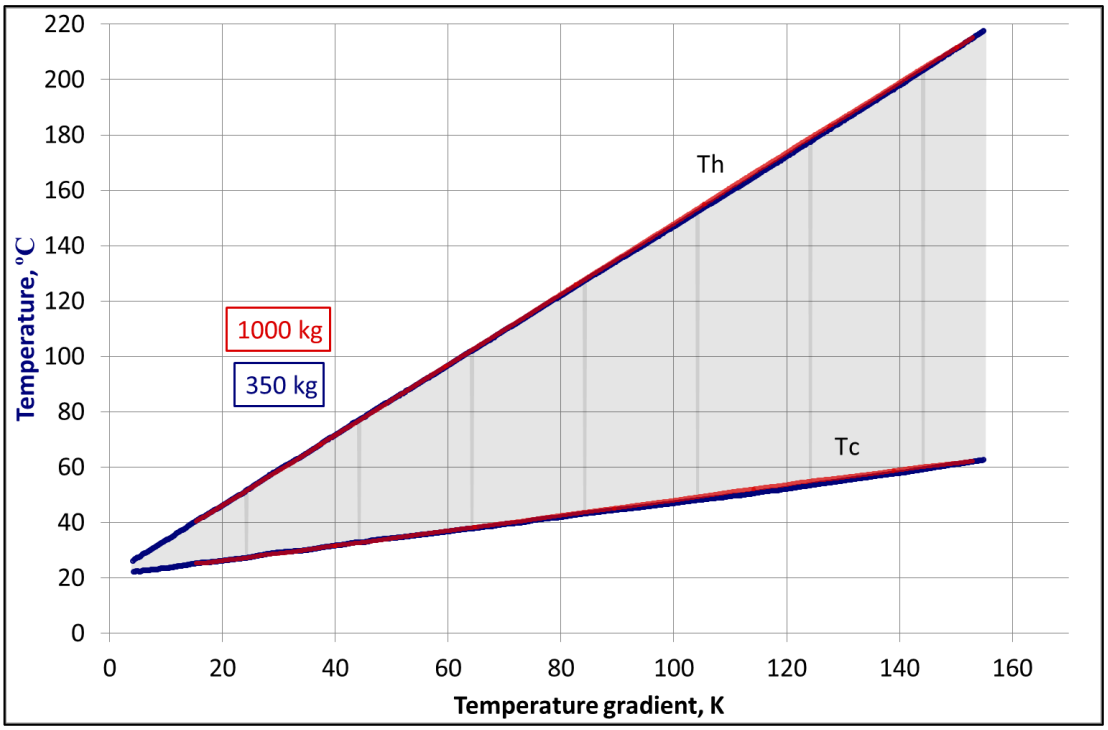

Figure 6.13. TEG127-50D module hot side temperature (Th) and cold side temperature (Tc) correlations with module thermal gradient (DT).

TEG127-50D module open circuit voltage (Voc) dependence on the module temperature gradient is shown in Figure 6.14. Together with the Voc, the QS MPPT algorithm predicted Voc(mpp) and QS MPP voltages are shown. The Voc(mpp) values are as expected lower than the Voc values due to the ceramic plate effect. Approximate measured Seebeck Coefficients for the TEG127-50D module are 35.4 mV/K and 40.6 mV/K for 350 kg and 1000 kg compression force, respectively. Meanwhile, the module's Seebeck Coefficient given in the literature is approximately 50 mV/K. It is likely to be similar to the measured values if adjusted for the ceramic plate effect. The temperature drop over the ceramic plates, calculated using typical material physical property data, can amount to roughly 10 % of the module's temperature gradient. In addition, the interfacial thermal resistances should be added, but unfortunately they are not known.

The module short circuit current (Isc) and MPP current (Impp) data is plotted in Figure 6.15. The module maximum power tracked by the QS MPPT algorithm is plotted in Figure 6.16. Unfortunately, no suitable literature data was found that could be compared with our results.

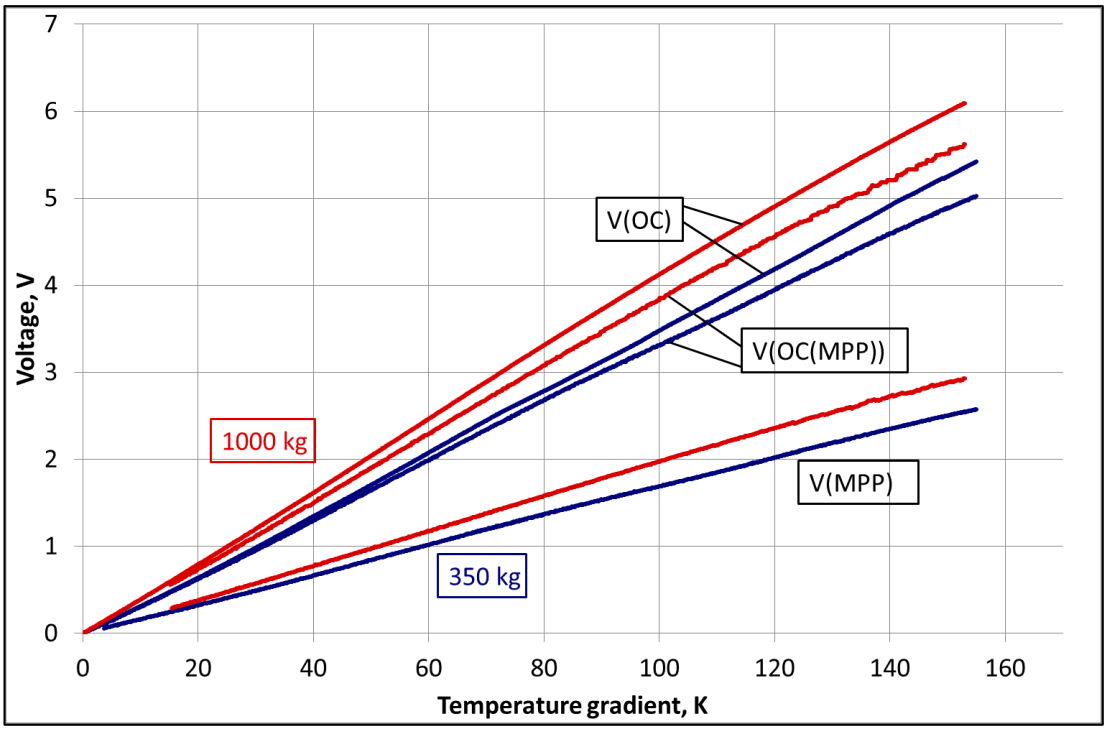

Figure 6.14. TEG127-50D module open circuit voltage (Voc), MPP voltage (Vmpp), and QS MPPT algorithm predicted open circuit voltage (Voc(mpp)) dependences on module temperature gradient.

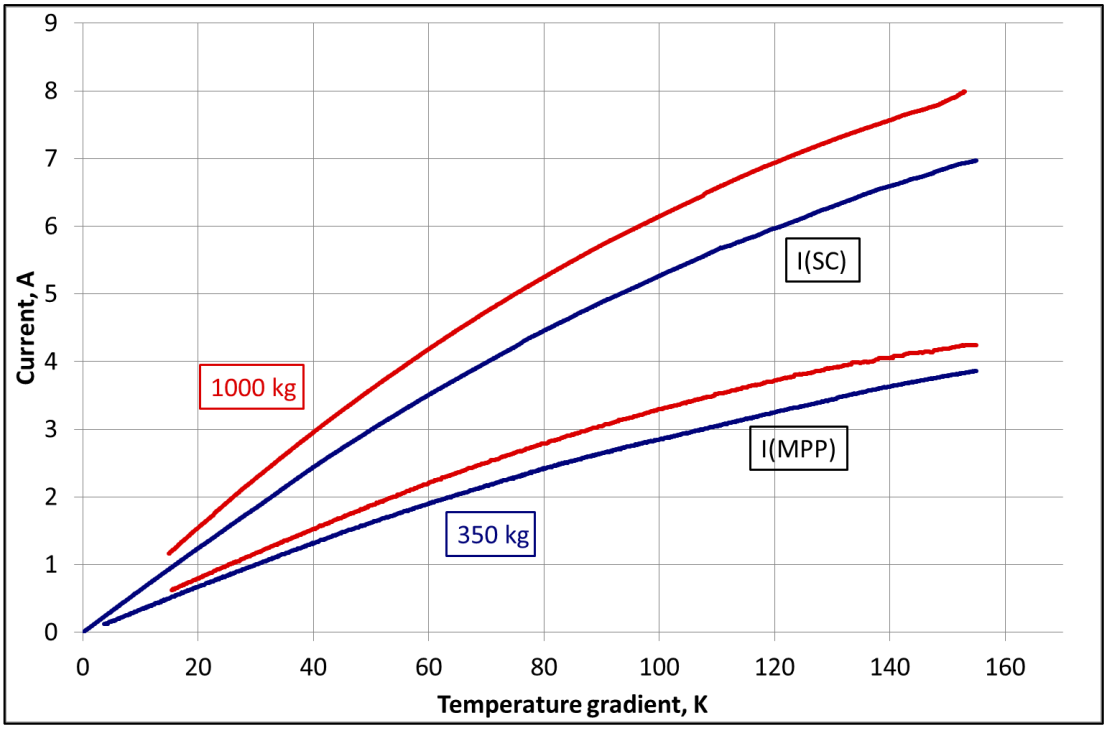

Figure 6.15. TEG127-50D module short circuit current (Isc) and MPP current (Impp) dependences on module temperature gradient.

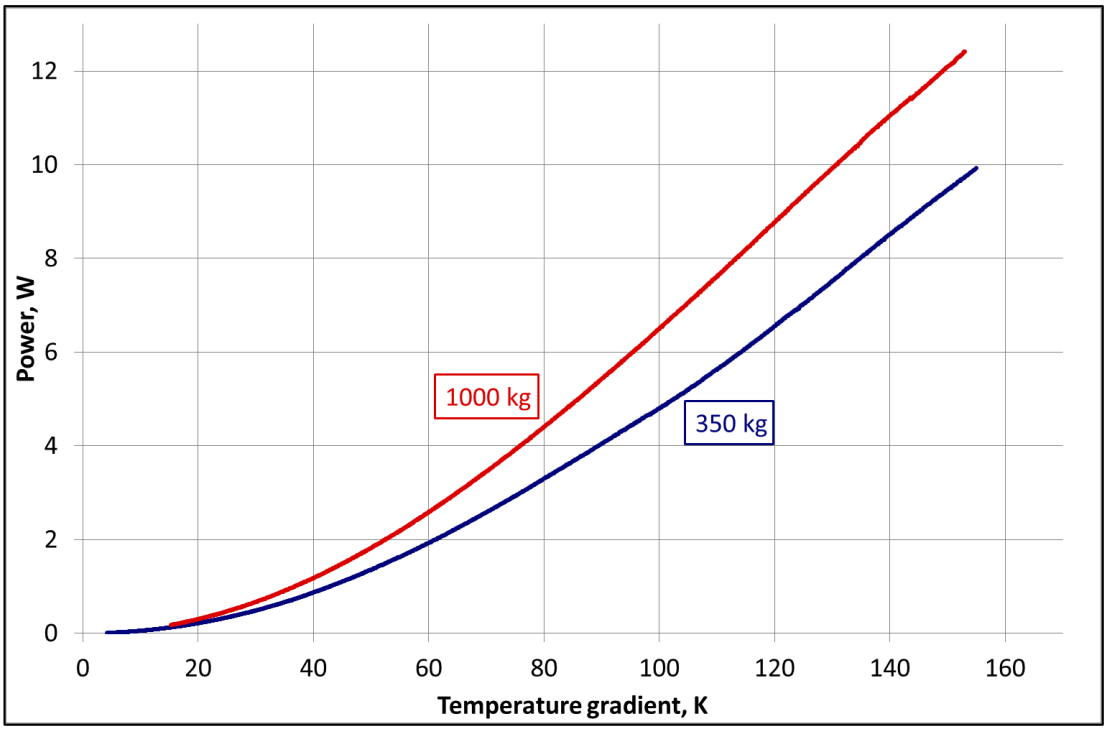

Figure 6.16. Electrical power generated by TEG127-50D module dependence on module temperature gradient.

TEG127-50D module resistance measurements are plotted in Figure 6.17. As seen in the plots, the module electrical resistance does not depend on the module compression force. Module resistance measured using conventionally measured V–I curve is overestimated due to the ceramic plate effect. TEG module ressitance extrapolated to room temperature is approximately 0.42 Ohm. TEG module resistance found in literature is 0.52 Ohm, however, it is not known what method was used to measure it, nor it is known at which the temperature it was measured. Even so, the two module resistance values are very close, and therefore considered to be in a good agreement.

TEG module heat flow depends on the electrical current flowing through it. From the applications point of view, information on the module heat flow is of great value. Figure 6.18 shows the heat flow of the TEG module for open circuit, QS MPPT, and short circuit states. Effectively, maximum and minimum possible module heat flow values, and most likely heat flow during module operation are shown, depending on the applied temperature gradient.

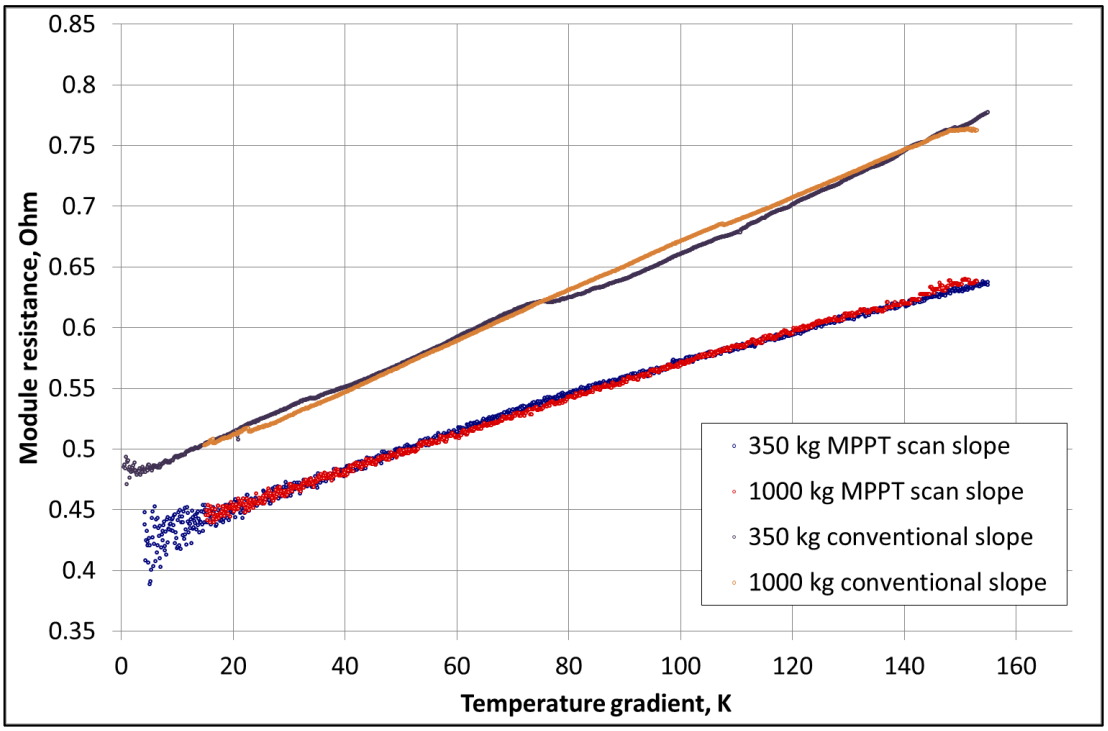

Figure 6.17. Comparison of TEG127-50D module resistances measured by the QS MPPT algorithm and the conventional V-I slope methods.

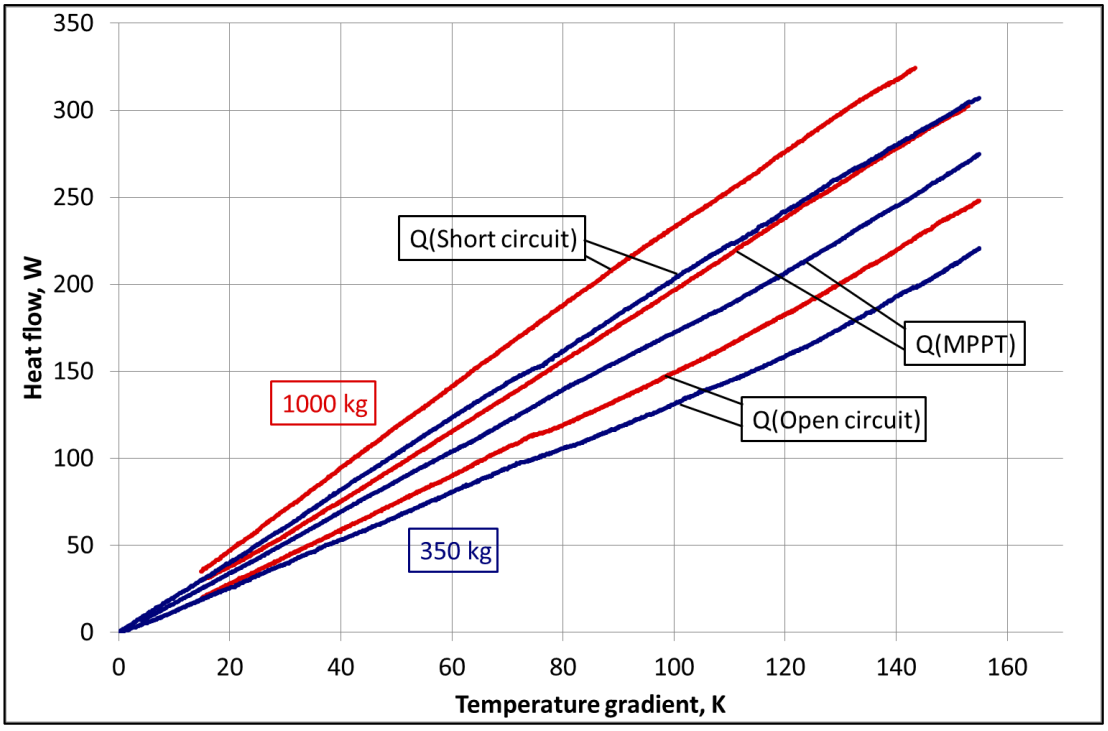

Figure 6.18. TEG127-50D module open circuit heat flow (Qoc), QS MPPT heat flow (Qmpp), and short circuit heat flow (Qsc) dependences on module temperature gradient.

TEG127-50D module efficiency dependence on the module's temperature gradient is shown in Figure 6.19. No literature data is available for comparison, but the measured module efficiency is compared with an estimated module efficiency calculated using the module dimensionless Figure of Merit (Figure 6.20) and Equation 2.15. A very good agreement can be seen for the measured and the calculated values. It should be pointed out that the module's efficiency is measured during the QS MPPT scan run data. Meanwhile, the module's dimensionless Figure of Merit is calculated using the open circuit run measurement data and module's resistance measured using the QS MPPT algorithm. The good agreement of the ZT values determined by using two different methods using two different scan data support high overall accuracy claim of the measurement system.

The ZT values depend on the module compression force due to the ceramic plate effect. In particular the ceramic plate and the reference block interfacial thermal conductance, which is compression force dependant. The ZT values increase with the increasing compression force because the CTE is reduced and the TE material temperature gradient get closer the TEG module temperature gradient. With absence of the CPE the module ZT would be exactly average of the TE material zT, which for the bismuth telluride materials is approximately 1.

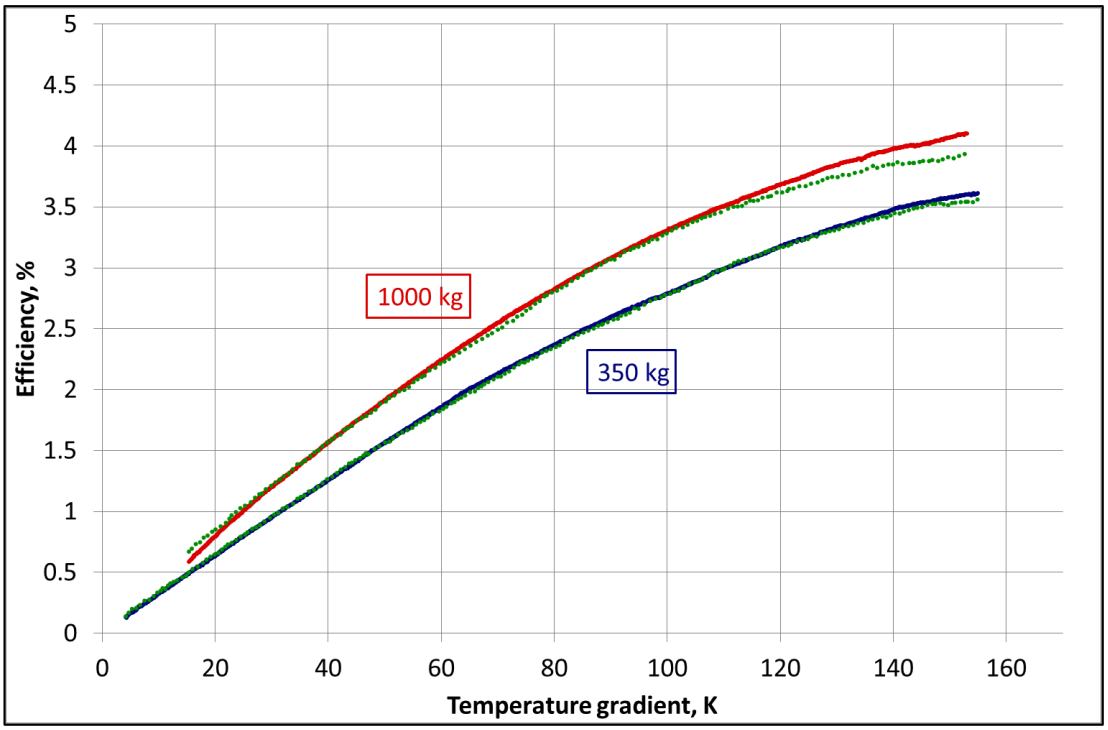

Figure 6.19. TEG127-50D module efficiency dependence on module temperature gradient. Red and blue lines are measured values, green dotted lines are calculated values.

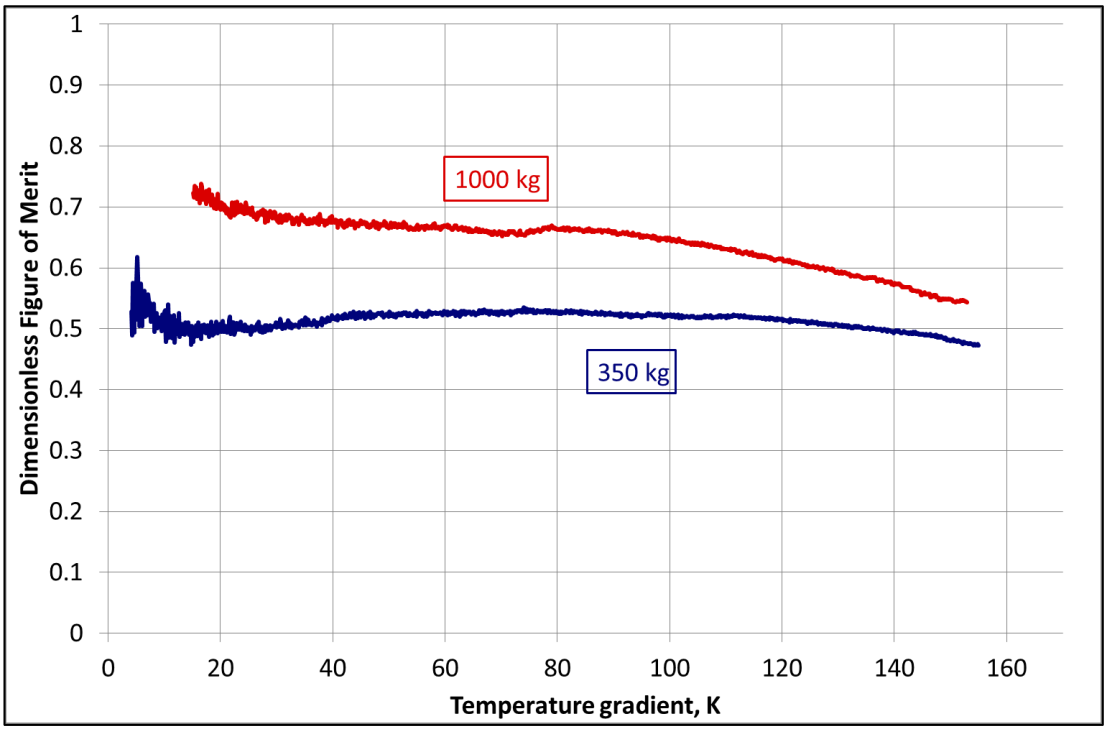

Figure 6.20. TEG127-50D module ZT dependences on the module temperature gradient.

7 CONCLUSIONS AND RECOMMENDATIONS FOR FUTURE SYSTEM DEVELOPMENT

7.1 Conclusions

The existing body of knowledge with regard to the characterisation of thermoelectric modules is expanded in this thesis by applying novel ideas and original work, which were implemented through the design and fabrication of a highly versatile thermoelectric generator module measurement system. Major structural, electronic, and software control innovations, such as variable atmosphere, compression force, and maximum power point tracking algorithms were introduced and realised.

A reliable engineering solution integrating high temperature heating, water cooling, hydraulic compression system, vacuum and gas system, high power and low level signal electrical systems into one comprehensive instrument was found and delivered. Our TEG module characterisation system has several important advantages as compared to the instruments with similar functionality described in the literature. These advantages include, but are not limited to: 1) our system being more versatile as it has capacity to measure modules of different physical size; 2) has high temperature measuring capability; 3) has controllable measurement environment; and 4) has an extensive range for the compression force, which is adjustable during the module measurement. The electronic circuits are closely linked and operate in tandem with the NI CompactDAQ data acquisition system. A wide operating range coupled with a fast response of the electronic load makes TEG module's electrical performance measurements using our system quick and effortless. An advanced computer instrument control and data acquisition software was created using NI LabVIEW programming language. The development and integration of a novel algorithm for maximum power point tracking (QS MPPT) and module's resistance measurements ensured rapid and precise data acquisition. These innovations were specially designed to minimize necessary operator interaction during module measurement process.

The performance of the system and essentially its capacity to undertake high quality measurement work was evaluated by investigating commercially available Thermonamic TEHP1-12656-0.3 and Ieverred TEG127-50D thermoelectric power generator modules and comparing measurement results to the known performance values. Major TEG module performance characteristics such as voltage, current, resistance, power, heat flow, efficiency, and dimensionless Figure of Merit were performed and analysed. The analysis of obtained data showed that TE module characterisation system developed at ISEM performs at the same or even better level as compared to other similar units. The importance of the compression force to the module performance is made evident and discussed. A newly developed algorithm for the estimation of a true module's resistance measurement is analysed and compared to the conventionally used methods.

Although the system performs exceptionally well, several possibilities exist to further improve system's functionalities and reliability. Recommendations for the future development are presented in the Sections below. These recommendations target better reliability, accuracy, functionality, and responsiveness of the measurement system.

7.2 Recommendations for Hardware

7.2.1 Water Chiller Unit

The module cold side temperature is kept low by circulating cooling water inside the cooler plate. The cooling water used is taken directly from the building cooling water supply. While the building cooling water is capable to efficiently extract the heat from the cold side of the TEG module, the module cold side temperature is not controllable and has a linear dependence on the module temperature gradient. A dedicated cooling water system should be added to the instrument to make the module's cold side temperature controllable and/or maintainable at constant temperature values.

7.2.2 Reference Block Calibration

TEG module's efficiency is the ratio between the extracted electrical power and thermal power supplied to the module. Typically, the heat flow measured at the cold side reference block is used for the calculations of module's efficiency. In this case thermal power supplied to the module equals to the sum of the cold side reference block heat flow and the extracted electrical power.

In our measurement system the heat flow at the cold side reference block is used to calculate module's efficiency. Any thermal radiation losses from this block are considered to be negligible because its temperature is close to the ambient temperature. Moreover, the convection losses are minimised by measuring in vacuum. Thermal conductivity values for copper available in literature are used for the heat flow calculations. A delicate calibration of the copper blocks should be carried out to obtain actual thermal conductivity values and confirm the literature data for the reference blocks. If the actual thermal conductivity values are lower than those used for heat flow measurements, the heat flow would be overestimated. Subsequently, the module's efficiency and ZT calculations would result in underestimated values.

7.3 Recommendations for Electronic Load Board (CB02)

7.3.1 Voltage Booster Add-On

Direct control functionality coupled with a 100 kS/s sampling rate of the NI 9263 module opens a possibility to operate the power transistor in high frequency switching mode. High frequency switching allows the electronic load board coupling with a voltage boost converter. A circuit diagram of the inverting voltage boost converter concept is shown in Figure 7.1. The diagram omits feedback and regulation components. Voltage booster add-on to the electronic load board option is feasible and should be considered for future development. It will find use when measuring TEG modules with very low voltage output, *e.g.* less than 1 Volt. While it is possible to measure and plot such TEG module performance curves, it would not be possible to physically demonstrate the electrical power generated. For example, a simple red LED would require at least 1.8 V to illuminate; a white LED or a small fan might need 3 V to operate.

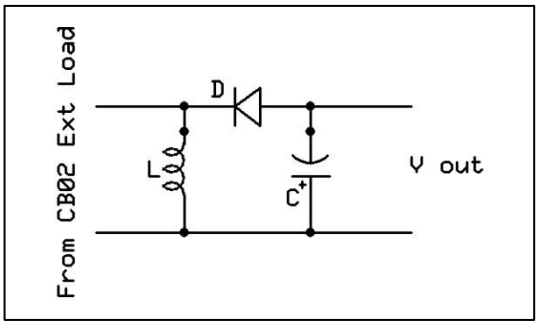

Figure 7.1. Inverting boost converter concept circuit diagram.

7.4 Recommendations for Control Software

7.4.1 Electronic Load Control Signal Adjustment for Electronic Load Gain Drift

Electronic Load current to control voltage gain is manually adjusted on P1 potentiometer to be 2 A/V. The adjustment is done at room temperature and is rather coarse. Any gain adjustment errors will appear as a relative offset from the current setpoint.

A current flowing through the electronic load current sensing resistance will result in Joule heating of the current sensing resistance. Any power dissipated on the electronic load board will raise the temperature of all its components. An increase of conductor temperature will cause an increase of the metallic conductor resistance. The conductor with increased resistance will have a larger voltage drop. As the comparator adjusts the current flow till the voltage drop of the current sensing resistance reaches a preset value, a rise of the sensing resistance temperature will result in a lowering of the electronic load current.

Empirical data shows 5% maximum total error in gain. In particular, up to 10 mA/min current drift rate with 100 mA maximum drift were observed upon 8 W of electric power getting dissipated in the electronic load board.

The gain error and gain drift can be accounted for in the control software. Instead of a 2 A/V constant used throughout the software for determining the NI 9263 module output for the desired electronic load current, a FGV, storing the current to voltage gain value, should be created. The FGV would monitor recent electronic load current measurements together with NI 9263 module output set points. It would then adjust the stored gain value to actual electronic load current to voltage set point ratio for further use.

7.4.2 Stream Measurement Data to TDMS Files Instead of Saving Tabulated Text Files

Measurement data and processed data are saved to a tabulated ASCII file with .TXT extension for future viewing and analysis. Save to Spreadsheet File.vi function is used to save the data. ASCII file format was chosen because it is compatible with MS Excel. Data saving takes place every ten seconds or when the user interface loop receives the program close command. First, a header row is saved with column names, read from a Data File Headers.ini settings file. Then, the file is appended with the two-dimensional array of measurement and calculation data values. File name starts with a timestamp value of the first measurement point. The whole dataset is retained in memory for graphing. The .TXT file is completely rewritten with each save.

As the dataset grows, it requires more space in the random access memory and more processing power to handle it. It has been observed that after 12 hours of acquisition the dataset becomes too large to be processed in a timely manner and timing critical VIs stop, crashing the program.

Solution to this problem is unloading the data table from memory to the hard disk at predetermined intervals, *e.g.* 15 minutes when there is no operator interaction with the program, and *e.g.* every 10 seconds, if the operator is interacting with the program. The data for graphing would have to be looked up and read back from the saved file. Technical Data Management Streaming (TDMS) file format developed by National Instruments is a better option when compared to ASCII file format. While it is compatible with MS Excel, it is also written quicker, searchable, and takes less disk space [127].

8 APPENDIX A – TECHNICAL DRAWINGS

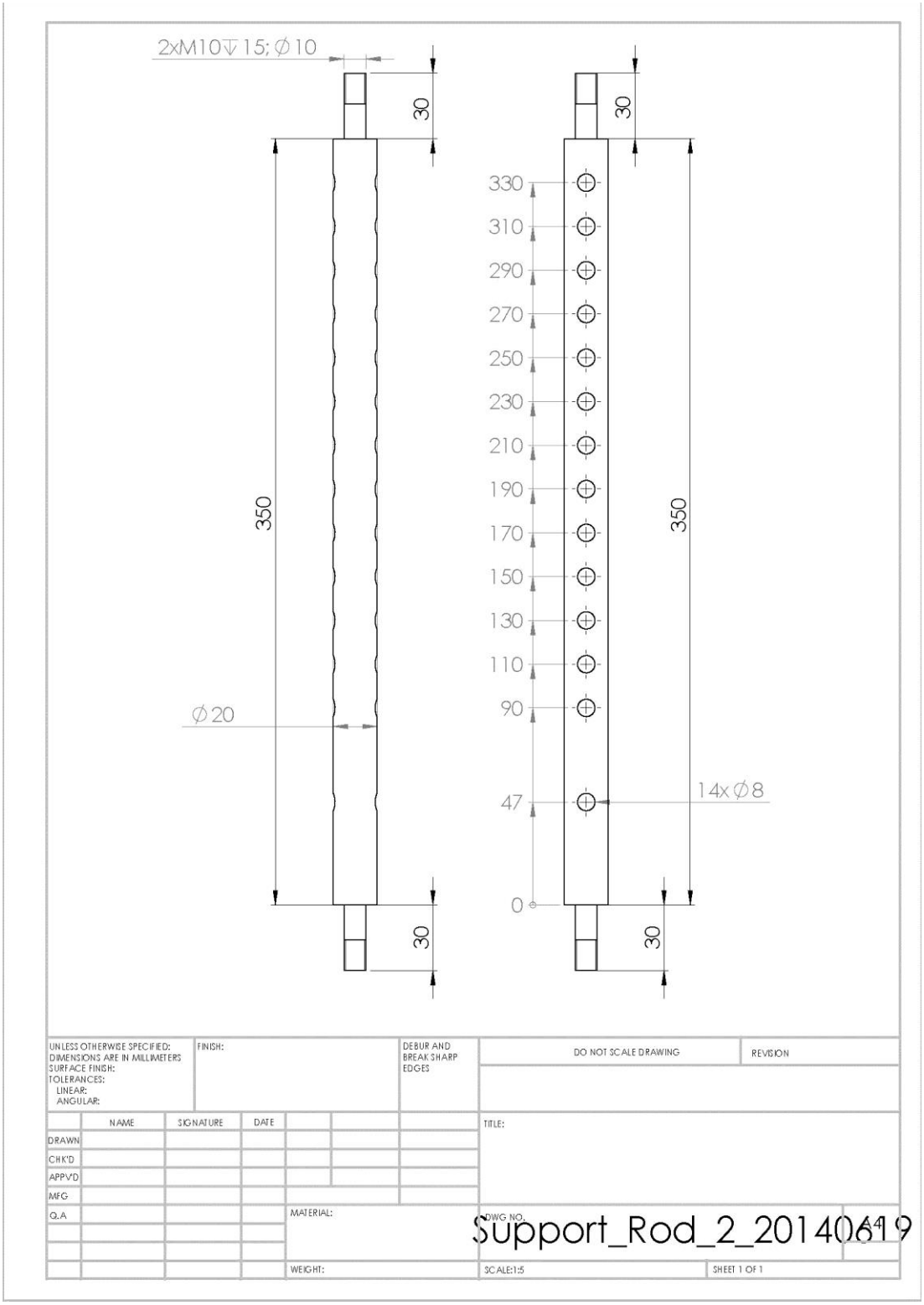

Technical Drawing 1. Support shaft.

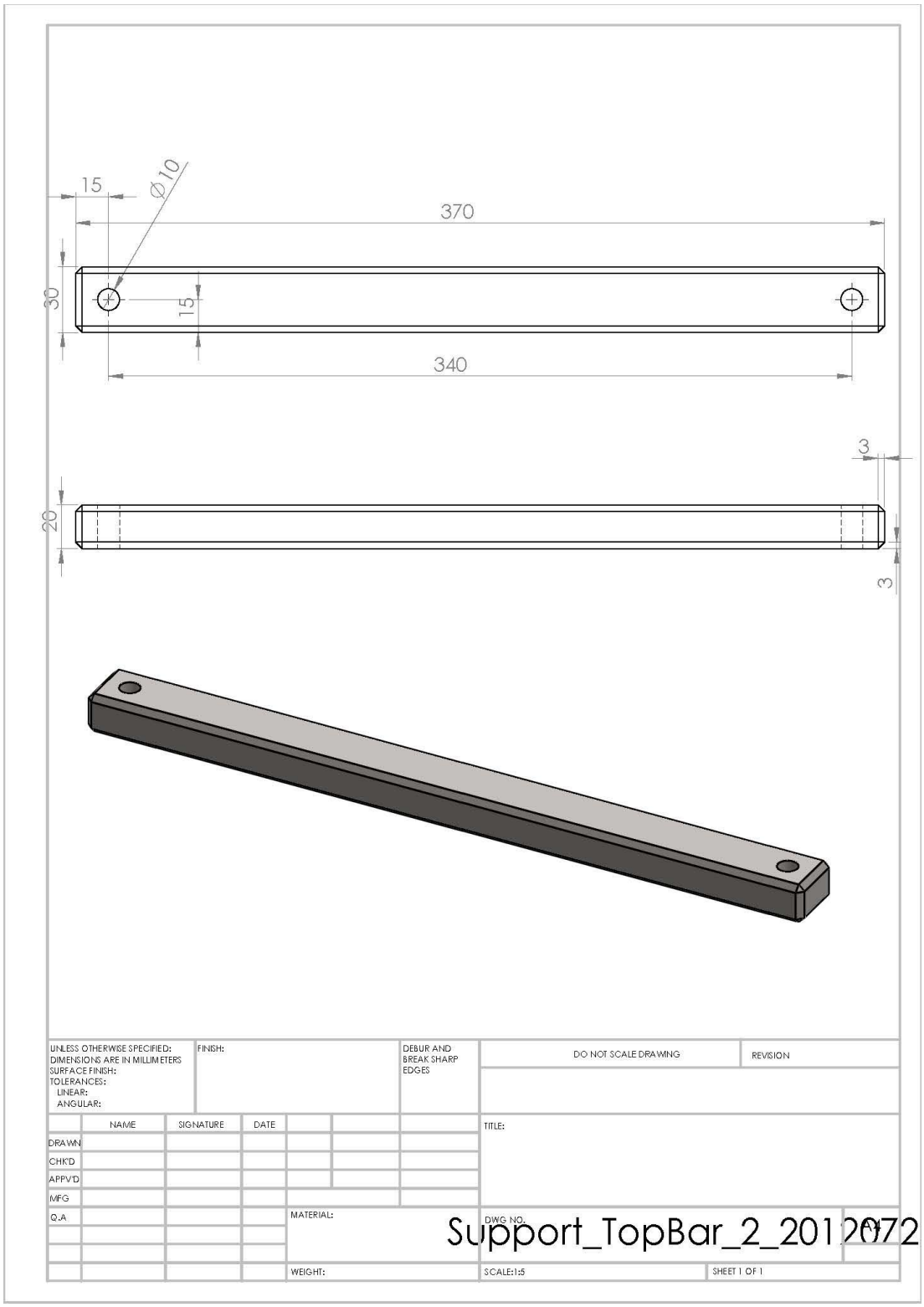

Technical Drawing 2. Top bar.

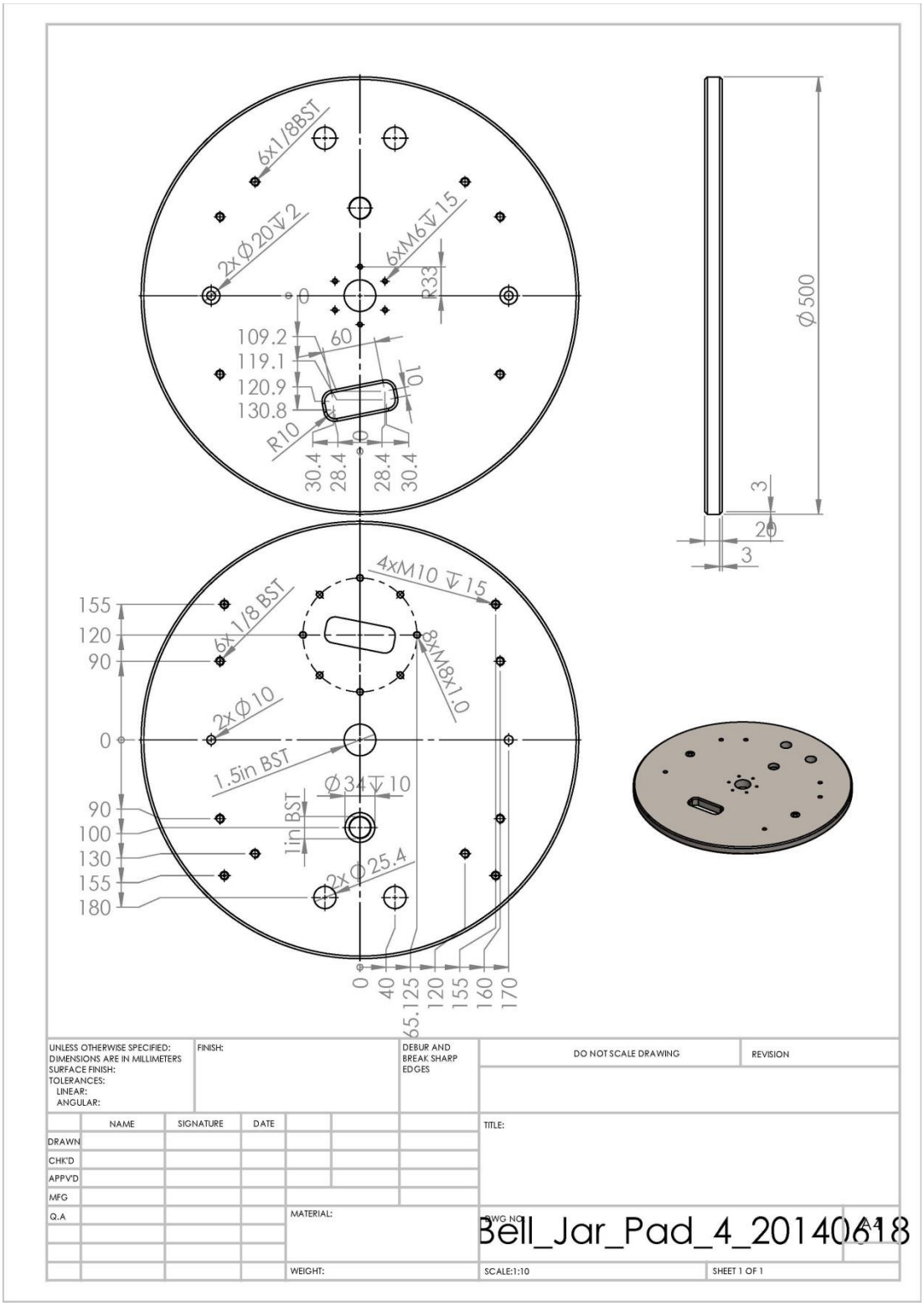

Technical Drawing 3. Bell jar baseplate.

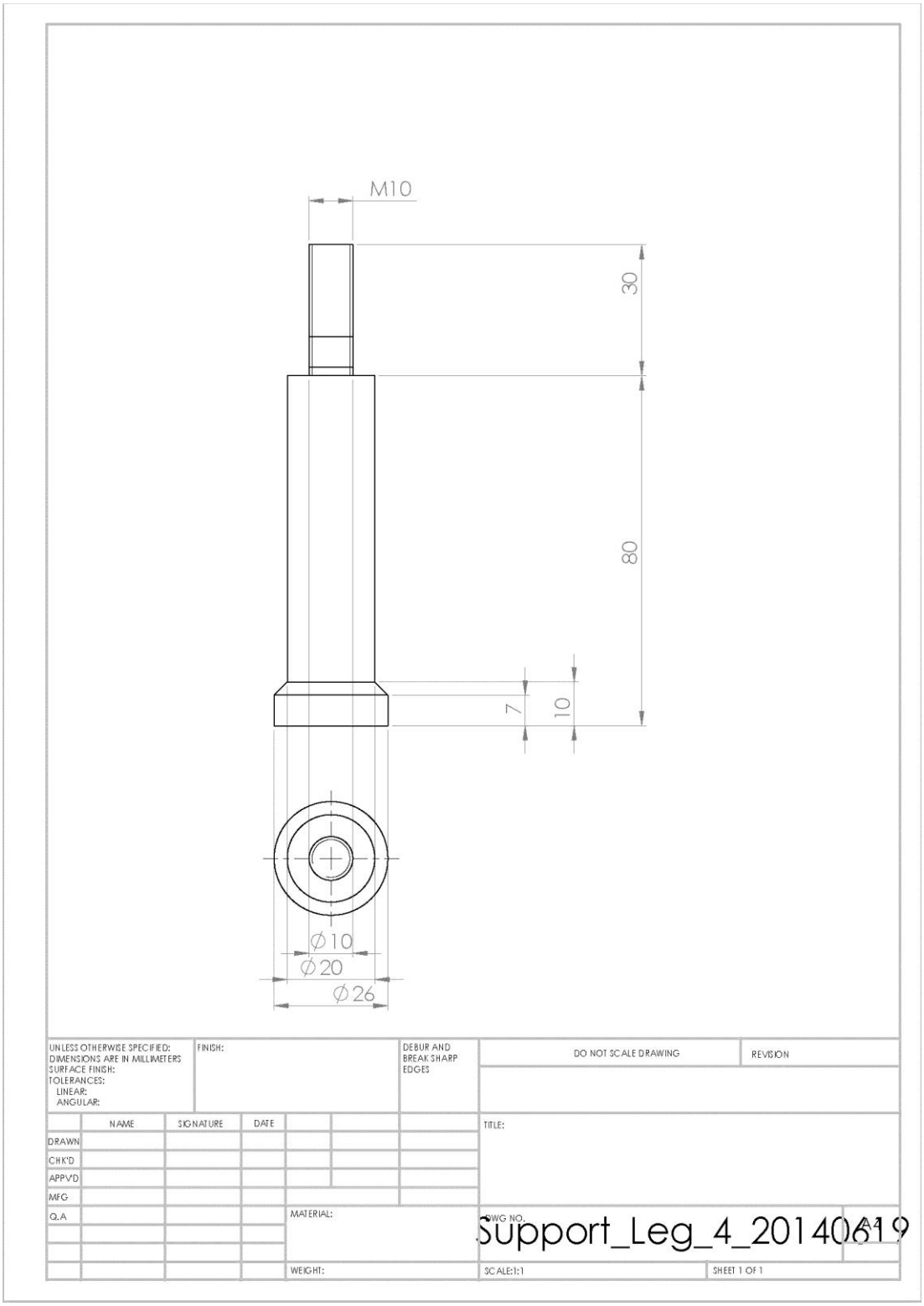

Technical Drawing 4. Baseplate leg.

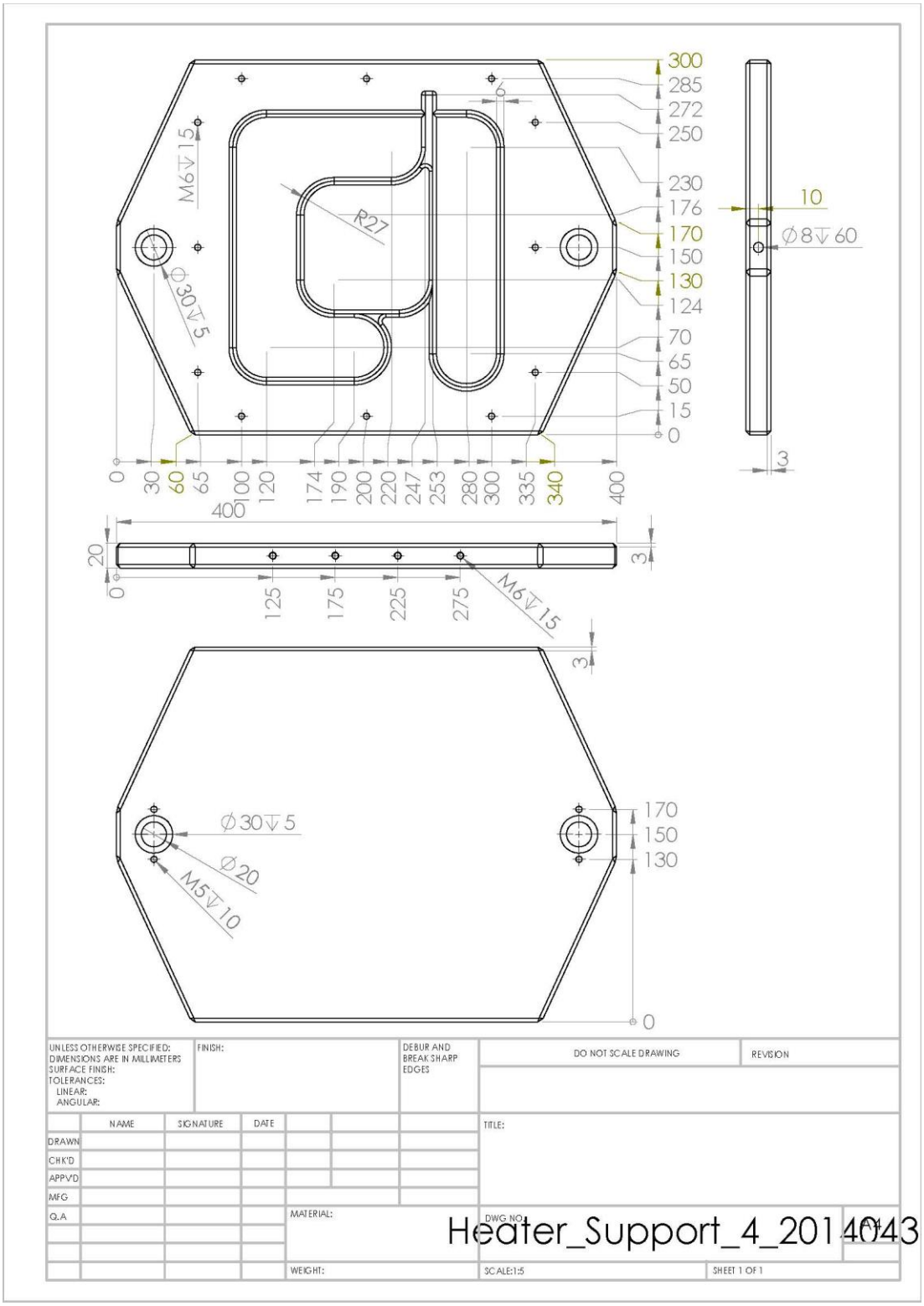

Technical Drawing 5. Heater support plate.

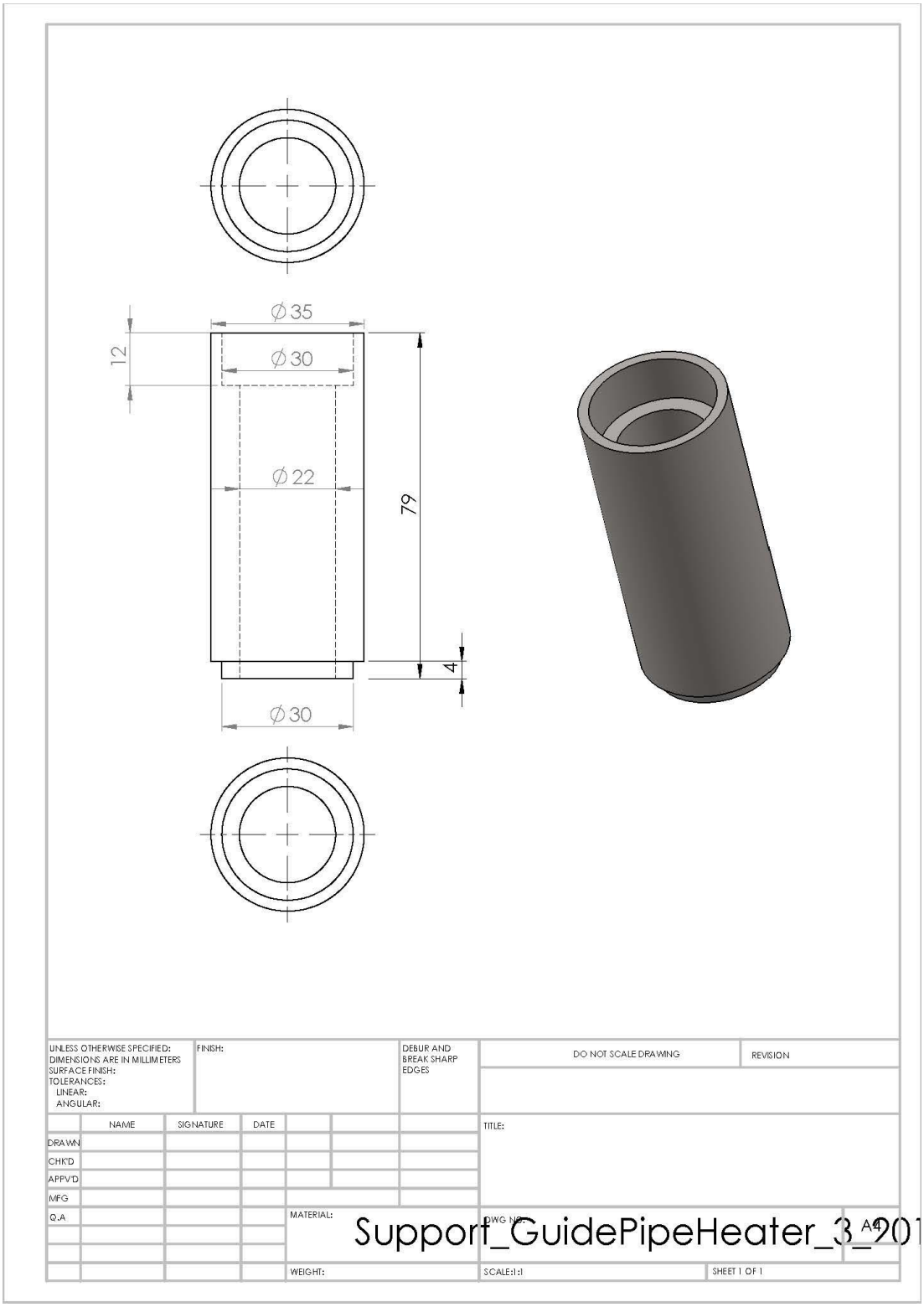

Technical Drawing 6. Heater guide tube.

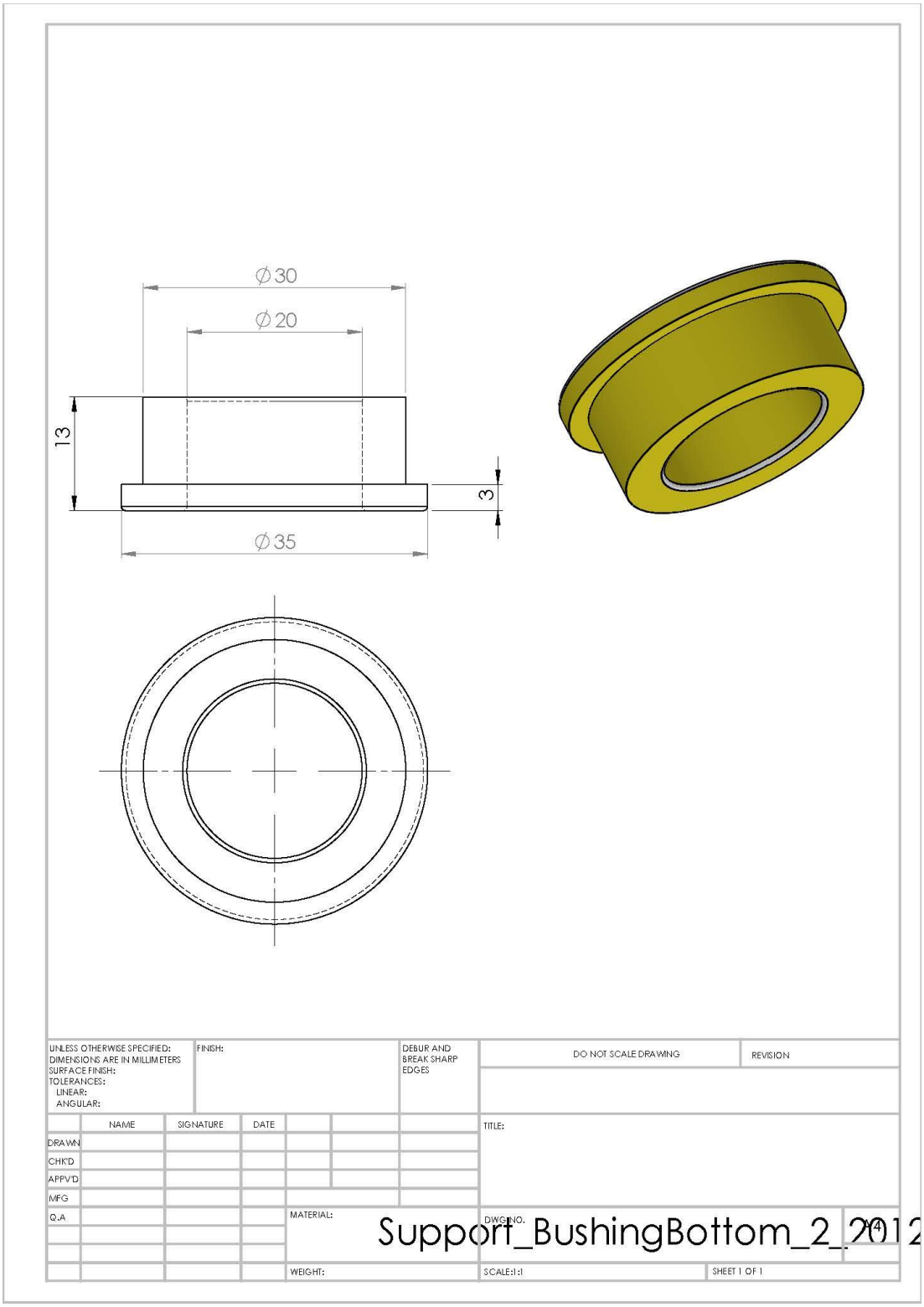

Technical Drawing 7. Nylon bushing for guide tubes.

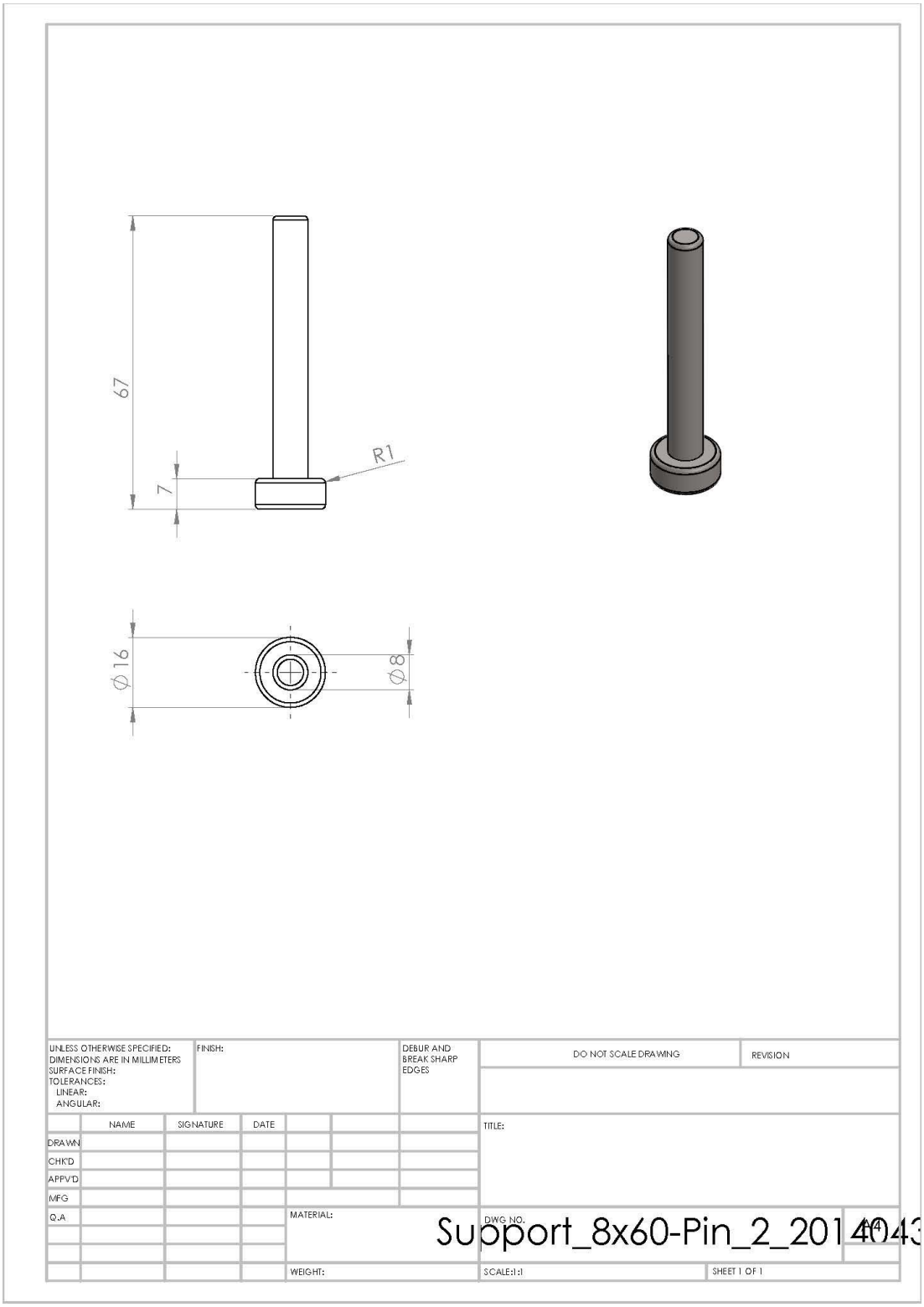

Technical Drawing 8. Heater and cooler height adjustment pin.

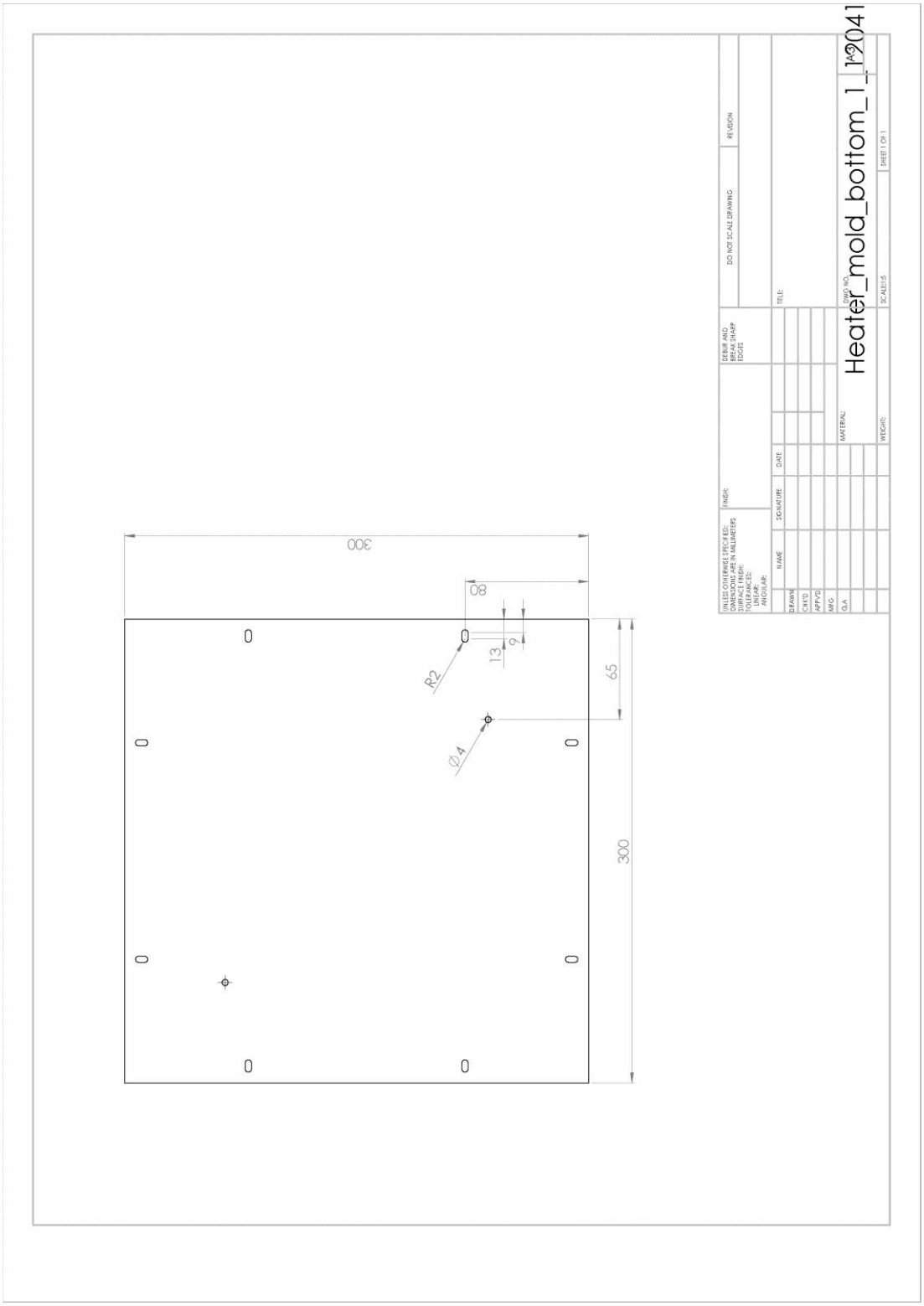

Technical Drawing 9. Mould bottom plate.

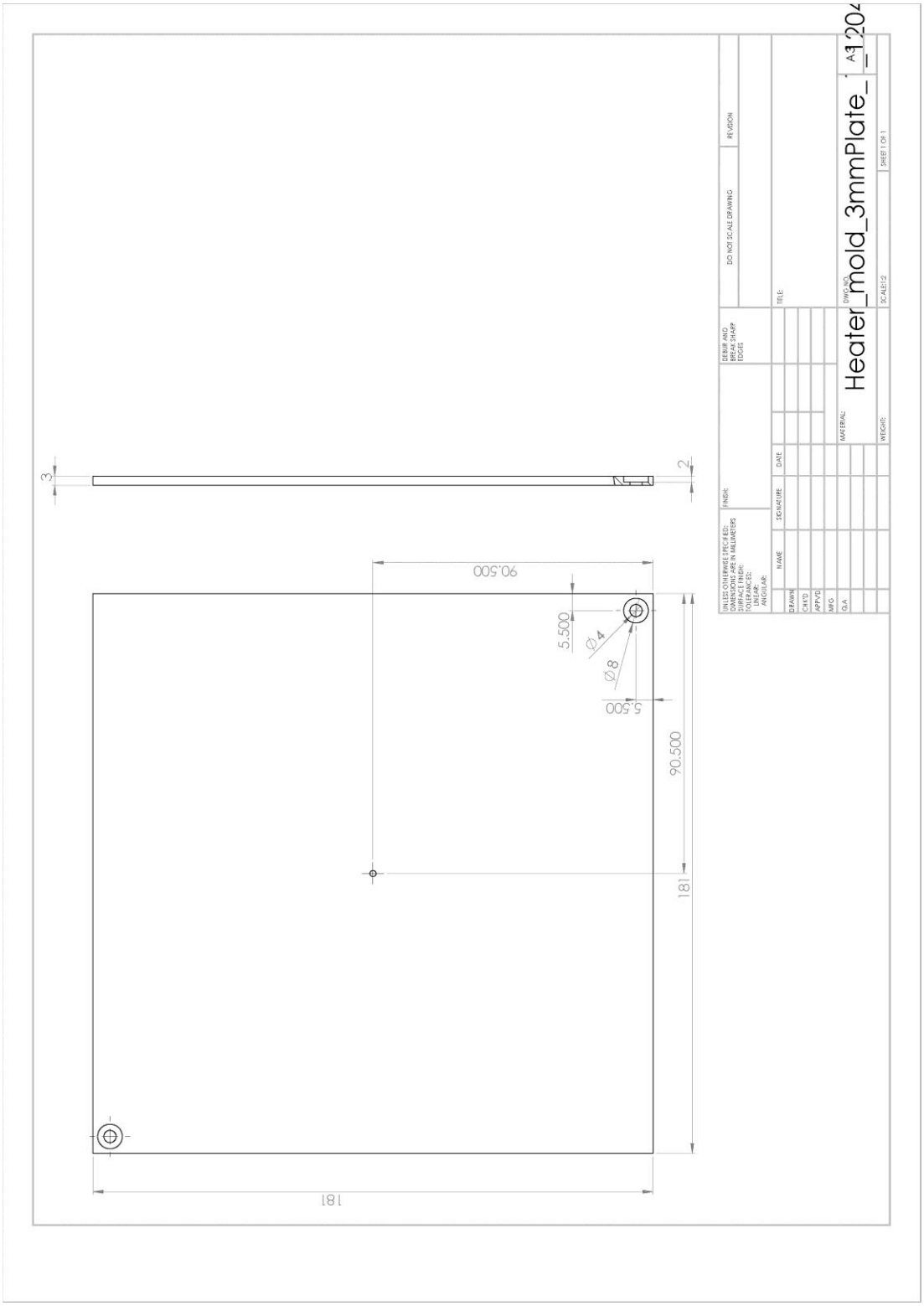

Technical Drawing 10. Mould 3 mm plate.

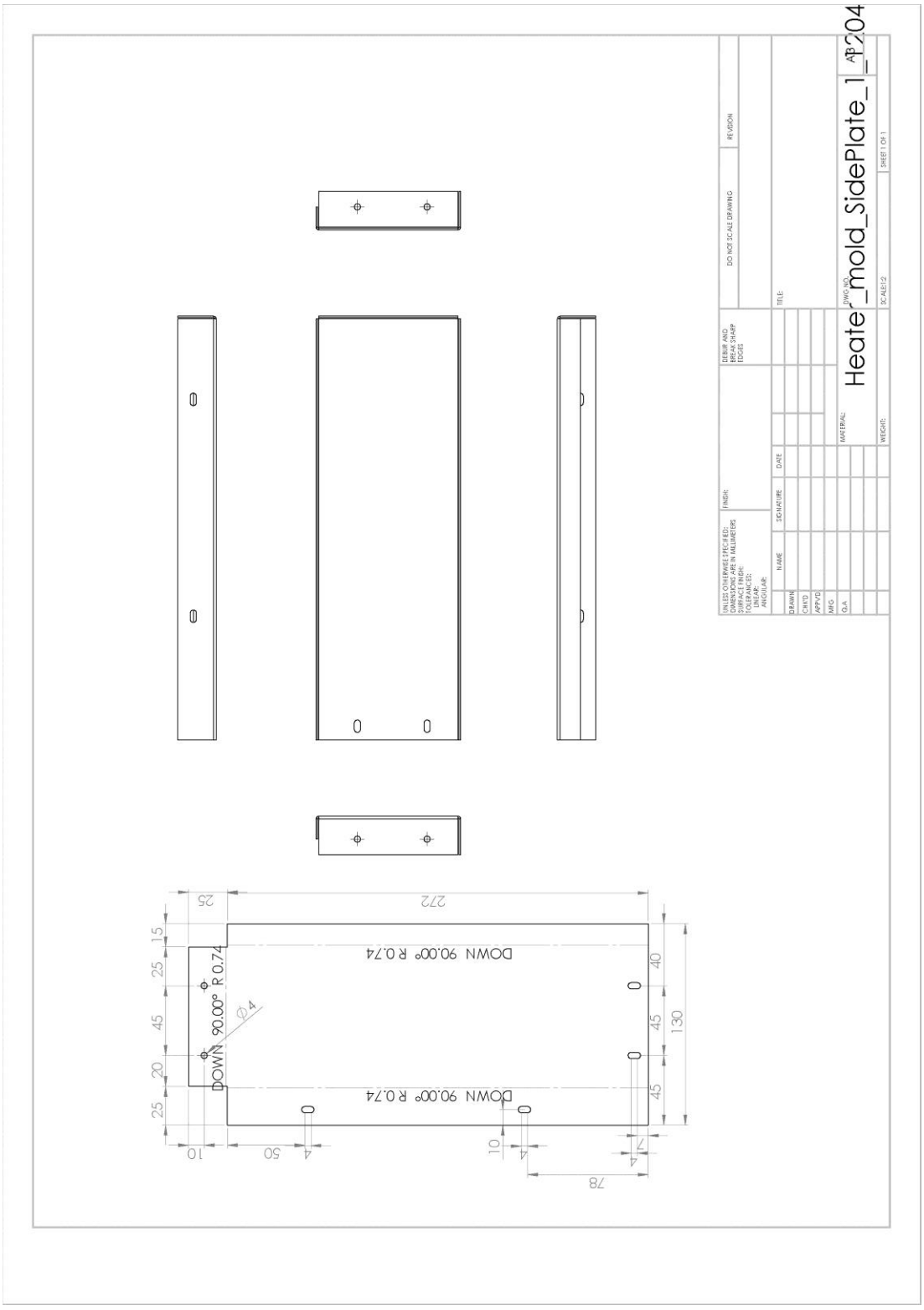

Technical Drawing 11. Mould side plate.

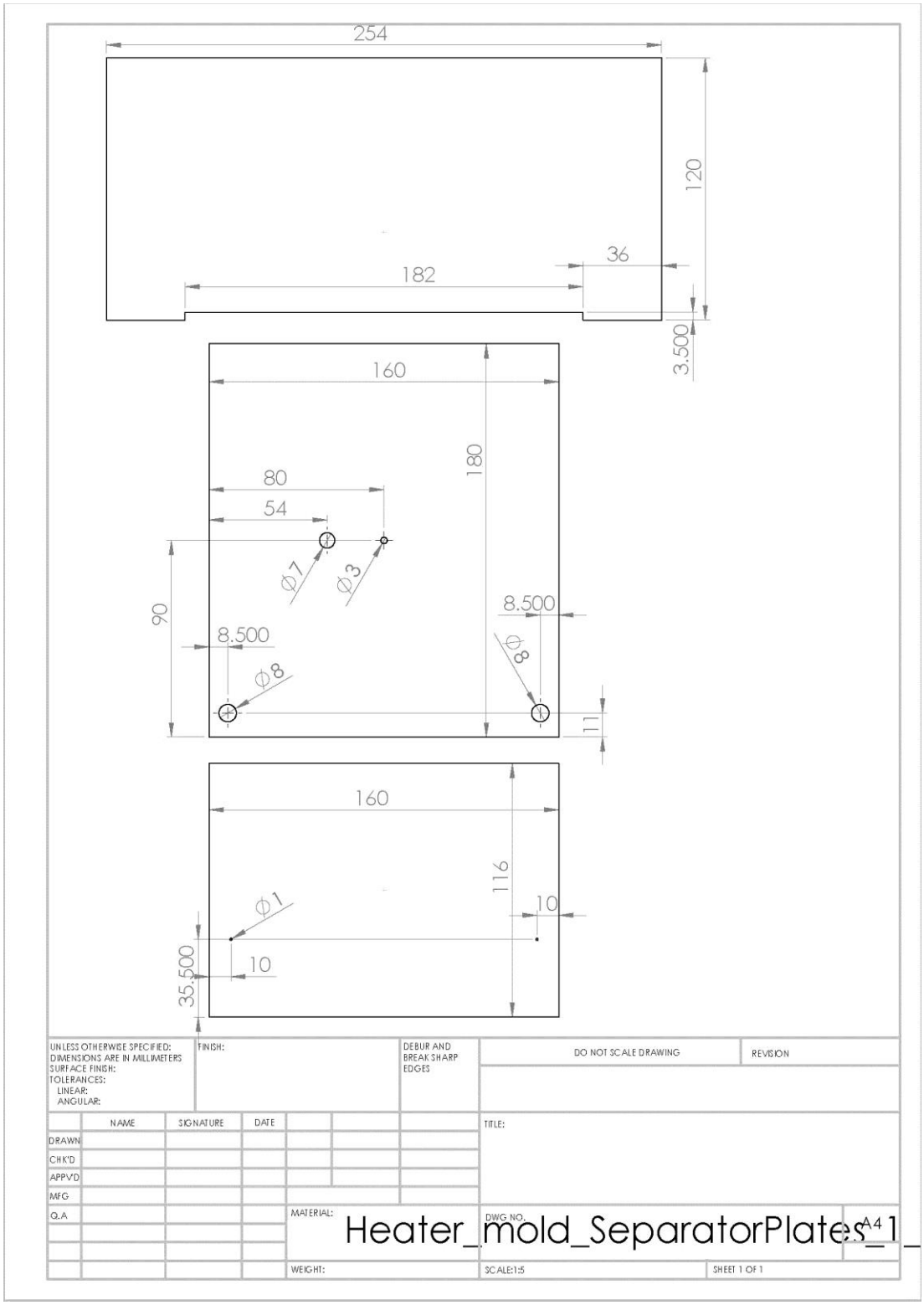

Technical Drawing 12. Mould internal ("long", "middle", and "short") separator plates.

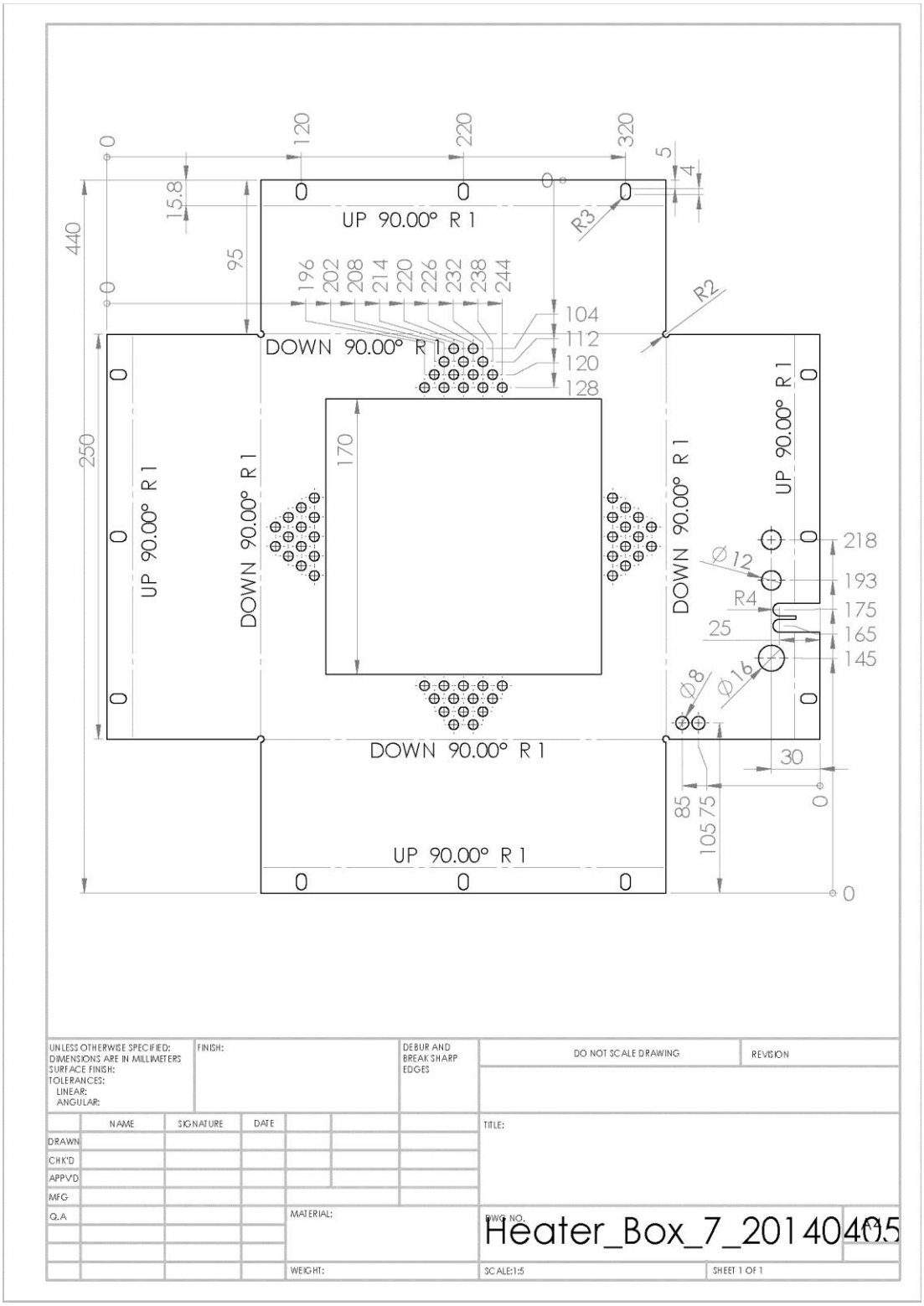

Technical Drawing 13. Heater box.

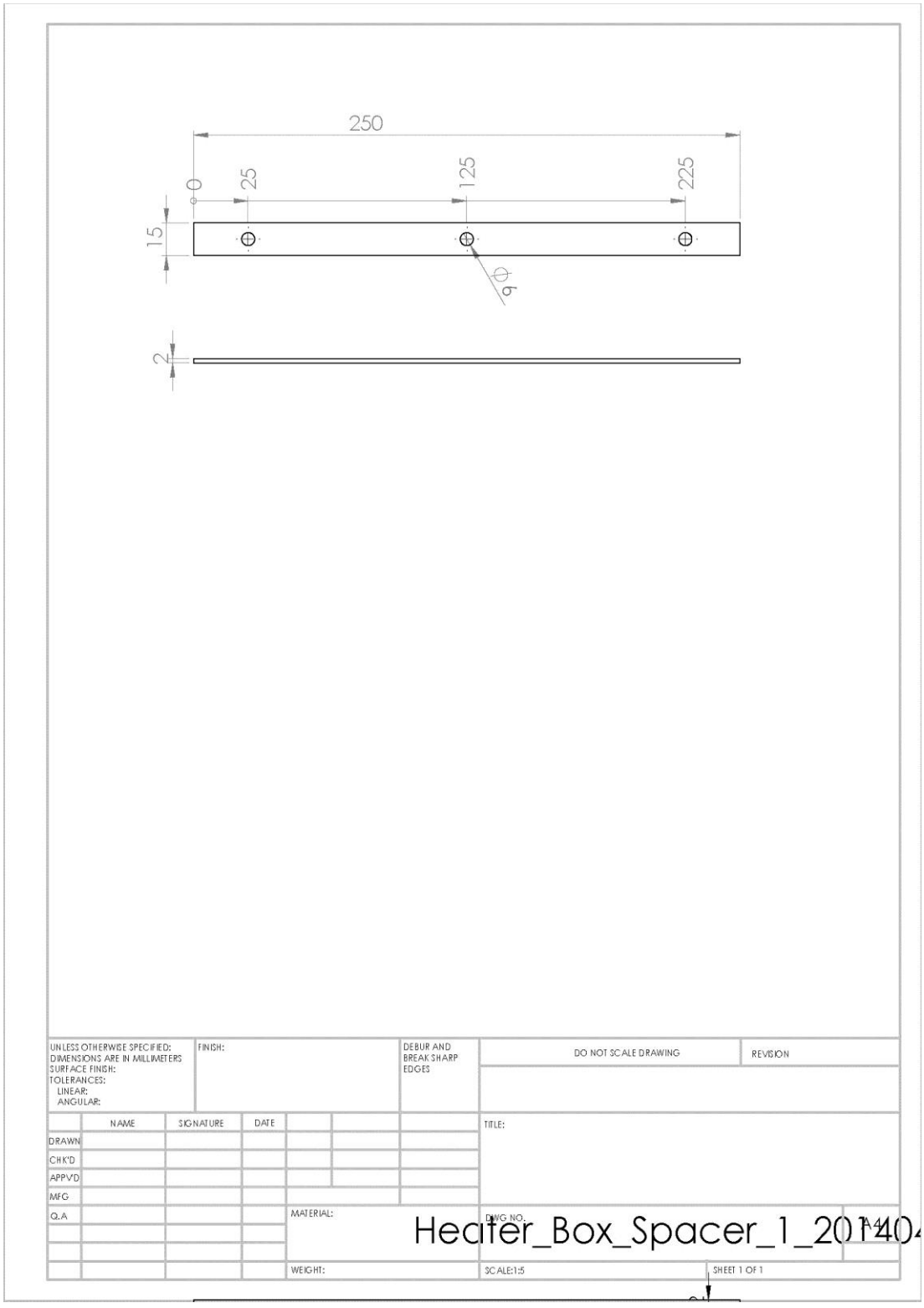

Technical Drawing 14. Heater box spacer.

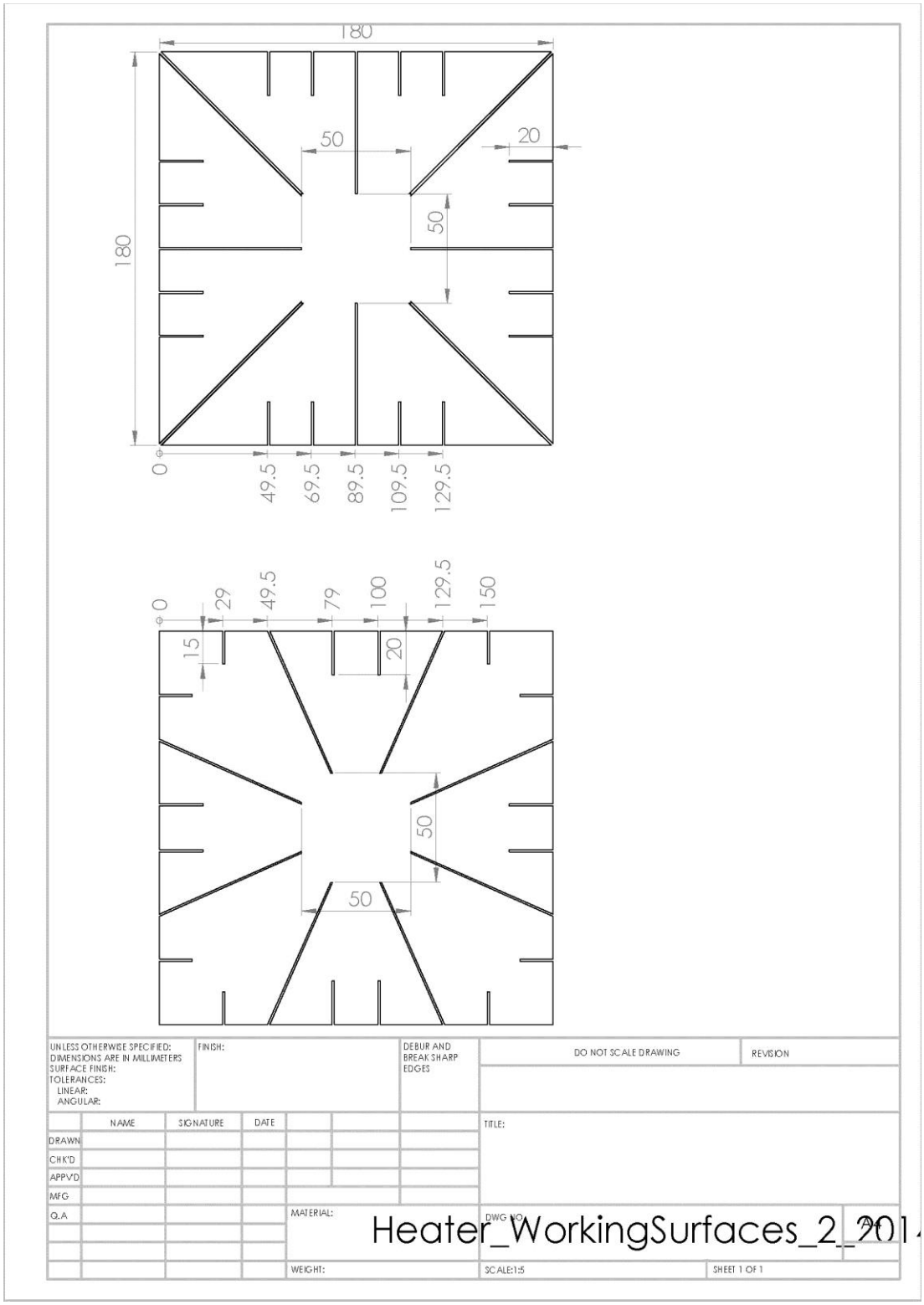

Technical Drawing 15. Heater working surface plates.

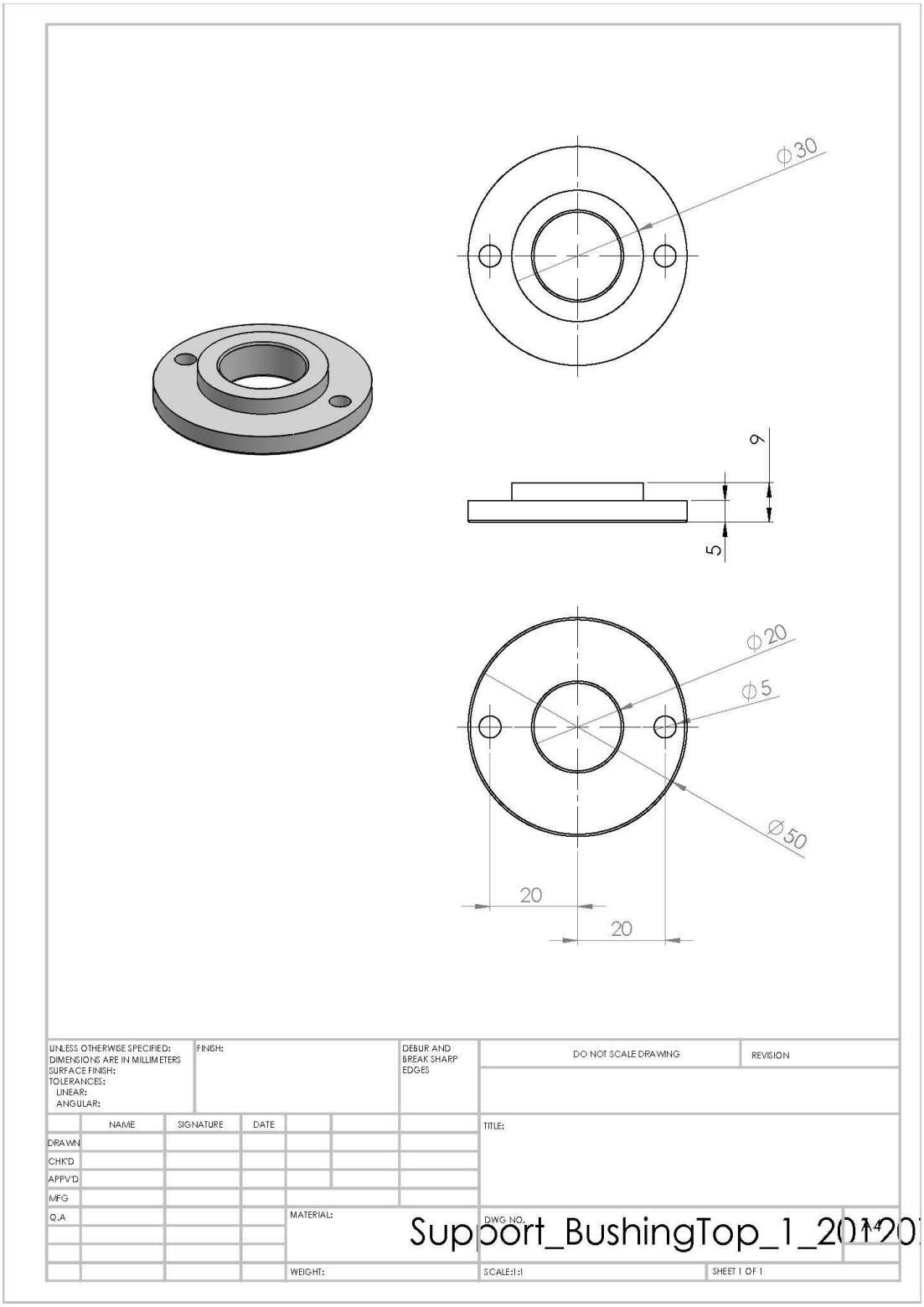

Technical Drawing 16. Nylon bushing for heater and cooler support plates.

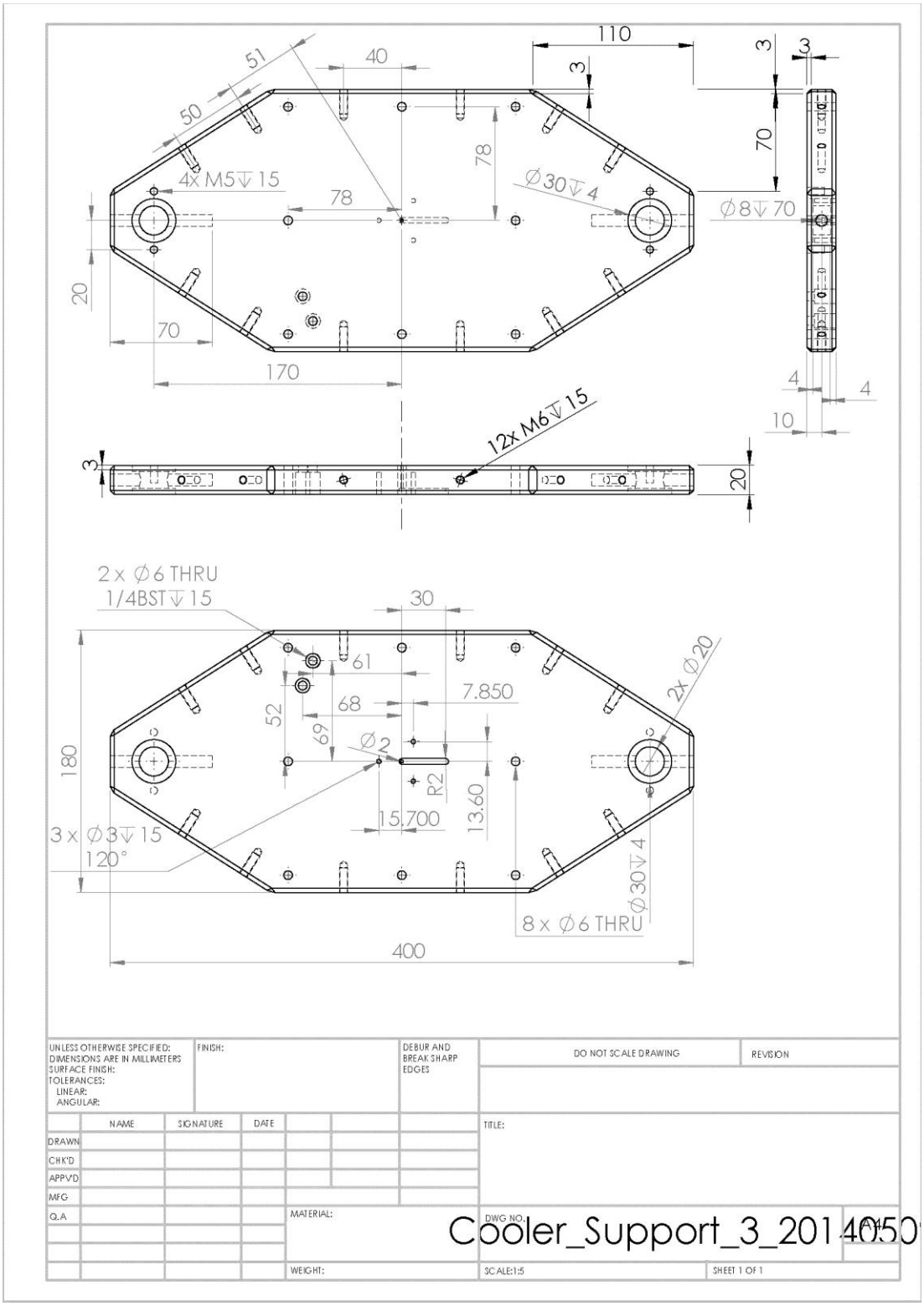

Technical Drawing 17. Cooler support plate.

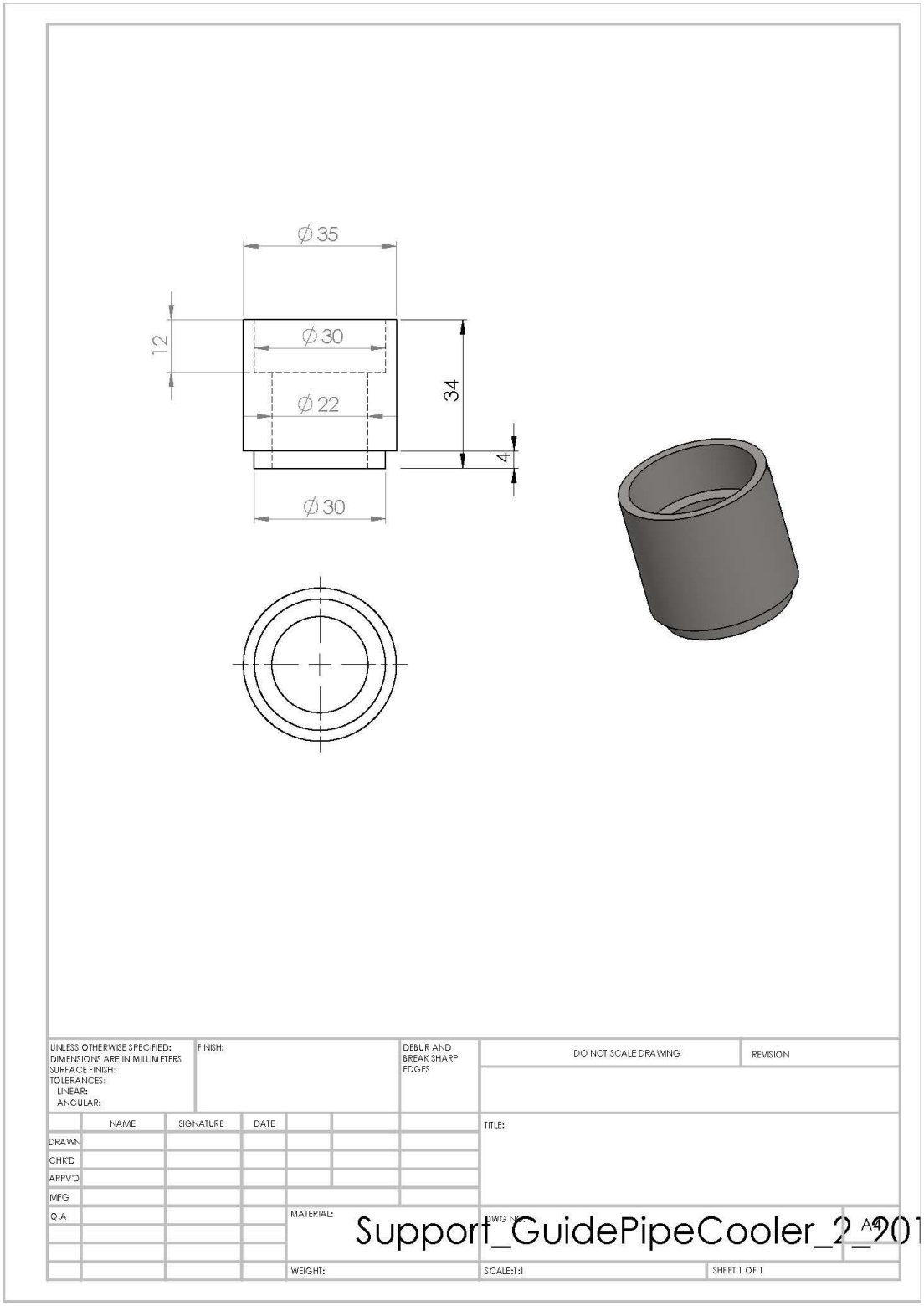

Technical Drawing 18. Cooler guide tube.

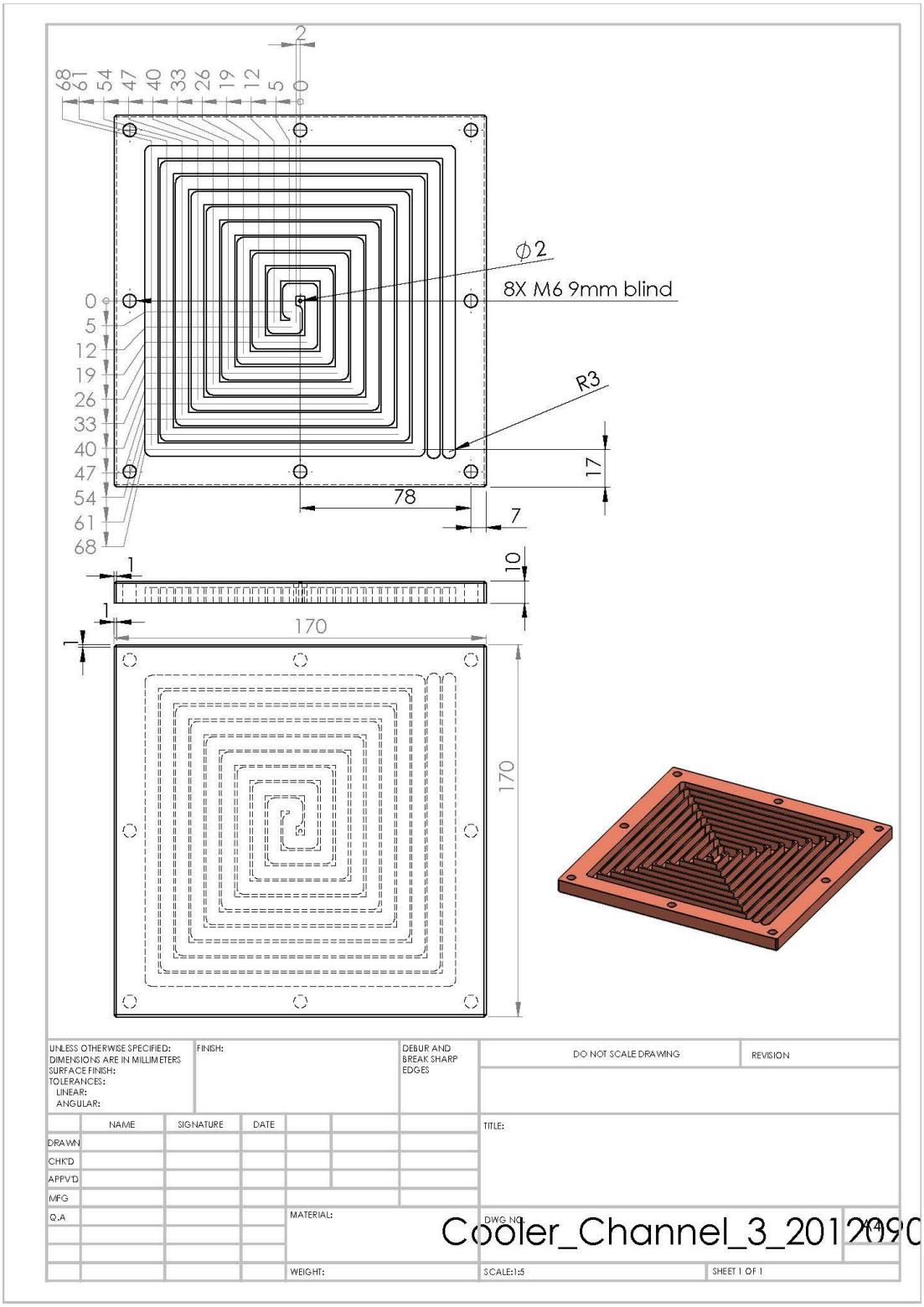

Technical Drawing 19. Cooler channel plate.

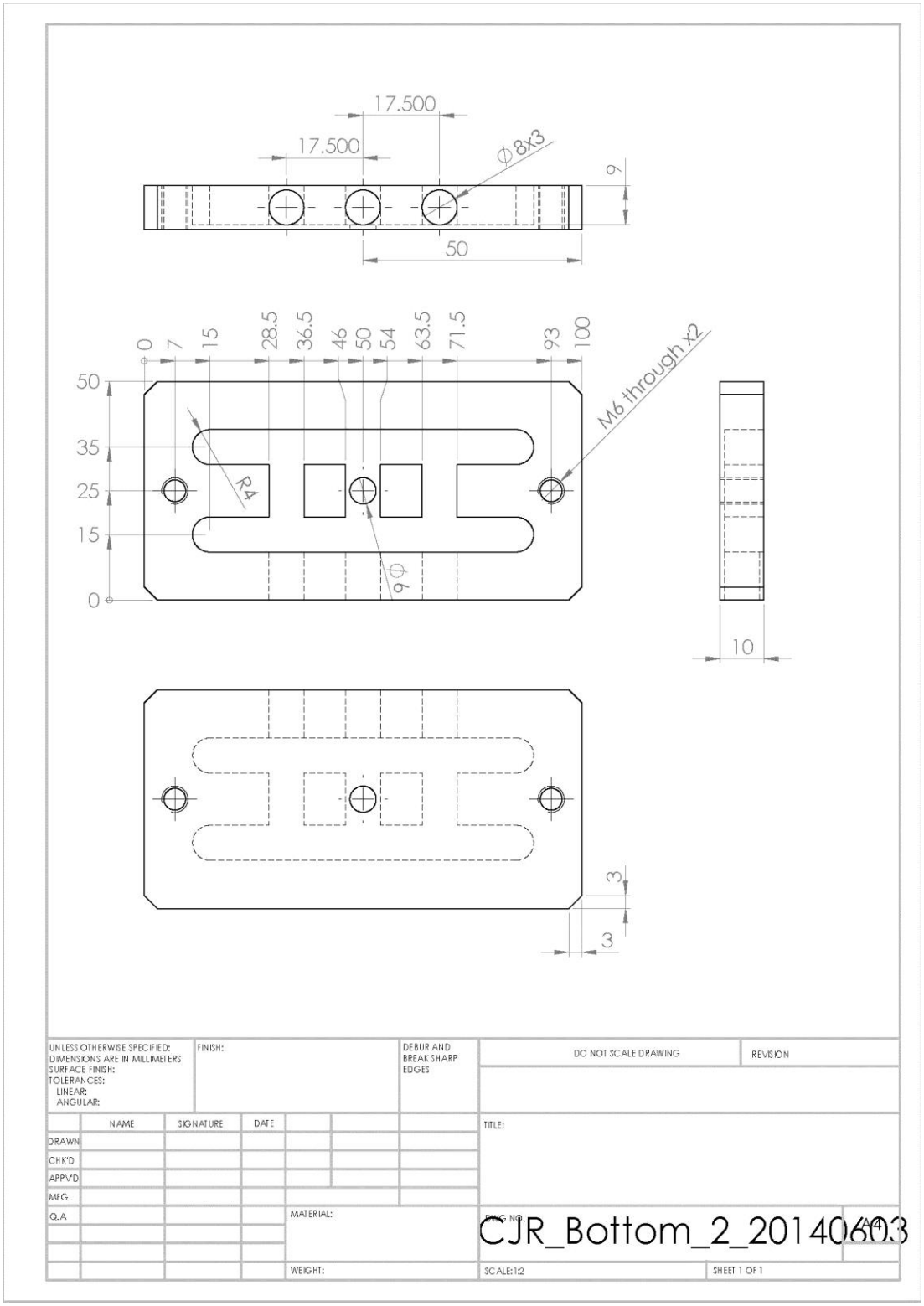

Technical Drawing 20. Cold Junction Reference bottom part.

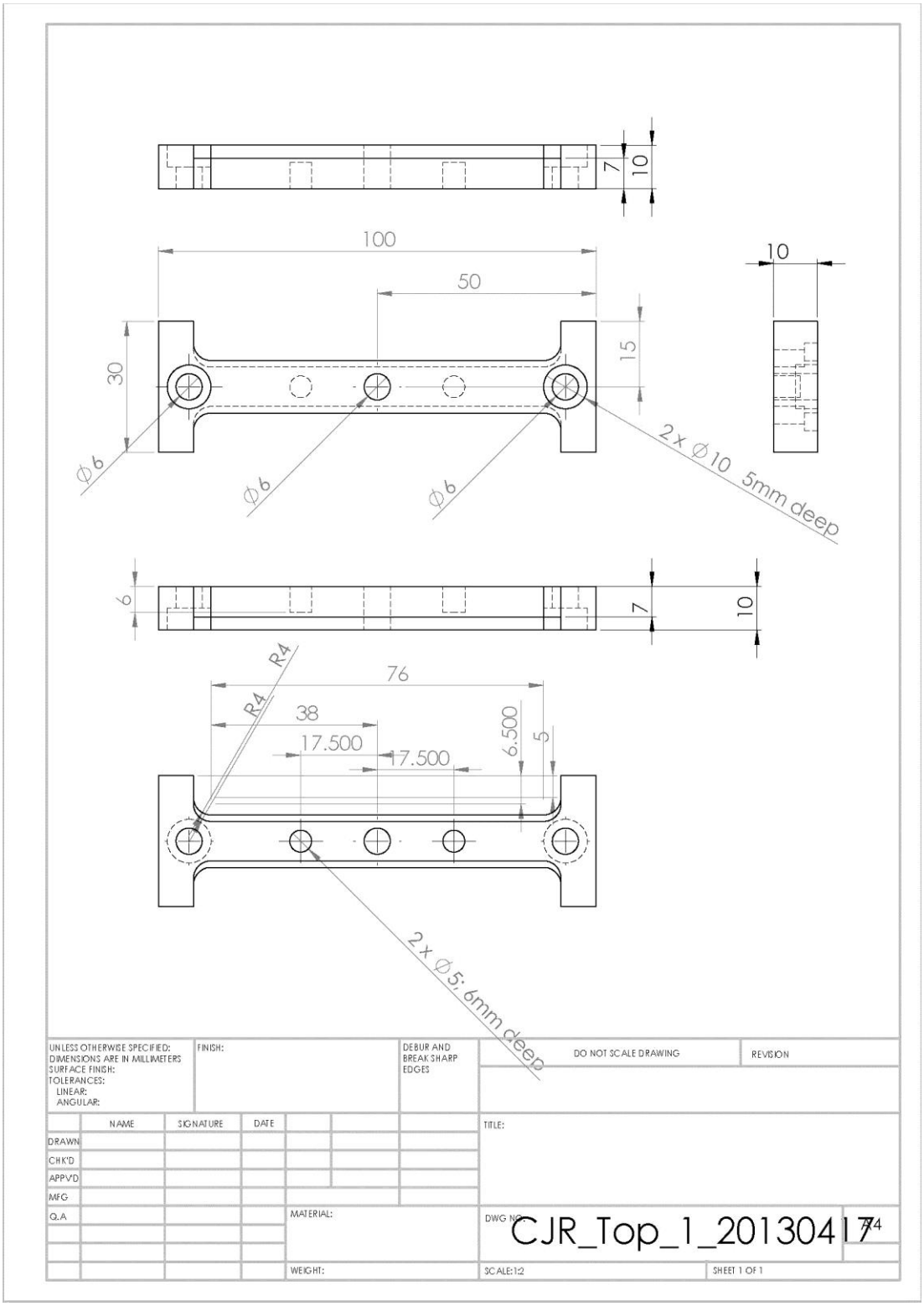

Technical Drawing 21. Cold Junction Reference top part.

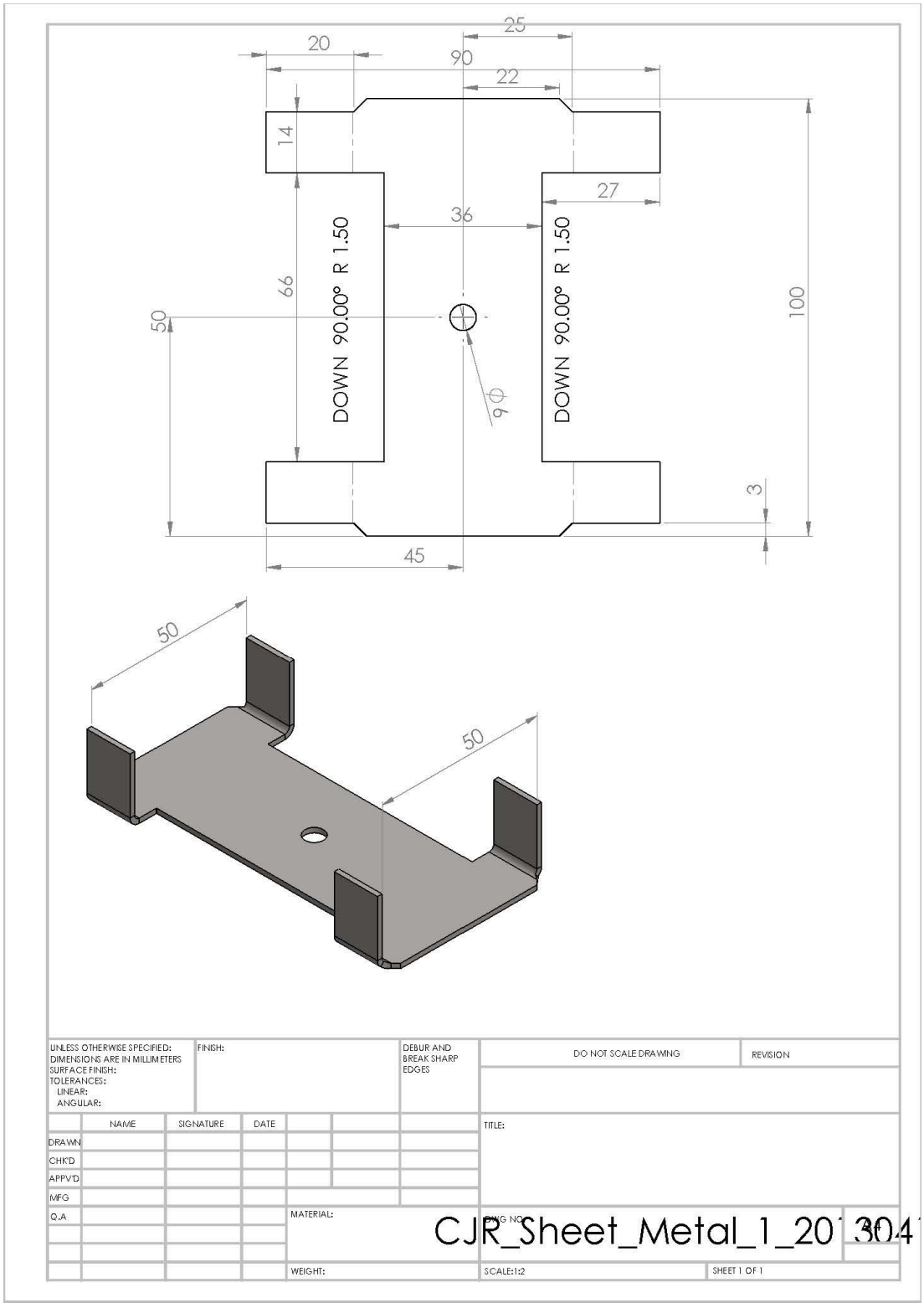

Technical Drawing 22. Cold Junction Reference cover.

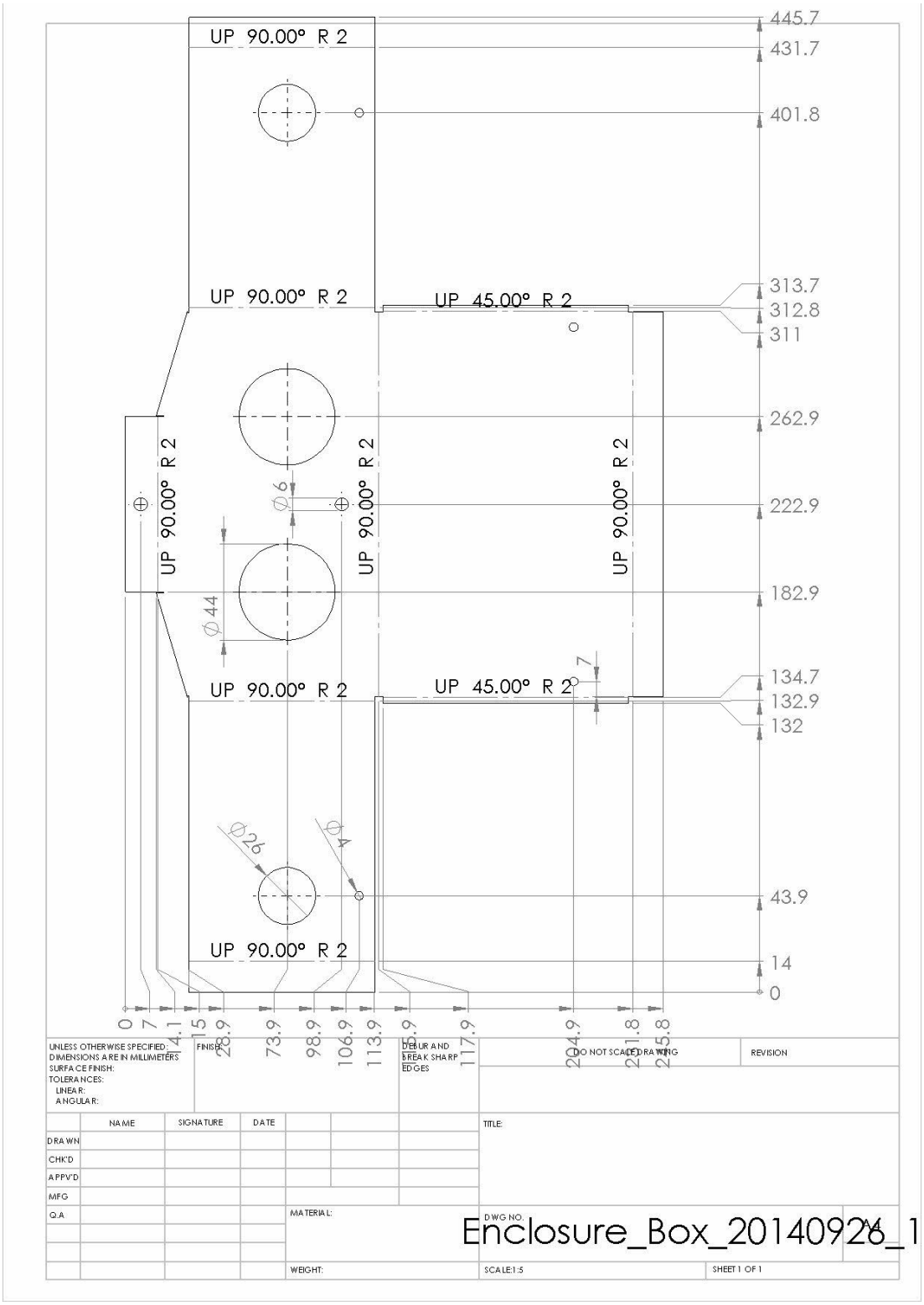

Technical Drawing 23. High power electrical feedthrough enclosure box.

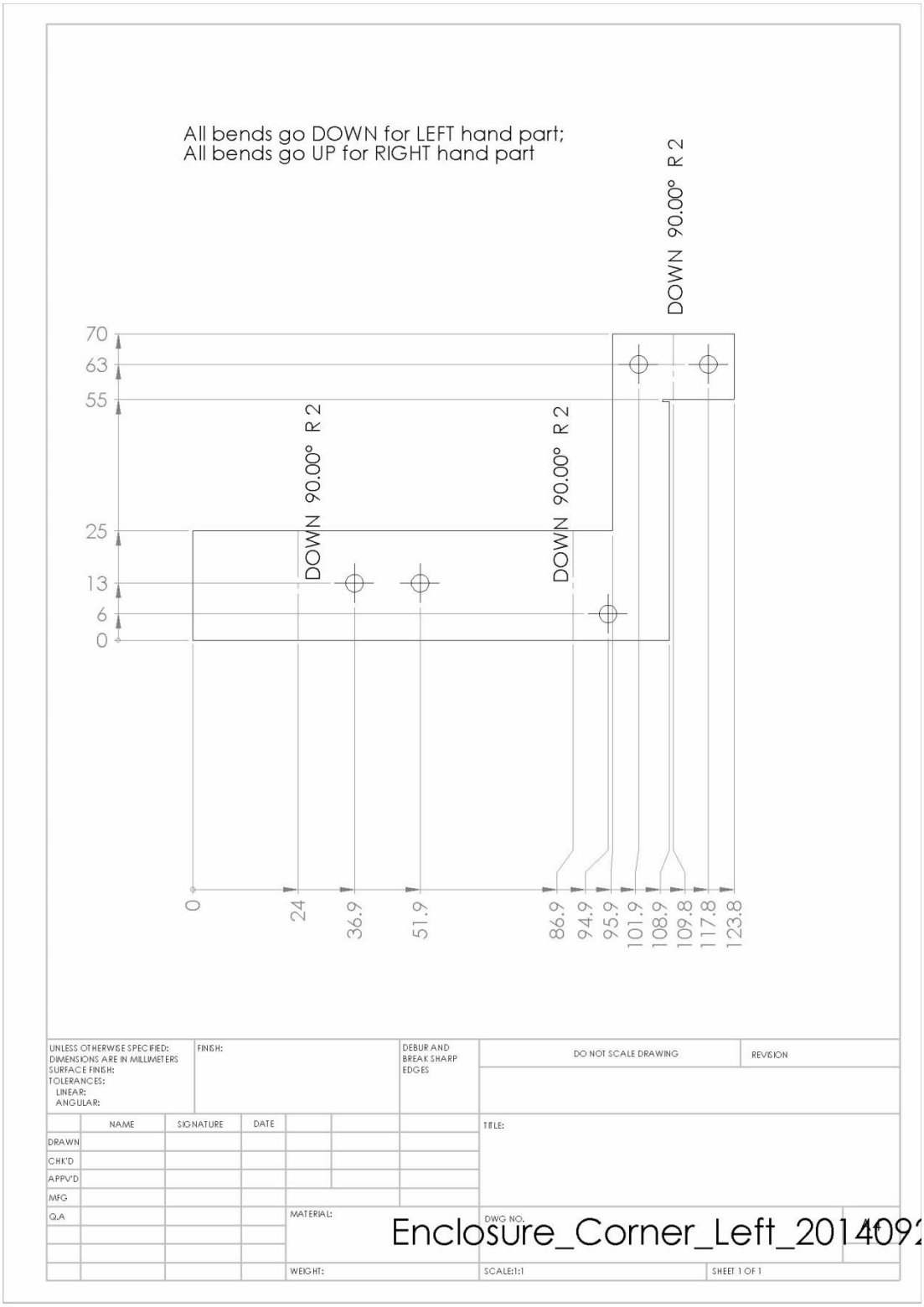

Technical Drawing 24. High power electrical feedthrough enclosure terminal block support plates.

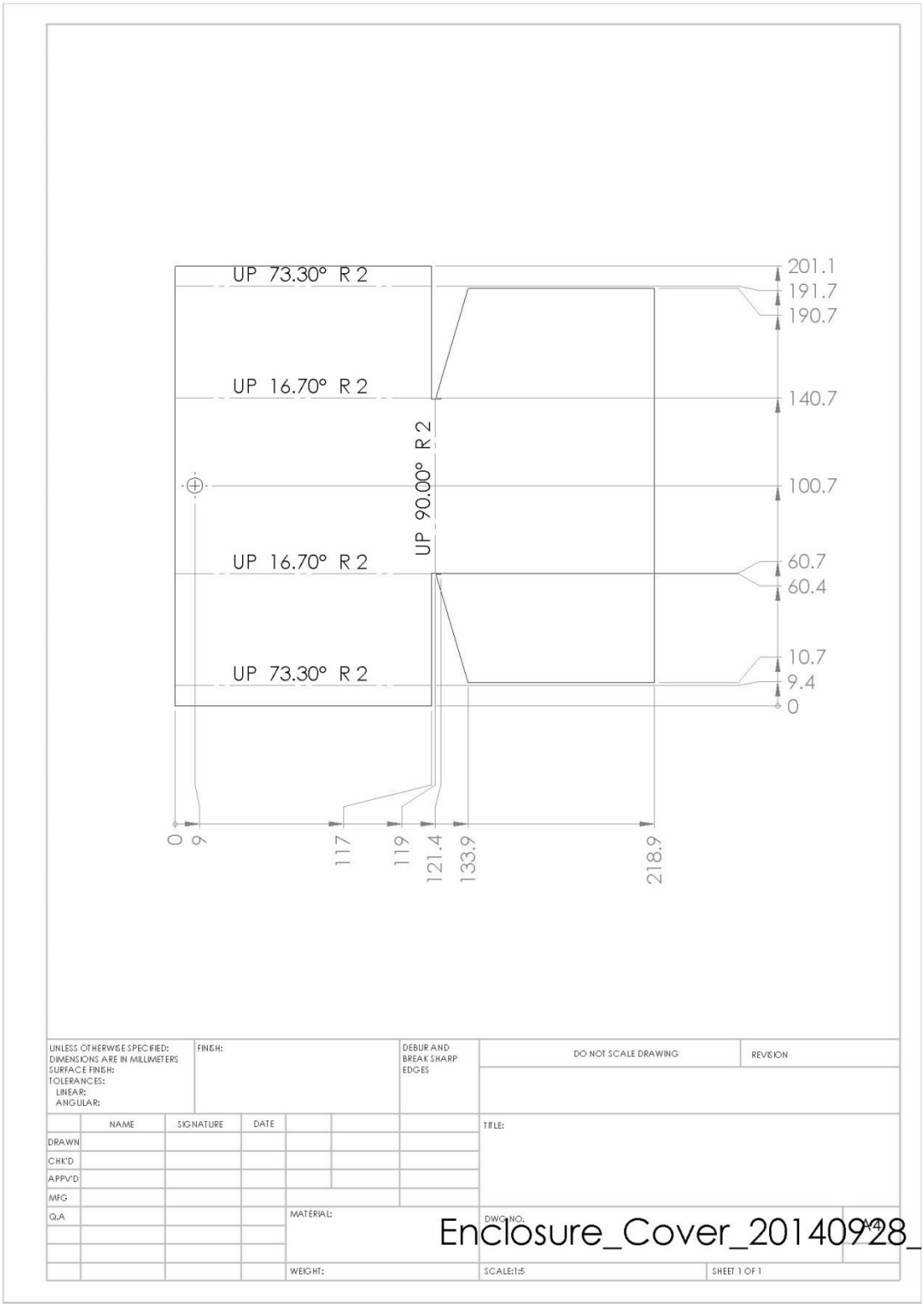

Technical Drawing 25. High power electrical feedthrough enclosure cover.

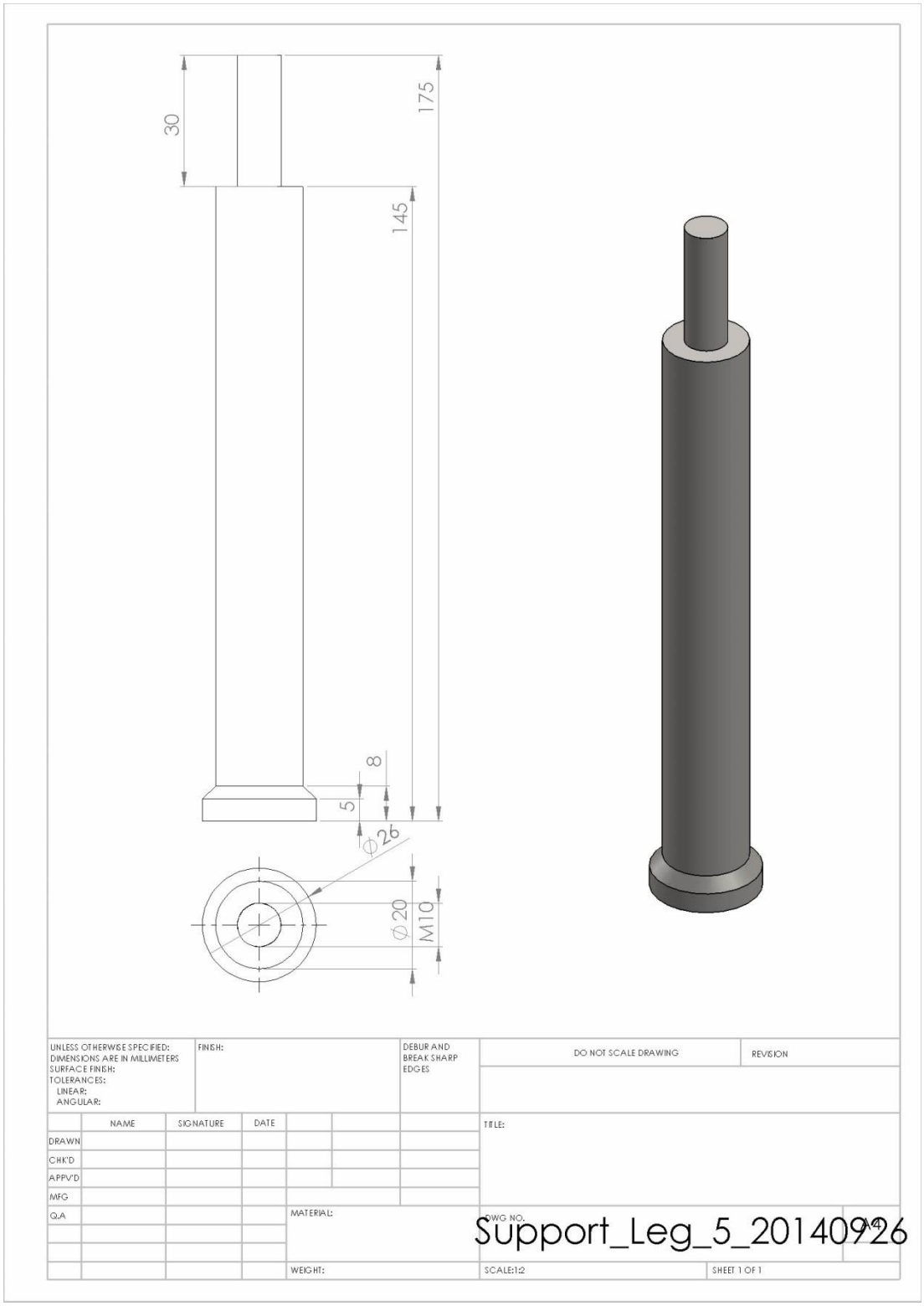

Technical Drawing 26. Revised baseplate leg.

9 APPENDIX B – WIRING TABLES

Table B1. Auxiliary board pinout and wiring table.

Tomas CB01 Rev. 5 Pinout legend															
5V 1mA			12V 20mA sink			cDAQ pin			Wire		Relay Terminals				
B	1		A	1		NI9403	3		GRN		J	1			
	2		C	1		NI9403	4		GRNW			2			
	3		A	2		NI9403	5		ORG			3	+12VDC out		
	4		C	2		NI9403	6		ORGW			4	+12VDC in from Power supply		
	5		A	3		NI9403	20		BRO			5			
	6		C	3		NI9403	21		BROW			6			
	7		A	4		NI9403	22		BLU			7			
	8		C	4		NI9403	23		BLUW			8			
E	1		D	1		NI9403	7		GRN			9			
	2		F	1		NI9403	8		GRNW			A			
	3		D	2		NI9403	26		ORG			B			
	4		F	2		NI9403	27		ORGW						
	5		D	3		NI9403	11		BRO						
	6		F	3		NI9403	12		BROW						
	7		D	4		NI9403	30		BLU						
	8		F	4		NI9403	31		BLUW						
Power input															
G	1		GND			From Power Supply									
	2		+12V												
	3		+12V												
	4		+12V												
	5		+12V			To CB02 C3									
	6		GND			To CB02 C1									
10V output															
H	1		GND			To force sensor			BLA						
	2		+10V			To force sensor			WHI						
	3		GND						BLA						
LM335A curren tlimiter															
L	1		GND			NI9219/ LM335A			WHI						
	2		1mA @12 V/ CJR output			NI9219/ LM335A			RED						
	3		GND						WHI						
12V 1A															
N	1		GND when K6 is high												
	2		+12V												
	3		GND when K6 is high												
5V 1mA			Action								cDAQ pin			Wire	
K	1		R	1		J1-J2 NC to Open					NI9403	15		RED	
	2		NC								NI9403	16		GRN	
	3		R	3		J5-J6 NO to Closed					NI9403	17		YEL	
	4		Buzzer On								NI9403	36		ORA	
	5		GND								NI9403	28		BLU	
	6		N			1A current max through 3710 On					NI9403	37		GRY	
	7		R	4		J7-J8 NO to Closed					NI9403	34		BRO	
	8		R	5		J9-J10 NC to Open J10-J11 NO to Closed					NI9403	35		PUR	
M	1		1Hz square wave SSR Ready input								NI9403	1		BLA	
	2		SSR + output								SSR	+		YEL	
	3		GND											PUR	
	4		SSR ON signal								NI9403	2		BRO	
	5		NC											GRY	
	6		NC											ORA	
	7		SSR - output								SSR	-		GRN	
	8		GND								NI9403	9		BLU	

Table B2. Electronic load circuit board pinout and wiring table.

	Tomas CB02 Rev. 11 Wiring legend								
Pin		I/O	Description	Wire color	Goes to				
A	1	I	R1 Control	GRY	NI 9403	13			
	2	O	Load Voltage -	BLU	NI 9219	C2	5		
	3	O	Load/ Module Voltage +	YEL+RED	NI 9219	C2	4	C1	4
	4	O	R1 Status	ORG	NI 9403	33			
	5			PUR					
	6	I	GND/ Module Voltage -	BRO+GRN	NI 9403	10		C1	5
	7	I	R2 Control	BLA	NI 9403	14			
	8	I	R3+R4 Control	WHI	NI 9403	32			
B	1	I	Direct mosfet control	RED	NI 9263	2			
	2	I	GND	BLA	NI 9263	3			
	3	O	20A current V+	BRO	NI 9213	15			
	4	O	20A current V-	GRY	NI 9213	33			
	5	O	5A current V+	YEL	NI 9213	16			
	6	O	5A current V-	GRN	NI 9213	34			
	7	I	GND	ORG	NI 9263	1			
	8	I	Current setting 0-10V	PUR	NI 9263	0			
				WHI	NI 9213	14			
				BLU	NI 9213	32			
C	1	I	GND		From CB01 G6				
	2								
	3	I	Power +12V		From CB01 G5				
	4								
	5	I	GND						
D	1				20A shunt				
	2				20A shunt				
	3	O	Load -		Load				
	4	O	Load +		Load				
	5	I	Module +	RED	Module				
	6	I	Module -	BLU	Module				
	7				5A shunt				
	8				5A shunt				
E	1								
	2								
	3								
	4								
e	1								
	2								
	3								
	4								
P	1		20A from PS @10V from 9263		Adjusts response to NI9263 signal				
	2		3.10V		Turns on fan @ 310K				
	3		3.40V		Turns off mosfet @ 340K				
	4		R1 ON @ 5A		5A shunt protector relay				

Table 9.1. NI C-Series module wiring and channel assignments.

cDAQ wiring

NI 9403		Cable	Wire	Description	CB Pin	Out Pin	NI 9219			Cable	Wire	Description	Data column	NI 9213		Wire			Wire	Cable	Description	CJR	Data column
1	DIO00	CB01LM	BLA	SSR Ready			Ch0	4	V+	CB01LM/	RED/ORG	CJR+	18	1	NC		19	NC					
2	DIO01	CB01LM	BRO	SSR ON				5	V-	C1	WHI/BLU	CJR-		2	TC00+	WHI	20	TC00-	BLA	C1	Heater thick	TC1	2
3	DIO02	CB01B	GRN	LED	B1	A1								3	TC01+	RED	21	TC01-	ORG	C2	Top-Top	TC4	3
4	DIO03	CB01B	GRNW	LED	B2	C1	Ch1	4	V+	CB02A	RED	Module V+	19	4	TC02+	BLU	22	TC02-	PUR	C2	Top-Bottom	TC5	4
5	DIO04	CB01B	ORA	LED	B3	A2		5	V-	CB02A	GRN	Module V-		5	TC03+	WHI	23	TC03-	BLA	C2	Bottom-Top	TC6	5
6	DIO05	CB01B	ORAW	LED	B4	C2								6	TC04+	GRY	24	TC04-	BRO	C2	Bottom-Bottom	TC7	6
7	DIO06	CB01E	GRN	LED	E1	D1	Ch2	4	V+	CB02A	YEL	Load V+	20	7	TC05+	GRN	25	TC05-	YEL	C1	Cooler	TC3	7
8	DIO07	CB01E	GRNW	LED	E2	F1		5	V-	CB02A	BLU	Load V-		8	TC06+	GRY	26	TC06-	BRO	C1	Heater thin	TC2	8
9	COM	CB01LM	BLU	GND										9	TC07+		27	TC07-					9
10	COM	CB02A	BRO	GND			Ch3	4	V+				21	10	TC08+		28	TC08-					10
11	DIO08	CB01E	BRO	LED	E5	D3		5	V-					11	TC09+		29	TC09-					11
12	DIO09	CB01E	BROW	LED	E6	F3								12	TC10+		30	TC10-					12
13	DIO10	CB02A	GRY	CB02 R1										13	TC11+		31	TC11-					13
14	DIO11	CB02A	BLA	CB02 R2										14	TC12+		32	TC12-					14
15	DIO12	CB01HK	RED	CB01 R1			NI 9263			Cable	Wire	Description		15	TC13+	BRO	33	TC13-	GRY	CB02B	20A shunt		15
16	DIO13	CB01HK	GRN	CB01 R2										16	TC14+	YEL	34	TC14-	GRN	CB02B	5A shunt		16
17	DIO14	CB01HK	YEL	CB01 R3				0	AO0	CB02B	PUR	Set comparator		17	TC15+	BRO	35	TC15-	GRN	C3	Force sensor		17
18	DIO15							1	Com	CB02B	ORG			18	Com		36	Com					
19	RSVD							2	AO1	CB02B	RED	Mosfet gate											
20	DIO16	CB01B	BRO	LED	B5	A3		3	Com	CB02B	BLA												
21	DIO17	CB01B	BROW	LED	B6	C3		4	AO2														
22	DIO18	CB01B	BLU	LED	B7	A4		5	Com														
23	DIO19	CB01B	BLUW	LED	B8	C4		6	AO3														
24	DIO20							7	Com														
25	DIO21							8	NC														
26	DIO22	CB01E	ORG	LED	E3	D2		9	Com														
27	DIO23	CB01E	ORGW	LED	E4	F2																	
28	COM	CB01HK	BLU	GND																			
29	COM																						
30	DIO24	CB01E	BLU	LED	E7	D4																	
31	DIO25	CB01E	BLUW	LED	E8	F4																	
32	DIO26	CB02A	WHI	CB02 R3+R4																			
33	DIO27	CB02A	ORG	CB02 R1 Status																			
34	DIO28	CB01HK	BRO	CB01 R4																			
35	DIO29	CB01HK	PUR	CB01 R5																			
36	DIO30	CB01HK	ORG	Alarm ON																			
37	DIO31	CB01HK	GRY	Mosfet ON																			

Table 9.2. CJR terminal assignments and wiring of the baseplate feedthrough connectors.

	CJR wires								
	CJR pin	Dedicated	Cable	Wire	Feedthr	Wire	Cable	Fdt Bottom	
					Top				
	1	NC							
	2	TC8+	1N	BLU	15	GRN	C2	3	
	3	TC8-	1N	WHI	16	YEL	C2	2	
	4	TC9+	1N	GRY	48				
	5	TC9-	1N	YEL	47				
	6	TC10+	2N	BRO	46				
	7	TC10-	2N	WHI	45	PUR	C3	39	
	8	TC11+	2N	BLU	44	BLU	C3	40	
	9	TC11-	2N	YEL	43	ORA	C3	41	
	10	F IN- BLK	2N	GRN	42	RED	C3	42	
	11	F IN+ RED	3N	YEL	41	YEL	C3	43	
	12	F O- GRN	3N	GRN	40	GRN	C3	44	
	13	F O+ WHI	3N	BLU	39	BRO	C3	45	
	14	NC							
	15	NC							
	16	NC							
	17	TC7-	1N	ORA	14	BRO	C2	4	
	18	TC7+	1N	PUR	13	RGY	C2	5	
	19	TC6-	1N	RED	12	BLA	C2	6	
	20	TC6+	1N	BLA	11	WHI	C2	7	
	21	TC5-	2N	ORA	10	PUR	C2	8	
	22	TC5+	2N	PUR	9	BLU	C2	9	
	23	TC4-	2N	RED	8	ORA	C2	10	
	24	TC4+	2N	BLA	7	RED	C2	11	
	25	TC3-	2N	GRY	6	YEL	C1	12	
	26	TC3+	3N	RED	5	GRN	C1	13	
	27	TC2-	3N	BLA	4	BRO	C1	14	
	28	TC2+	3N	PUR	3	GRY	C1	15	
	29	TC1-	3N	BRO	2	BLA	C1	16	
	30	TC1+	3N	GRY	1	WHI	C1	17	
	A-	335A1-	1N	BRO	24	BLU	C1	27	
	B+	335A1+	1N	GRN	25	PUR	C1	26	
	C-	335A2-	3N	WHI	22	RED	C1	29	
	D+	335A2+	3N	ORA	23	ORA	C1	28	

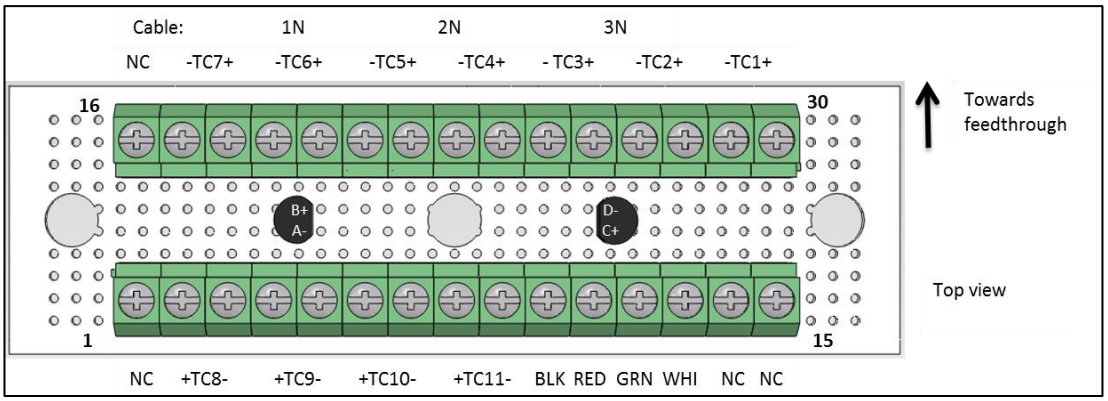

Figure 9.1. CJR terminal assignments.

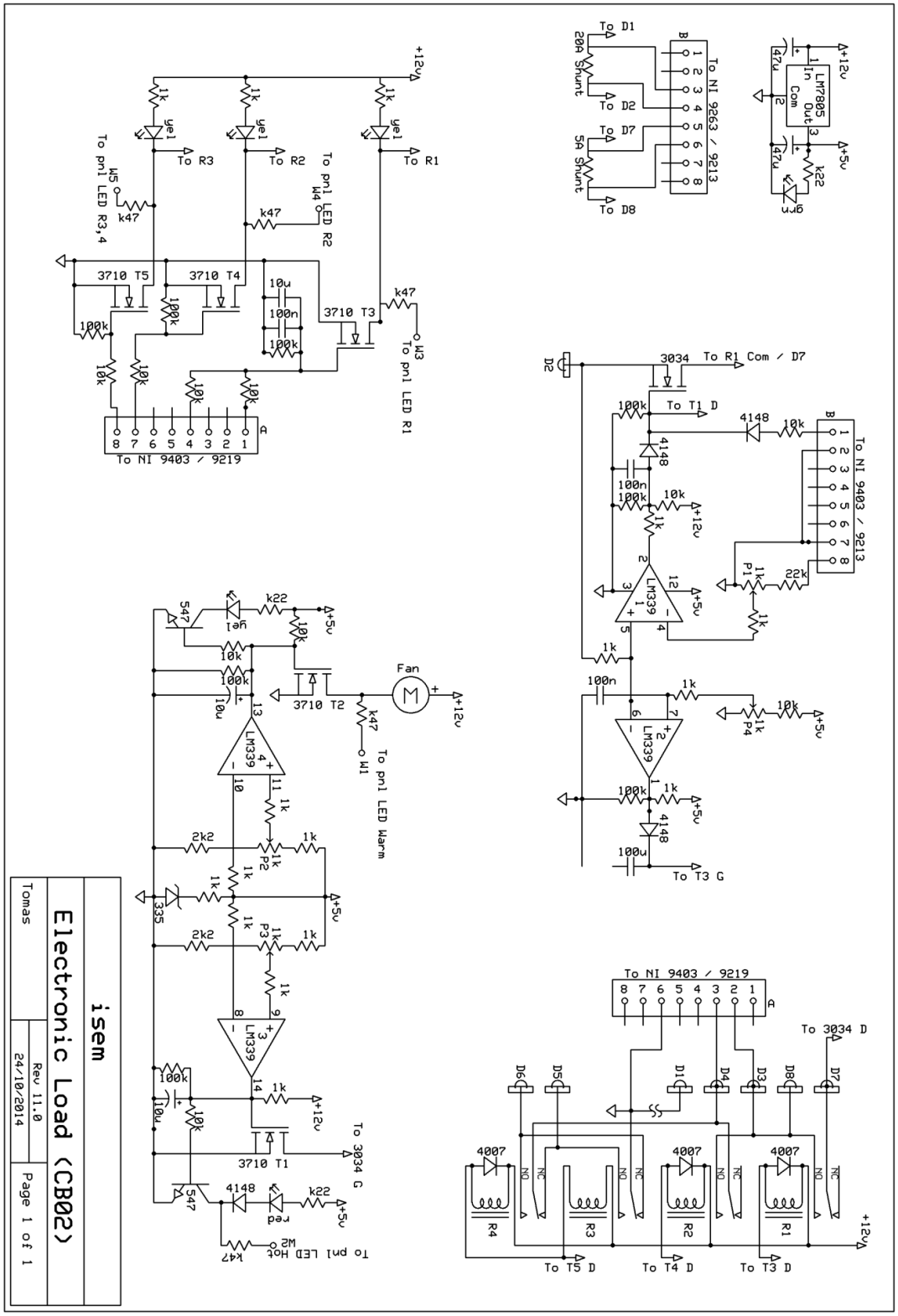

Figure 9.2. Electronic circuit diagrams for the Electronic Load board.

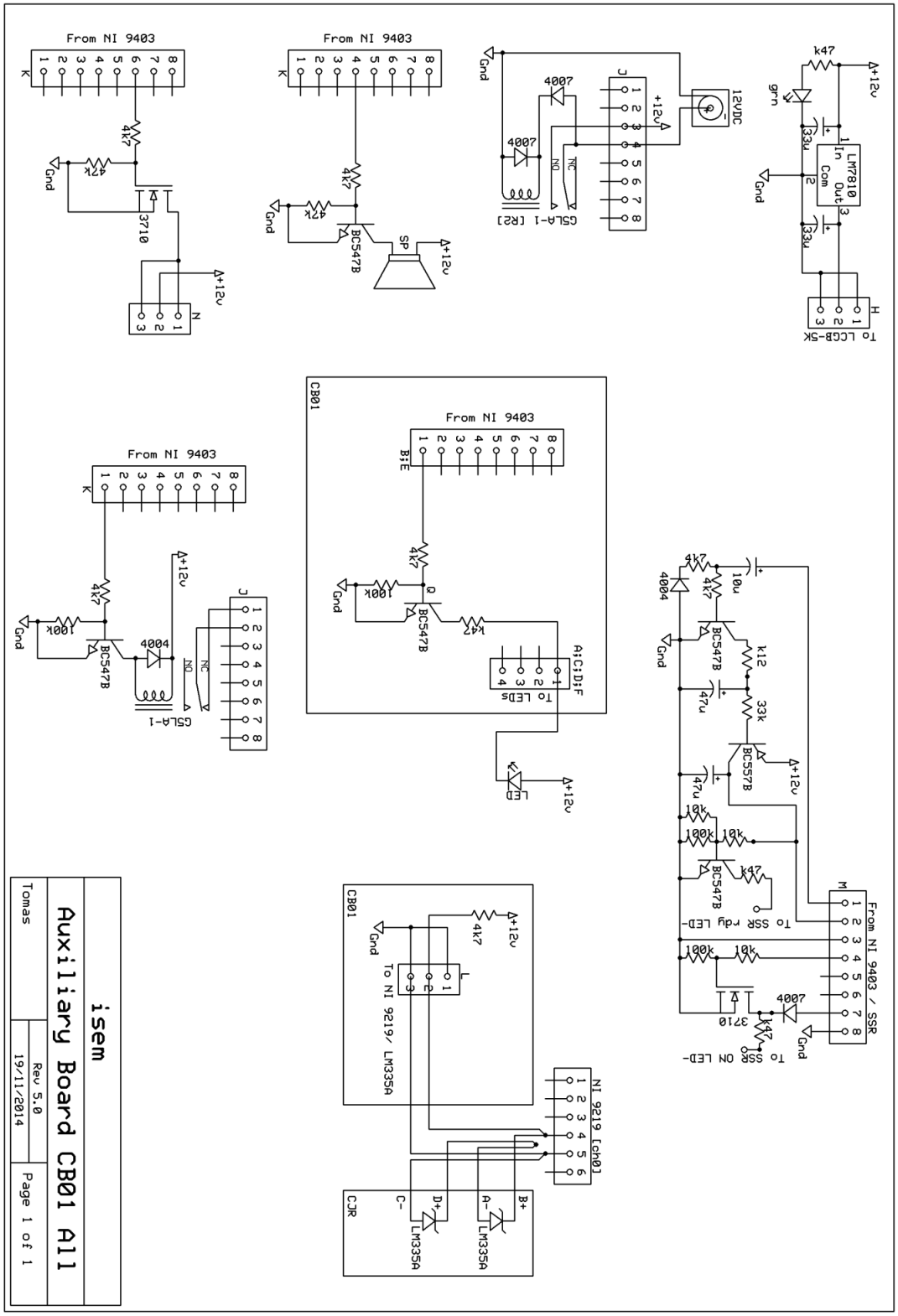

Figure 9.3. Electronic circuit diagrams for the Auxiliary Circuit Board.

10 REFERENCES

1. Decher, R., *Direct Energy Conversion: Fundamentals of Electric Power Production*. 1997: Oxford University Press.
2. Du, C.Y. and C.D. Wen, *Experimental investigation and numerical analysis for one-stage thermoelectric cooler considering Thomson effect.* International Journal of Heat and Mass Transfer, 2011. **54**(23–24): p. 4875-4884.
3. Chen, J., Z. Yan, and L. Wu, *The influence of Thomson effect on the maximum power output and maximum efficiency of a thermoelectric generator.* Journal of Applied Physics, 1996. **79**(11): p. 8823-8828.
4. Gao, M., D.M. Rowe, and K. Kontostavlakis, *Thermoelectric figure-of-merit under large temperature differences.* Journal of Physics D: Applied Physics, 2004. **37**(8): p. 1301.
5. Han, C., Z. Li, and S.X. Dou, *Recent progress in thermoelectric materials.* Chinese Science Bulletin, 2014. **59**(18): p. 2073-2091.
6. Brignone, M. and A. Ziggiotti, *Impact of novel thermoelectric materials on automotive applications.* AIP Conference Proceedings, 2011. **1449**(1): p. 493-496.
7. Gao, M. and N.M. Yatim, *Variable thermal resistor based on self-powered Peltier effect.* Journal of Physics D: Applied Physics, 2008. **41**(22): p. 222001.
8. Chiwanga, S., et al., *Characterisation of commercial thermoelectric module using experimental and numerical Techniques to compile performance data*. 2012.
9. Rowe, D.M. and G. Min, *Evaluation of thermoelectric modules for power generation.* Journal of Power Sources, 1998. **73**(2): p. 193-198.
10. McCarty, R. and R. Piper, *Voltage–Current Curves to Characterize Thermoelectric Generators.* Journal of Electronic Materials, 2015: p. 1-6.
11. Simons, R.E. and R.C. Chu. *Application of thermoelectric cooling to electronic equipment: a review and analysis*. in *Semiconductor Thermal Measurement and Management Symposium, 2000. Sixteenth Annual IEEE*. 2000.
12. Min, G. and D.M. Rowe, *Experimental evaluation of prototype thermoelectric domestic-refrigerators.* Applied Energy, 2006. **83**(2): p. 133-152.
13. Astrain, D., A. Martinez, and A. Rodriguez, *Improvement of a thermoelectric and vapour compression hybrid refrigerator.* Applied Thermal Engineering, 2012. **39**: p. 140-150.
14. Luo, Q., et al., *A novel water heater integrating thermoelectric heat pump with separating thermosiphon.* Applied Thermal Engineering, 2005. **25**(14–15): p. 2193-2203.
15. Knox, A.R., et al., *Megawatt-Scale Application of Thermoelectric Devices in Thermal Power Plants.* Journal of Electronic Materials, 2013. **42**(7): p. 1807-1813.
16. Rowe, D.M., *Thermoelectrics Handbook: Macro to Nano*. 2005: CRC Press.
17. Rowe, D.M., *Thermoelectrics, an environmentally-friendly source of electrical power.* Renewable Energy, 1999. **16**(1–4): p. 1251-1256.

18. NASA. *Radioisotope Power Systems*. 2012; Available from: https://solarsystem.nasa.gov/rps/voyager.cfm.
19. Rowe, D.M., *Thermoelectric Waste Heat Recovery as a Renewable Energy Source*. 2006.
20. Heywood, J., *Internal Combustion Engine Fundamentals*. 1988: McGraw-Hill Education.
21. Haidar, J.G. and J.I. Ghojel. *Waste heat recovery from the exhaust of low-power diesel engine using thermoelectric generators*. in *Thermoelectrics, 2001. Proceedings ICT 2001. XX International Conference on*. 2001.
22. Anatychuk, L.I., R.V. Kuz, and Y.Y. Rozver, *Efficiency of thermoelectric recuperators of the exhaust gas energy of internal combustion engines.* AIP Conference Proceedings, 2012. **1449**(1): p. 516-519.
23. Crane, D., et al., *TEG On-Vehicle Performance and Model Validation and What It Means for Further TEG Development.* Journal of Electronic Materials, 2013. **42**(7): p. 1582-1591.
24. Risse, S. and H. Zellbeck, *Close-Coupled Exhaust Gas Energy Recovery In A Gasoline Engine.* MTZ worldwide, 2013. **74**(1): p. 54-61.
25. Fergus, J.W., *Oxide materials for high temperature thermoelectric energy conversion.* Journal of the European Ceramic Society, 2012. **32**(3): p. 525-540.
26. Nuwayhid, R.Y., A. Shihadeh, and N. Ghaddar, *Development and testing of a domestic woodstove thermoelectric generator with natural convection cooling.* Energy Conversion and Management, 2005. **46**(9–10): p. 1631-1643.
27. Killander, A. and J.C. Bass. *A stove-top generator for cold areas*. in *Thermoelectrics, 1996., Fifteenth International Conference on*. 1996.
28. Rinalde, G.F., et al., *Development of thermoelectric generators for electrification of isolated rural homes.* International Journal of Hydrogen Energy, 2010. **35**(11): p. 5818-5822.
29. Champier, D., et al., *Study of a TE (thermoelectric) generator incorporated in a multifunction wood stove.* Energy, 2011. **36**(3): p. 1518-1526.
30. O'Shaughnessy, S.M., et al., *Small scale electricity generation from a portable biomass cookstove: Prototype design and preliminary results.* Applied Energy, 2013. **102**(0): p. 374-385.
31. Kinsella, C.E., et al., *Battery charging considerations in small scale electricity generation from a thermoelectric module.* Applied Energy, 2014. **114**(0): p. 80-90.
32. Chen, M., et al., *Energy efficiency analysis and impact evaluation of the application of thermoelectric power cycle to today's CHP systems.* Applied Energy, 2010. **87**(4): p. 1231-1238.
33. Vieira, J.A.B. and A.M. Mota. *Thermoelectric generator using water gas heater energy for battery charging*. in *Control Applications, (CCA) & Intelligent Control, (ISIC), 2009 IEEE*. 2009.
34. Min, G. and D.M. Rowe, *"Symbiotic" application of thermoelectric conversion for fluid preheating/power generation.* Energy Conversion and Management, 2002. **43**(2): p. 221-228.
35. Furue, T., et al. *Case study on thermoelectric generation system utilizing the exhaust gas of interal-combustion power plant*. in *Thermoelectrics, 1998. Proceedings ICT 98. XVII International Conference on*. 1998.

36. Kyono, T., R.O. Suzuki, and K. Ono, *Conversion of unused heat energy to electricity by means of thermoelectric generation in condenser.* Energy Conversion, IEEE Transactions on, 2003. **18**(2): p. 330-334.
37. Kaibe, H., et al., *Thermoelectric generating system attached to a carburizing furnace at Komatsu Ltd., Awazu Plant.* AIP Conference Proceedings, 2011. **1449**(1): p. 524-527.
38. Suter, C., Z.R. Jovanovic, and A. Steinfeld, *A 1kW thermoelectric stack for geothermal power generation – Modeling and geometrical optimization.* Applied Energy, 2012. **99**(0): p. 379-385.
39. Sark, W.G.J.H.M., *Feasibility of photovoltaic – Thermoelectric hybrid modules.* Applied Energy, 2011. **88**(8): p. 2785-2790.
40. Dajiang, Y. and Y. Huiming, *Energy Conversion Efficiency of a Novel Hybrid Solar System for Photovoltaic, Thermoelectric, and Heat Utilization.* Energy Conversion, IEEE Transactions on, 2011. **26**(2): p. 662-670.
41. Xiao, J., et al., *Thermal design and management for performance optimization of solar thermoelectric generator.* Applied Energy, 2012. **93**(0): p. 33-38.
42. Qiu, K. and A.C.S. Hayden, *Development of a novel cascading TPV and TE power generation system.* Applied Energy, 2012. **91**(1): p. 304-308.
43. Date, A., et al., *Progress of thermoelectric power generation systems: Prospect for small to medium scale power generation.* Renewable and Sustainable Energy Reviews, 2014. **33**(0): p. 371-381.
44. Ferrari, M., et al. *Characterization of Thermoelectric Modules for Powering Autonomous Sensors*. in *Instrumentation and Measurement Technology Conference Proceedings, 2007. IMTC 2007. IEEE*. 2007.
45. Yu, H., et al. *Design and investigation of photovoltaic and thermoelectric hybrid power source for wireless sensor networks*. in *3rd IEEE International Conference on Nano/Micro Engineered and Molecular Systems*. 2008.
46. Ramadass, Y.K. and A.P. Chandrakasan, *A Battery-Less Thermoelectric Energy Harvesting Interface Circuit With 35 mV Startup Voltage.* Solid-State Circuits, IEEE Journal of, 2011. **46**(1): p. 333-341.
47. Kim, J. and C. Kim, *A DC-DC Boost Converter With Variation-Tolerant MPPT Technique and Efficient ZCS Circuit for Thermoelectric Energy Harvesting Applications.* Power Electronics, IEEE Transactions on, 2013. **28**(8): p. 3827-3833.
48. Elefsiniotis, A., et al., *A thermoelectric-based energy harvesting module with extended operational temperature range for powering autonomous wireless sensor nodes in aircraft.* Sensors and Actuators A: Physical, 2014. **206**(0): p. 159-164.
49. Elefsiniotis, A., et al., *Efficient Power Management for Energy-Autonomous Wireless Sensor Nodes for Aeronautical Applications.* Journal of Electronic Materials, 2013. **42**(7): p. 1907-1910.
50. Buckle, J.R., et al., *Autonomous Underwater Vehicle Thermoelectric Power Generation.* Journal of Electronic Materials, 2013. **42**(7): p. 2214-2220.
51. Patyk, A., *Thermoelectrics: Impacts on the Environment and Sustainability.* Journal of Electronic Materials, 2010. **39**(9): p. 2023-2028.
52. Patyk, A., *Thermoelectric generators for efficiency improvement of power generation by motor generators – Environmental and economic perspectives.* Applied Energy, 2013. **102**(0): p. 1448-1457.

53. Ismail, B.I. and W.H. Ahmed, *Thermoelectric Power Generation Using Waste-Heat Energy as an Alternative Green Technology.* Recent Patents on Electrical Engineering, 2009. **2**(1): p. 27.
54. Zebarjadi, M., et al., *Perspectives on thermoelectrics: from fundamentals to device applications.* Energy & Environmental Science, 2012. **5**(1): p. 5147-5162.
55. Biswas, K., et al., *High-performance bulk thermoelectrics with all-scale hierarchical architectures.* Nature, 2012. **489**(7416): p. 414-418.
56. Mehta, R.J., et al., *A new class of doped nanobulk high-figure-of-merit thermoelectrics by scalable bottom-up assembly.* Nat Mater, 2012. **11**(3): p. 233-240.
57. Rauscher, L., et al., *Efficiency determination and general characterization of thermoelectric generators using an absolute measurement of the heat flow.* Measurement Science & Technology, 2005. **16**(5): p. 1054-1060.
58. Takazawa, H., et al. *Efficiency measurement of thermoelectric modules operating in the temperature difference of up to 550K*. in *Thermoelectrics, 2006. ICT '06. 25th International Conference on*. 2006.
59. Sandoz-Rosado, E. and R.J. Stevens, *Experimental Characterization of Thermoelectric Modules and Comparison with Theoretical Models for Power Generation.* Journal of Electronic Materials, 2009. **38**(7): p. 1239-1244.
60. Hun Sik, H., et al. *Performance measurement and analysis of a thermoelectric power generator*. in *Thermal and Thermomechanical Phenomena in Electronic Systems (ITherm), 2010 12th IEEE Intersociety Conference on*. 2010.
61. Anatychuk, L.I. and M.V. Havrylyuk, *Procedure and Equipment for Measuring Parameters of Thermoelectric Generator Modules.* Journal of Electronic Materials, 2011. **40**(5): p. 1292-1297.
62. Faraji, A.Y. and A. Akbarzadeh, *Design of a Compact, Portable Test System for Thermoelectric Power Generator Modules.* Journal of Electronic Materials, 2013. **42**(7): p. 1535-1541.
63. Populoh, S., et al., *Construction of a High Temperature Teg Measurement System for the Evaluation of Thermoelectric Oxide Modules.* Functional Materials Letters, 2013. **6**(5).
64. Montecucco, A., et al., *A New Test Rig for Accurate Nonparametric Measurement and Characterization of Thermoelectric Generators.* Journal of Electronic Materials, 2013. **42**(7): p. 1966-1973.
65. Hejtmanek, J., et al., *Test System for Thermoelectric Modules and Materials.* Journal of Electronic Materials, 2014. **43**(10): p. 3726-3732.
66. Nielsen, K.K., et al., *Development of High - Temperature Thermoelectric Module Characterisation in Vacuum*, in *ICT2014*. 2014: Nashville.
67. Lineykin, S. and S. Ben-Yaakov, *Modeling and Analysis of Thermoelectric Modules.* Industry Applications, IEEE Transactions on, 2007. **43**(2): p. 505-512.
68. Laird, I., et al. *Comparative study of maximum power point tracking algorithms for thermoelectric generators*. in *Power Engineering Conference, 2008. AUPEC '08. Australasian Universities*. 2008.
69. Alata, M., M.A. Al-Nimr, and M. Naji, *Transient Behavior of a Thermoelectric Device Under the Hyperbolic Heat Conduction Model.* International Journal of Thermophysics, 2003. **24**(6): p. 1753-1768.

70. Brignone, M., et al., *Generator of electric energy based on the thermoelectric effect*. 2013, Google Patents.
71. Wang, Y., C. Dai, and S. Wang, *Theoretical analysis of a thermoelectric generator using exhaust gas of vehicles as heat source.* Applied Energy, 2013. **112**(0): p. 1171-1180.
72. Min, C., et al., *Numerical Modeling of Thermoelectric Generators With Varing Material Properties in a Circuit Simulator.* Energy Conversion, IEEE Transactions on, 2009. **24**(1): p. 112-124.
73. Chen, L.H., et al., *Modeling and Power Conditioning for Thermoelectric Generation.* 2008 Ieee Power Electronics Specialists Conference, Vols 1-10, 2008: p. 1098-1103.
74. Nagayoshi, H. and T. Kajikawa. *Mismatch Power Loss Reduction on Thermoelectric Generator Systems Using Maximum Power Point Trackers*. in *Thermoelectrics, 2006. ICT '06. 25th International Conference on*. 2006.
75. Rae-young, K. and L. Jih-Sheng, *A Seamless Mode Transfer Maximum Power Point Tracking Controller For Thermoelectric Generator Applications.* Power Electronics, IEEE Transactions on, 2008. **23**(5): p. 2310-2318.
76. Rae-young, K., et al., *Analysis and Design of Maximum Power Point Tracking Scheme for Thermoelectric Battery Energy Storage System.* Industrial Electronics, IEEE Transactions on, 2009. **56**(9): p. 3709-3716.
77. Sungkyu, C., et al. *A coreless maximum power point tracking circuit of thermoelectric generators for battery charging systems*. in *Solid State Circuits Conference (A-SSCC), 2010 IEEE Asian*. 2010.
78. Schwartz, D.E. *A maximum-power-point-tracking control system for thermoelectric generators*. in *Power Electronics for Distributed Generation Systems (PEDG), 2012 3rd IEEE International Symposium on*. 2012.
79. Pilawa-Podgurski, R.C.N. and D.J. Perreault. *Sub-module integrated distributed maximum power point tracking for solar photovoltaic applications*. in *Energy Conversion Congress and Exposition (ECCE), 2012 IEEE*. 2012.
80. Wu, H., et al., *Evaluation of Power Conditioning Architectures for Energy Production Enhancement in Thermoelectric Generator Systems.* Journal of Electronic Materials, 2014. **43**(6): p. 1567-1573.
81. Poshtkouhi, S., et al., *A General Approach for Quantifying the Benefit of Distributed Power Electronics for Fine Grained MPPT in Photovoltaic Applications Using 3-D Modeling.* Power Electronics, IEEE Transactions on, 2012. **27**(11): p. 4656-4666.
82. Molina, M.G., et al., *Design of improved controller for thermoelectric generator used in distributed generation.* International Journal of Hydrogen Energy, 2010. **35**(11): p. 5968-5973.
83. Laird, I. and D.D.C. Lu, *High Step-Up DC/DC Topology and MPPT Algorithm for Use With a Thermoelectric Generator.* Power Electronics, IEEE Transactions on, 2013. **28**(7): p. 3147-3157.
84. Sun, K., et al., *Evaluation of High Step-Up Power Electronics Stages in Thermoelectric Generator Systems.* Journal of Electronic Materials, 2013. **42**(7): p. 2157-2164.
85. Yu, C. and K.T. Chau, *Thermoelectric automotive waste heat energy recovery using maximum power point tracking.* Energy Conversion and Management, 2009. **50**(6): p. 1506-1512.

86. Damaschke, J.M., *Design of a low-input-voltage converter for thermoelectric generator*. Industry Applications, IEEE Transactions on, 1997. **33**(5): p. 1203-1207.
87. Carlson, E.J., K. Strunz, and B.P. Otis, *A 20 mV Input Boost Converter With Efficient Digital Control for Thermoelectric Energy Harvesting.* Solid-State Circuits, IEEE Journal of, 2010. **45**(4): p. 741-750.
88. Orellana, M., et al. *Four Switch Buck-Boost Converter for Photovoltaic DC-DC power applications*. in *IECON 2010 - 36th Annual Conference on IEEE Industrial Electronics Society*. 2010.
89. Dassault Systemes, *Sketching with SolidWorks*. 2014.
90. Dassault Systemes, *Modeling in 3D with SolidWorks*. 2014.
91. Dassault Systemes, *Creating Drawings with SolidWorks*. 2014.
92. Shinagawa Refractories Australasia PTY LTD, *Installation of Refractory Castables by Casting*. 2004.
93. Shinagawa Refractories Australasia PTY LTD, *Shiralite 160MW*. 2009.
94. Shinagawa Refractories Australasia PTY LTD, *HS/002 - Conventional Insulating Castables*. 2004.
95. Riken Environmental System Co. Ltd., *Heating materials / Electrical resistance materials / Heat-resistant construction materials*. 2008.
96. Thermcraft Inc., *Furnace Heating Elements – Design Considerations and Maintenance*. 2013.
97. Willis, J., *Kiln Design - An Introduction to Electric Kiln Heating*. 2013.
98. Hsu, C.T., et al., *An effective Seebeck coefficient obtained by experimental results of a thermoelectric generator module.* Applied Energy, 2011. **88**(12): p. 5173-5179.
99. Thermonamic, *Power Module Installation Notes*. 2014.
100. Texas Instruments Inc, *LM335A Precision Temperature Sensor Datasheet*. 2013.
101. National Instruments, *NI CompactDAQ USB Data Acquisition Systems*. 2014.
102. National Instruments, *NI 9403 5 V/TTL, Bidirectional Digital I/O, 32 Ch Module Datasheet*. 2014.
103. National Instruments, *NI 9403 Operating Instructions and Specifications*. 2014.
104. National Instruments, *NI 9263 ±10 V, Analog Output, 100 kS/s, 4 Ch Module Datasheet*. 2014.
105. National Instruments, *NI 9263 Operating Instructions and Specifications*. 2014.
106. National Instruments, *NI 9219 24-Bit Universal Analog Input Datasheet*. 2014.
107. National Instruments, *NI 9219 Operating Instructions and Specifications*. 2014.
108. National Instruments, *NI 9213 16-Channel Thermocouple Module Datasheet*. 2014.
109. National Instruments, *NI 9213 Operating Instructions and Specifications*. 2014.
110. Marktech Optoelectronics, *LC503AHR1−15Q-A Ultra Bright Red 5mm LED Datasheet*. 2010.
111. Motorola Inc., *BC547B NPN Silicon Amplifier Transistor Datasheet*. 1996.
112. Maxim Integrated Products, *MAX6969 16-Port, 5.5V Constant-Current LED Driver*. 2010.

113. Semiconductor Components Industries LLC, *CAT4016 16-Channel Constant Current LED Driver*. 2010.
114. Fairchild Semiconductor, *LM78XX 3-Terminal 1A Positive Voltage Regulator Datasheet*. 2012.
115. Omron Electronic Components LLC, *G5LA Cubic, Single-pole 10A Power PCB Relay*. 2011.
116. International Rectifier, *IRF3710 HEXFET Power MOSFET Datasheet*. 2002.
117. National Semiconductor, *LM339 Quad Comparator Datasheet*. 1994.
118. International Rectifier, *IRLP3034PbF HEXFET Power MOSFET Datasheet*. 2009.
119. NAIS, *CB1a-12V Relay Datasheet*. 2000.
120. Standards Australia, *AS/NZS 3000:2007 Wiring Rules*. 2007.
121. National Instruments. *What is LabVIEW*. 2015; Available from: www.ni.com.
122. Min, G. and D.M. Rowe, *Optimisation of thermoelectric module geometry for 'waste heat' electric power generation.* Journal of Power Sources, 1992. **38**(3): p. 253-259.
123. Rowe, D.M. and G. Min, *Design theory of thermoelectric modules for electrical power generation.* Science, Measurement and Technology, IEE Proceedings -, 1996. **143**(6): p. 351-356.
124. Thermonamic, *Specifications of Thermoelectric Module TEHP1-12656-0.3*. 2011.
125. Lienhard, J.H., *A Heat Transfer Textbook*. 2011: Dover Publications.
126. Maharaj, S. and P. Govender. *Waste energy harvesting with a thermoelectric generator*. in *Domestic Use of Energy Conference (DUE), 2013 Proceedings of the 21st*. 2013.
127. National Instruments, *The NI TDMS File Format*. 2014.